EXPLOITING THE OPTICAL PROPERTIES OF

EARTH ABUNDANT CUPROUS OXIDE

NANOCATALYSTS FOR ENERGY AND HEALTH

APPLICATIONS

By

RAVI TEJA ADDANKI TIRUMALA

Bachelor of Technology in Chemical Engineering
Sathyabama University
Chennai, India
2013

Master of Technology in Chemical Engineering
University of Petroleum and Energy Studies
Dehradun, India
2015

Submitted to the Faculty of the
Graduate College of the
Oklahoma State University
in partial fulfillment of
the requirements for
the Degree of
DOCTOR OF PHILOSOPHY
July, 2022

EXPLOITING THE OPTICAL PROPERTIES OF

EARTH ABUNDANT CUPROUS OXIDE

NANOCATALYSTS FOR ENERGY AND HEALTH

APPLICATIONS

Dissertation Approved:

Dr. Andiappan Marimuthu
_____
Dissertation Adviser

Dr. Jeffery L White
_____
Committee Chair

Dr. Seok-Jhin Kim
_____
Committee Member

Dr. Toby Larue Nelson
_____
Committee Member

ACKNOWLEDGEMENTS

Name: RAVI TEJA ADDANKI TIRUMALA

Date of Degree: JULY, 2022

Title of Study: EXPLOITING THE OPTICAL PROPERTIES OF EARTH ABUNDANT CUPROUS OXIDE NANOCATALYSTS FOR ENERGY AND HEALTH APPLICATIONS

Major Field: CHEMICAL ENGINEERING

Abstract: In this dissertation, we explore the optical properties of semiconductor materials, for energy and photocatalytic applications. In the past semiconductor materials used in photocatalytic reactions are prominently known through electron transfer mechanisms such as redox reactions, and local surface plasmon resonance (LSPR). In this work, we show substantial understanding and advantages of Mie resonances-based photocatalysis. Mie resonance-based photocatalytic mechanisms can find various applications in chemical manufacturing, pollution mitigation, and pharmaceutical industries. We developed an understanding that Mie resonances of metal-oxide nanoparticles are affected by material properties such as absorption and scattering coefficients, dielectric permittivity physical properties like geometry, size of these nanoparticles, and wavelength, and intensity of the incident light. In this work, we experimentally, demonstrate that the dielectric Mie resonances in cuprous oxide (Cu_2O) spherical and cubical nanostructures can be used to enhance the dye-sensitization rate of methylene blue dye. The Cu_2O nanostructures exhibit dielectric Mie resonances up to an order of magnitude higher dye-sensitization rate and photocatalytic rate as compared to Cu_2O nanostructures not exhibiting dielectric Mie resonances. We further established structure-property-performance relationships of these nanostructures and experimentally found evidence, that rate of dye sensitization is directly proportional to the overlap of absorption characteristics of the nanocatalyst, absorption of the dye, and the wavelength of incident light. This work has the potential to be used in pollution mitigation applications, Dye-Sensitized Solar Cells, etc. Gaining a deeper understanding of the characteristics of Cu_2O nanostructures, we have experimentally observed that tuning selectivity and activity of reactions can be achieved by modulating the incident wavelength of light. We performed intensity-dependent studies for methylene blue degradation for gaining mechanistic insights into selective photocatalysis. We explored C-C coupling reactions with small molecules which find applications majorly in the chemical and health industry. Carbon-carbon (C-C) coupling reactions are widely used to produce a range of compounds including pharmaceuticals, aromatic polymers, high-performance materials, and agrochemicals. For these reactions industrially, homogenous palladium (Pd) catalysts are used at high temperatures and are a solvent-intensive process. Palladium is expensive, toxic, and rare earth metal. However, the identification of truly heterogeneous versus homogeneous catalytic conditions remains an ongoing challenge within the field. In this research, we gained insights into the homogenous versus heterogeneous pathways using various analytical, experimental, and computational techniques. In this work, we found that Cu_2O nanoparticles can catalyze C-C coupling reactions under ligandless and base-free conditions via a truly heterogeneous pathway paving the way for the development of highly efficient, robust, and sustainable flow processes.

TABLE OF CONTENTS

LIST OF FIGURES

CHAPTER I

INTRODUCTION

Effects of climate change on the environment like rise in global temperatures, and exponential increase of CO_2 emissions are closely connected to the unsustainable anthropogenic consumption of fossil fuels[1,2]. These emissions are majorly contributed by coal, natural gas, and petroleum, occupying 84% of the total world energy mix as of 2019[3] leading to greenhouse gas (GHG) emissions. This sense of urgency has shifted the global energy policies[4–6] towards renewable energy generation through the rapid development of sustainable energy solutions. There has been lot of emphasis on using renewable energy for various applications ranging from energy generation (solar-electrical energy)[7–9] to photocatalytic processes where solar energy is harnessed for performing chemical transformations.[10]

1.1. Energy Generation

Solar energy is harnessed using photovoltaic cells, which converts incident solar radiations directly into electrical energy. Photovoltaic panels (monocrystalline, polycrystalline) are often made with silicon citing greater thermal stability, greater stability in light and in the presence of electric fields[11,12]. Thin film solar cells (TFSCs) are frequently stated as second-generation solar cells, made with amorphous silica, CdTe, multilayer systems based on III-IV group[13] elements like Copper indium gallium selenide (CIGS)[14], GaAs/AlGaAs are pursued as the materials of interest for harnessing solar energy. To improve the efficiency of these TFSCs, absorber layers

are added.[15] Absorber materials, with desired characteristics such as direct bandgap of ~1.5 eV, high absorption across solar spectrum~10^5/cm, higher quantum efficiency, longer diffusion length, etc are considered.[16] Silicon has an indirect bandgap of ~1.1 eV, consequently its inability to absorb photons lower than ~3.4 eV[13] which is higher wavelength than ~365 nm limits its applications in harnessing visible light region (400-700 nm). Various limiting parameters such as high recombination rate, multiple engineering designs are under research.

Recently, perovskite solar cells (PSCs) have attracted a lot of attention due to its ability to accommodate large cations in its structure.[18] Mineral name of Perovskite is calcium titanate ($CaTiO_3$), which is generally applied to the classification of materials having the same type of crystal lattice as $CaTiO_3$.[19]   Hybrid perovskite solar cells[20] such as carbon nanotube[21], fullerenes[22], triarylamine[23] based and interfacial engineering and careful considerations of materials gaining insights on electron-hole transports[24], can lead to developing high efficiency PSCs. The third generation of solar cells, commonly called Dye Sensitized Solar Cells (DSSCs) which were first developed by O'Regan and Grätzel[25]. Fundamentally DSSCs work on the electrochemical principle in which the dye absorbs the incident light, these excited molecules can inject electrons into the conduction band of TiO_2[25] semiconductor allowing for photocatalysis.
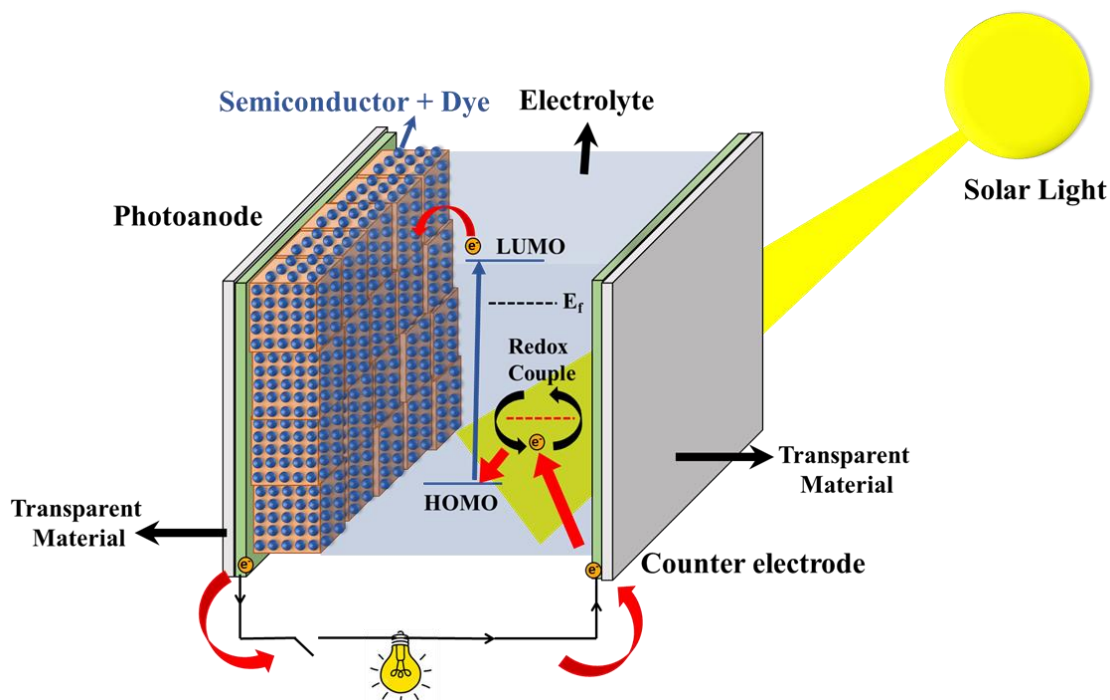
Figure 1.1 Schematic diagram of Dye Sensitized Solar Cell.

DSSCs due to their simplistic cell fabrication[26], low production cost[27] and low toxicity[28] are lucrative for exploiting solar radiation. Major challenge DSSC faces are its lower efficiency than silicon solar cells, which is attributed to the barrier of electron transfer in the TiO_2 semiconductor layer.[29] To overcome these challenges significant attention is given specifically to photoelectrode, electrolyte and photosensitizer[30–32]. Recently, using a stable blue dye based on polycyclic aromatic hydrocarbon as a photosensitizer, efficiency upto 12.6% is obtained[27]. Different photosensitizers and co-sensitizers such as porphyrin[33,34], organic photosensitizers such as naphthodithienothiophene[35] and computational techniques like DFT[36] are been used. Recently, organic photosensitizer based DSSC achieved efficiency upto 13.6 %.[37] Recently, National Renewable Energy Laboratory in Colorado has developed a photocatalytic system which can harness up to 47.1 % of the incident radiation[17].

1.2. Photocatalysis

In the past years, heterogeneous photocatalysis has received significant research interest because of its potential applications in tackling essential energy requirements in the chemical[38], pharmaceutical[39,40], water treatment[41,42], manufacturing industries as photocatalysts have the capability to convert solar-chemical energy[43] as shown in Figure 1.3. Photocatalysts are materials that alter the speed of a chemical reaction by the action of light, and do not get consumed in the reaction. Storage of large amounts of electricity for use during the night without powering by other emerging technologies like high density batteries as supercapacitors as sole energy is a discontinuous source. The production of green fuels using photocatalytic materials provides a substitute method for storing the solar energy in chemical bonds[44,45] like the splitting of water[46] to hydrogen and oxygen, which can be released later without affecting the environment.
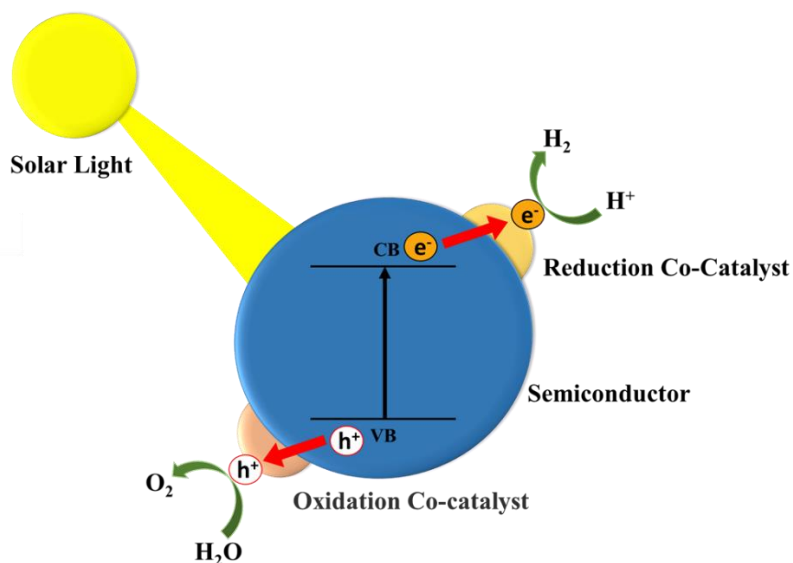
Figure 1.2 Schematic diagram of photocatalytic processes on a semiconductor material.

Several photocatalytic materials such as semiconductors and its composites[47–51] (e.g. Cu_2O, SiO_2, and TiO_2), metal[10,52–54] and multi-metallic[55] nanostructures (e.g., Ag, Au, and Cu), hybrid (metal-semiconductor)[56–59] (e.g. Au/TiO_2), and corresponding fundamental mechanisms such as electron-

hole charge carriers, LSPR of metal nanostructures, LSPR enhanced semiconductor based photocatalysis has been widely studied. Desired characteristics of catalysts in general are stability, selectivity, and activity. Photocatalysts operate at low temperature in contrast to conventional thermo-catalytic processes and require avoiding effects like sintering, which relatively needs high temperature and pressure, photocatalysts can tune activity, selectivity[60–63] based on their shape, size, and geometry[64] favoring reaction mechanisms selectively. Significant activity increase was observed for phenol degradation using Ag nanoparticles when illuminated with a 532 nm pulsed laser at different intensities.[10] and significant activity increase was observed for phenol degradation, Photocatalytic ethylene oxidation experiments were conducted as a function of temperature ranging from 60-520°C by Schwank et.al[65] and it was observed that the oxidation peaks out between 100-200°C and drastically falls near 500°C, in contrast to these finding Linic.et al.[62] investigated the ethylene oxidation reaction using Ag nanocubes, for the same probe reaction and observed that photocatalytic rate of ethylene oxidation and quantum efficiency, increase with an increase in reaction temperature (373-473 K) and light intensity (100-800 mW/cm^2). Despite many advantages, plasmonic materials cannot be suited for conventional semiconductor manufacturing and, show large joule loss.
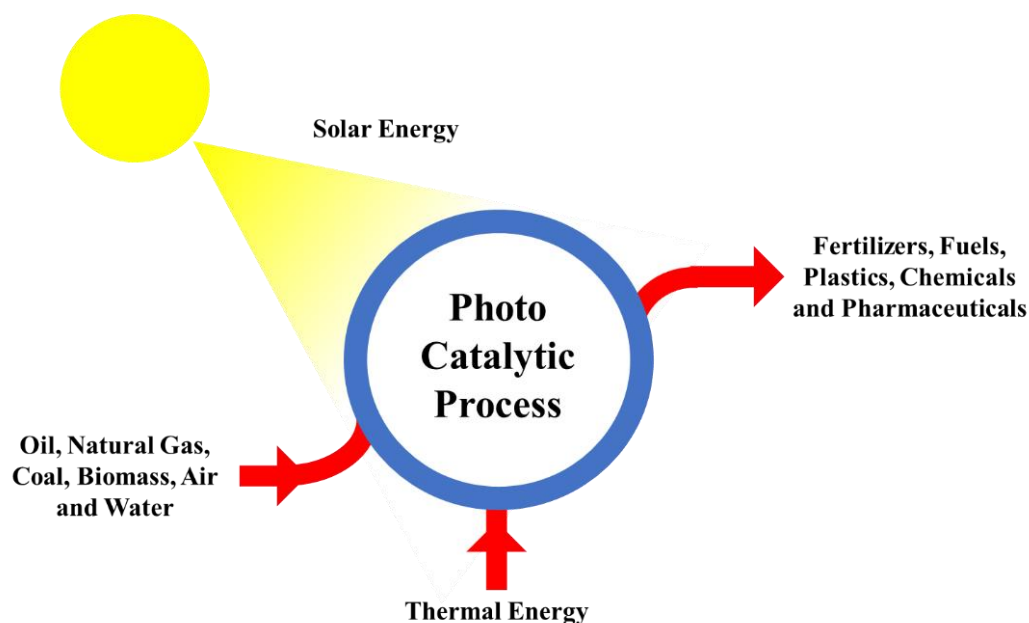
Figure 1.3 General process flow of photocatalytic processes which involves raw materials and solar energy and thermal energy as inputs and outcome is products at the other end.

Despite many advantages plasmonic materials are scarce, expensive, cannot be suited for conventional semiconductor manufacturing[66] and, due to its negligible magnetic resonance modes[67,68] they show large joule losses as a consequence of energy conservation in the resonances.[69] Negative effect of interband transitions, where valence electrons absorb photons to occupy the higher unoccupied orbitals, consequently heating the local environment.[70,71] Alternative solutions like, non-plasmonic[72–74], low-loss materials[75–77], dielectric nanostructures [66,78] can be used in photocatalysis.

1.3. Mie Resonance

Dielectric nanostructures having a high-moderate refractive index (n) exhibit distinct properties of their electric and magnetic resonance modes (dipole, quadrupole, etc.) of comparable magnitude [66,67] in comparison to plasmonic materials for different sizes and geometries[79] to modulate and control light in the similar wavelength range[68]. In these nanostructures, the fields can fully penetrate the particles and field maxima are typically found inside of the nanoparticles

as compared to fields limited to the surface of the nanostructure in plasmonics.[67,68]The magnetic dipoles are formed from the coupling of incoming light incident on the particle to circular displacement currents of the electric resonances, owing to the field penetration and phase retardation inside the particle[68,80]. These high index materials possess an increased non-linear optical response due to non-linearities arising from magnetic and electric resonance modes[68], giving singular characteristics like surface enhanced absorption[81,82], fluorescence and Raman scattering[82–85], and efficient sensing[4,86,87] and photodetection[88,89]. Exploiting the characteristics of Si (dielectric) and Au plasmonic materials which have strong near field emission enhancements and strong far field scattering, respectively Yang et al[90] have designed Si-Au nanoresonators. Recently, Mitrofanov and Co-workers[88] have developed an optically thin GaAs-based metasurface which can perfectly absorb all the radiation between 715-840 nm. GaAs nanoantennas were developed exploiting the non-linear effects, to obtain properties forward or backward emission by switching the polarity of light[91]. In a novel contribution by Kuznetsov and co-workers[92] have experimentally demonstrated that Si spherical nanoparticles with sizes in the range from 100 nm to 200 nm have strong magnetic dipole, all over the visible region, which can be visually seen under a dark field microscope, coined it as magnetic light. From our group's previous contribution, we have shown that cuprous oxide (Cu_2O) nanostructures with various sizes and geometries exhibit strong Mie resonances modes that are dominated by magnetic resonances in UV-Visible and Near IR region.[93] Herein, we demonstrate exploiting the singular characteristics of cuprous oxide (Cu_2O) nanostructures through photocatalysis for health and energy applications.

1.4. Objective and Specific Aims

Our long-term goal is to develop novel heterogeneous photocatalysts like Cu_2O nanostructures of various sizes and shapes, that can be used for harvesting solar energy in the UV-Visible region for energy and photocatalytic applications with desired stability, activity, and selectivity. In this research plan, special emphasis will be given to C-C coupling reactions for wider interest in pharmaceutical applications.

Through controllable syntheses of Cu_2O spheres and developing a fundamental understanding of reaction mechanisms using various characterization techniques and novel reaction conditions, performing dye degradation studies, exploiting unique characteristics of Cu_2O nanostructures of various shapes and sizes, *exploiting its Mie resonance characteristics in the UV-Visible region* with different reaction conditions to delve into the charge transfer mechanisms involved

Further evaluate its synergistic photocatalytic performance for applications in pollution mitigation, solar energy harvesting, thin film solar cells, dye sensitized solar cells, textile, cosmetic, and chemical related industries.

In order to achieve the research goal, three specific tasks will be performed:

Aim-1: To exploit the light harvesting capability of Cu_2O nanostructures, through its Mie Resonance Characteristics, for visible light driven Dye sensitization.

- **Task-1.1:** To synthesize Cu_2O nanostructures of different sizes and shapes.
- **Task-1.2:** To investigate Methylene Blue dye degradation using Cu_2O Small Spheres and Cu_2O Large Cubes under red light illumination.
- **Task-1.3:** To elucidate the influence of oxygen in the reaction mechanism by introducing Benzoquinone as Oxygen quencher.
- **Task-1.4:** To computationally and experimentally demonstrate structure-performance relationships of Cu_2O nanostructures of different sizes and geometries.

Aim-2: To exploit optical properties of Cu_2O nanostructures to enhance light harvesting capability for visible light driven Photocatalytic dye degradation

- **Task-2.1:** To synthesize Cu_2O nanostructures of different sizes and shapes to understand their photocatalytic properties.

- **Task-2.2:** To probe photocatalytic properties of Cu_2O Small Spheres and Cu_2O Large Cubes under Green and Blue light by Methylene Blue dye degradation.

- **Task-2.3:** Determine the role of oxygen in the reaction mechanism by introducing Benzoquinone as Oxygen Scavenger.

- **Task-2.4:** To experimentally demonstrate structure-performance relationships of Cu_2O nanostructures of different sizes and geometries.

Aim-3: To gain insights on optical properties of Cu_2O nanostructures to tune Catalytic Activity and Selectivity in Photocatalysis

- **Task-3.1:** To synthesize Cu_2O nanostructures of by-pyramidal shapes to understand their photocatalytic properties.

- **Task-3.2:** To probe photocatalytic properties of Cu_2O nanostructures by conducting wavelength dependent studies by Methylene Blue dye degradation.

- **Task-3.3:** To probe photocatalytic properties of Cu_2O nanostructures by conducting intensity dependent studies by Methylene Blue dye degradation.

- **Task-3.4:** To exhibit the effect of wavelength on selectivity and activity of the Cu_2O photocatalysts.

Aim-4: To develop highly active, stable thermal and photocatalytic conditions in C-C coupling reactions for pharmaceutical applications

- **Task-4.1:** To synthesize Cu_2O nanostructures of different sizes and shapes to understand their catalytic performance in C-C couplings.

- **Task-4.2:** Develop and investigate, with and without base (K_2CO_3) to determine stability of Cu_2O nanoparticles in Oxidative Homocoupling Reaction with Phenylacetylene as the probe molecule and perform Sonogashira Coupling Reactions using Iodo-benzene and Phenylacetylene to determine effect of base on Selectivity, under thermal conditions.

- **Task-4.3:** Role of Oxygen and Solvent in Homocoupling Reactions for use in Cu_2O Nanoparticle-mediated polymerization

CHAPTER II

REVIEW OF LITERATURE

2.1. Introduction to Mie Resonance-Enhanced Dye sensitization

Dye-sensitized photocatalytic (DSP) systems have emerged as a promising approach for a number of applications, including renewable hydrogen (H_2) production via photocatalytic water splitting, photocatalytic conversion of carbon dioxide (CO_2) into value-added products, and pollution mitigation. In a typical DSP system, a dye molecule is used as a photosensitizer that is adsorbed on a semiconductor nanostructure. As shown in Figure 2.1a, in the DSP system, the dye molecules absorb incident light and inject the excited electrons into the conduction band (CB) of the semiconductor. These excited electrons can be used to drive reduction reactions, such as the reduction of water for H_2 production. The regeneration of the dye molecule for cyclic utilization can be accomplished using the electron donor. In the last two decades, significant progress has been made in the field, and studies have shown that by appropriately selecting and matching the energy levels of dye molecules and semiconductors, DSP systems can be designed to cover the visible region and even the near-infrared region of the solar spectrum. Despite these great successes achieved in the field, DSP systems are still affected by significant drawbacks, such as low light absorption efficiency.[94–98]

Recently, it has been demonstrated that plasmonic Mie resonances of metal nanostructures, such as silver (Ag) and gold (Au) can be used to enhance the light absorption efficiency of dye molecules

in the dye-sensitized photocatalytic and photovoltaic systems.[99–110] The plasmonic metal nanostructures (PMNs) under Mie resonance conditions can exhibit very high absorption cross section values that are up to 5 orders of magnitude higher than dye molecules.[111–113] Therefore, PMN (e.g., Ag and Au) can harvest a large fraction of the incident light and transfer the energy into the nearby dye molecules and enhance their light absorption efficiency via a number of pathways, including nanoantenna effect and plasmon-induced resonance energy transfer (Figure 2.1b).[114–116] These plasmonic Mie resonance-mediated effects are utilized to enhance the rate of dye sensitization in DSP systems. However, these PMNs-based DSP systems also possess inherent challenges, such as compatibility issues with conventional semiconductor manufacturing, high material costs, and issues of commercialization with increasing complexity due to the need for both metals and semiconductors.

Herein, we propose a solution to the aforementioned issues through an alternate approach, dielectric Mie resonance-enhanced dye sensitization shown schematically in Figure 2.1c. The Mie resonances can occur in plasmonic materials that exhibit negative permittivity ($\varepsilon < 0$) as well as dielectric ($\varepsilon > 0$) materials with moderate (2.5-3.5) and high refractive index values (>3.5).[72,117–124] The dielectric Mie resonance-enhanced dye-sensitization proposed in Figure 2.1c is, therefore, most suitable for DSP systems built on metal oxide semiconductors with moderate and high refractive index values. Such metal oxide semiconductors include cerium(IV) oxide (CeO_2), cuprous oxide (Cu_2O), hematite iron oxide (α-Fe_2O_3), and titanium dioxide (TiO_2).

Similar to the plasmonic Mie resonances of PMNs, the dielectric Mie resonances of nanostructures of medium- and high-refractive-indexed metal oxide semiconductors can transfer the photonic energy into the adsorbed dye molecules via pathways such as nanoantenna effect, resonance energy transfer, and Mie resonance-mediated intense scattering effect. These dielectric Mie-resonance effects are expected to enhance the light absorption efficiency of the dye molecules in the DSP systems (Figure 2.1c). One major difference is that, unlike the plasmonic

Mie resonance-based system (Figure 2.1b), in a dielectric Mie resonance-based system (Figure 2.1c), there is no need for a separate light-enhancing material. Being a major advantage, this system solely requires a dielectric semiconductor nanostructure and dye. Specifically, the dielectric semiconductor nanostructure can play the role of a Mie resonator for enhancing the light absorption efficiency of the dye molecule as well as a source for harvesting excited electrons from the dye molecules and facilitating the reduction reaction (Figure 2.1c).
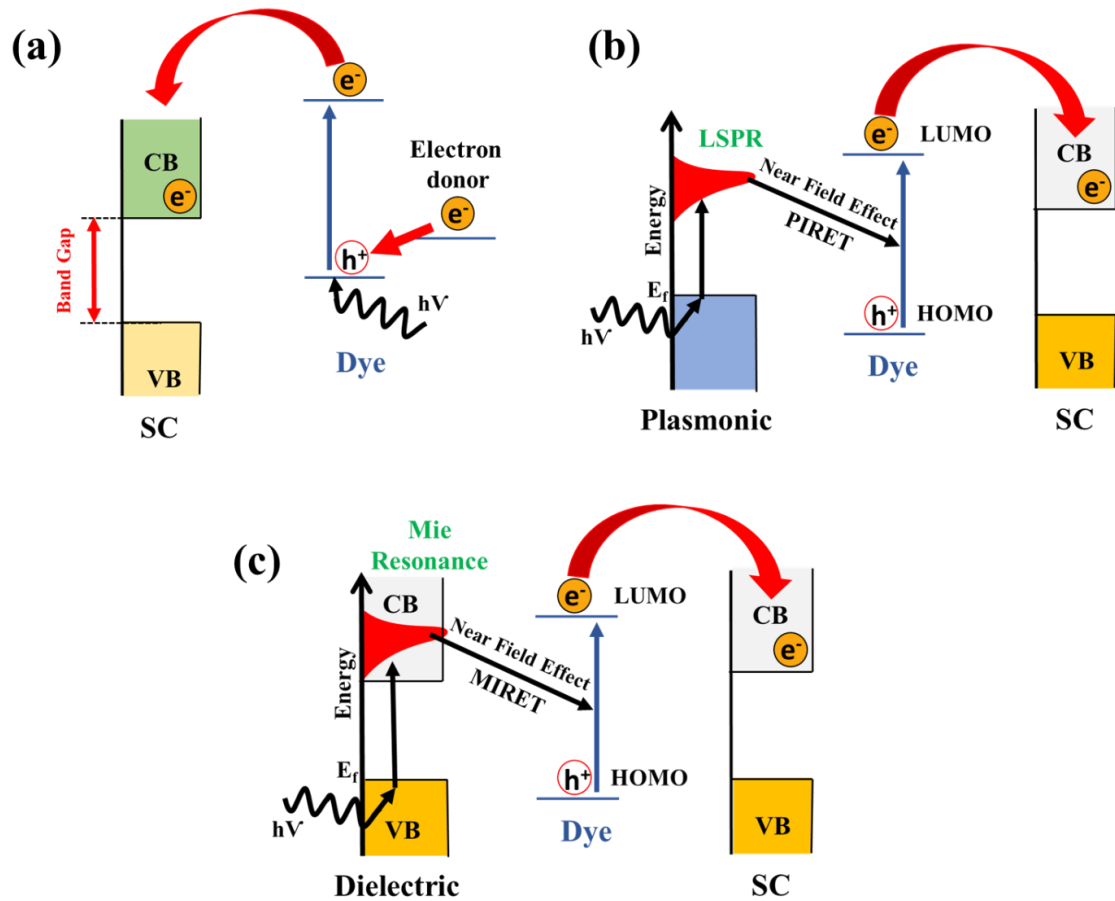
Figure 2.1 Schematic diagram of **(a)** Dye-Sensitization and electron transfer into the conduction band (CB) of semiconductor (SC), **(b)** localized surface plasmon resonance (LSPR)-enhanced dye-sensitization, and **(c)** dielectric Mie resonance-enhanced dye-sensitization.

2.2. Introduction to Mie Resonance-Enhanced Photocatalysis

The discovery of photoelectrochemical water splitting using a TiO_2 photoelectrode by Fujishima and Honda in 1972, has opened the gateway for semiconductor-assisted photocatalysis.[125] In bandgap-facilitated photocatalysis using semiconductors, the photo-excited electrons and holes drive reduction and oxidation reactions, respectively (Figure 2.2a). For example, in photocatalytic water splitting, the photoexcited electrons reduce protons (H^+) to hydrogen (H_2) while photoexcited holes oxidize water to oxygen (O_2).

Researchers have explored the properties of semiconductors, such as cerium oxide (CeO_2), cuprous oxide (Cu_2O), hematite iron (III) oxide (α-Fe_2O_3), and TiO_2 in the last four decades, for solar-to-chemical energy conversion and pollution mitigation applications.[126–131] However, some challenges still exist in using semiconductor-only-based photocatalysts for efficient conversion of solar energy to chemical energy. For instance, semiconductor nanostructures lack efficient harvesting of incoming photons because of their inherently poor absorption cross sections.[10] Plasmonic metal nanostructures (PMNs) have emerged as promising materials to overcome some of these limitations. Specifically, studies in the last decade have shown that hybrid and composite photocatalysts built on PMNs (e.g., Al, Ag, Au, and Cu) and metal oxide semiconductors (e.g., Cu_2O, α-Fe_2O_3, and TiO_2) can exhibit enhanced photocatalytic activity as compared to semiconductor-only photocatalysts.[10,132–138]

The absorption cross sections of PMNs are four to five orders of magnitude higher than dye molecules.[139] This strong interaction of PMNs with the incident ultraviolet/visible (UV/Vis) light is due to the localized surface plasmon resonance (LSPR).[139–141] The PMN can therefore efficiently harvest the incident light and transfer the energy into the nearby metal oxide semiconductor via a number of electron- and energy-transfer pathways, including plasmon-induced hot electron transfer, nanoantenna effect, and plasmon-induced resonance energy transfer

(Figure 2.2b).[10,132–134] The plasmonic resonance-mediated energy transfer from PMN into the nearby metal oxide semiconductor can result in an enhanced rate of generation of excited electrons and holes in the conduction and valence bands of the semiconductor, respectively (Figure 2.2b).[132] These enhanced rates of generation of charge carriers are shown to result in enhanced photocatalytic activity in PMN-metal oxide composite and hybrid photocatalysts.[10,132–135,142]

In our previous contribution,[93] we have reported that similar to the plasmonic resonances in PMNs, dielectric resonances in metal oxide particles can be spectrally tuned by controlling their size and shape. Herein, we demonstrate that these dielectric resonances can be utilized to enhance the inherent photocatalytic activity of metal oxide photocatalysts (Figure 2.2c). In the plasmonic resonance-mediated photocatalytic approach shown in Figure 2.2b, two building blocks are required: PMN to facilitate the plasmonic resonance and semiconductor for the bandgap-facilitated reduction and oxidation (redox) reactions. In contrast, in the proposed dielectric resonance-mediated photocatalytic approach shown in Figure 2.2c, a single metal oxide building block can serve the dual function and exhibit both the dielectric resonance behavior and the bandgap-facilitated redox reactions.
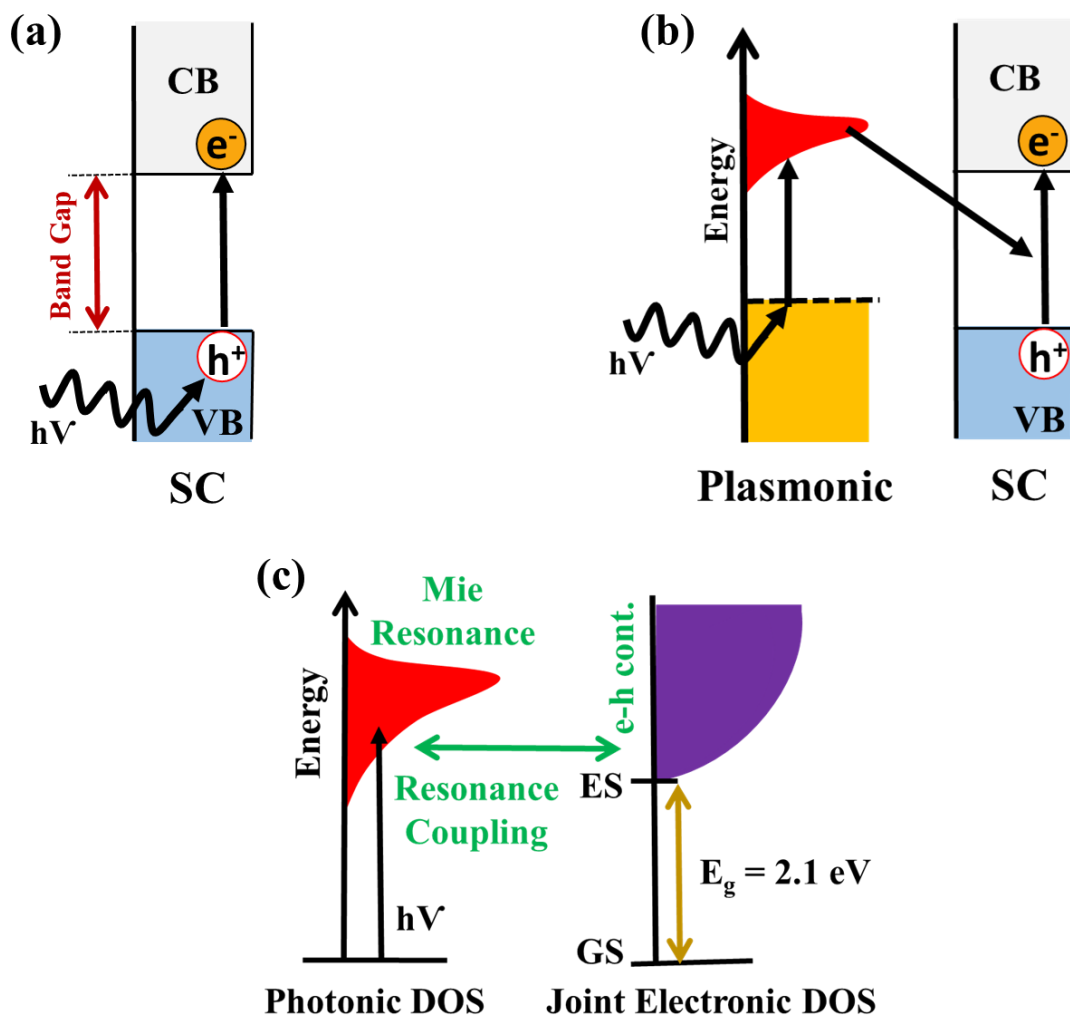
Figure 2.2 Schematic diagram illustrating (a) generation of a photoexcited electron-hole pair (e^--h^+) in a semiconductor (SC), (b) plasmonic resonance-mediated generation of excited electrons and holes in a SC, and (c) the proposed dielectric resonance-mediated generation of excited electrons and holes in a SC. In (a), (b), and (c), excited electrons in the conduction band (CB) and excited holes in the valence band (VB) of SC can drive reduction and oxidation reactions, respectively.

The plasmonic and dielectric resonances are two distinct sub-categories of Mie resonances.[143,144] The plasmonic resonances occur for materials with negative values of the real part of the permittivity ($\varepsilon < 0$). When Mie resonances occur in the positive permittivity region ($\varepsilon > 0$), the

resonances are known as dielectric resonances. Specifically, dielectric resonances can occur in materials with moderate (2.5-3.5) and high refractive index (>3.5).[145] Compared to plasmonic Mie resonances which exhibit only the electric multipole resonances (e.g., electric dipole, quadrupole. etc.), the dielectric Mie resonances can exhibit electric and magnetic multipole resonances upon light excitation.[93] Similar to the plasmonic resonances, the dielectric resonance wavelengths are also tunable with the particle size and shape.[93] At the resonance wavelengths, the dielectric nanostructures can act as optical nanoantennas and exhibit orders of magnitude enhancements for the local electric and magnetic fields over the incident far fields. The nanoantenna and light trapping effects of dielectric nanostructures are utilized for dielectric resonance-enhanced light absorption, fluorescence, and Raman scattering.[143] For example, dielectric Mie resonances have been demonstrated for their use in controlling and enhancing light absorption for solar fuel generation and thin-film solar cell applications.[146,147]

Mie dielectric resonances exhibit themselves as peaks in the UV-Vis-near infrared (UV-Vis-near IR) absorption/extinction spectra of medium- and high-refractive index dielectric particles.[93] These resonances, which are not present in their bulk counterparts, provide the opportunity for enhanced light harvesting in dielectric particles. For example, FeS_2 nanocubes with dielectric Mie absorption have been demonstrated to exhibit a higher photothermal conversion efficiency as compared to the small FeS_2 nanoparticles not exhibiting dielectric Mie absorption.[148] Herein, we demonstrate that Cu_2O nanospheres and nanocubes, exhibiting dielectric Mie resonances, deliver an enhanced photocatalytic rate per unit mass as compared with smaller Cu_2O nanoparticles not exhibiting dielectric Mie resonances (despite lower total surface area).

Cu_2O is a semiconductor with a dipole-forbidden direct gap of ~2.1 eV.[129–131,149] It is also a moderate refractive index material with the values of the real part of the refractive index in the range of ~ 2.6 - 3.1 (SI).[93] Cu_2O is also known for exhibiting a relatively long lifetime of excitons (excited and bound electron-hole pairs) that is on the order of milliseconds.[150,151] In our previous

contribution[93], we have demonstrated that: (i) Cu_2O nanocubes of edge lengths larger than ~100 nm exhibit strong dielectric resonances in the Vis-NIR range; (ii) the extinction cross section of these Cu_2O cubic particles are comparable to or larger than those of plasmonic Ag particles of similar sizes; and (iii) smaller Cu_2O spherical and cubic nanoparticles of sizes less than 100 nm do not exhibit any Mie resonances in the Vis-NIR range.

2.3.   Introduction to Tuning Catalytic Activity and Selectivity in Photocatalysis

The field of plasmonics has grown significantly since the coining of the term by Mark L. Brongersma in early 2000. Research and development in plasmonics have grown ever since then exponentially both from the physics and chemistrstandpointnt. The metals gold, silver, aluminum, and copper (Au, Ag, Al, and Cu) fall into this category. These materials have a special property called *localized surface plasmon resonance* (LSPR) which they exhibit when electromagneticectromagentic radiations, namely photons. At resonant frequencies, there is a significant enhancement in the light-matter interaction resulting in high electric fields. The elevated fields generate a large number of charge carriers (electron-hole pairs) which can induce chemical transformations either through localized heating or transfer of charges to the adsorbate on the nanostructure surface. The excitement and growth surrounding plasmonics stem from the ability to use the excitation of energetic charge carriers to drive surface chemistry.[152] These demonstrations show that visible-light-driven chemical transformations on plasmonic metal nanostructures (PMNs) have led to the emergence of a new field in heterogeneous catalysis known as plasmonic photocatalysis. Generally, nanoparticles are an important part of the heterogeneous catalysis being in various chemical reactions such as dehydrogenation, partial oxidations, reduction reactions, ammonia synthesis, hydrocarbon reforming etc.[153–167] However, these plasmonic materials suffer from losses arising from heat and the incompatibility in scaling up on the lines of conventional metal-oxide-semiconductor fabrication. Recent reports have shown a new class of dielectric, medium-high refractive indexed, metal-oxides are playing in

important role in nanophotonics. When light interaction in these materials induces *Dielectric-Enhanced Mie resonances*, which has reduced heat losses, and enhancing both electric and magnetic near-fields of comaprable strength. While in plasmonics there is only strong eletric fields enhancement. The new class of high indexed dielectric materials exhibit the same features as plasmonics like enhanced scattering, nanoantennas, magnetism, and meta-materials making them superior compared to their lossy plasmonic counterparts. So far, these dielectric materials have been studied and reported from a physics point of view, they have not studied from the chemistry point of view especially in the field of catalysis. Mohammadparast et al. have shown in their recent work that these high-indexed-dielectric materials exhibit strong scattering property acting as nanoantennas by concentrating and directing light.[168] The metal oxide used in the work is Cu_2O nanocubes (NCs). The work also shows through finite-difference-time-domain simulation (FDTD) of strong enhancement of electric and magnetic fields. In this work, we show how Cu_2O NCs can be applied to photocatalysis that focuses not only on conversion, but also on yield and selectivity. Also, in addition to improving selectivity, we have demonstrated through concrete results that, we can tune selectivity through degradation of methylene blue (MB) dye using various LED light sources in the visible-light region. In the process, we narrowed our focus to Cu_2O (bandgap ~ 2.1 eV). Compared to plasmonic metals which have multiple modes of electric field excitation due to LSPR, the dielectric Cu_2O exhibits multiple-modes of electric and magnetic enhancement upon light excitation. In this study, we are shown how we can selectively degrade methylene blue (MB) peaks through Mie resonance mediated photocatalysis using Cu_2O as a catalyst. Most literature studies have shown that catalysts are made from metals, semiconductors, or their hybrids to break MB in the photocatalytic process using visible light or ultraviolet. In addition, very little literature work has shown the coupling of dye excitons and Mie resonances in dielectric semiconductors. Here, we are showing the MB degradation using different light sources such as green (510-530 nm), blue (450-460 nm), red (630-650 nm), and amber (585-595 nm) and validate how different light sources affect the outcome of the process

differently. As discussed above the catalyst used, is Cu_2O (MPCs). These cubes exhibit strong Mie resonance peaks over a broad range of wavelengths and act as dielectric nanoantennas or nanoresonators by directing a significant portion of light into their localized neighborhood at nanoscale. Predominantly in MB dye degradation researchers have just focused on primary peak reduction, while in this work we show how can selectively focus different peaks by varying the different wavelengths in the visible-light region. We all know that breaking can happen in multiple pathways depending on the type of catalyst, light source, solvent, and dye itself. The most commonly occurring ones are complete mineralization of dye or dye sensitization followed by dye degradation. All the probe reactions were performed in dimethylformamide (DMF).

2.4. Introduction to Mie-resonance enhanced C-C coupling reactions

Metal-catalyzed coupling reactions (MCCRs) have emerged as a premier synthesis method for a variety of products ranging from polymers to pharmaceutical compounds.[169–179] Indeed, approximately 25% of all the reactions performed in the pharmaceutical industry consist of MCCRs.[169,170] These reactions have been conventionally performed through homogeneous metal complex catalyzed batch processes.[175,176,180,181] The National Science and Technology Council of the USA has recently identified the continuous manufacturing of pharmaceuticals as one of five manufacturing areas of emerging priority.[182] Continuous processes have the potential to reduce manufacturing costs and improve product quality. Also, they would reduce waste generation, plant space, and fluctuations in production.[182,183] Given these advantages of continuous processes, in recent years, there have been great interest in the development of metal- and metal-oxide-based heterogeneous nanocatalysts since they are the most suitable catalysts for continuous flow reactors.[174,176,183–203] Additionally, heterogeneous nanocatalysts can be immobilized on rigid support in the form of a packed-bed flow reactor, and therefore, can avoid the need for subsequent difficult steps to separate the catalyst and product.

In a nanoparticle-catalyzed coupling reaction, the catalysis can occur on the surface of nanoparticles via a heterogeneous pathway and or on leached ions in solution via a homogeneous pathway. To be an effective heterogeneous catalyst that can be repeatedly used in continuous flow reactors, a nanocatalyst must be able to drive the coupling reaction via a surface-catalyzed heterogeneous pathway without undergoing leaching. In that vein, copper-based nanoparticles (i.e., metallic Cu, Cu_2O, and CuO) have recently emerged as attractive nanocatalysts for a diversity of bond formations, such as C-C, C-N, C-O, C-S, and C-Se.[176,179,202] However, the identification of truly heterogeneous versus homogeneous catalytic conditions remains an ongoing challenge within the field.

CHAPTER III

EXPERIMENTAL METHODOLOGY

3.1. Catalysts Synthesis and Characterization

3.1.1. Synthesis of Cu_2O nanospheres

Smaller Cu_2O nanospheres with diameters in the range of 35-45 nm were synthesized using the microemulsion technique at room temperature (~20 $^{\circ}$C). In this synthesis method, 54.5 mL of n-heptane (oil phase) and polyethylene glycol-dodecyl ether (Brij, average Mn ~362) as a surfactant were added to a 250 mL round bottom flask and allowed to stir at 550 rpm. 5.4 mL of 0.1 M copper(II) nitrate aqueous solution was added to this mixture and 1 M hydrazine solution (5.4 mL) was added as a reducing agent. The mixture was allowed to stir for 12 hours after which acetone was added to break the emulsion and centrifuged. These nanoparticles were washed three times (sonicated and centrifuged) to remove the surfactant and to obtain Cu_2O spherical nanoparticles. 5.8 mg of Cu_2O nanoparticles were weighed and used as photocatalyst for methylene blue dye degradation and DSD experiments, photocatalytic reactions and used as the catalyst for the coupling reactions.
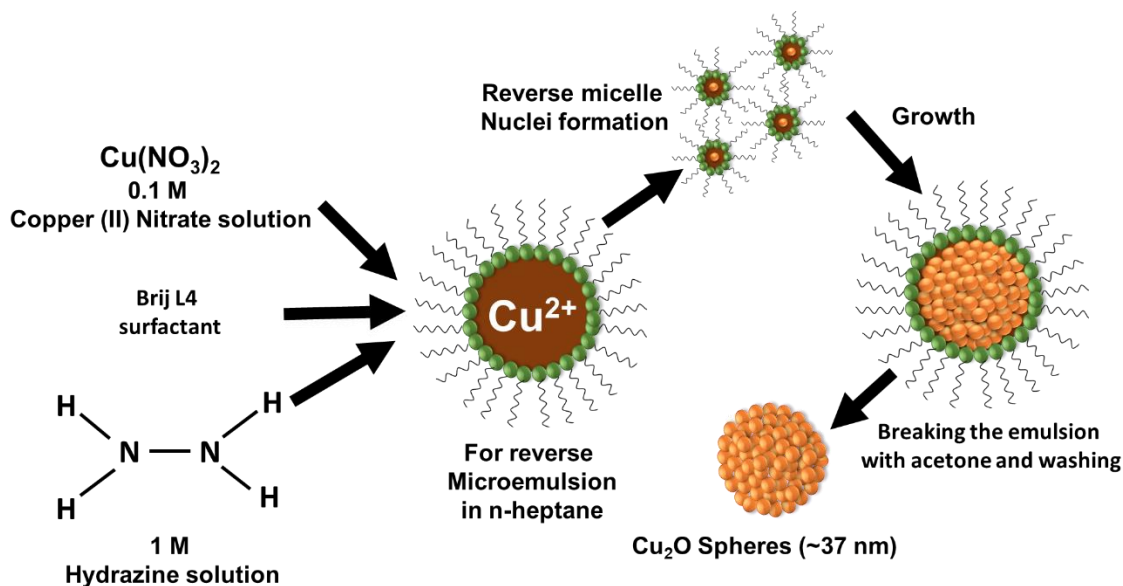
Figure 3.1 Schematic diagram of synthesis of Cu₂O nanospheres of 35-45 nm using microemulsion technique.

The chemical reduction method at a synthesis temperature of 55°C was used for the synthesis of larger Cu₂O nanospheres of 145 ± 41 nm diameter. 50 mL of 10 mM CuCl₂solution was prepared in a 100 mL round bottom flask. The aqueous mixture was allowed to stir at 900 rpm at 55°C. 5 mL of 2 M NaOH solution was added to the mixture and allowed to stir under constant heating (55 °C) for 30 minutes, followed by the addition of 5 mL of 0.6 M ascorbic acid aqueous solution as reducing agent. The synthesis mixture was allowed to stir for 5 hours. The resulting nanoparticles were separated by washing them in DI water and ethanol three times each to remove all residue from the synthesis mixture. 5.8 mg of washed and clean larger Cu₂O spherical nanoparticles were then used in the photocatalytic experiments and DSD experiments. The chemical reduction method at a synthesis temperature of 55°C was used for the synthesis of larger Cu₂O nanospheres of 145 ± 41 nm diameter. 50 mL of 10 mM CuCl₂
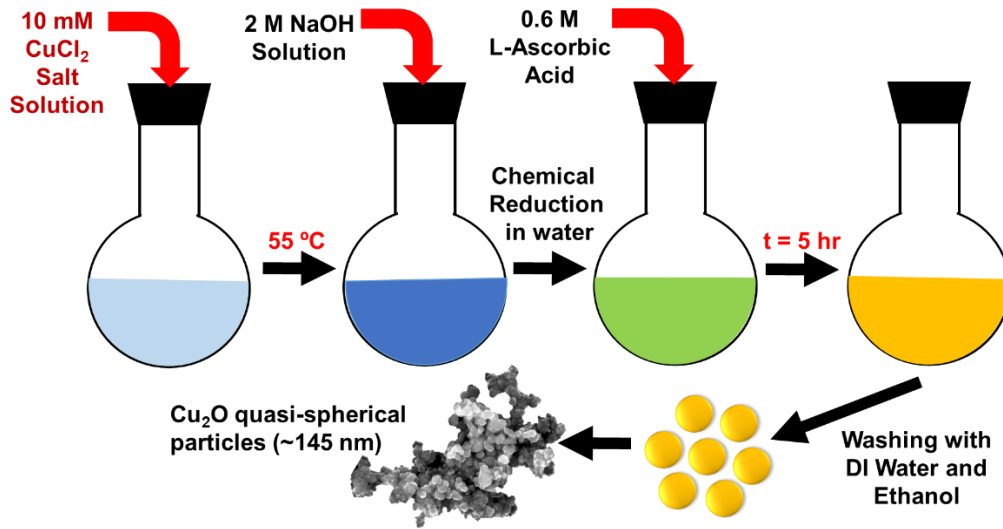
Figure 3.2 Schematic diagram of synthesis of Cu_2O nanospheres of ~145 nm using chemical reduction method.

3.1.2. Synthesis of Cu_2O nanocubes

Larger Cu_2O nanocubes with average edge lengths in the range of 280-300 nm were synthesized using a chemical reduction method performed at room temperature (~20 ˚C). In this method, we first prepared a copper source of 30 mL of 0.0032 M aqueous $CuCl_2$ solution. This solution was put into a three-neck round bottom flask, which was put in an inert environment filled with nitrogen. We added 1 mL of 0.35 M aqueous NaOH solution to this solution at room temperature, which resulted in the creation of blue-colored $Cu(OH)_2$ colloids almost immediately. The sodium ascorbate (reducing agent) was then added in 1 mL increments. The solution subsequently became orangish-yellow, suggesting that Cu_2O cubic particles were formed. The synthesis duration was a period of one hour after which, the Cu_2O cubes were washed using ethanol three times (sonicated and centrifuged). 5.8 mg of as-prepared Cu_2O nanoparticles were suspended in 4 mL of the reaction solvent and used in photocatalytic experiments.

To synthesize Cu$_2$O nanocubes with average edge lengths in the range of 90-120 nm, chemical reduction method was used at room temperature (~20 ˚C). A 500 mL-three-neck round bottom flask (reactor) at room temperature (~20 ˚C) was flushed with N$_2$ gas for 30 minutes to make sure there was no oxygen in the reactor atmosphere. 0.0032 M aqueous CuCl$_2$ solution of 360 mL was added to the reactor as a precursor. 0.35 M aqueous NaOH solution of 12 mL was added to this mixture and 0.1 M sodium ascorbate of 12 mL was added to the reactor, after which the solution turned yellowish-orange in color, it was allowed to stir for 45 minutes. The synthesis was stopped and washed using ethanol three times (sonicate and centrifuge) to obtain Cu$_2$O nanocubes (90-120 nm edge lengths).

Smaller Cu$_2$O nanocubes of 33 ± 6 nm edge length were synthesized using chemical reduction method performed at room temperature (~20 ˚C). An aqueous CuCl$_2$ solution of 120 mL of 0.0032 M was added to a 250 mL three-neck round bottom flask, which was put in an inert environment filled with nitrogen for 45 min. We added 4 mL of 0.35 M aqueous NaOH solution and 0.1 M sodium ascorbate (reducing agent) was then added (4 mL). The solution subsequently became bright yellow, suggesting that Cu$_2$O nanoparticles are formed giving Cu$_2$O nanocubes of 33 ± 6 nm edge length. After 45 minutes Cu$_2$O nanocubes were washed using same washing procedure mentioned above and 5.8 mg of Cu$_2$O nanoparticles were weighed and used in photocatalytic experiments.

Cu$_2$O nanocubes of 456 ± 35 nm edge length was synthesized using 165.5 mL of 0.0032 M aqueous CuCl$_2$ as a precursor solution in water. 250 mL three neck flask was flushed with nitrogen for inertion. 5.52 mL of 0.35 M aqueous NaOH solution was added to the flask. Then, 0.1 M sodium ascorbate solution of 5.52 mL was added to the mixture. The mixture turned bright orange in color. The mixture was allowed to stir under a nitrogen environment for 1 hour after which the Cu$_2$O nanocubes were washed three times using ethanol (sonicated and centrifuged).

5.8 mg of catalyst was weighed and separated from the synthesized nanoparticles and then suspended in 4 mL of the reaction solvent for use in photocatalytic experiments.
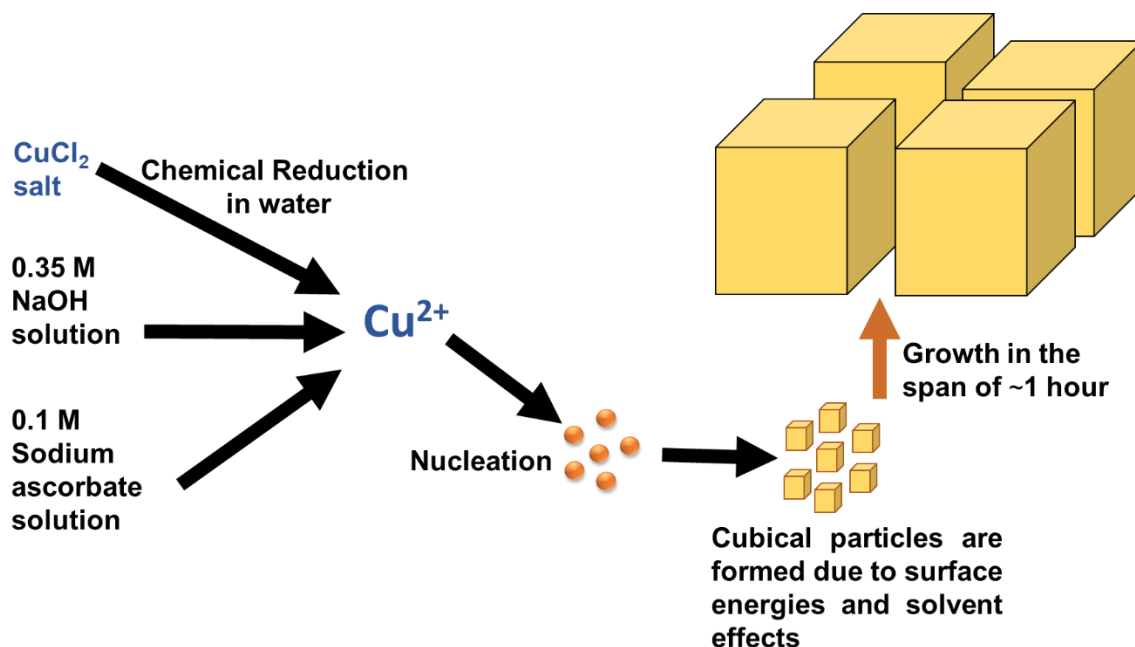
Figure 3.3 Schematic diagram of synthesis of Cu_2O nanocubes using chemical reduction method.

3.1.3. Characterization for Cu_2O quasi-spherical and cubical particles

The synthesized Cu_2O quasi-spherical, cubical particles ,and by-pyramidal shaped particles were characterized using UV-Vis-near IR extinction spectroscopy, X-ray diffraction (XRD) analysis as shown in Figure A.S1(a,b), APPENDIX A and transmission electron microscopy (TEM) and scanning electron microscopy (SEM). All UV-Vis-near IR extinction spectra were taken using an Agilent Cary 60 Spectrophotometer. XRD patterns were acquired using a Philips X-Ray diffractometer (Phillips PW 3710 MPD, PW2233/20 X-Ray tube, Copper tube detector – wavelength - 1.5418 Angstroms), operating at 45 KW, 40 mA. The SEM images were taken

using an FEI Quanta 600 F. The TEM images were taken using JEOL JEM-2100 TEM and Thermo Fisher Scientific Titan Themis 200 G2 aberration-corrected TEM. The JEOL JEM-2100 system is equipped with a LaB6 gun and an accelerating voltage of 200 kV. The Titan Themis 200 system is equipped with a Schottky field-emission electron gun and operated at 200 kV.

3.2.   Experimental procedure for performing DSD experiments

In our MB dye-sensitization followed by dye-degradation (DSD) experiments, a 6 mL quartz test tube (i.e., photoreactor) is added with 5.8 mg of Cu_2O nanocatalyst (quasi-spherical or cubical nanoparticles) that is uniformly dispersed (sonicated for 2 minutes) in 4 mL of dimethylformamide (DMF). To keep the soluble oxygen (O_2) content in the solvent same for all experiments, DMF was sparged with air for 30 minutes. 10 mM methylene blue (MB) solution is made in the DMF from which 150 uL is added to the reaction mixture in the quartz test tube and allowed to stir at 1150 rpm. The photoreactor is shifted to the Luzchem LED Panels (arranged with 4 Luzchem Exposure panels), where Red LED bulbs are attached as shown in Figure S1c. Details of intensity measurements are given below. Sampling was done as a function of reaction time by taking 100 μL of the reaction mixture and diluted in 4 mL of DMF. To measure the extent of degradation in DSD experiments with various catalysts Cu_2O spheres and Cu_2O cubes of various sizes, the MB concentration (C) in the reaction mixture was quantified as a function of reaction time. The MB absorption value at its peak absorption wavelength (i.e., 665 nm) was used to quantify the MB concentration in the reaction mixture. The concentration versus time profiles were fitted to obtain the apparent rate constant values. The fittings were tried with zeroth-order, first-order, and second-order rate equations. Among these trials, the second-order fittings showed the best fit. The fitted apparent rate constant values are provided in Table A.S1 in APPENDIX A.

The temperature measurements were also done as shown in Figure S3(a-e). Specifically, the temperature of the sample in the photoreactor, temperature of the reactor surrounding, and ambient room temperature of the laboratory are measured. Incident light intensities were

measured using Intell Pro Instruments Pro, Smart Sensor purchased from Luzchem Research Inc. The detector is placed exactly where the reactor is placed inside the Luzchem reactor (arranged with 4 Luzchem Exposure panels). Using the Smart sensor and AR823 Digital Lux meter (i.e., purchased from Luzchem Research Inc), the corresponding settings based on the wavelength range of the LED light intensity are measured in Lux. The values are converted to Light intensity in mW/m^2 by multiplying measured lux with the calibration factors. Red light source intensity at the surface of the photoreactor was 6.1375 mW/cm^2 and was kept constant for all the experiments reported in this study.

3.1. Understanding enhancement in Dye Sensitization Experiments

A schematic diagram of the DSD pathway for the dye-only condition is shown in Figure A.S4a in APPENDIX A. For the calculations and predictions of the enhancements of the rate of DSD by the Cu$_2$O nanostructures, we mainly consider here two possible enhancements. The first enhancement (G1) we consider is the enhancement of the light absorption efficiency of the dye molecules. This enhancement can occur via several pathways, including the electromagnetic nearfield or nanoantenna effect and Mie resonance-induced resonance energy transfer (MIRET). In our experiments with Cu$_2$O nanostructures of different shapes and sizes, the weight load of the Cu$_2$O nanostructures in the reaction mixture was kept constant. For this condition, the enhancement G1 can be written as equation (3.3.I) shown below.[2]

$$G1 \propto \int I_0(\lambda) Abs_{MB}(\lambda) E_{Cu2O}(\lambda) \, d\lambda \qquad (3.3.I)$$

where λ is the wavelength of the incident light, Ext$_{Cu2O}$ is the wavelength-dependent volume-normalized extinction cross section of the Cu$_2$O nanostructure, Abs$_{MB}$ is the wavelength-dependent absorbance of MB, and I$_0$ is the wavelength-dependent intensity of the incident light.

The second enhancement (G2) we consider is the enhancement by the catalytic surface effect of Cu$_2$O nanostructures that can also facilitate and enhance the electron transfer between adsorbed MB and O$_2$ molecules and the subsequent degradation of the excited MB molecules. This enhancement (G2) will be proportional to the ratio of the surface area to the volume of the Cu$_2$O nanostructures (S/V). The rate of DSD in the presence of Cu$_2$O nanostructures will be proportional to the overall enhancement, which is the product of these two enhancements (G1 and G2). Based on this overall enhancement, the rate (r) of DSD in the presence of Cu$_2$O nanostructures can be written as equation (3.3.2) shown below.

$$ r \propto \int I_0(\lambda) Abs_{MB}(\lambda) E_{Cu2O}(\lambda) d\lambda \times \frac{S}{V} \qquad (3.3.2) $$

In the above equation, the volume-normalized extinction cross section (E$_{Cu2O}$) is the ratio of extinction cross section of the Cu$_2$O nanostructure to its volume (σ_{Ext}/V). Therefore, σ_{Ext}/V will be proportional to A^{-3} for nanocubes (where A is the edge length), and D^{-3} for the nanospheres (where D is the diameter). The surface to volume (S/V) ratio in the above equation will be proportional to the A^{-1} for nanocubes, and D^{-1} for the nanospheres. Therefore, the extinction cross section value normalized to the fourth power of the edge length (σ_{Ext}/A^4, for nanocubes) or the fourth power of diameter ((σ_{Ext}/D^4, for nanospheres) would be a good descriptor to predict the relative rate of DSD on Cu$_2$O nanostructures of different sizes. For example, the normalized extinction value (σ_{Ext}/A^4) in Figure 4.3a is a good descriptor to predict the relative rate of DSD on Cu$_2$O nanocubes of different sizes.

3.2. Experimental procedure for Photocatalytic MB degradation

Photocatalytic MB degradation reaction conditions: A 6 mL quartz tube and the Luzchem Exposure Panels provided with green LED lamps   (in Figure B.S2, APPENDIX B)

was used as a reaction chamber and the visible-light source, respectively. To measure the photocatalytic activity of Cu_2O nanospheres and nanocubes of different sizes, the reaction mixture containing 1 mM concentration of MB and 5.8 mg of Cu_2O photocatalyst in 4 ml of solvent (dimethylformamide, DMF) was first allowed to equilibrate at room temperature (~20 °C) for 3 hours in the dark. The reaction mixture was then sparged with air for 30 minutes to keep the soluble oxygen (O_2) content in the solvent, same for all experiments. The equilibrated mixture under the stirring conditions at room temperature was then exposed te visible light (i.e., 20 number of green LEDs). The intensity of this light source, when measured at the surface of the photoreactor, was 8.868 mW/cm^2. To measure the extent of photodegradation of MB by the Cu_2O nanostructures, the MB concentration (C) in the reaction mixture was quantified as a function of reaction time. The MB absorption value at its peak absorption wavelength (i.e., 665 nm) was used to quantify the MB concentration in the reaction mixture. To obtain the apparent rate constant values, we fitted the concentration versus time profile to the zeroth-order, first-order, and second-order kinetics. Among these fittings, the first-order fittings showed the best fit.

More specific details of the photocatalytic experiments are also provided below.

5.8 mg of Cu_2O nanocatalyst (nanospheres or nanocubes) is uniformly dispersed (sonicated for 2 minutes) in 4 mL of reaction solvent (DMF). The mixture is added to a 6 mL quartz test tube (i.e., photoreactor). For experiments with benzoquinone, 43.2 mg (100 mM) of benzoquinone is added to the reaction mixture. 10 mM methylene blue (MB) solution is made in the same reaction solvent (DMF) used for photocatalytic reaction. 150 uL of 10 mM MB solution is added to the reaction mixture in the quartz test

tube and allowed to stir at 1150 rpm and equilibrate at room temperature for three hours in the dark environment. The reactor is transferred to the Luzchem LED Panels (arranged with 4 Luzchem Exposure panels), where LED lamps can be attached as shown in (in Figure B.S2, APPENDIX B)

Sampling was done as a function of reaction time by taking 100 µL of the reaction mixture and diluted in 4 mL dilution solvent (DMF). Care was taken to make sure the reaction solvent and diluent are the same. These samples were characterized by UV-Vis to obtain absorption of methylene blue and corresponding C/C_0 values as a function of time were obtained. Incident light intensities were measured using Intell Pro Instruments Pro, Smart Sensor purchased from Luzchem Research Inc. The detector is placed exactly where the reactor is placed inside the Luzchem reactor (arranged with 4 Luzchem Exposure panels). Using the Smart sensor and AR823 Digital Lux meter (i.e., purchased from Luzchem Research Inc), the corresponding settings based on the wavelength range of the LED light intensity are measured in Lux. The values are converted to Light intensity in mW/m^2 by multiplying measured lux with the calibration factors. For the solvent-dependent studies, the photocatalytic experiments were performed using ethanol (EtOH) as well as DMF. In the solvent-dependent studies and benzoquinone experiments (e.g., Figure 4.8a-b), 10 green LEDs and 10 blue LEDs were used as a light source.

3.3. Approximations to relate photocatalytic rates to the absorption

For the calculation of the relative photocatalytic rates of Cu_2O nanospheres and nanocubes of different sizes, we propose here a simple approximation to relate the photocatalytic rates to the absorption cross section of the Cu_2O nanoparticles. This approximation is similar to the approximation proposed by Ingram et al[2]. for

understanding plasmonic resonance-enhanced photocatalysis. In our proposed approximation, the photocatalytic rate (r) on a single nanoparticle for given incident light wavelengths is proportional to the overlap between the absorption spectrum and incident light spectrum.

$$r_{NP} \propto \int \sigma_{abs}(\lambda) I_o(\lambda) d\lambda \qquad (3.5.1)$$

where $\sigma_{abs}(\lambda)$ is wavelength-dependent absorption cross and $I_o(\lambda)$ is wavelength-dependent incident light intensity.

The photocatalytic rate for a system that a has known weight of Cu_2O nanostructure can then be written as

$$r \propto \int N \times \sigma_{abs}(\lambda) I_o(\lambda) d\lambda \qquad (3.5.2)$$

where N is the total number of nanoparticles present in the system of a known weight. The total number (N) of nanoparticles present in the system can be written as

$$N = \frac{m}{\rho V} \qquad (3.5.3)$$

where m is the total weight of nanoparticles in the system, and ρ and V are density and volume of a single nanoparticle. Assuming constant density for Cu_2O nanospheres and nanocubes of different sizes, equation (3.5.2) can be written as

$$r \propto \int \frac{\sigma_{abs}(\lambda)}{V} I_o(\lambda) d\lambda \qquad (3.5.4)$$

From equation (3.5.4), for a given system of known total weight of Cu_2O nanostructures, the photocatalytic rate is proportional to the overlap between the volume-normalized absorption spectrum and the incident light spectrum. The relative photocatalytic rate of Cu_2O nanostructures of two different sizes (say nanoparticles of Size 1 and nanoparticles of Size 2) can be written as the one shown in equation (3.5.5) below. Equation (3.5.5) also shows that the overlap between the FDTD-simulated volume-normalized absorption spectrum and incident light spectrum can be used as a critical descriptor for rationally predicting the relative photocatalytic rates.

$$\frac{r_1}{r_2} \propto \frac{\int \left(\frac{\sigma_{abs}(\lambda)}{V}\right)_1 I_o(\lambda)d\lambda}{\int \left(\frac{\sigma_{abs}(\lambda)}{V}\right)_2 I_o(\lambda)d\lambda} \quad (3.5.5)$$

Equation (3.5.5) is used to predict and model the relative photocatalytic rates of Cu_2O nanospheres and nanocubes of different sizes shown in Figure 4.7 (i.e., the volcano plot) in Chapter 4, Section 4.2.2. It is worth mentioning here that the particles shown in Figure 2a-b consist of aggregates and particles of various sizes and shapes. So, the consideration of these particles as spheres in the model is a rough approximation. This approximation could be one of the possible reasons for the slight deviation between the model predicted value and the experimentally observed value for the 145-nm particle in Figure 4.7 (i.e., the volcano plot).

3.4. Details of finite-difference time-domain (FDTD) simulations

To compute the extinction spectra of Cu_2O, CeO_2, CuO, α-Fe_2O_3, and TiO_2 of various sizes and shapes, FDTD simulations were used by employing the Lumerical FDTD package.[1] For the calculations and predictions of the dye-sensitization rate enhancements by the Cu_2O

nanostructures of different shapes and sizes, we propose a simple approximation, i.e., equation (1) shown in the main draft. This approximation is similar to the approximation proposed by Ingram et al.[2] and used for predicting plasmonic resonance-enhanced photocatalysis. For FDTD simulations, the optical properties (i.e., real and imaginary parts of the refractive index, n and k values) of CeO_2, CuO, Cu_2O, α-Fe_2O_3, and TiO_2 are obtained from the literature.[3-7] The perfectly matched layer (PML) boundary conditions were used for the simulations in all x, y, and z directions. For the simulations of extinction, scattering, and absorption spectra, the respective cross sections as a function of wavelengths were calculated using the total-field/scattered-field (TFSF) formalism. The incident light source used for these simulations was the Gaussian source in the simulated wavelength region. For cubes simulation, the propagation direction of the incident light is perpendicular or parallel to the principal axes. On implementing the simulations of the magnetic and electric field distributions, a plane wave was used as electromagnetic field incidence with propagation in the x-axis direction, and polarization along the y-axis and the z-axis for the electric field and the magnetic field, respectively.

3.5. Tuning Catalytic Activity and Selectivity Experiments

Dark Conditions

Cu_2O NPs of Bipyramidal shape were synthesized using the chemical reduction technique as discussed in Section **Error! Reference source not found.**, were suspended in d imethylformamide (DMF, 4 mL) before starting the reaction (5.8 mg). The suspended NPs were added to a quartz test tube and sonicated for 2-3 minutes for obtaining a homogenous mixture. 150 uL of 0.01 M methylene blue was added to the mixture as a reactant and stirred at 1150 rpm. The quartz tube was wrapped in aluminum foil/opaque foil from the outside to make sure ambient light is not affecting the reaction mixture. Sampling to obtain absorption spectra as shown in Figure 1d, 100 uL of the reaction mixture in 4 mL of DMF. Car was taken that the same solvent

was used across the experimental conditions. The temperature was recorded using a thermocouple before each sample.

Light Conditions

5.8 mg of catalyst (Cu_2O NPs) is suspended in 4 mL DMF and 150 uL 0.01 M MB is added to the concoction similar to dark conditions. The quartz tube is carefully suspended using support into the Luzchem reactor as shown in Figure and the mixture was stirred at 1150 rpm. The luzchem reactor needs to be arranged with bulbs of the desired wavelength before the start of the reaction. 100 uL of the reaction mixture in 4 mL of DMF, sampling was used to track the dye degradation. Light intensity in mW/cm2 is measured using Intellpro.

Light Intensity Measurements and Constant Intensity Measurements

Measuring Light Intensity was done using Intellpro Intensity meter in Lux and converted to mW/cm2 using a calibration factor specific to wavelength provided. As shown in photocatalytic reactor as shown the Figure (SI) light intensities were measured placing all 20 bulbs of different wavelength in UV-Visible range. Green Light is used as reference for measuring constant light intensity across the spectrum by varying the number of bulbs to obtain constant light intensity conditions irrespective of the wavelength.

3.6. C-C Coupling Reaction Conditions

Cu_2O NPs were synthesized using the microemulsion synthesis technique a discussed in Section 3.1.1. The NPs were suspended in dimethylformamide (DMF, 15 mL) before starting the reaction (34.08 mg, 0.598 mmol). The suspended NPs were added to a 25 mL round bottom flask (RBF) connected with a condenser and a thermocouple for temperature control. Air or nitrogen (purity-99.999%) was continuously flowed through the RBF to maintain the respective gas environment in the oxidative homocoupling reaction (OHR) and Sonogashira cross-coupling reaction (SCR).

Potassium carbonate (K$_2$CO$_3$) was weighed out (207 mg, 1.64 mmol) and added while stirring the nanoparticles and DMF. For cross-coupling reactions, Iodobenzene (IB, 0.91 mmol) was added while still stirring. The mixture was then heated for ~15 minutes to reach 110 °C for homocoupling and 147 °C for cross-coupling reaction. At this point, phenylacetylene (PA, 0.91 mmol) was added, and the reaction was started. The reaction mixture was sampled at frequent time intervals to quantify the reaction conversion and product selectivity using GC-MS (Shimadzu QP2010SE). The homocoupling of PA into diphenyladiacetylene (DPDA) was observed only in the presence of oxygen. A Shimadzu C184-E037A GC Column (Phase: SH-Rxi™-5Sil MS Column, Length-30 m; ID – 25 mm; df – 0.25 µm) was used for gas chromatography. The column had an operating temperature range of -60 °C to 320/350 °C. Peak detection and integration were handled by the software provided by the Shimadzu Corporation. Identification was verified using NIST spectral libraries with matching higher than 95%. No smoothing was used to process the samples to ensure accurate peak identification and quantification. The calibration curves were built independently using area versus concentration response from prepared reference samples.

The conversion was calculated based on the equation shown below:

$$Conversion\ (X, \%) = \frac{C_{A0} - C_A}{C_{A0}} * 100$$

where C$_{A0}$ is the initial concentration (in mmol) of reactant (i.e., PA) and C$_A$ is the concentration at any time, t.

The product selectivity for SCR was calculated based on the equation shown below:

$$Selectivity\ (DPA\ or\ DPDA, \%) = \frac{C_{DPA\ or\ DPDA}}{C_{DPA} + C_{DPDA}} * 100$$

where C_{DPA} and C_{DPDA} are the concentration (in mmol) of the desired cross-coupling product (diphenylacetylene, DPA) and the undesired homocoupling product (diphenyldiacetylene, DPDA), respectively.

The conversion of PA at a reaction temperature of 147 °C under reflux and nitrogen flow (99.999% purity) as a function of reaction time for SCR under the base and base-free conditions are shown in Fig. D.S4 and Fig. D.S5, respectively. The product selectivity towards DPA and DPDA under the respective conditions are shown in Fig. D.S6 and Fig. D.S7, APPENDIX D.

3.7. C-C Coupling Reaction Characterization

Electrospray ionization mass spectrometry (ESI-MS) spectra of the supernatant solution of the reaction mixture were collected on LTQ Orbitrap system with an ESI source. The spray voltage was set at 5.0 kV with 15.0 mL/min sample flow rate. To achieve proper spraying conditions, the sample was prepared by mixing 1 mL of sample with 1 mL of a mixture of 18 mL dichloromethane, 2 mL Acetone, 400 µL DI water. The sample was sprayed with nitrogen as the sheath and auxiliary gas. Fig. D.S10 shows the representative HR-ESI-MS spectrum measured in negative spray mode for the supernatant solution of the reaction mixture collected from SCR in the presence of the base. The signals from this ESI-MS spectrum in the m/z range of 281-284 and 299-302 match the predicted isotope distributions of copper complexes, $[CuO(C_8H_5)_2]^-$ and $[CuO(C_8H_5)_2H_2O]^-$, respectively, shown in Figure. D.S11a-b, APPENDIX D. The combination of ESI-MS, UV-Vis extinction spectroscopy and DFT results confirm that in the presence of base, the homogeneous Cu complex, $[CuO(C_8H_5)_2]^-$, is the common catalytic species formed under homo-coupling as well as cross-coupling conditions via PA-induced leaching of Cu_2O NPs surface atoms. The reactor study results using GC-MS analysis also show that this homogeneous Cu complex can efficiently catalyze both reactions: (i) OHR with ~100% selectivity towards the desired homocoupling product, DPDA when the reaction is performed under air flow at a reaction

temperature of 110 °C, and (ii) SCR with >95% selectivity towards the desired cross-coupling product, DPA at 147 °C (under reflux) and under nitrogen (99.999% purity) flow.

Flame-atomic absorption spectroscopy (FAAS) analysis of the supernatant solution of the reaction mixture was performed on a Varian Fast Sequential AA240FS – Flame Spectrophotometer. For the quantification of Cu content, the calibration curve was built using area versus concentration response using standard samples with known concentrations of copper nitrate. A hollow cathode lamp (324.7 nm) for the element copper is used with the slit width 0.5 mm. The flame temperature was 2000 °C and was produced using acetylene and air as the fuel mixture. The detection limit of the instrument for Cu is 100 parts per billion (ppb).

3.8. Density-Functional Theory (DFT) Calculations:

DFT calculations were performed by Dr. Bin Wang's group from School of Chemical, Biological and Materials Engineering, The University of Oklahoma

DFT computations were carried out using Vienna ab initio simulation package (VASP).[189] The projector-augmented wave (PAW) approach was used to describe the interaction between ion cores and valence electrons.[190] For the structural optimization, the exchange and correlation energy was represented using the Perdew-Burke-Ernzerhof (PBE) functional of the generalized gradient approximation (GGA).[191] The DFT-D3 semi-empirical van der Waals (vdW) correction proposed by Grimme has been taken into account in all calculations.[192,193] An implicit solvation model, VASPsol [194,195], was employed in all the calculations, to account for liquid solvent environments. The Brillouin zone was sampled by a k-point mesh of $1 \times 1 \times 1$ for geometry optimizations and optical property calculations. The energies of complex molecules in vacuum were computed using a $20 \times 20 \times 20$ Å unit cell. An extra electron was manually placed at LUMO (lowest unoccupied molecular orbital) of the molecule to include the negative charge. The

cutoff energy was set at 400 eV. The structures were relaxed until the atomic force is smaller than 0.02 eV/Å, and the energy tolerance was set to 10-5 eV. All the ion relaxations were performed using a Gaussian smearing with a width of 0.2 eV, and 0.4 eV for optical absorption spectra calculations, respectively. The OPTICS code of Furthmüller was employed to compute the imaginary part of the dielectric constant and hence the absorption spectra.[196] The imaginary part of the dielectric constant, which is proportional to the optical absorption, is determined by the summation of empty states in the conduction band that can be compared to the features of the experimental spectra. The DFT-predicted structures of the proposed homogeneous Cu complexes, $[CuO(C_8H_5)_2]^-$ and $[CuO(C_8H_5)_2H_2O]^-$, are shown in Figure. D.S11d and Fig. D.S11e, respectively in APPENDIX D.

CHAPTER IV

FINDINGS

4.1. Results and observations of Mie Resonance-Enhanced Dye Sensitization

4.1.1. Summary

Dye-sensitized photocatalytic (DSP) approach is considered as one of the promising approaches for developing visible light- and near-infrared light-responsive photocatalysts. DSP systems are still affected by significant drawbacks, such as low light absorption efficiency. Recently, it has been demonstrated that the plasmonic metal nanostructures can be used to enhance the light absorption efficiency and the overall dye-sensitization rate of DSP systems through the plasmonic Mie resonance-enhanced dye-sensitization approach. In this dissertation, we report an alternate and novel approach, dielectric Mie resonance-enhanced dye sensitization. Specifically, we demonstrate that the dielectric Mie resonances in cuprous oxide (Cu_2O) spherical and cubical nanostructures can be used to enhance the dye-sensitization rate of methylene blue dye. The Cu_2O nanostructures exhibiting dielectric Mie resonances exhibit up to an order of magnitude higher dye-sensitization rate as compared to Cu_2O nanostructures not exhibiting dielectric Mie resonances. Our model system developed from finite-difference time-domain simulation predicts a volcano-type relationship between the dye sensitization rate and the size of Cu_2O nanostructures. The predicted structure-property-performance relationship is experimentally verified and the optimal size ranges of Cu_2O nanospheres and nanocubes are identified. Although we demonstrate the dielectric Mie resonance-enhanced dye-sensitization approach using Cu_2O

nanostructures, the proposed approach can be used to design a wide range of DSP systems, including CeO_2, α-Fe_2O_3, and TiO_2 nanostructures-based DSP systems.

4.1.2. Specific Findings on Mie Resonance-Enhanced Dye Sensitization

In this dissertation, we demonstrate the dielectric Mie resonance-enhanced dye-sensitization approach using methylene blue (MB) dye-sensitization on Cu_2O nanostructures as an example. We have developed the structure-property-performance relationships of Cu_2O nanostructures for MB dye-sensitization. Specifically, different sizes of Cu_2O nanospheres and nanocubes are synthesized and the structure of these Cu_2O nanostructures are characterized using transmission electron microscopy (TEM) and scanning electron microscopy (SEM). The size-dependent optical properties of the Cu_2O nanospheres and nanocubes are predicted using finite-difference time-domain (FDTD) simulations. Based on these FDTD simulation results, we predict a volcano-type relationship between the size of Cu_2O nanostructures and the enhancement of dye-sensitization rate by the respective nanostructures. The predicted structure-property-performance relationships of Cu_2O nanospheres and nanocubes are experimentally verified by measuring the rate of MB dye-sensitization followed by dye-degradation (DSD). The procedures followed for FDTD simulations, syntheses and characterizations of Cu_2O nanospheres and nanocubes,[24,33,34] and MB dye-sensitization and degradation experiments are detailed in the EXPERIMENTAL METHODOLOGY section 3.1.1, 3.1.2, 3.1.3, 3.2, 3.1. Briefly, Cu_2O nanospheres with average diameters of 37 nm and 145 nm and Cu_2O nanocubes with average edge lengths of 92 nm, 165 nm and 325 nm were synthesized using the synthesis protocols reported in our previous contributions.[24,33,34] The sizes and Cu_2O phases of the nanostructures were confirmed using TEM and SEM, and X-ray diffraction patterns, respectively (Figure A.S1a-b in APPENDIX A). The performance of the Cu_2O nanostructures towards MB dye-sensitization was evaluated through the measurement of the rate of MB degradation that occurs in the MB dye-sensitization region.

The MB degradation was carried out in the solution phase using dimethylformamide (DMF) as a solvent. To quantify the extent of MB degradation, the concentration (C) of MB in the reaction mixture was quantified as a function of irradiation time. The MB absorption value at its peak absorption wavelength (i.e., 665 nm) in the ultraviolet-visible (UV-Vis) absorption spectrum was used to quantify the concentration of MB.

Figure 4.1a-d shows the representative TEM and SEM images of quasi-spherical Cu_2O nanoparticles with an average diameter of 37 nm and 145 nm, and Cu_2O nanocubes with an average edge length of 165 and 325 nm, respectively. Figure 4.1e-f shows the experimentally measured UV-Vis-near IR extinction spectra of these Cu_2O nanostructures. The representative SEM image and UV-Vis-near IR extinction spectra of Cu_2O nanocubes of 92 nm average edge length are also provided in Figure A.S1d-A.S1e in APPENDIX A. The extinction spectra shown in Figure 4.1e-f are consistent with the extinction features predicted from the FDTD simulations (Figure A.S2a-d in APPENDIX A). Specifically, as seen from Figure 4.1e, Cu_2O nanospheres of 37 nm average diameter exhibit extinction features similar to the bulk Cu_2O, which is a semiconductor with a bandgap of 2.1 eV.[24] For these 37 nm Cu_2O nanospheres, the dielectric Mie resonances are absent in the UV-Vis-near IR regions. In contrast, Cu_2O nanospheres and nanocubes of sizes larger than 90 nm exhibit strong dielectric Mie resonances in the UV-Vis-near IR regions, as shown in Figure 4.1e-f (also see Figure A.S1c and Figure A.S2a-d in APPENDIX A). The lowest Mie resonance peak in the UV-Vis-near IR extinction spectrum corresponds to the combination of the electric dipole and magnetic dipole (Figure A.S2e in APPENDIX A).[24] Similarly, the second-lowest energy peak and higher-order peaks correspond to the combination of electric quadrupole and magnetic quadrupole, and the combination of higher-order electric and magnetic modes, respectively (Figure A.S2f in APPENDIX A).[24]
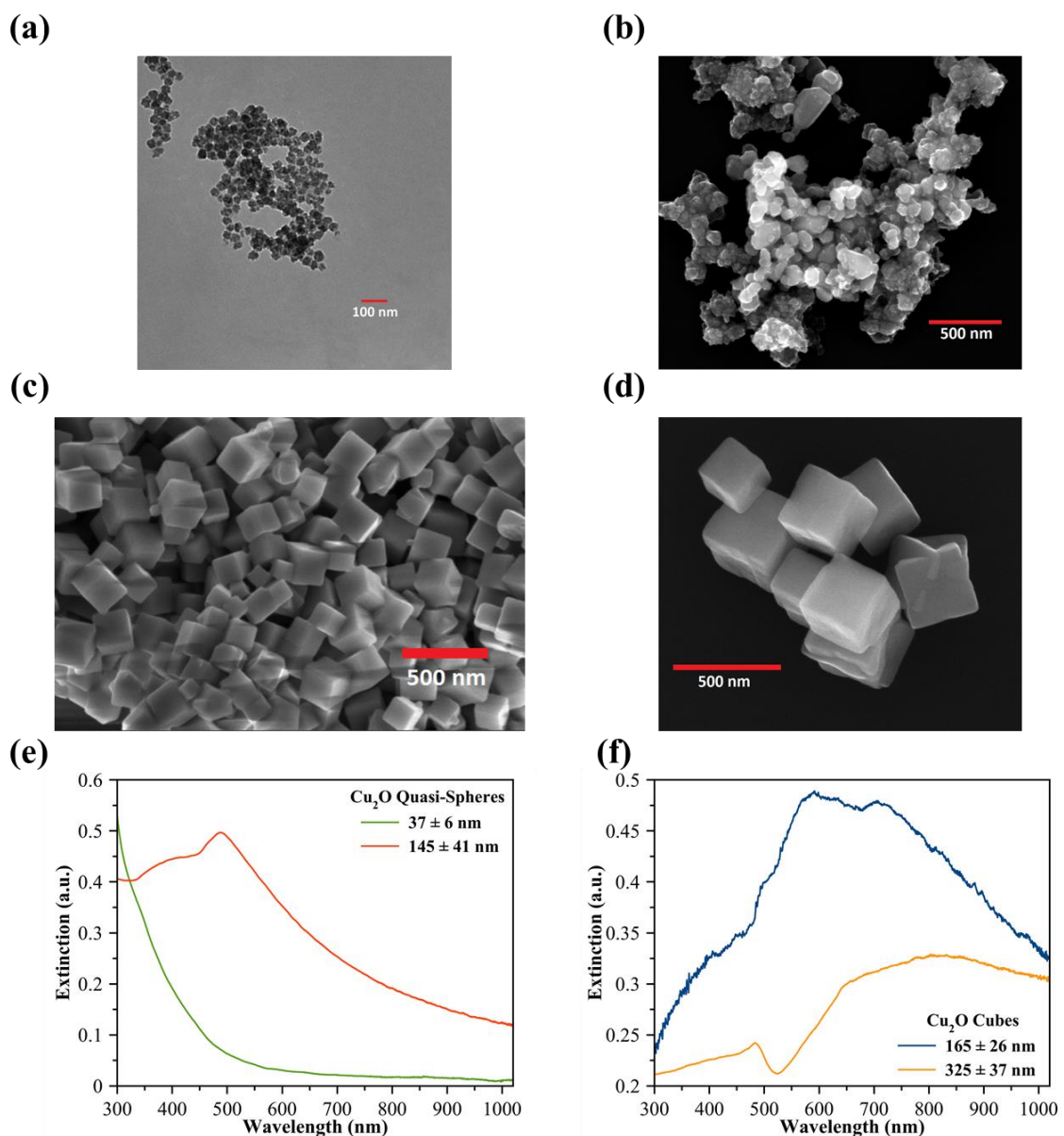
Figure 4.1 **(a-d)** Representative TEM/SEM images of **(a)** quasi-spherical Cu$_2$O nanoparticles of 37 ± 6 nm diameter, **(b)** quasi-spherical Cu$_2$O nanoparticles of 145 ± 41 nm diameter, **(c)** Cu$_2$O nanocubes of 165 ± 26 nm edge length, and **(d)** Cu$_2$O nanocubes of 325 ± 37 nm edge length. **(e-f)** UV-Vis-near IR extinction spectra of **(e)** quasi-spherical Cu$_2$O nanoparticles of 37 ± 6 nm and 145 ± 41 nm diameters, and **(f)** Cu$_2$O nanocubes of 165 ± 26 nm and 325 ± 37 nm edge lengths, dispersed in DMF.

To evaluate the performance of the Cu_2O nanostructures towards the MB DSD, we have selected red LEDs as the illumination source. The intensity of the light, when measured at the surface of the photoreactor, was 7.49 mW/cm^2, and it was kept constant for all dye-sensitization experiments reported in this dissertation. In Figure 4.2a, we show the spectrum of red LEDs and UV-Vis absorption spectrum of MB dye. As seen from Figure 4.2a, there is a significant overlap between the spectrum of red LEDs and the absorption spectra of methylene blue in the 590-670 nm region. It has been previously shown that, in this region (590-670 nm), MB molecules can undergo dye-sensitization and inject the excited electrons into the conduction band of the semiconductor (Figure 4.2b)[35,36]. In the presence of dissolved oxygen (O_2), these electrons can form superoxide (O_2^-), which can attack and cause the degradation of excited MB molecules (Figure 4.2b) [35,36]. Since the bandgap of Cu_2O is 2.1 eV (~590 nm)[24,37], the rate of MB degradation via direct photocatalysis by Cu_2O nanostructures is expected to be minimal in this MB dye-sensitization region (590-670 nm) investigated in this study.

To illustrate the role of dielectric Mie resonances on the MB dye-sensitization, we carried out the experiments to quantify the rate of MB DSD using quasi-spherical Cu_2O nanoparticles with an average diameter of 145 nm and Cu_2O nanocubes with an average edge length of 92 nm, 165 nm, and 325 nm. These Cu_2O nanostructures exhibit dielectric Mie resonances in the MB dye-sensitization region (590-670 nm), as seen from Figure 4.1e-f. We also carried out the same experiments using quasi-spherical Cu_2O nanoparticles with an average diameter of 37 nm, in which the dielectric Mie resonances are absent in the MB dye sensitization region (Figure 4.1e). In these dye-sensitization experiments performed with different sizes of Cu_2O nanospheres and nanocubes, the weight load of the Cu_2O nanostructures in the reaction mixture was kept constant. Before exposing the reaction mixture to the red-light illumination, the MB dye molecules are stirred with Cu_2O nanostructures dispersed in DMF for 3 hours to reach the adsorption equilibrium. Also, the reaction mixture is sparged with air for 30 minutes to start with the same

level of dissolved oxygen for all experiments. Figure 4.2c shows the extent of MB degradation (C/C_0) under the red-light illumination (590-670 nm) conditions in the presence of different sizes of Cu_2O nanospheres and nanocubes, and also in the absence of Cu_2O nanostructures.

As seen from Figure 4.2c, the slowest rate of MB degradation is observed for the dye-only conditions carried in the absence of Cu_2O nanostructures. For the experiments performed in the presence of different sizes of Cu_2O nanospheres and nanocubes, the Cu_2O nanostructures with dielectric Mie resonances exhibit a higher rate of MB degradation than the 37 nm quasi-spherical Cu_2O nanoparticles that exhibit no Mie resonance in the dye sensitization region. Specifically, the increasing rate of MB degradation is observed in the following order: 165 nm Cu_2O nanocubes > 92 nm Cu_2O nanocubes > 145 nm quasi-spherical Cu_2O nanoparticles > 325 nm Cu_2O nanocubes > 37 nm quasi-spherical Cu_2O nanoparticles (also see Table A.S1 in APPENDIX A). To investigate the possible role of the light-induced heating effect on MB degradation, we measured the light-induced increase in the temperature of the reaction mixture. We found that the temperature of the reaction mixture was increased from ~20 ˚C to ~30 ˚C under MB dye-sensitization conditions (Figure A.S3a-e in APPENDIX A). This increase in the temperature was uniform for all experiments performed in the presence of different sizes of Cu_2O nanospheres and nanocubes as well as for the experiments performed in the absence of Cu_2O nanostructures (Figure A.S3a-e in APPENDIX A). We also performed heating experiments at the elevated temperature of 60 ˚C. No significant degradation was observed in these heating experiments performed under dark conditions in the absence of red-light irradiation (Figure A.S3f in APPENDIX A). These results confirm that the difference in the rate of MB degradation observed in the presence of Cu_2O nanospheres and nanocubes of different sizes is not due to the light-induced heating effect. Therefore, we attribute the higher rate of MB degradation observed on the Cu_2O nanostructures with dielectric Mie resonances (e.g., 165 nm Cu_2O nanocubes) in Figure 4.2c to the dielectric Mie resonance-enhanced MB dye-sensitization.
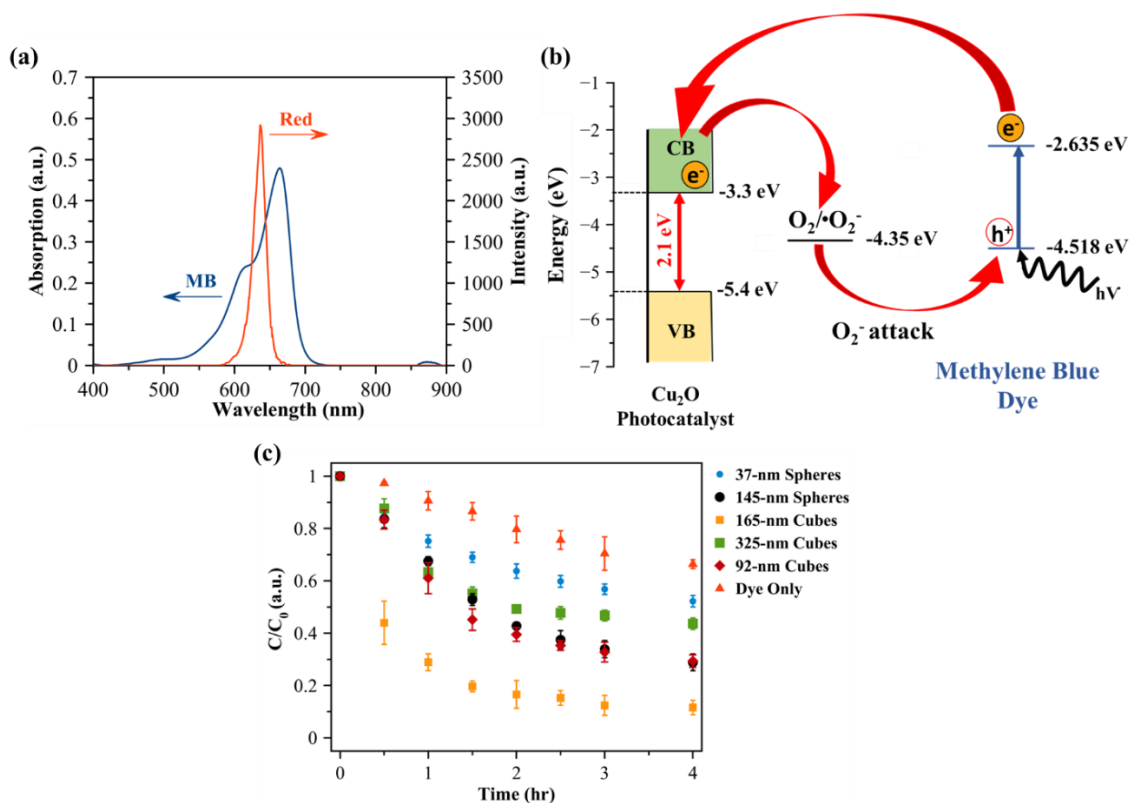
Figure 4.2 **(a)** Absorption spectrum of MB (left ordinate) and spectrum of red LED light source used for MB dye-sensitization (right ordinate). **(b)** Schematic diagram illustrating the MB DSD via superoxide (O_2^-) intermediate species.[38,39] **(c)** Plot of C/C_0 versus irradiation time for MB DSD in DMF using quasi-spherical Cu_2O nanoparticles of 37 ± 6 nm diameter (blue circles), quasi-spherical Cu_2O nanoparticles of 145 ± 41 nm diameter (black circles), Cu_2O nanocubes of 92 ± 13 nm edge length (maroon diamonds), Cu_2O nanocubes of 165 ± 26 nm edge length (orange squares), Cu_2O nanocubes of 325 ± 37 nm edge length (green squares), and under blank conditions in the absence of photocatalyst (red triangles).

For the dye-only conditions, in the absence of Cu_2O nanostructures, the MB degradation can occur via the absorption of the incident photons by the dye molecules followed by the photoexcited electron-transfer from the excited MB molecules into the dissolved oxygen to form superoxide radicals (O_2^-). The superoxide radicals can then attack and degrade the excited MB molecules (Figure A.S4a in APPENDIX A).[35] The Cu_2O nanostructures can enhance the light

absorption efficiency of the dye molecules via a number of pathways, including the electromagnetic nearfield or nanoantenna effect and Mie resonance-induced resonance energy transfer (MIRET). The Cu_2O nanostructures can also facilitate and enhance the electron transfer between adsorbed MB and O_2 molecules and the subsequent degradation of the excited MB molecules. In this dissertation, to develop the structure-property-performance relationships of Cu_2O nanostructures for MB DSD, we propose the following simple approximation as shown in equation (1) below (see Chapter 3, Section 3.1 for more details). This equation relates the rate of MB dye degradation that occurs vis dye-sensitization pathway in the presence of Cu_2O nanostructures and the optical and geometrical properties of the respective Cu_2O nanostructures.

$$r \propto \int I_0(\lambda) Abs_{MB}(\lambda) E_{Cu2O}(\lambda) d\lambda \times \frac{S}{V} \qquad (1)$$

where, r is the rate of dye-degradation per unit mass of the Cu_2O nanostructures, Ext_{Cu2O} is the volume-normalized extinction cross section of the Cu_2O nanostructure, Abs_{MB} is the absorbance of MB, I_0 is the intensity of the incident light, and λ is the wavelength of the incident light, and S and V are the surface area and volume of the Cu_2O nanostructure.

To predict the structure-property-performance relationships of Cu_2O nanostructures using equation (1), we performed FDTD simulations of Cu_2O nanospheres and nanocubes of different sizes (25-400 nm) and simulated the extinction cross section of the respective nanostructures as a function of incident light wavelength. The representative FDTD-simulated extinction spectra of these Cu_2O nanocubes are provided in Figure 4.3a (also see Figure A.S4b-e in APPENDIX A). Based on equation (1), in Figure 4.3a, the extinction cross section values are normalized to the fourth power of the edge length. These FDTD-simulated values are used in equation (1) to predict the performance of Cu_2O nanospheres and nanocubes of different sizes in the range of 25 to 400 nm. Figure 4.3b shows the rate of MB degradation that can occur in the dye-sensitization region (590-670 nm) in the presence of these Cu_2O nanostructures. In Figure 4.3b, the rate values in the

y-axis are normalized with respect to the Cu_2O nanosphere of 37 nm diameter. As seen from Figure 4.3b, our model that is based on equation (1) and FDTD-simulated extinction cross section values predicts a volcano-type relationship between the rate of DSD and the size of Cu_2O nanostructures. From the kinetic data collected from the experiments performed with quasi-spherical Cu_2O nanoparticles of 37 nm and 145 nm average diameters and Cu_2O nanocubes of 92 nm, 165 nm and 325 nm edge lengths (Figure 4.2c), we calculated the relative rate of DSD for these Cu_2O nanostructures (see Figure A.S4v-z and Table A.S1 in APPENDIX A for more details). As seen from Figure 4.3b, the experimentally measured values are in very well agreement with the predicted values. The optimum sizes of Cu_2O nanospheres and nanocubes in the volcano plot shown in Figure 4.3b are in the range of 165-200 nm. The main reason for these Cu_2O nanostructures to appear in the optimum range is their high extinction cross section values in the MB dye sensitization region (i.e., 590-670 nm), as seen from Figure 4.3a. Moreover, the dielectric Mie resonance-enhanced dye-sensitization causes the 165-nm nanocubes to exhibit approximately an order of magnitude (~9 times) higher dye-sensitization rate as compared to 37-nm nanospheres, in which the Mie resonance is absent (see Figure 4.3b and Table A.S1 in APPENDIX A).

The structure-property-performance relationships developed in this dissertation can be used for designing a wide range of DSP systems. For example, when the Cu_2O nanostructures are used for DSP systems consist of a dye that absorbs in the shorter wavelength region (e.g., 460-500 nm), our model shown in equation (1) predicts that optimum sizes of Cu_2O nanostructures move towards smaller sizes (e.g., 120-150 nm Cu_2O nanocubes in Figure 4.3a). Similarly, for dyes that can absorb in the near-IR wavelength region (e.g., 800-900 nm), the optimum sizes are predicted to move towards larger sizes (e.g., 240-270 nm Cu_2O nanocubes in Figure 4.3a). The approach demonstrated in this study can also be used to design DSP systems that can involve a wide range of combinations of medium- and high-refractive-index semiconductors and dye molecules. Our

FDTD simulation results shown in Figure A.S4f-u in APPENDIX A predict that such combinations can include semiconductors such as CeO_2, CuO, α-Fe_2O_3, and TiO_2 and appropriate dye molecules that can absorb anywhere in the visible and near-IR wavelength regions. The energy levels of these dye molecules need to be in alignment with the conduction band edge of the semiconductors so that the excited electrons can be transferred from the dye molecules into the semiconductor.
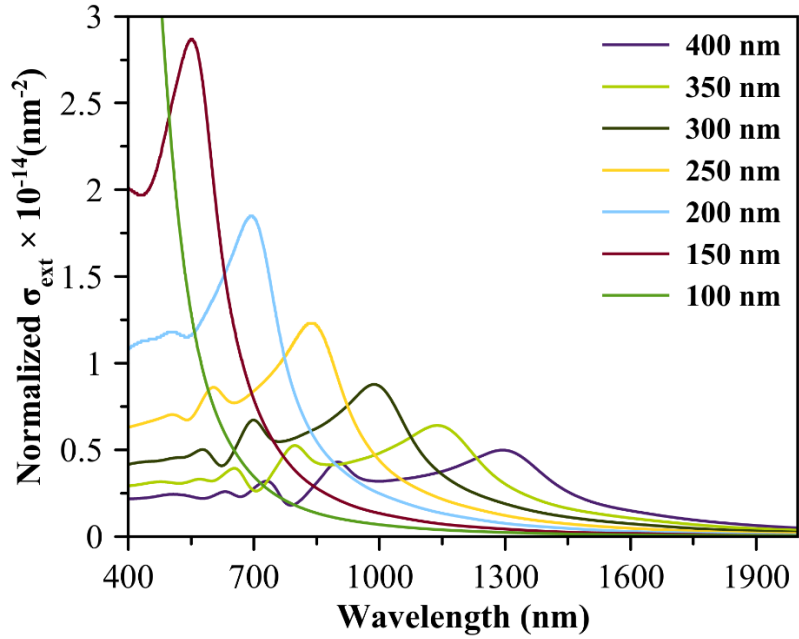
Figure 4.3 **(a)** FDTD-simulated normalized-extinction (normalized-σ_{Ext}) cross section of Cu_2O nanocubes of different edge lengths in the range of 25 to 400 nm as a function of incident light wavelength. Normalized-σ_{Ext} = Ratio of extinction cross section (σ_{Ext}) of nanocube to the fourth power of its edge length (A^4).
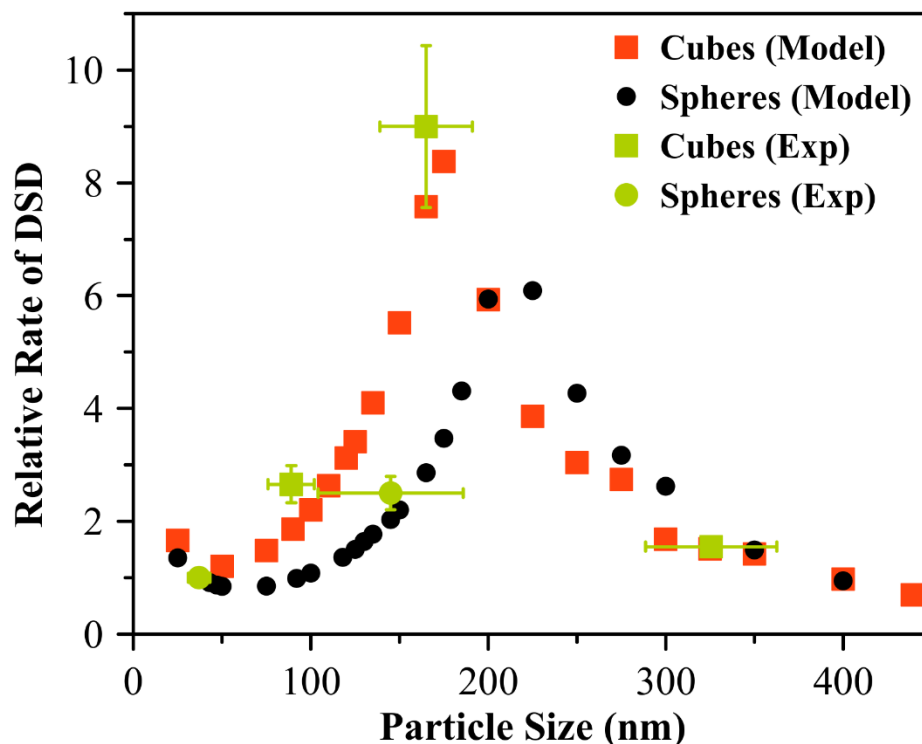
Figure 4.3 (b) Volcano plot showing the predicted and experimentally measured relative rate of MB DSD as a function of size of Cu_2O nanospheres and nanocubes. Black circles and red squares represent predicted relative rates for Cu_2O nanospheres and nanocubes, respectively. Green circles, and green squares represent experimentally measured relative rates on quasi-spherical Cu_2O nanoparticles of 37 ± 6 nm diameter, quasi-spherical Cu_2O nanoparticles of 145 ± 41 nm diameter, Cu_2O nanocubes of 92 ± 13 nm edge length, Cu_2O nanocubes of 165 ± 26 nm edge length and Cu_2O nanocubes of 325 ± 37 nm edge length, respectively. Rate of MB DSD on quasi-spherical Cu_2O nanoparticles of 37 ± 6 nm diameter is used as a reference.

4.2. Mie Resonance-Enhanced Photocatalysis

4.2.1. Summary

Nanostructured metal oxides, such as Cu_2O, CeO_2, α-Fe_2O_3, and TiO_2 can efficiently mediate photocatalysis for solar-to-chemical energy conversion and pollution remediation. In this dissertation, we report a novel approach, dielectric Mie resonance-enhanced photocatalysis, to

enhance the catalytic activity of metal oxide photocatalysts. Specifically, we demonstrate that Cu$_2$O nanostructures exhibiting dielectric Mie resonances can exhibit up to an order of magnitude higher photocatalytic rate as compared with Cu$_2$O nanostructures not exhibiting dielectric Mie resonances. Our finite-difference time-domain (FDTD) simulation and experimental results predict a volcano-type relationship between the photocatalytic rate and the size of Cu$_2$O nanospheres and nanocubes. Using transient absorption measurements, we reveal that a coherent electronic process associated with dielectric Mie resonance-mediated charge carrier generation is dominant in Cu$_2$O nanostructures that exhibit higher photocatalytic rates. Although we experimentally demonstrate dielectric Mie resonance-enhanced photocatalysis with only Cu$_2$O nanoparticles here, based on our FDTD simulations, we anticipate the same can be achieved with other metal oxide photocatalysts, including CeO$_2$, α-Fe$_2$O$_3$, and TiO$_2$.

4.2.2. Specific Findings on Mie Resonance-Enhanced Photocatalysis

In this dissertation, we show particle-size dependent photocatalytic activity under visible radiation. In particular, the photocatalytic activity is maximized for particle size of 145 nm for nanospheres as monitored from photocatalytic degradation of a model dye molecule, methylene blue (MB), under irradiation with green LEDs. In this case, we owe the highest photocatalytic activity in 145 nm nanospheres to dielectric Mie resonances, whose absorption spectrum overlaps maximum with the incident light source. We obtain similar results with Cu$_2$O nanocubes. The results from the photoreactor studies are supported by the transient-absorption measurements that are used to identify the incoherent or coherent charge carrier dynamics that are markedly different for different size particles. We have also provided structure-photocatalytic performance relationships that capture the proposed dielectric Mie resonance-enhanced photocatalysis in Cu$_2$O spherical and cubical particles. Specifically, our finite-difference time-domain (FDTD)

simulation and experimental results predict a volcano-type relationship between the relative photocatalytic rate and the size of Cu_2O nanoparticles.

Figure 4.4a-d shows the representative TEM image of 42-nm Cu_2O nanospheres and SEM images of 145-nm spheres, 92-nm nanocubes, and 286-nm nanocubes, respectively. The representative SEM image of 456-nm nanocubes is provided in B.S6f Figure in APPENDIX B. The particles seen in Figure 4.4a-b are faceted with rounded edges and corners. Despite the distribution of shapes, they are equiaxed on the average. Therefore, we refer to them as 'nanospheres' in this study. As confirmed by XRD analysis (e.g., Figure B.S2a-b in APPENDIX B), all particles exhibit the cubic Cu_2O crystal structure. Photocatalytic performance of the particles toward MB degradation is evaluated for the same weight load of Cu_2O nanoparticles. Green LED lamps with peak emission at 519 nm are used as the excitation source. A representative picture of the photoreactor is provided in Figure B.S2c in APPENDIX B. In Figure 4.5a, we provide the excitation spectrum of green LEDs as well as the absorption spectrum of MB. As seen, there is minimal spectral overlap between the excitation and the MB absorption ensuring minimal dye degradation by direct excitation of MB. In Figure 4.5b, we show the extent of MB dye degradation (i.e., the ratio of the concentration of MB to its initial concentration, C/C_0) by 42-nm and 145-nm Cu_2O nanospheres and 92-nm, 286-nm, and 456-nm Cu_2O nanocubes as a function of visible light irradiation time. As seen from Figure 4.5b, the 145-nm Cu_2O nanospheres exhibit the highest MB degradation rate while 42-nm Cu_2O nanospheres exhibit the lowest rate among the Cu_2O nanostructures investigated in the photocatalytic experiments. Despite their enhanced photocatalytic rate, the 145-nm spheres have only 29% of the total surface area of the 42-nm spheres. We have also performed

photocatalytic experiments under visible light irradiation in the absence of Cu_2O particles and found no significant MB degradation under these blank conditions.

To confirm that the MB degradations shown in Figure 4.5b are not due to light-induced heating, we measured the change in temperature of the reaction mixture as a function of irradiation time. We found that visible light irradiation increases the temperature of the reaction mixture from ~20 °C to a maximum of ~28 °C (Figure B.S3a-e in APPENDIX B Specifically, we observed a similar extent of increase in temperature for the photocatalytic experiments performed using the 42-nm and 145-nm Cu_2O nanospheres, 92-nm, 286-nm, and 456-nm cubes, and under blank conditions in the absence of Cu_2O nanoparticles (Figure B.S3a-e in APPENDIX B. The heat localization in our system is also expected to be minimal since the photocatalytic experiments are performed in the liquid medium under stirring.[32] We also carried out heating experiments with Cu_2O nanospheres and nanocubes under dark conditions. In these heating experiments, the temperature of the reaction mixture is maintained at 60 °C. For all tested experimental conditions, the heating trials revealed no significant MB degradation in the absence of light exposure across an extended period (e.g., Figure B.S3f in APPENDIX B.

(a)

(b)

(c)

(d)

.
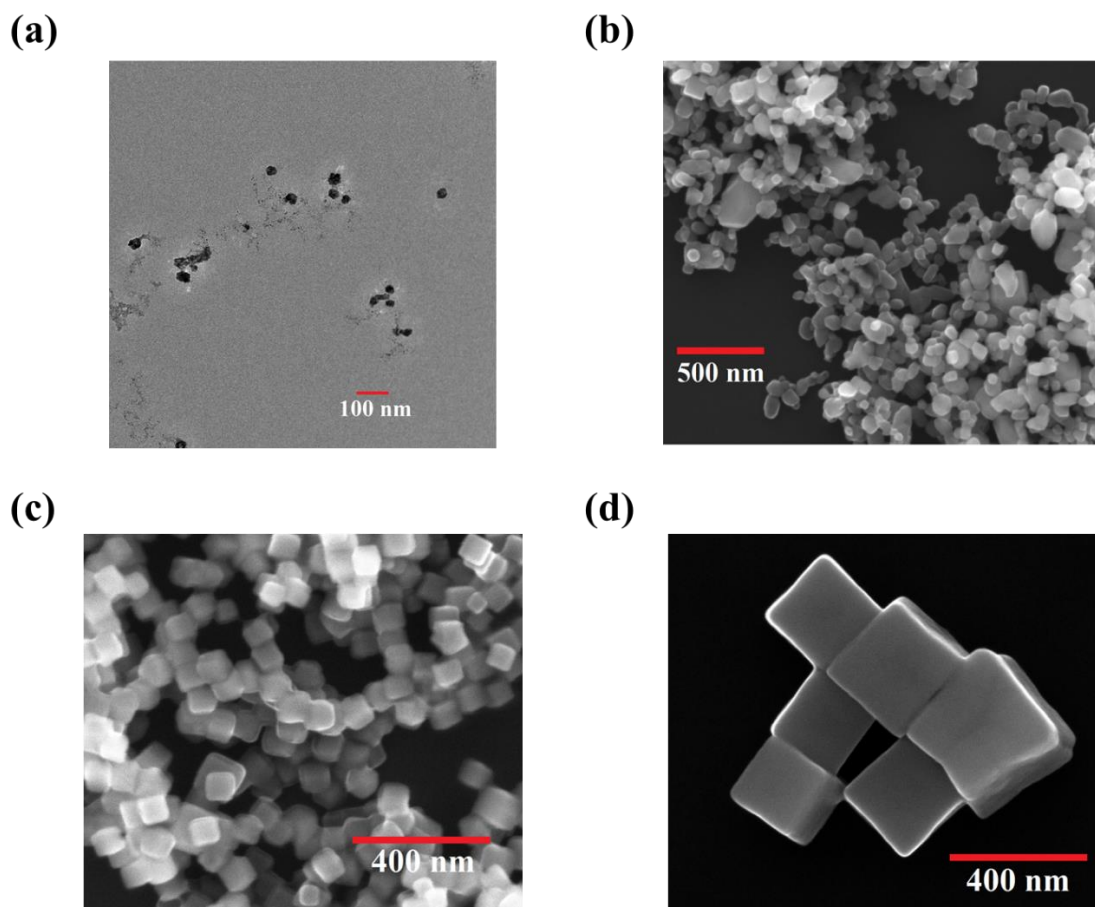
Figure 4.4 **(a)** Representative TEM image of smaller Cu_2O nanospheres of 42 ± 6 nm diameter. **(b-d)** Representative SEM images of **(b)** larger Cu_2O nanospheres of 145 ± 41 nm diameter, **(c)** Cu_2O nanocubes of 92 ± 13 nm edge length, and **(d)** Cu_2O nanocubes of 286 ± 47 nm edge length.
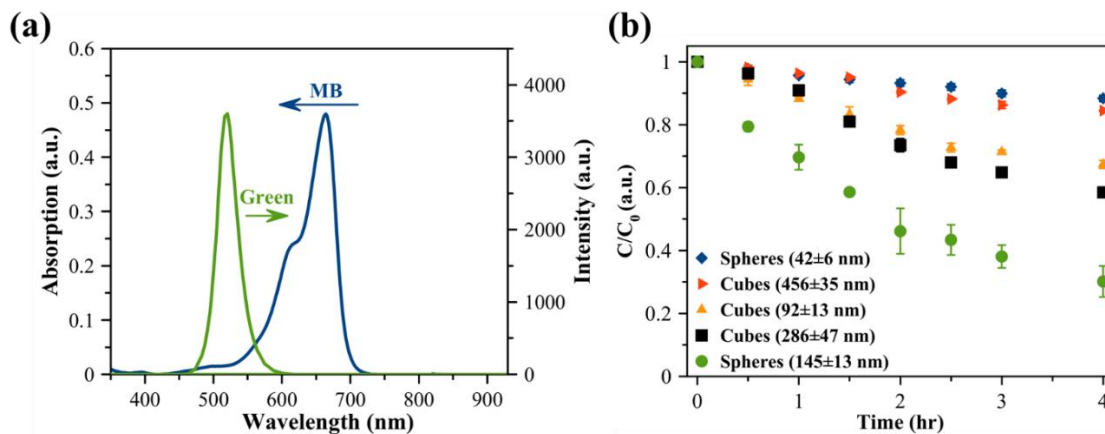
Figure 4.5 **(a)** Absorption spectrum of MB (left ordinate) and spectrum of green LED light source used for photocatalytic degradation of MB (right ordinate). **(b)** Plot of C/C_0 versus irradiation time for photocatalytic degradation of MB using 42-nm Cu_2O nanospheres (blue diamonds), 456-nm Cu_2O nanocubes (red forward triangles), 92-nm Cu_2O nanocubes (orange triangles), 286-nm Cu_2O nanocubes (black squares), and 145-nm Cu_2O nanospheres (green circles).

To validate that the differences in the photocatalytic rates of Cu_2O nanostructures Figure 4.5b originate from their distinct dielectric Mie resonance characteristics, we examine their UV-Vis extinction spectra in Figure 4.6a-b (also see Figure B.S6e in APPENDIX B As seen from Figure 4.6a, the 42-nm spheres, being consistent with what is expected for their bulk counterparts, exhibit no resonance peaks in the UV-Vis-near IR extinction spectra. In contrast, the 145-nm nanospheres in Figure 4.6a, and 92-nm and 286-nm Cu_2O nanocubes in Figure 4.6b and 456-nm nanocubes in Figure B.S6e in APPENDIX B exhibit Mie resonance peaks in the visible to near IR regions. To understand the nature of these resonance peaks, we performed FDTD simulations. The representative simulated extinction spectra of the 42-nm Cu_2O nanosphere and 286 nm-nanocube are shown in

Figure B.S4a in APPENDIX B. The features observed in the simulated extinction spectra of the 42-nm spheres and 286-nm cubes are consistent with the experimentally measured extinction spectra of the respective Cu_2O nanoparticles shown in Figure 4.6a-b. The magnetic and electric field distributions at different wavelengths across the resonance peaks of the 286-nm nanocubes are also provided in Figure B.S4b-c in APPENDIX B. The field distributions confirm that the resonance peaks observed in the extinction spectra of the 286-nm cube are due to the dielectric Mie resonances.[20] From the field distribution maps, we assign the lowest energy resonance peak observed in the extinction spectrum of the Cu_2O cube to the combination of electric and magnetic dipoles (Figure B.S4b-c in APPENDIX B .[20] Similarly, we assign the second lowest energy resonance peak and higher-order resonance peaks to the combination of electric and magnetic quadrupoles and the combination of higher-order electric and magnetic resonance modes, respectively.[20] From the Figure 4.5b and Figure 4.6a-b, it is clear that 145-nm Cu_2O nanospheres and 92-nm and 286 nm nanocubes, exhibiting dielectric Mie resonances, are associated with a higher photocatalytic rate as compared to 42-nm Cu_2O nanospheres not exhibiting dielectric Mie resonances. Also, based on the FDTD simulation results (e.g., Figure B.S4a-c in APPENDIX B, we attribute that both the magnetic and electric components of the dielectric Mie resonances are responsible for the Mie resonance-enhanced photocatalysis observed in the 145-nm Cu_2O nanospheres and 92-nm and 286 nm nanocubes.
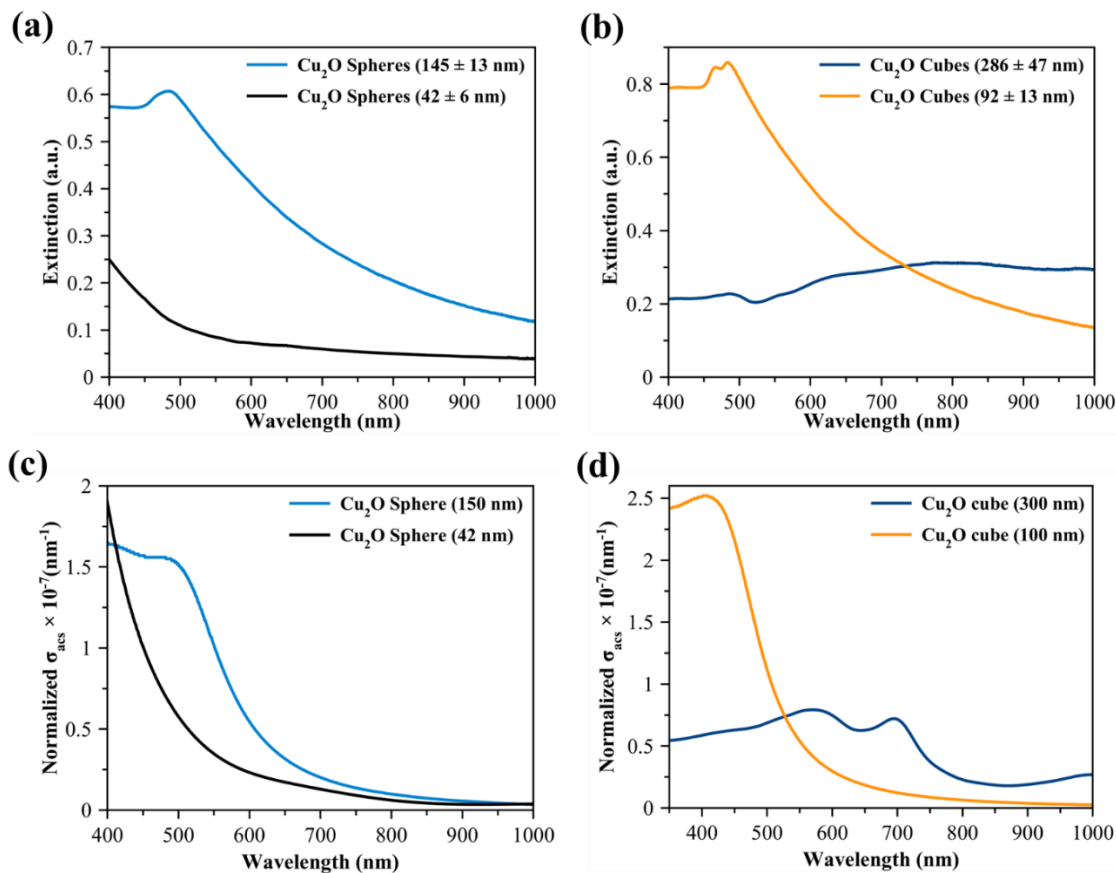
Figure 4.6 **(a-b)** Experimentally measured UV-Vis extinction spectra of **(a)** Cu_2O nanospheres of 42 ± 6 nm and 145 ± 41 nm diameters, and **(b)** Cu_2O nanocubes of 92 ± 13 nm and 286 ± 47 nm edge lengths. **(c-d)** FDTD-simulated volume-normalized absorption cross section (σ_{acs}) as a function of incident light wavelength for **(c)** Cu_2O nanospheres of 42 and 150 nm diameters, and **(d)** Cu_2O nanocubes of 100 nm and 300 nm edge lengths.

To develop the structure-property-photocatalytic performance relationships of Cu_2O nanostructures, we propose a rational approach to predict the photocatalytic reaction rate on Cu_2O nanospheres and nanocubes of different sizes. In this approach, it is approximated that the photocatalytic rate on Cu_2O nanostructures is proportional to their charge carrier generation capacity. From this approximation, the photocatalytic rate per

photocatalyst mass at a given incident light wavelength is proportional to the incident light intensity and the volume-normalized absorption cross section of the Cu_2O nanostructures. The FDTD simulations are used to predict this key optical property, i.e., volume-normalized absorption cross section of the Cu_2O nanostructures of different sizes as a function of incident light wavelength. The photocatalytic MB dye degradation studies in our system are carried out for the same weight load of Cu_2O nanospheres and nanocubes. Therefore, the comparison of the volume-normalized absorption cross section values of Cu_2O nanostructures is a good descriptor to predict their relative light absorption capacity in our system (see Section 3.3 for more details). In Figure 4.6c-d, we show the representative simulated absorption spectra of the 42-nm and 150 nm-nanospheres and 100-nm and 300-nm nanocubes, respectively. The simulated absorption spectra of a wide range of sizes are also provided in Figure B.S5a-b in APPENDIX B (also see Figure B.S5h-i). The y-axis values in these figures correspond to the volume-normalized absorption cross section. The overlap between the FDTD-simulated absorption spectra of the Cu_2O nanostructures and the incident light spectrum is used as a descriptor to predict the photocatalytic rate of the respective nanostructures. We used this approach to predict the relationship between the size of the Cu_2O nanospheres and nanocubes and their photocatalytic performance for the photocatalytic degradation of methylene blue molecules. The representative results are shown in Figure 4.7. The photocatalytic rate on 286-nm Cu_2O nanocubes is used as a calibration reference to calculate the relative photocatalytic rate of Cu_2O nanospheres and nanocubes of different sizes in Figure 4.7. The experimentally measured kinetic data shown in Figure 4.5b are fitted to obtain the apparent first-order rate constant values (see Figure B.S5c-f and Table

B.S1 in APPENDIX B. The experimental value for the relative photocatalytic rate of Cu_2O nanospheres and nanocubes of a given size is obtained from the ratio of the rate constant value of the respective nanostructures to that of 286-nm Cu_2O nanocubes. As seen from Figure 4.7, our simulation and experimental results predict a volcano-type relationship between the photocatalytic rate and the size of Cu_2O nanospheres and nanocubes. Specifically, among the Cu_2O nanospheres and nanocubes investigated in our photocatalytic experiments, the absorption spectrum of the 145-nm nanosphere provides a better overlap with the green LED spectrum in the ~490-560 nm wavelength region due to the dielectric Mie resonance peak. This better overlap results in the highest photocatalytic rate by 145-nm nanospheres. The dielectric Mie resonance-enhanced absorption causes the 145-nm nanospheres to exhibit an order of magnitude (9.76 times) higher photocatalytic rate as compared to 42-nm nanospheres, in which the Mie resonance is absent (see Figure 4.7 and Table B.S1 in APPENDIX B.

It is also important to mention here that our model prediction (i.e., equation# 5 in the supporting information) is based only on the absorption effect by the Cu_2O nanostructures. The scattering effect of Cu_2O nanostructures may lengthen the light path and may also improve photocatalytic activity. For example, the larger size Cu_2O particles (e.g., 286 nm Cu_2O cube) scatter light strongly as we demonstrated from the single particle scattering measurements in our recent contribution.[20] Therefore, in addition to the absorption effect, the scattering effect may also improve the photocatalytic activity of Cu_2O nanostructures. However, as shown in Figure 4.7, our model prediction that is based on only the absorption effect is in good agreement with the experimentally observed results. This good match between the model prediction and experimentally observed

results in Figure 4.7 indicates that the absorption effect by the Cu_2O nanostructures plays the dominant role and the contribution from the scattering effect is minimal.
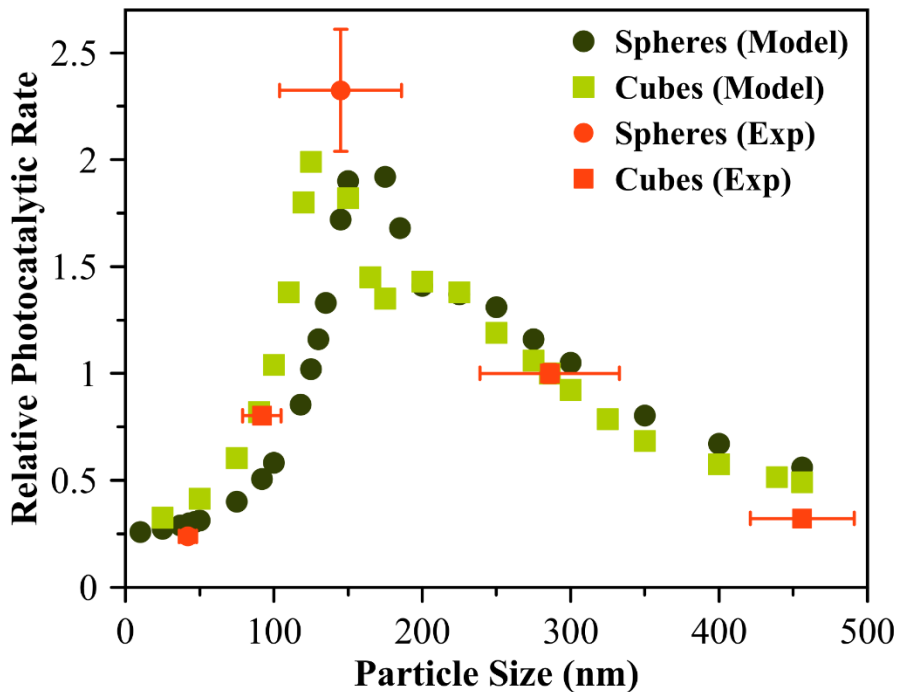
Figure 4.7. Volcano plot showing the predicted and experimentally measured relative photocatalytic rate as a function of size of Cu_2O nanospheres and nanocubes. The photocatalytic rate on Cu_2O nanocubes of 286 nm average edge length is used as a calibration reference.

To illustrate the photocatalytic mechanism that is responsible for the MB degradation on Cu_2O cubes, we investigated the possible role of the solvent and superoxide (O_2^-) on MB degradation. To investigate the solvent dependency on MB degradation, we performed photocatalytic experiments using two different solvents, DMF and ethanol, and the representative results for 286-nm Cu_2O nanocubes are shown in Figure 4.8a. In the solvent-dependent studies, Cu_2O nanocubes exhibited a similar or slightly faster MB degradation in DMF compared to ethanol. We attribute the observed slightly faster MB degradation to the expected higher solubility of dissolved oxygen in DMF compared to ethanol. Previous studies have demonstrated that MB

degradation on semiconductor photocatalysts can occur via a superoxide-mediated mineralization mechanism.[38,39]

To investigate whether photocatalytic MB degradation occurs via a superoxide-mediated mechanism, we performed the photocatalytic experiments with and without benzoquinone, a well-known scavenger of the superoxide.[40] The results from these experiments are shown in Figure 4.8b. The direct evidence of the superoxide-mediated mechanism can be gathered from Figure 4.8b, with the benzoquinone successfully inhibiting the MB degradation via scavenging of the superoxide. Based on these findings, we propose the following photocatalytic mechanism for the MB degradation on large Cu_2O cubes. This mechanism, schematically illustrated in Figure 4.8c, involves the excitation of dielectric Mie resonances by the incident photons. The energy stored in Mie extinction dissipates into Mie scattering and Mie absorption. A major fraction of the energy that corresponds to Mie absorption transfers into and results in the coherent generation of excited electrons (e^-) and holes (h^+) in the conduction and valence bands of Cu_2O, respectively. The excited electrons from the conduction band reduce the dissolved oxygen (O_2) into superoxide (O_2^-). The superoxide then reacts with the MB molecule and forms several intermediate products, one of them being a carboxylic acid ($RCOO^-$) intermediate.[38,39] This intermediate can be oxidized by the excited hole (h^+) in the valence band into degradation products.[38,39]
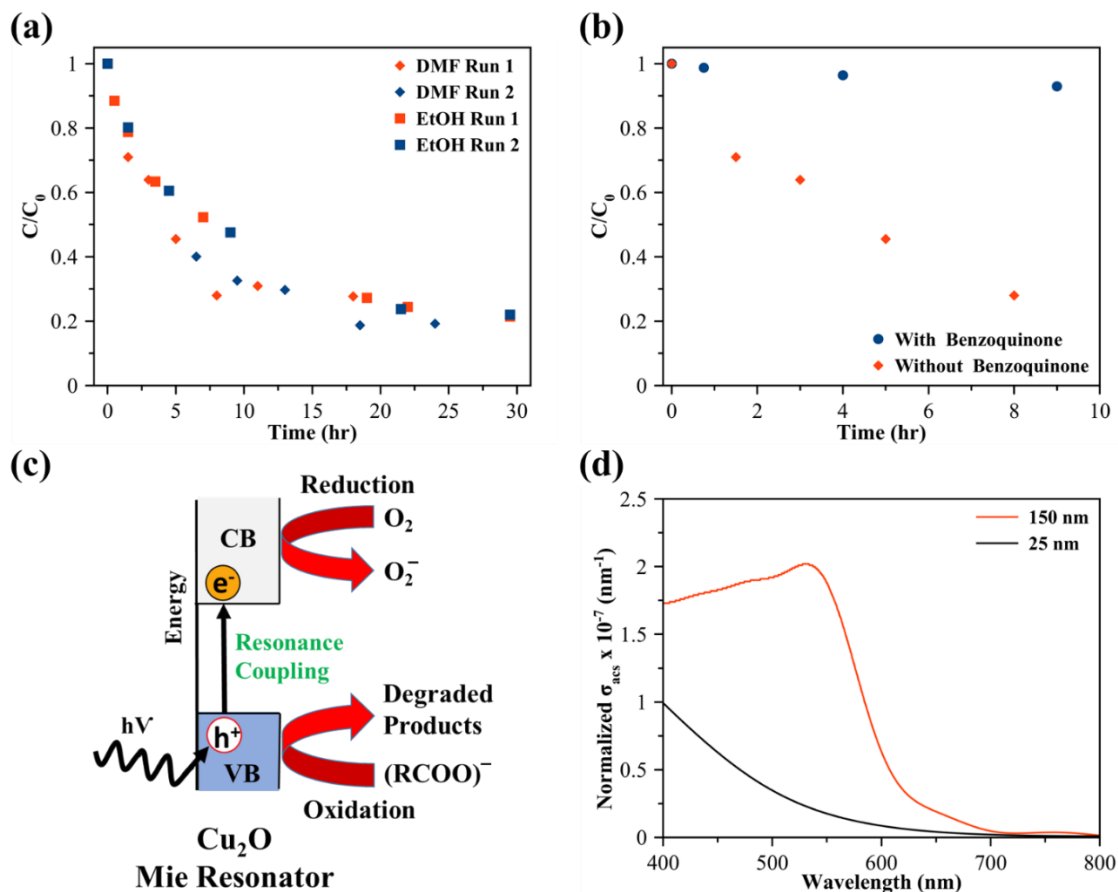
Figure 4.8. **(a)** Plot of C/C_0 versus irradiation time for photocatalytic degradation of MB in DMF (red and blue diamonds) and ethanol (red and blue squares) using 286-nm Cu_2O nanocubes. **(b)** Plot of C/C_0 versus irradiation time for photocatalytic degradation of MB in the presence (blue circles) and absence (red diamonds) of benzoquinone using 286-nm Cu_2O nanocubes in DMF. **(c)** Schematic diagram illustrating the proposed dielectric resonance-enhanced photocatalytic degradation of MB that occurs via a superoxide (O_2^-)-mediated mechanism. **(d)** FDTD-simulated volume-normalized absorption cross section (σ_{acs}) as a function of incident light wavelength for a larger α-Fe_2O_3 nanosphere of 150 nm diameter and a smaller α-Fe_2O_3 nanosphere of 25 nm diameter.

The dielectric resonance-enhanced photocatalysis demonstrated herein can be potentially applied to other metal oxide photocatalysts. For example, CeO_2, α-Fe_2O_3, and TiO_2 semiconductors are also moderate and high refractive index materials with the values of the real part of the refractive index in the range of 2.1-2.5, 2.7-3.3, and 1.4-5.4, respectively (APPENDIX B)

To investigate whether these metal oxide particles exhibit dielectric resonance characteristics similar to that of Cu_2O, we performed FDTD simulations to simulate the absorption spectra of different sizes of CeO_2, α-Fe_2O_3, and TiO_2 particles. The representative spectra are shown in Figure 4.8d and also in Figure B.S7a-c in APPENDIX B. Our FDTD simulations show that CeO_2, α-Fe_2O_3, and TiO_2 particles exhibit dielectric resonance characteristics that are similar to Cu_2O particles. Specifically, our findings show that small nanoparticles such as spherical nanoparticles of 25 nm diameter exhibit light absorption features similar to their bulk counterparts and do not exhibit any Mie resonances in the near UV-Vis-near IR regions. In contrast, large nanoparticles such as spherical nanoparticles of 150 nm diameters exhibit strong dielectric resonances. For example, Figure 4.8d shows the volume-normalized absorption cross section values as a function of incident light wavelengths for 25 and 150 nm spherical α-Fe_2O_3 particles. As seen from Figure 4.8d, in the visible region, 150 nm spherical nanoparticle exhibits relatively higher light absorption capacity than small spheres of 25 nm diameter. Similar to the dielectric resonance-enhanced photocatalysis demonstrated in larger Cu_2O cubic particles in this dissertation, the dielectric resonance features of larger CeO_2, α-Fe_2O_3, and TiO_2 particles can be possibly explored to enhance their inherent photocatalytic activity.

We also investigated the morphological and phase stability of the Cu_2O nanostructures after exposure to photocatalytic conditions. We characterized the as-prepared and used Cu_2O nanostructures using SEM, XRD, and Raman spectroscopy. Essentially, no significant change in the morphology of the Cu_2O nanostructures is observed (e.g., see Figures B.S6f-g in

APPENDIX B. Similarly, no change in the Cu_2O phase is observed as can be seen from the XRD and Raman spectra of the as-prepared and used Cu_2O nanostructures in Figure 4.9a and Figure 4.9b, respectively. Specifically, Figure 4.9a compares the representative XRD spectra of the 145-nm Cu_2O nanospheres before and after exposure to the photocatalytic conditions. In Figure 4.9a, the as-prepared and used samples show the XRD signals for only the Cu_2O phase, and no detectable signal is observed for the CuO phase (see Figure B.S6h in APPENDIX B for the CuO reference spectrum). Similarly, Figure 4.9b compares the representative Raman spectra of 145-nm Cu_2O nanospheres, as-synthesized versus after 4 hours of exposure under the photocatalytic conditions. The Raman samples were obtained by spotting and drying 5 μL aliquots of fresh and exposed colloids on glass slides. The Raman peak observed at 215 cm^{-1} in the fresh sample is a second-order overtone, $2\Gamma_{12}^-$, which is characteristic of crystalline Cu_2O.[20,41] The peak at 630 cm^{-1} is assigned to the infrared-allowed Γ_{15}^- (TO) mode in Cu_2O crystals.[20,41] Finally, the weak peak at 415 cm^{-1} is attributed to the overtone of four phonons, $3\Gamma_{12}^- + \Gamma_{25}^-$ in crystalline Cu_2O.[20,41] On the other hand, the strongest characteristic peaks of CuO, being at 298, 330, and 602 cm^{-1}, are not detected.[20,41] The exposed samples exhibit peak shifts of 2-3 cm^{-1} from the as-synthesized ones, which are within the spectral resolution (accuracy) of our 600 lines/mm grating, which is about 4 cm^{-1}. Therefore, the nanoparticles are inferred to remain stable as Cu_2O during the light exposures.

In Figure 4.9b, we also reproducibly observe additional peaks for the exposed Cu_2O nanoparticles (i.e., 4 hr reaction sample), being characteristic of MB. The peaks at 1618 and 1429 cm^{-1} are assigned to C—C ring stretching and C—N asymmetric stretching respectively.[42] Also, the peaks at 895 and 1128 cm^{-1} are assigned to in-plane C—H bending and out-of-plane C—H bending in MB respectively.[42] The weaker MB peaks are not labeled in Figure 4.9b. Therefore, despite washing of the nanoparticles after exposures, residual MB is inferred to remain on the nanoparticle surfaces, indicative of the strong affinity of MB to the Cu_2O nanoparticles.

Therefore, the insignificant shifts in Cu_2O peaks of the exposed nanoparticles, may also be due to the presence of a thin layer of MB, changing: i) the Cu_2O spectrum baseline with weak fluorescence/Raman bands (i.e., MB fluorescence band is already seen); or ii) the stress state of the Cu_2O nanoparticles by surface energy/tension effects. In summary, both XRD and Raman spectra in Figure 4.9a-b confirm that the Cu_2O phase of the nanoparticles does not undergo any detectable change into the CuO phase under the photocatalytic conditions investigated in this study.
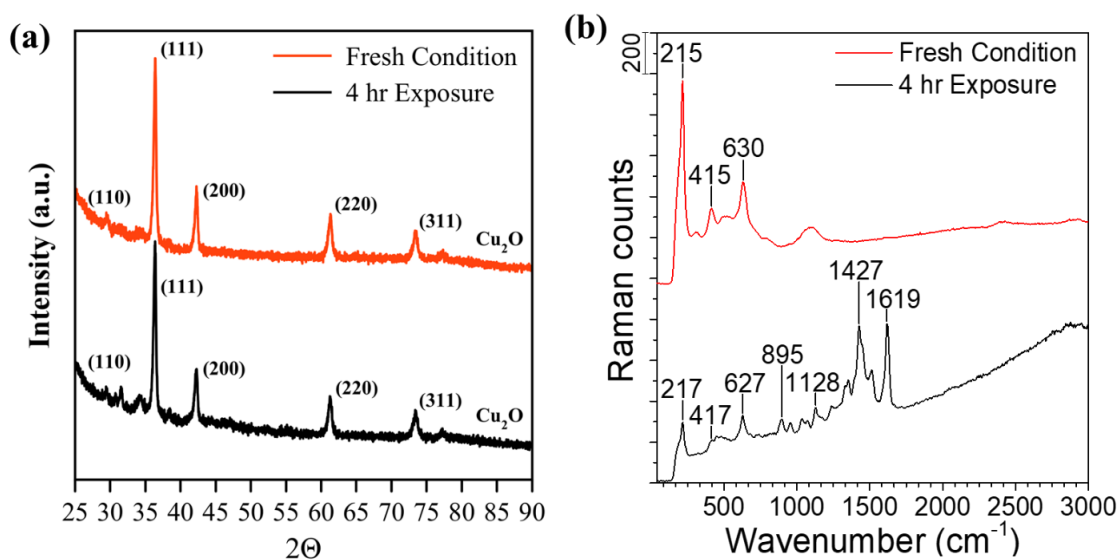

Figure 4.9. (a) Representative X-ray diffraction patterns of as-prepared 145-nm Cu_2O nanospheres sample (Fresh Condition) and the same batch of sample after exposure to 4 hours of photocatalytic degradation of MB under the green light illumination (4 hr Exposure). (b) Representative Raman spectra of 145-nm Cu_2O nanospheres in the as-synthesized sample (Fresh Condition) and after exposure to 4 hours of the photocatalytic conditions (4 hr Exposure).

4.3. Tuning Catalytic Activity and Selectivity in Photocatalysis

4.3.1. Summary

Dye degradation has been for more than forty years in the scientific community. All these studies have primarily focused on breaking various dyes using catalysts driven by either light or heat.

Most studies started to focus on metal-oxides after the discovery of water-splitting by TiO_2. Among the many catalysts used plasmonic metal nanostructures have been explored significantly in recent times due to their special property called localized surface plasmon resonances (LSPR). However, facing multiple problems of heat losses and instability, people started to focus on dielectric medium-to-high refractive indexed materials for photonic applications. Most of these dielectric materials have been studied from a physics point of view and less from chemistry. In this work, we have focused on how these materials can be used for tuning selectivity through wavelength-dependent studies by performing methylene blue (MB) dye degradation.

4.3.2. Specific Findings on Tuning Catalytic Activity and Selectivity in Photocatalysis

This dissertation reports interesting results about how different peaks of MB can be degraded by tuning multiple lights in the visible region. Herein we show some promising new ideas about using medium-refractive indexed semiconductor material being used in achieving this control over breaking down MB peaks. Figure 4.10(a, b) shows the scanning electron microscopy (SEM) images of the Cu_2O nanoparticles of the bi-pyramidal shape (Cu_2O BPPs) taken at the end of synthesis. Figure 4.10b shows SEM Figure 4.10a focused on single particle. The ultraviolet-visible (UV-Vis) extinction spectra of after-washed catalyst (see, Figure 4.10c) and X-ray diffraction (XRD) spectra (see, Figure 4.10d). The UV-Vis spectra in Figure 4.10c shows BPPs have multiple mie resonance peaks, the major one which overlaps with the MB covers a region of 600-700 nm. This strong overlap is crucial in determining the outcome of MB degradation reaction.
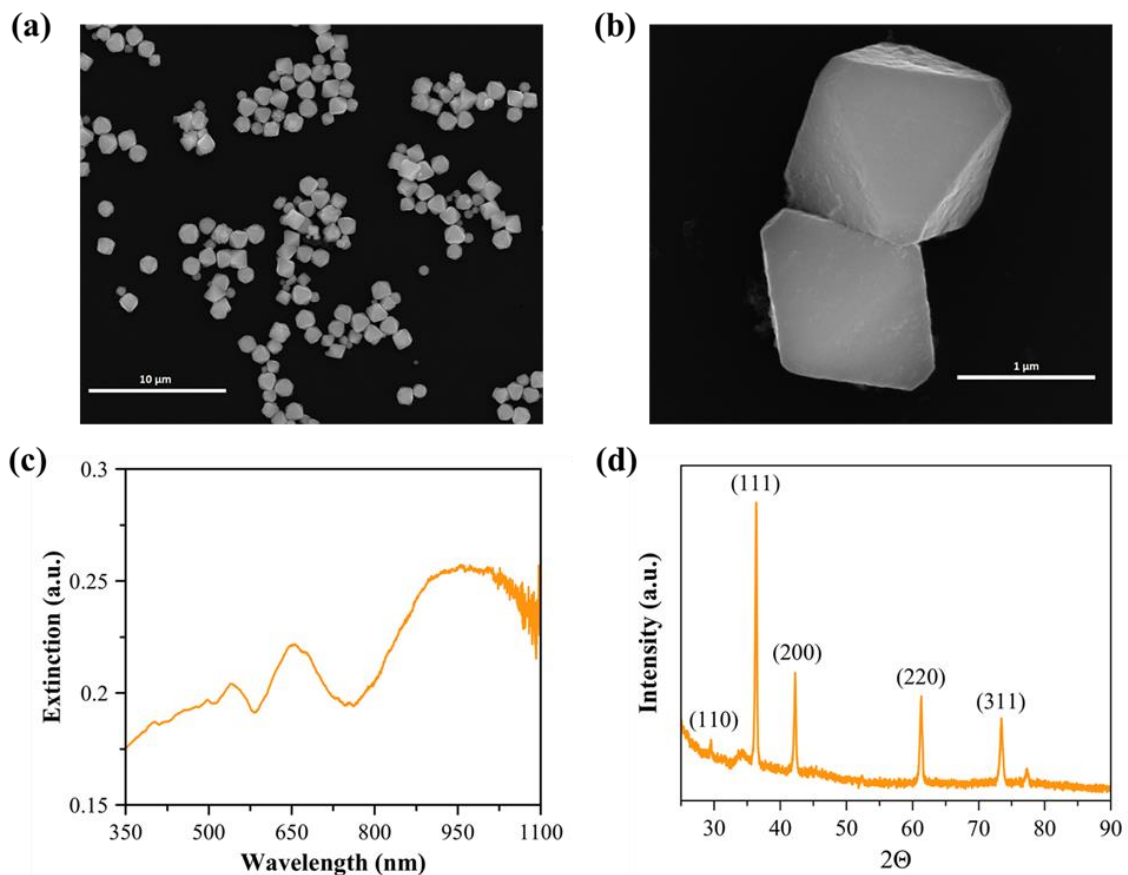
Figure 4.10. Cu_2O nanoparticles synthesized using chemical reduction technique **(a, b)** SEM Images showing Cu_2O nanoparticles of the bi-pyramidal shape of size 1052 ± 96 nm **(c)** UV-Vis spectra measured of washed catalyst showing resonance peaks. **(d)** XRD of Cu_2O BPPs.

MB degradation experiments with Cu_2O nanoparticles of the bi-pyramidal shape under illumination of desired wavelength of light are detailed in the Chapter 3, Section 3.5. To the distinguish role of light from heat, reactions in the absence of light were carried out at various temperatures ranging 20-40 ℃ (see, Figure C.S1a-c) in APPENDIX C). and corresponding temperatures were also measured as shown in Figure C. S2a-c, APPENDIX C. It can be seen that in dark conditions, the monomer peak breaks down slightly faster as we raise the temperature from 20 to 40 ˚C. We can see that the oligomer peak also increases with the temperature rise. The MB degradation was calculated with primary absorption peak of MB from samples taken at

different time intervals. The primary MB peak (monomer) at ~665 nm decreases with time, in parallel with the increase in oligomer of MB peak (~480 nm) as shown in Figure C.S3, APPENDIX C.

The plot shows the measure conversion of MB into its components such as CO2, NH3, etc. The increase in tertiary peak (oligomer) represents the measure of oligomer yield. It can be seen that in

Figure 4.11a the activity of Cu_2O BPPs under red light illumination is several times higher than in light off conditions, and corresponding oligomer yield Figure 4.11b is also higher under illumination. As we can observe from Figure 4.11c under illumination the normalized oligomer remains similar, except at higher conversions (degrdation og MB) it drops, attributing to higher activity of the catalyst.
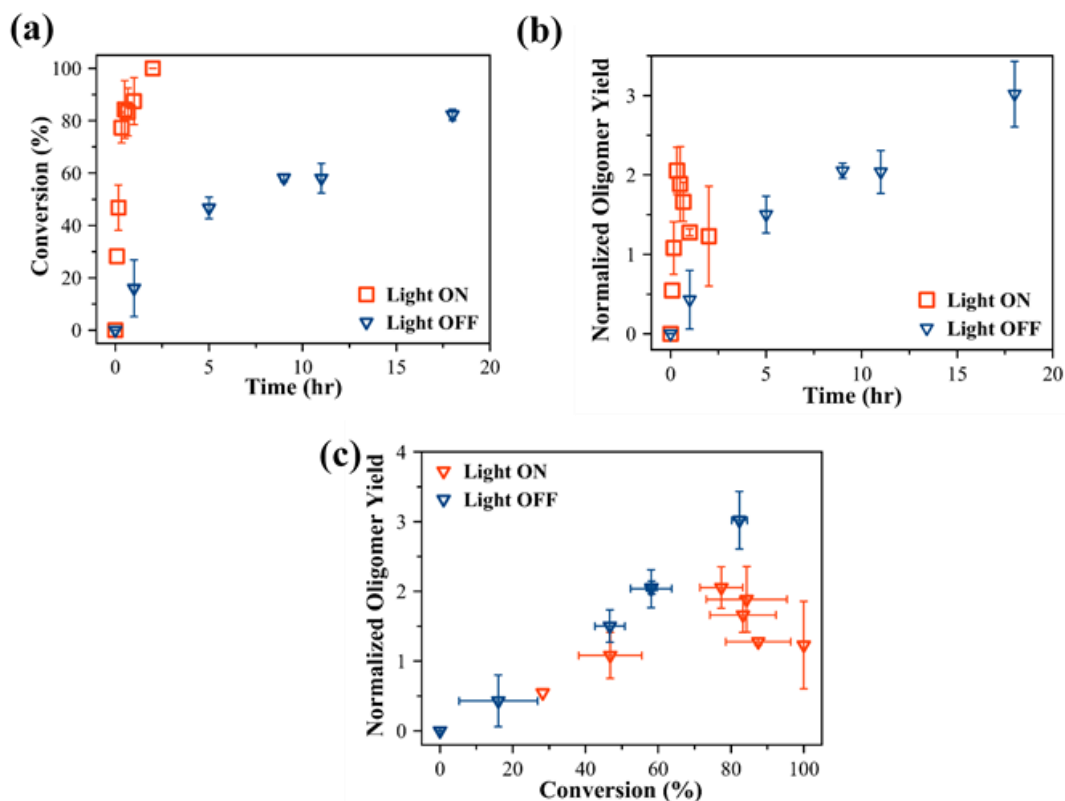
Figure 4.11. Methylene blue (MB) Degradation observed under light on (Red Light) and off conditions at room temperature **(a)** Degradation of primary absorption peak of MB showing comparison of activity in presence and absence of red light. **(b)** Oligomer absorption peak of MB, showing comparison of normalized yield.

Key observation can be made that at a given degradation of methylene blue the oligomer yield remains constant for different temperatures (Figure C.S1c) in APPENDIX C. The temperature profiles of the system, ambient, and reactor under these dark and heating conditions suggest that there is consistency in maintaining temperature Figure C. S2a-c, APPENDIX C. Intensity dependent studies were performed under illumination of different intensities of red light as shown in Figure 4.12. The intensities were varied by reducing the number of bulbs used in the photoreactor. Here we can clearly see that as the intensity is decreasing the activity of the photocatalyst i.e. degrdation of methylene blue can be tuned as shown in Figure 4.12a. We

observe that, Rate of degradation was enhanced with increasing intensities in linear trend a shown in Figure 4.12b and we can clearly observe that as the intensity of red light was lowered the oligomer yield started stabilizing as in Figure 4.12c, and it is observed that oligomer yield is lower when compared to light OFF conditions in Figure 4.12d, suggesting higher mineralization of MB into other products.
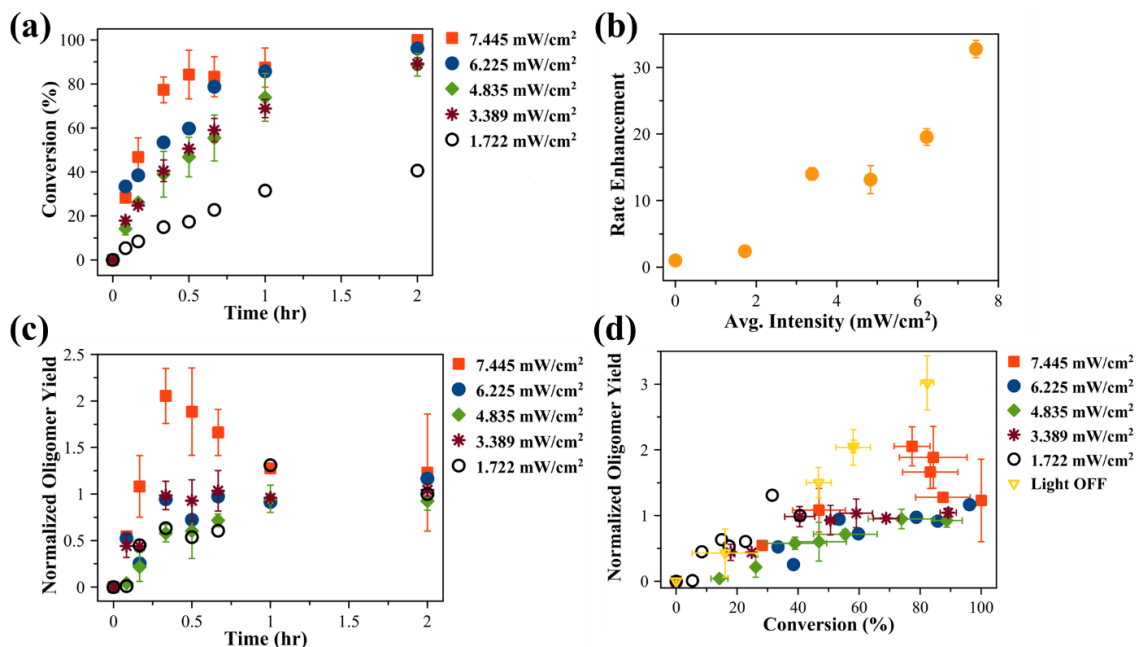

Figure 4.12. Intensity dependent studies showing Methylene blue (MB) Degradation observed under illumination of different intensities of red light **(a)** Degrdation Characteristics of methylene blue under decreasing in intensities of red light **(a)** Rate enhancement with average Intensity (mW/cm^2) measured in the reaction conditions **(c)** plot showing Normalized oligomer yield with time with varying intensities of red light **(d)** comparing activity of catalyst with normalized oligomer yield with varying intensities of red light.

These light experiments are compared with degradation experiments under dark and heating conditions, Figure C.S7a-c, APPENDIX C to show that heating is not responsible for this process, it's mainly driven by light. All these light experiments were performed under constant

intensity conditions. For complete insight into the role of light, we see the extent of degradation using different wavelengths of light as shown in Figure 4.13. As seen in Figure 4.13a The green light shows the least degradation of methylene blue while highest degradation was observed under red light illumination (see, Figure 4.13b). The differences in the rate of MB degradation process under different wavelengths illumination is due to the reaction pathway it follows. The red light has a strong overlap with the monomer peak (663 nm), while the green light has the least (see, Figure 4.13d). The red light causes dye sensitization followed by complete mineralization resulting in the faster breakdown of the dye , along with strong growth of the oligomer yield. On the contrary, if we see the interaction between green light and MB, the degradation of MB remains low even after 11 hours Figure C.S4, APPENDIX C, but there is no formation of oligomer as seen in Figure C.S5, APPENDIX C and Figure 4.13b, where we casn see the oligomer peak Figure C.S6, C.S8,APPENDIX C under red light illumination. This is due fact that the oligomer (~580 nm) has a strong overlap with green light. As a result, the oligomer that forms immediately disappears due to dye sensitization of the oligomer resulting in mineralization forming other products. While in the case of Amber light illumination, the overlap with MB is in between red and green. In the case of reactions with Red and Amber light, the overlap triggers the transfer of electrons from the valence band (VB) to CB of the dye, which inturn transfers this electron to the CB of the semiconductor. The pathway for photodegradation is the formation of oxygen radicals that attack the dye resulting in complete mineralization. The resulting rate of MB breakdown in Amber stays within Red and Green wavelength region. The plot of measure of conversion and measure of oligomer yield, Figure 4.13c shows that at a given conversion selectivity is different when placed under different light sources. This is due to the fact various light sources overlap with MB peaks over the wider region allowing for selective catalysis. On comparing dark conditions at higher temperature (30 ˚C), where the outcome is slightly faster compared to room temperature. This validates the fact that light sources such as red and amber raise the temperature through light intensity up to ~30 ˚C as shown in Figure C.S9,APPENDIX C.

While comparing the dark at 30 ˚C in Figure C.S1, APPENDIX C with green light exposure in Figure C.S4, APPENDIX C we can see that it overlaps suggesting that despite rising in reactor temperature we don't see monomer degradation suggesting that these reactions are purely light-driven.
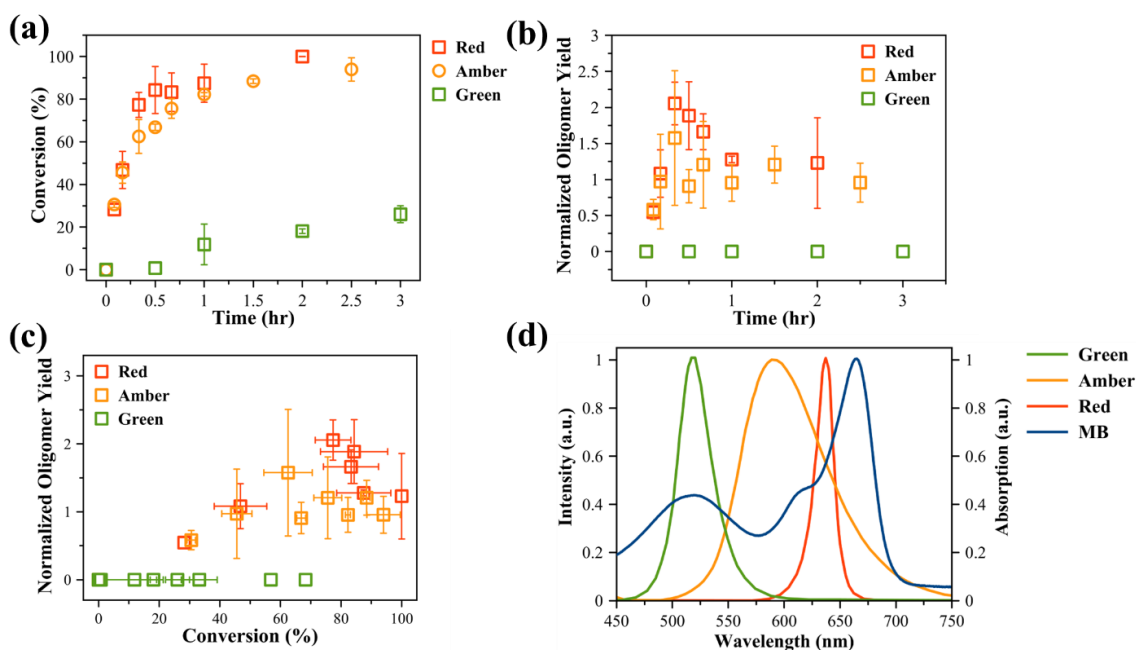

Figure 4.13. Wavelength dependent studies showing Methylene blue (MB) Degradation observed under illumination of different wavelengths light with constant intensity **(a)** Tuning Selectivity comparison showing formation of tertiary absorption peak of MB under various conditions showing extent of mineralization to tertiary species formed **(b)** Exposure standards of different light illumination used in dye degradation experiments.

4.4. Mie-resonance enhanced C-C coupling reactions

4.4.1. Summary

Copper based nanocatalysts have recently emerged as attractive catalysts for a diversity of bond formations, such as C-C, C-N, C-O, C-S, and C-Se. However, the identification of truly heterogeneous versus homogeneous catalytic conditions remains an ongoing challenge within the

field. Herein, we report that in cuprous oxide (Cu$_2$O) nanoparticle-mediated C-C homo-coupling and cross-coupling reactions, the presence of a base facilitates the copper complex mediated homogeneous catalytic pathway. Whereas in the absence of a base, the reaction can proceed heterogeneously on the surface of Cu$_2$O nanoparticles. We distinguished the homogenous versus heterogeneous pathways using a combination of reactor study, ultraviolet-visible extinction spectroscopy, electrospray ionization mass spectrometry, flame atomic absorption spectroscopy, transmission electron microscopy, and density-functional theory calculations. Our findings indicate that Cu$_2$O nanoparticles can catalyze C-C coupling reactions under ligandless and base-free conditions via a truly heterogeneous pathway paving the way for the development of highly efficient, robust and sustainable processes.

4.4.2. Specific Findings on Mie-resonance enhanced C-C coupling reactions

Herein, we report that in cuprous-oxide (Cu$_2$O) nanoparticle-mediated C-C coupling reactions, the presence of a base facilitates the substrate-induced leaching of Cu$_2$O surface atoms to form homogeneous Cu catalytic species. The leaching from Cu$_2$O nanoparticles and the corresponding in-situ formation of homogeneous Cu complexes are confirmed using ultraviolet-visible (UV-Vis) extinction spectroscopy, electrospray ionization mass spectrometry (ESI-MS), flame atomic absorption spectroscopy (FAAS), transmission electron microscopy (TEM), and density-functional theory (DFT) calculations. We also show that, in contrast to the observations made in the presence of a base, Cu$_2$O nanoparticles are stable under base-free conditions, do not undergo leaching, and catalyze C-C coupling reactions via a truly heterogeneous pathway.

We investigated Glaser-type oxidative homo-coupling reaction (OHR) of phenylacetylene (PA) and Sonogashira-type cross-coupling reaction (SCR) between PA and iodobenzene (IB) as model reactions for C-C homo-couplings and cross-couplings, respectively (see Scheme 1.a and 1.b). Dimethylformamide (DMF) and potassium carbonate (K$_2$CO$_3$) were used as solvent and base,

respectively. Cu$_2$O nanoparticles (NPs) prepared by a microemulsion synthesis method were used as the catalyst.[63] The procedures for Cu$_2$O NPs preparation and coupling reactions are described in detail in EXPERIMENTAL METHODOLOGY Section 3.1.1, 3.6, 3.7. A representative TEM image of quasi-spherical Cu$_2$O NPs of 34 ± 4 nm size used for the coupling reactions is shown in APPENDIX D Figure. D.S1 The Cu$_2$O phase is confirmed by the X-ray diffraction (XRD) as well as the UV-vis extinction spectrum of the respective Cu$_2$O nanoparticles, as shown in APPENDIX D Figure. D.S2-D.S3, respectively.
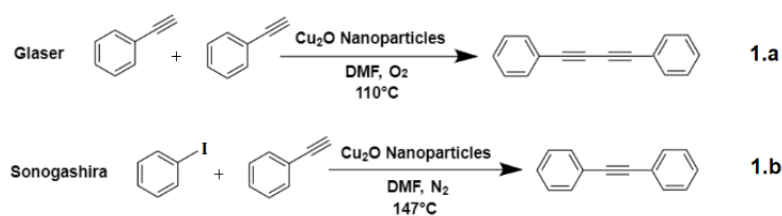
Scheme 1.a. Glaser type oxidative C-C homo-coupling reaction (OHR) of phenylacetylene.

Scheme 1.b. Sonogashira type C-C cross-coupling reaction (SCR) between phenylacetylene and iodobenzene.

To investigate the catalytic pathway, we carried out OHR in the presence and absence of K$_2$CO$_3$. The conversion of PA into homocoupling product, diphenyldiacetylene (DPDA), with and without the base at 110 °C is shown in Figure 4.14 (a) and (b), respectively. The data show that Cu$_2$O nanoparticles can successfully catalyze C-C coupling reactions with and without the base. The data in Figure 4.14 (a) and (b) also show that longer reaction completion time is required under base-free conditions compared to that in the presence of base. We also performed SCR in the presence and absence of the base, and observed similar results, i.e., longer reaction completion time under base-free conditions (see APPENDIX D Figure. D.S4-D.S7)

For OHR performed under air flow, we observed the homocoupling product, DPDA, as the only reaction product with and without the base. For SCR performed under nitrogen (purity, 99.999 %)

flow, we observed more than 95% selectivity towards the desired cross-coupling product, DPA, and less than 5% selectivity towards the undesired homocoupling product, DPDA, at the end of the reaction, for both with-base and base-free conditions (see APPENDIX D Figure. D.S6-D.S7). No significant yield for the undesired iodobenzene homocoupling product, biphenyl (BP), was observed. To confirm that the observed conversions are due to Cu_2O-NP-mediated catalytic activity, we also carried out control experiments. No significant reaction progress was observed in the absence of Cu_2O NPs.
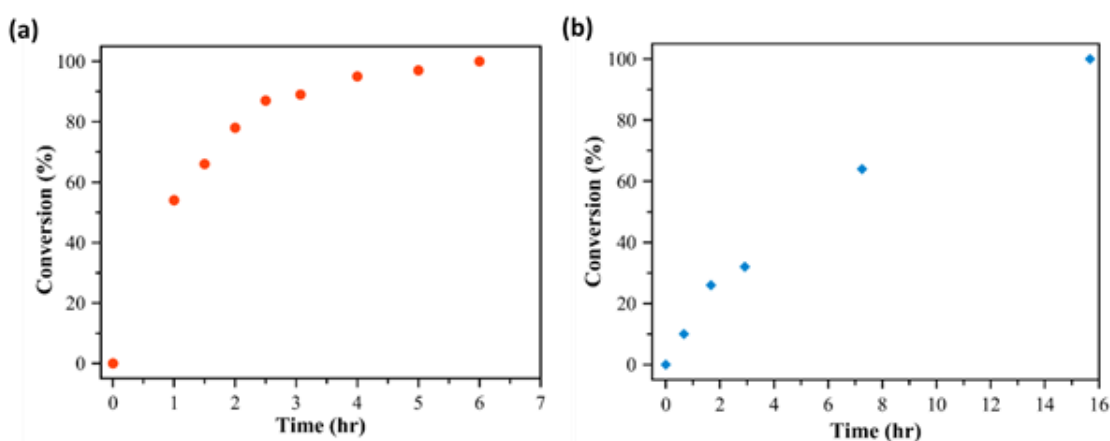
Figure 4.14 **(a)** Conversion as a function of Reaction Time for OHR of PA at 110 °C in the presence of base (K_2CO_3). **(b)** Conversion as a function of Reaction Time for OHR of PA at 110 °C in the absence of base.

The results of the complete reaction conversion observed with our Cu_2O nanoparticles under base-free conditions (e.g., Figure 4.14 (b)) are consistent with the previous surface science studies where it has been shown that homocoupling between terminal alkynes can happen on noble metal surfaces even in the absence of a base via a truly heterogeneous pathway.[144–146] The mechanism in the conventional homogeneous metal-complex-catalyzed coupling reactions may involve elementary steps like oxidative addition, transmetalation, reductive elimination, etc. The elementary step(s) involved in these homogeneous catalytic mechanisms may require a base in the catalytic cycle. However, the heterogeneous catalytic mechanism is distinct and different from

the homogeneous catalytic mechanisms. The heterogeneous catalytic mechanism typically involves elementary steps like adsorption of reactants on nanocatalyst surface sites, activation of adsorbed species, the reaction between adsorbed species to form the adsorbed products, and desorption of the product molecules from the surface. Therefore, it is possible for the nanocatalysts to drive C-C couplings without the base when the entire catalytic cycle occurs truly heterogeneously. To elucidate whether the differences observed between the with-base and base-free cases in Figure 4.14 (a) and (b) originate from different catalytic pathways (i.e., homogeneous versus heterogeneous pathway), we characterized the reaction mixture using UV-Vis extinction spectroscopy. In Figure 4.15 (a) and (b) we show the UV-Vis extinction spectra of the reaction mixture measured before the addition of substrate (i.e., PA) and at different conversions for OHR in the presence and absence of the base, respectively. As seen from Figure 4.15 (a) and (b) the extinction spectra acquired before the addition of PA show mainly the features expected from Cu_2O NPs shown in APPENDIX D. For reaction conditions in the presence of base, upon addition of PA, new extinction peaks centered at ~385 and ~450 nm emerge. The appearance of the new extinction peaks indicates the in-situ formation of homogeneous Cu complexes in the reaction solution. For reactions performed under base-free conditions, as shown in Figure 4.15 (b), such new extinction features are not present in the UV-Vis extinction spectra. We also characterized the reaction mixture of SCR performed under with-base and base-free conditions. We observed similar results, i.e., the new extinction peaks centered at ~385 and ~450 nm emerge only in the presence of the base and PA (see Figure. D.S8-D.S9 in APPENDIX D).
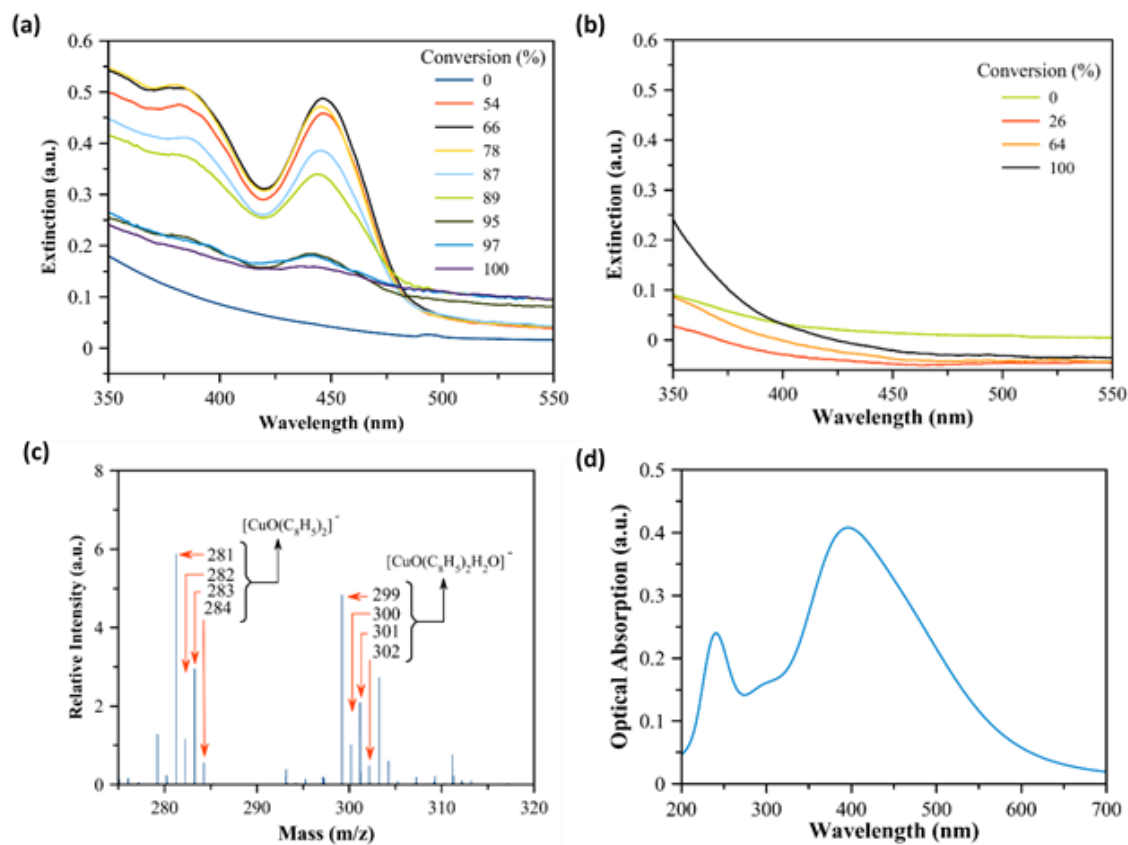
76

Figure 4.15 **(a)** UV-Vis extinction spectra of reaction mixture measured after the addition of base and before the addition of PA (i.e., 0 % conversion) and at different reaction conversions during OHR at 110°C in presence of base. **(b)** UV-Vis extinction spectra of reaction mixture measured before the addition of PA (i.e., 0 % conversion) and at different reaction conversions during OHR at 110 °C in the absence of base. **(c)** Representative HR-ESI-MS spectrum measured in negative spray mode for the supernatant solution of the reaction mixture taken from Cu_2O-NP-catalyzed OHR in the presence of base. **(d)** DFT calculated optical absorption spectra of homogeneous Cu complex, $[CuO(C_8H_5)_2]^-$. *DFT computations were performed by Dr. Bin Wang's group from School of Chemical, Biological and Materials Engineering, The University of Oklahoma.*

To gain structural insight into the homogeneous Cu complexes present in the reaction solution, we performed ESI-MS on the supernatant solution of the reaction mixture. No significant signal

that matches the Cu isotopic ratio was observed in the ESI-MS spectra of the samples collected from the reactions under base-free conditions. On the other hand, for the samples collected from the OHR and SCR in the presence of the base, as shown in Figure 4.15 (c) and Figure. D.S10 in APPENDIX D, we observe the signals for two homogeneous Cu complexes in the ESI-MS spectra when measured in negative ion mode. The predicted isotope distributions of the two proposed copper complexes are shown in Figure. D.S11 (a)-(b) (see APPENDIX D). As seen from Figure 4.15 (c) and Figure. D.S11 (a)-(b), the signals from the measured ESI-MS spectrum in the m/z range of 281-284 and 299-302 match the predicted isotope distributions of copper complexes, $[CuO(C_8H_5)_2]^-$ and $[CuO(C_8H_5)_2H_2O]^-$, respectively. Water molecule found in the complex is the expected byproduct of OHR. The ESI-MS results provide the direct evidence for PA (C_8H_6) induced leaching of surface atoms of Cu_2O NPs in the presence of the base to form soluble Cu complexes in the reaction solution.

To confirm the structures of Cu complexes found in the UV-Vis extinction and ESI-MS spectra, DFT calculations were carried out on the atomic configurations and optical absorption spectra of potential Cu complexes by employing implicit solvent model. Detailed DFT computational methods are described in Section II of APPENDIX D. The absorption spectrum of $[CuO(C_8H_5)_2]^-$ is presented in Figure 4.15 (d). It consists of two major peaks from 200 – 600 nm. We find that the significant peak at around 395 nm in the calculated spectrum corresponds to the appearance of ~385 nm extinction peak in the measured UV-Vis extinction spectra. The calculated absorption spectrum of another Cu species, $[CuO(C_8H_5)_2H_2O]^-$, is plotted in Figure. D.S11 (c) in APPENDIX D. It is found that the peak wavelength of ~ 500 nm in the calculated spectrum is likely associated with the extinction peak centered at ~ 450 nm in Figure 4.15 (a). The red-shift of the peak positions in our calculation in comparison to the experimental counterpart is likely caused by the fact that we took into account the aqueous solvent phase implicitly rather than explicitly describing the solvation of the molecules. Also, it is noted that the peak at lower

wavelength (higher energy) persists in the calculated absorption spectra of both Cu species. The higher energy peaks are not verified experimentally since the extinction peaks of reactants and products overlap in this region (see Figure. D.S12.). The combination of DFT results (Figure 4.15 (d)) and measured extinction peaks in Figure 4.15 (a) along with the ESI-MS results (Figure 4.15 (c)) confirm that in the presence of the base, PA (C_8H_6) induces a leaching process from the surface of Cu_2O NPs and forms homogeneous Cu complexes in the reaction solution.

To further illustrate the role of homogeneous Cu complexes in the reaction, Figure 4.16 (a) shows the UV-Vis extinction peak position of homogeneous Cu species observed in the 380-390 nm region as a function of conversion for OHR (also see Figure. D.S13. (a)-(c)). The data in Figure 4.16 (a) and Figure. D.S13. (a)-(c) in APPENDIX D show that there is a significant change in the extinction peak position as a function of reaction time and conversion. This change in peak potion indicates that in-situ formed homogeneous Cu species further interact with the reactant(s) to form other homogeneous Cu species in the catalytic cycle.[177,178] When the extinction peaks of two or more Cu complexes present in the reaction solution are closely spaced, their combined extinction peaks can appear as a single peak in the measured UV-Vis extinction spectrum. In that case, the change in extinction peak position can be used as a measure of the relative change in concentration of one species compared to that of the other species. The changes observed in the measured extinction peak position support that the relative concentration of homogeneous Cu complexes in the reaction solution changes with reaction time and conversion as expected for the catalytic species in the homogeneous catalytic cycle. Therefore, Figure 4.16 (a) and Figure. D.S13. (a)-(c) as in APPENDIX D, confirm that the homogeneous Cu complexes observed in the reaction solution are indeed homogeneous catalytic species that participate in the catalytic cycle
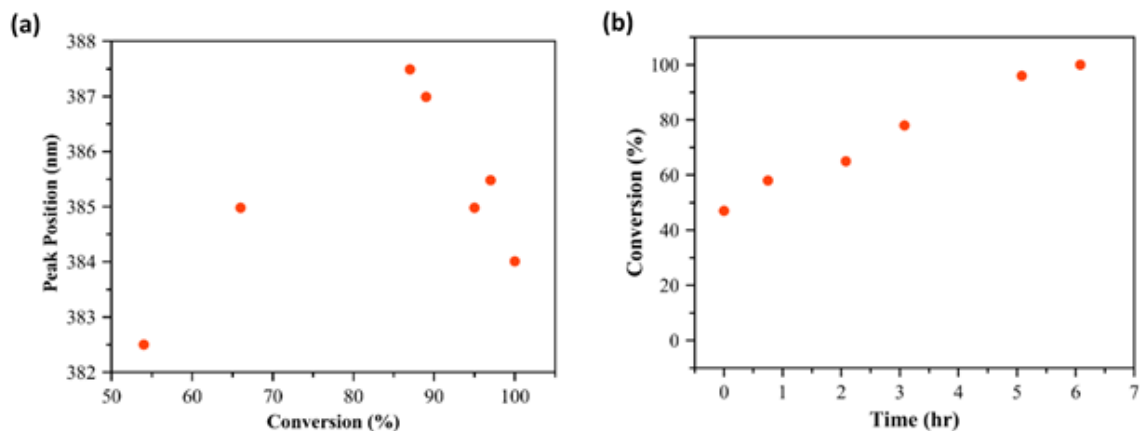
Figure 4.16 **(a)** Extinction peak position in the 380-390 nm region of the UV-Vis extinction spectrum as a function of PA conversion for OHR in the presence of base. **(b)** Reaction conversion as a function of reaction time for oxidative homocoupling of PA with the base at 110°C using Cu complexes in supernatant solution as the only catalyst.

To further verify the conclusion derived from Figure 4.16 (a) that the homogeneous Cu complexes observed in the reaction solution are homogeneous catalytic species, we carried out the reactions with the base using the supernatant solution containing homogeneous Cu complexes as the only catalytic species. The reaction was first carried out in the presence of the base using Cu_2O nanoparticles as the catalyst. When the reaction conversion was ~45%, the formation of Cu complexes was confirmed using UV-Vis extinction spectra, the reaction was stopped, Cu_2O nanoparticles were removed from the reaction solution using centrifugation. The reaction was then allowed to continue, and PA conversion was monitored in this reaction solution. The results from this experiment showed that the homogeneous Cu complexes can indeed catalyze the reaction to complete conversion as shown in Figure 4.16 (b).

To quantify the concentration of leached, soluble Cu content in the reaction solution, we characterized the supernatant solution using FAAS. As shown in Figure 4.17 (a), only the reaction performed with base showed the presence of soluble Cu. No significant soluble Cu content was observed for the samples collected from reactions under base-free conditions.

Moreover, for the reaction in the presence of the base, as seen from Figure 4.17 (a)-(b), the trend of UV-Vis extinction peak intensity observed as a function of reaction conversion (Figure 4.17 (b)) follows the concentration profile of soluble Cu content obtained from FAAS analysis at different conversions (Figure 4.17 (a)). These results confirm that the extinction peaks observed in the UV-Vis extinction spectra are indeed associated with the soluble homogeneous Cu complexes. The data in Figure 4.17 (a) and (b) also show that there is a dramatic decrease in the concentration of homogeneous Cu complexes towards the end of the reaction. It has been shown that the in-situ generated homogeneous catalytic species such as homogeneous palladium (Pd) complexes can undergo decomposition to form Pd black when the concentration of a stabilizing species such as the ligand is starved.[142,165,179,180] Since PA act as ligand for Cu complexes observed in this study the decreasing trends observed in the concentration of in-situ generated homogeneous Cu complexes (in Figure 4.17 (a) and (b)) can be attributed to the expected blackout of the homogeneous Cu catalytic species towards the end of the reaction (i.e., when the concentration of PA is low). We also confirmed the presence of blacked-out Cu clusters in the end of the reaction sample using TEM (see Figure D.S14) in APPENDIX D.
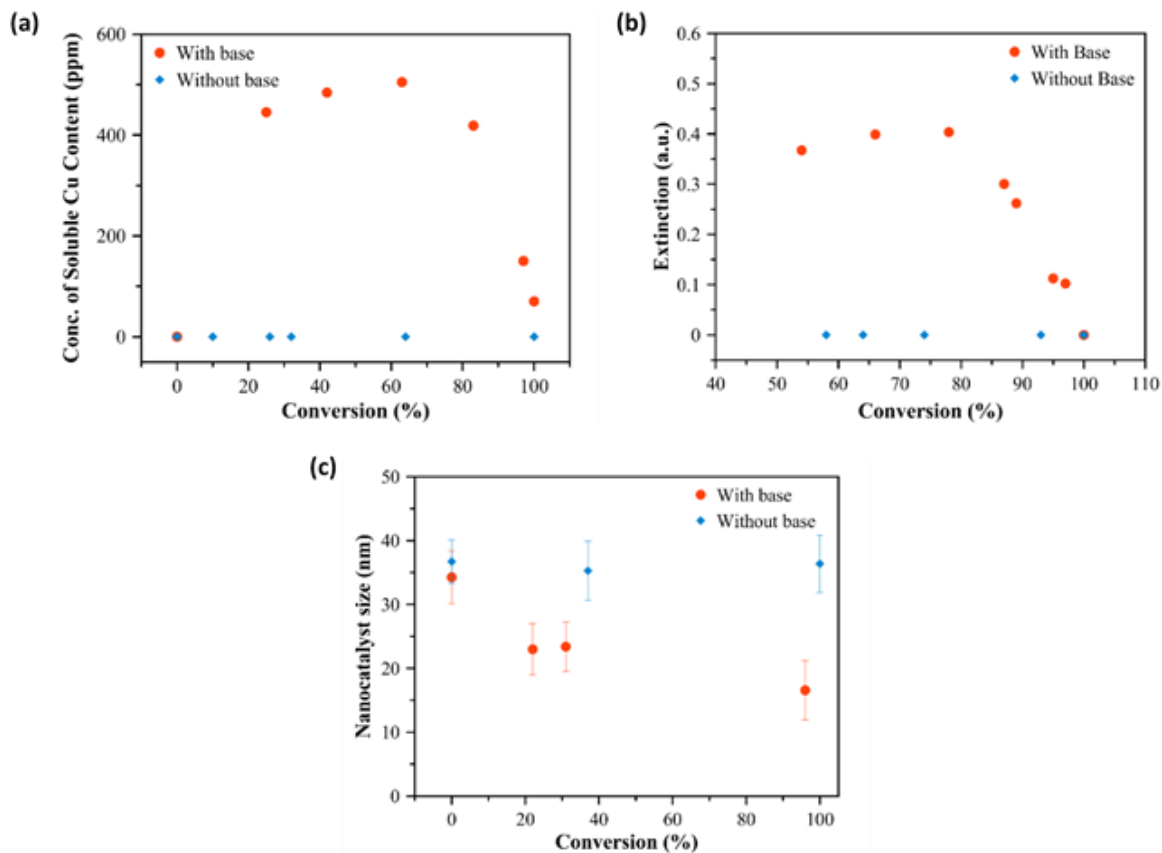
Figure 4.17 **(a)** FAAS-quantified concentration of soluble Cu contents in the reaction solution as a function of PA conversion for OHR in the presence and absence of base. **(b)** Normalized extinction intensity at the peak wavelength (~385 nm) in the UV-Vis extinction spectrum of the reaction solution as a function of PA conversion for OHR in the presence and absence of base. **(c)** TEM-measured size of Cu_2O nanoparticles in the reaction solution as a function of PA conversion for OHR in the presence and absence of the base.

The differences shown in Figure 4.15 (a)-(b). and Figure 4.17 (a)-(b). for with-base and base-free reaction conditions were further supported by TEM analysis of the Cu_2O NPs used under the respective conditions. Figure 4.17 (c) shows that the average size of Cu_2O NPs remains constant throughout the reaction in the absence of the base. In contrast, for the reaction performed with the base, the average size of Cu_2O NPs decreased, confirming the leaching of surface atoms.

4.4.3. Role of Base in C-C homocoupling reaction

We have reported the catalytic pathways of Cu_2O nanoparticle-mediated carbon–carbon (C-C) homocoupling reaction of a simple terminal alkyne substrate, i.e., phenylacetylene (PA).[40] Specifically, we have demonstrated that in the presence of a base (i.e., K_2CO_3), the Cu_2O nanoparticles catalyze the homocoupling of phenylacetylene (PA) via homogeneous catalytic pathway as discussed above. A detailed summary of Catalytic pathway of Cu_2O NPs-mediated oxidative C-C homocoupling of phenylacetylene are mentioned in APPENDIX E. The summary of these findings and the representative results are provided in Figure E.S1 in the APPENDIX E. We have demonstrated that cuprous oxide (Cu_2O) NP-mediated C-C homocoupling of phenylacetylene (PA) exhibits ~100% in-situ yield towards the desired homocoupling product, diphenyldiacetylene (DPDA).[40] Also, Cu_2O NPs-mediated C-C cross-coupling between PA and aryl halides exhibits more than 95% selectivity towards the desired cross-coupling product, diphenylacetylene (DPA), and less than 5% selectivity towards the undesired homocoupling product, DPDA.[40] we have also investigated in detail the role of oxygen and the role of solvent in the Cu_2O nanoparticles-mediated C-C homocoupling of phenylacetylene.

4.4.4. Role of Oxygen in C-C homocoupling reaction

To investigate the role of oxygen in the C-C homocoupling of terminal alkynes, we first carried out C-C homocoupling of phenylacetylene in the presence of nitrogen environment (purity>99.999%). The representative results are shown in Figure 4.18a-f. As seen from Figure 4.18a, in the first 20 hours, the reaction progress was very slow in the absence of oxygen in the reaction mixture. For the same conditions, the homogeneous complexes were still formed even in the absence of oxygen, as evidenced from UV-Vis extinction spectra of homogeneous complexes in Figure 4.18c and Figure 4.18e. The peaks at ~385 and ~450 nm in the extinction spectra are associated with homogeneous Cu catalytic species, $[CuO(C_8H_5)_2]^-$ and $[CuO(C_8H_5)_2.H_2O]^-$ (see

Figure E.S1 and description in APPENDIX E, for more details). The presence of homogeneous Cu complexes, $[CuO(C_8H_5)_2]^-$ and $[CuO(C_8H_5)_2.H_2O]^-$, was also confirmed using ESI-MS analysis of the supernatant solution of the reaction mixture as shown in Figure E.S1c, APPENDIX E,. The ESI-MS was used to analyze the structure of the Cu complex, $[CuO(C_8H_5)_2]^-$, and suggested that two PA (C_8H_6) molecules first adsorb on the surface of Cu_2O NPs (i.e., one molecule on surface Cu atom and another molecule on neighboring surface O atom), and subsequently cause the leaching of Cu and O surface atoms. The second complex, $[CuO(C_8H_5)_2.H_2O]^-$, can then form from the first complex, $[CuO(C_8H_5)_2]^-$, and water (H_2O) molecule, which was the expected byproduct of oxidative C-C homocoupling of terminal alkynes. In summary, the representative results shown in Figure 4.18 confirm that the oxygen atom present in the homogeneous complexes, $[CuO(C_8H_5)_2]^-$ and $[CuO(C_8H_5)_2H_2O]^-$, was formed from the surface oxygen atoms of Cu_2O nanoparticles.

In Figure 4.18a, when the oxygen (in the form of air) was introduced into the reaction mixture at ∼20 hours, the reaction progress was relatively faster and complete conversion occurred as expected. These results confirmed that, although the homogeneous Cu catalytic species can be formed in the absence of oxygen, the homogeneous Cu species an catalyzed the C-C homocoupling reaction only in the presence of oxygen.

For the second cycle, the same quantity of reactant (PA) was charged to the reaction mixture, and the reaction was allowed to start at ∼22 hours in Figure 4.18a. In the presence of oxygen, the complete conversion was again achieved. The evidence for the homogeneous complexes formed during the second cycle can also be evidenced by Figure 4.18d and Figure 4.18f. The UV-Vis extinction peak appearances of homogenous Cu complexes in Figure 4.18d and Figure 4.18f are similar to the homocoupling reaction conditions shown in Figure E.S1, APPENDIX E,. These results provide evidence of rejuvenation of catalyst activity, and the formation of the homogenous complexes from the spent Cu_2O nanoparticles. Similar to results shown in Figure E.S1-

APPENDIX E,, in Figure 4.18e and Figure 4.18f, the concentration of homogenous Cu complexes increases initially and decreases as the reactant (PA) was depleted with time. A similar pattern was observed in peak position with time as shown in Figure E.S4a and E.S4b, APPENDIX E as the end of the reaction cycle. These trends confirm that the homogenous Cu complexes are indeed participating in the catalytic cycle.
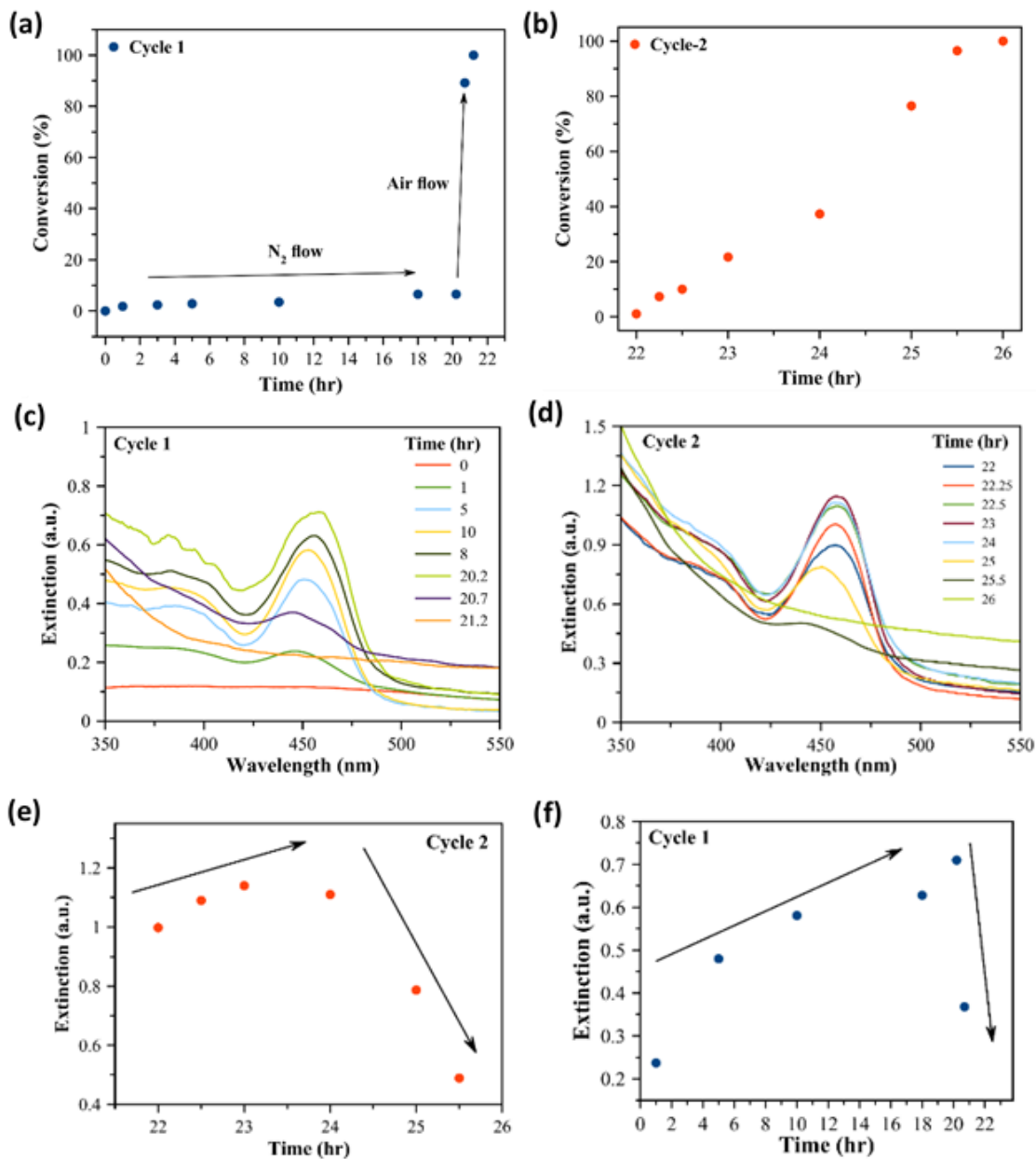
Figure 4.18 **(a)** Conversion as a function of reaction time for homocoupling reaction of PA at 110 °C, where the gas was switched from N₂ to dry air after 20 hr of reaction time in Cycle 1. **(b)** Conversion as a function of reaction time for homocoupling of PA at 110 °C, where the gas used was continued Dry Air after the end of the first cycle, for the second cycle. **(c)** UV-Vis spectra for homocoupling reaction of PA at 110 °C, where the gas was switched from N₂ to dry air after 20 h of reaction time for Cycle 1. **(d)** UV-Vis spectra for homocoupling reaction of PA at 110 °C in the

presence of base, where the gas was continued to be dry air after the end of the first cycle, for Cycle 2. **(e)** Extinction position for homocoupling reaction of PA at 110 $^\circ$C in the presence of base, where the gas was switched from N_2 to Dry Air after 20 hours of reaction time for Cycle 1.

Cu_2O nanoparticle synthesis and characterization summary

The copper (I) oxide (Cu_2O) spherical nanoparticles were synthesized using a microemulsion technique.[63] Detailed synthesis methods are discussed in Section 3.1.1 The TEM image of as-prepared Cu_2O nanoparticles (diameter = 34 ± 4 nm) is shown in Figure E.S2a as in APPENDIX E,.[40,93] Both the experimental and computationally generated extinction spectra match well with each other as shown in APPENDIX E Figure E.S2b. The UV-Vis extinction spectra shown in APPENDIX E, Figure E.S2b is unswerving with the band gap (i.e., 2.1 eV) of Cu_2O. The measured XRD pattern was used to confirm the Cu_2O phase of as prepared nanospheres as shown in APPENDIX E, , Figure E.S2c.[40,93]

Homocoupling reaction with nitrogen and air switch conditions

DMF was degassed with N_2 for 6 hours for the removal of oxygen. Cu_2O nanoparticles were suspended in N_2 sparged DMF (15 mL) prior to starting the reaction (32 mg, 0.598 mmol). The reaction mixture was heated to 147 °C (reflux conditions) to minimize the dissolved oxygen content in the solvent and blanked with N_2 flow. Phenylacetylene (0.91 mmol) was added to the reaction mixture. The reaction could proceed under these conditions for 20 hours and observed minimal (2-6%) conversion of the reactant as shown in Figure 4.18a. The reaction temperature was brought down to 110°C and then airflow was used instead of N_2 gas for blanketing the reaction mixture. The conversion shot up and all the reaction was completed in an hour at the end of Cycle 1 (Figure 4.18a).

Cycle 2 Reaction conditions: To ensure further activity of the catalyst, the reactant i.e. phenylacetylene (0.91 mmol) and potassium carbonate was (207 mg, 1.64 mmol) were added to the spent reaction mixture from Cycle 1. The temperature was kept at 110°C and airflow

continued to blanket the reaction mixture. The complete conversion was obtained after 4 hours of reaction time as shown in Figure 4.18b.

4.4.5. Role of Solvent in C-C homocoupling reaction

To investigate the role of solvent on the rate of homocoupling reaction, we investigated the reaction using Cu_2O spheres in the presence of dimethylformamide (DMF), acetonitrile and ethanol at the reaction temperature of 70 °C. Ethanol and acetonitrile are comparatively greener solvents than DMF.[181,182] The representative results are shown in Figure 4.19. As seen from Figure 4.19a, similar catalytic activity is observed using the three solvents. The representative UV-Vis extinction spectra of homogeneous Cu complexes observed in the experiment using ethanol as the solvent is shown in Figure 4.19b. The results shown in Figures E.S1, APPENDIX E and Figure 4.19a are performed in DMF. As seen from the UV-Vis extinction spectra shown in Figures E.S1, APPENDIX E and Figure 4.19b, the homogenous Cu complexes and their peak positions are similar in DMF and ethanol. These results confirm that the degree of leaching and formation of homogenous Cu complexes does not strongly depend on the nature of the solvent. Instead, the substrate (phenylacetylene, PA)-induced leaching mainly depends on the size and shape of Cu_2O nanoparticles.
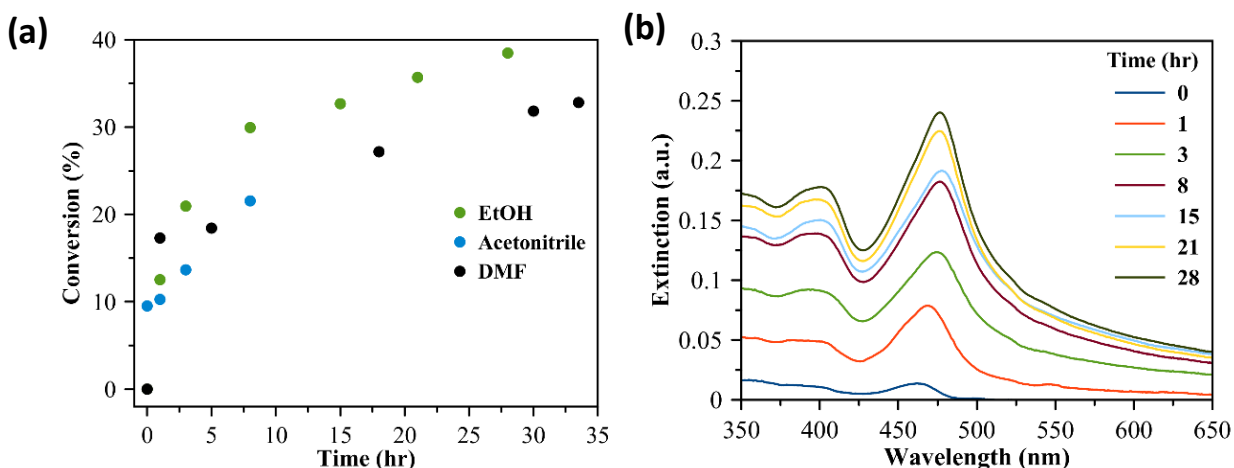
Figure 4.19 **(a)** Conversion as a function of reaction time for homocoupling reaction of PA at 70 °C in the presence air in various solvents catalyzed by Cu_2O nanoparticles. **(b)** Extinction Spectra for homocoupling reaction of PA at 70 °C in the presence of air in ethanol (greener solvent)

CHAPTER V

CONCLUSIONS AND CONSEQUENCES

5.1. Mie Resonance-Enhanced Dye Sensitization

In conclusion, we have demonstrated that the rate of dye-sensitization can be enhanced in the presence of semiconductor nanostructures with dielectric Mie resonances. Using FDTD simulation results, we have developed the structure-property-performance relationship for the dielectric Mie resonance-enhanced dye-sensitization. The predicted volcano-type relationship between the rate of MB dye-sensitization and the size of Cu_2O nanostructures is experimentally verified using the rate measurements of MB DSD in the presence of Cu_2O nanospheres and nanocubes of different sizes. The flexibility of tuning the dielectric Mie resonance peaks across the visible and near-IR regions by controlling the size of the dielectric nanostructures marks its applicability to a wide range of DSP systems. Specifically, the findings of this dissertation open a novel approach to design efficient DSP systems that can involve semiconductors such as CeO_2, CuO, Cu_2O, α-Fe_2O_3, and TiO_2 and a wide range of visible- and near-IR-responsive dye molecules.
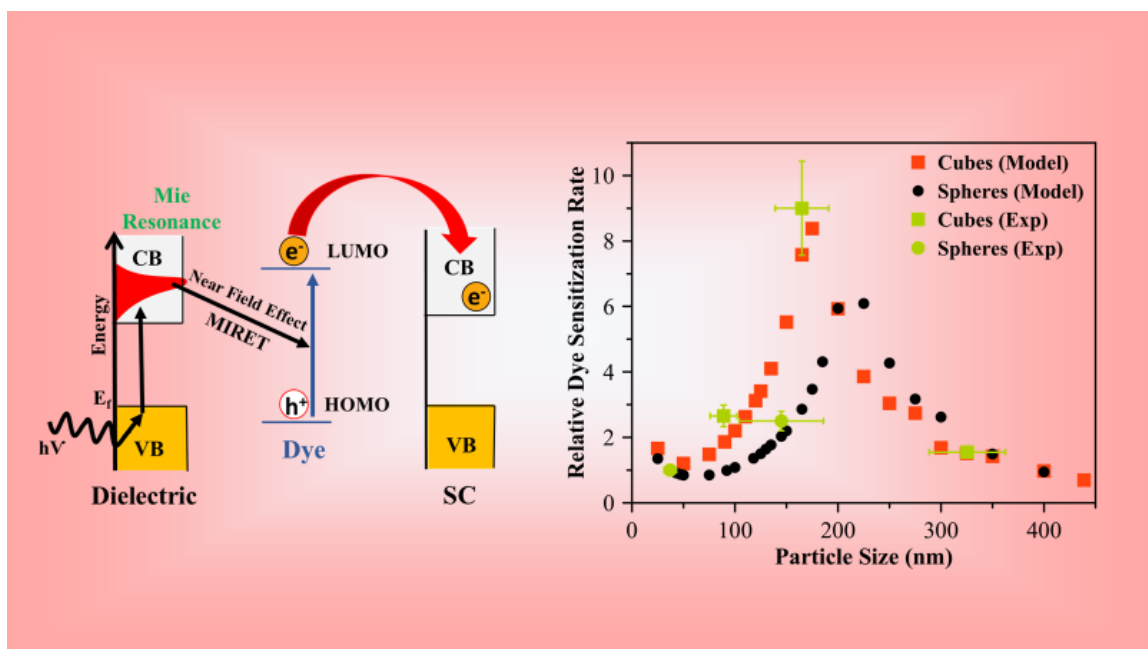
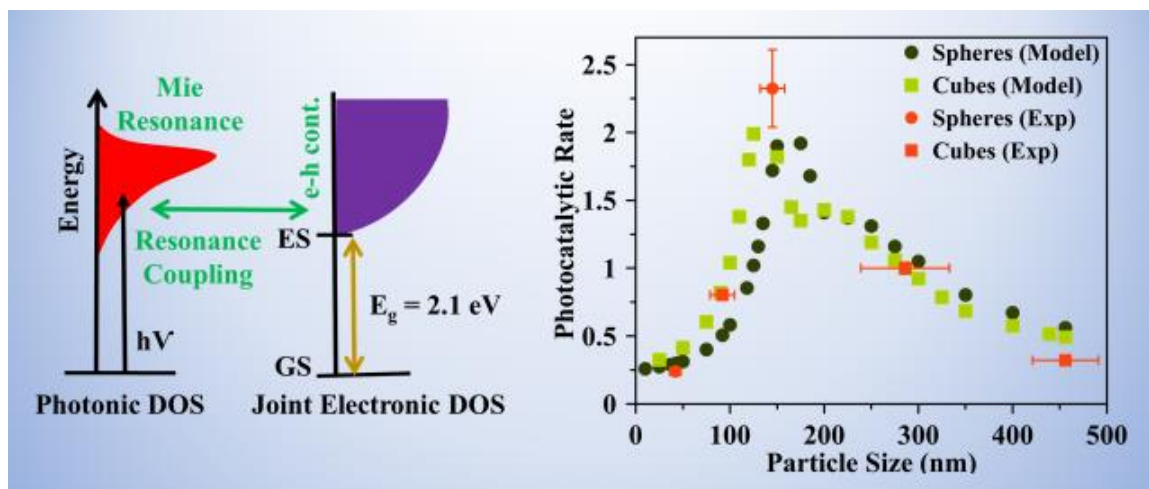**Figure 5.1** Graphical Representation of Cu_2O nanostructures exhibiting dielectric Mie resonances exhibit up to an order of magnitude higher dye-sensitization rate as compared to Cu_2O nanostructures not exhibiting dielectric Mie resonances. Our simulation, as well as experimental results, exhibit a volcano-type relationship between the dye-sensitization rate and the size of Cu_2O nanostructures.

5.2. Mie Resonance-Enhanced Photocatalysis

The present work demonstrates dielectric resonance-enhanced photocatalysis in Cu_2O cubical and spherical particles. Specifically, larger 145-nm Cu_2O spherical nanoparticles with dielectric resonances exhibit a higher photocatalytic rate for MB degradation in comparison with smaller 42-nm Cu_2O spherical nanoparticles not exhibiting dielectric resonances. These results are supported by the transient absorption measurements that differentiate the charge carrier dynamics of larger and smaller Cu_2O nanospheres, indicating an optical resonance process that involves the coherent generation of charge

carriers in the larger 145-nm nanospheres. This present work also presents volcano-type structure-performance relationships between the size of Cu_2O nanostructures and their relative photocatalytic rates. The dielectric resonance-enhanced photocatalytic approach demonstrated in this study using Cu_2O nanoparticles is expected to translate to other metal oxide photocatalysts such as CeO_2, α-Fe_2O_3, and TiO_2 that exhibit size- and shape-dependent dielectric resonances. The dielectric Mie resonance-mediated charge carrier generation in the metal oxide semiconductors has a number of advantages over plasmonic resonance-mediated charge carrier generation. Specifically, in the latter case, the plasmonic Mie mode decays to a hot electron (and hole). In comparison to the lifetime of hot electron (and hole), the electron-hole pair lifetime in the metal oxide semiconductor is longer, which will translate to a much more efficient photocatalysis. Therefore, the dielectric resonance-enhanced photocatalysis demonstrated in our study opens a new avenue for solar light harvesting and photocatalysis.

Figure 5.2 Graphical Representation of Cu_2O nanostructures exhibiting dielectric Mie resonances exhibit up to an order of magnitude higher photocatalytic rate as compared to

Cu$_2$O nanostructures not exhibiting dielectric Mie resonances. Our simulation, as well as experimental results, exhibit a volcano-type relationship between the photocatalytic rate and the size of Cu$_2$O nanostructures.

5.3. Tuning Catalytic activity and selectivity using Mie Resonances

In this study, we show how we can selectively tune the outcomes of breaking down different peaks of MB dye using MPCs and light of appropriate wavelength. Also, giving a brief information about the reaction pathway facilitating the same. This very idea gives strong possibility about selectively degrading various other dye molecules like methyl orange, rhodomine B and other pollutants. The role of light in driving the reaction is well establised from heat driven through multiple base experiments. The notion of selective tuning can be expanded to other areas of photochemistry

5.4. Mie Resonance Enhanced C-C Coupling

The trends obtained from UV-Vis extinction spectroscopy, ESI-MS, FAAS, and TEM for the reactions under the base and base-free conditions are consistent with each other. It can be concluded from these characterizations that the reaction conversion without a base occurs through a heterogeneous catalytic pathway on the surface of Cu$_2$O NPs. Whereas, for reactions performed in the presence of the base, homogeneous catalytic pathway can also contribute to the observed overall reaction conversion.

The present work advances a number of critical concepts in the field. First, although the study focused on Cu$_2$O-NP-catalyzed C-C coupling reactions, similar principles and techniques could be used to identify truly heterogeneous catalytic conditions for coupling reactions such as C-N, C-S, and C-O couplings.[149,175,176] Role of oxygen and solvent were also identified using switch conditions. Second, in the pharmaceutical and chemical industries, the conventional homogeneous metal-catalyzed C-C coupling processes generally require a number of expensive

downstream unit operations to separate and reduce the metal content and ligand levels below the acceptable limit in the final product (e.g., Active pharmaceutical ingredient, API).[142,143,183] The traditional processes also several equivalents of base, which generates a large amount of salts as wastes. Our results show that Cu_2O NPs can catalyze C-C coupling reactions under ligandless and base-free conditions via a truly heterogeneous pathway. Therefore, the Cu_2O-NP-based heterogeneous catalysts can (i) be potentially used in continuous flow reactors with no purification step required to separate the catalyst from the product, and (ii) result in significant reduction in the waste generated from the coupling processes. In summary, the findings reported herein may pave the way for the development of highly efficient, robust and sustainable coupling processes.

As shown in Figure 4.14b for OHR of PA at 110 °C, in the absence of base conditions the activity of the catalyst is very low, though stability of the nanocatalyst is as desired, since it is a heterogenous pathway. To increase the activity of the catalyst in the heterogenous conditions (absence of base) we can exploit the optical properties of Cu_2O nanostructures, thus achieving the desired characteristics such as high activity, stability, selectivity. To elucidate the structure-performance relationships between Cu_2O nanostructures it has been predicted that Mie resonance-induced rate enhancements (r/r_o) are proportional to the spectral overlap with green light (460-600 nm) and absorption spectra of the photocatalysts (Cu_2O Spheres and Cubes) as shown in Figure 5.3 using the model which was adapted from Ingram et al[56] for composite photocatalysts such as TiO_2/Ag cubes and n-TiO_2/Au spheres. This provides unique ability of these dielectric nanostructures to tune the activity of the catalyst based on shape and size in the UV-Visible region and increase the activity in C-C couplings in the absence of base conditions, thus providing a truly heterogeneous pathway along with all the desired characteristics, this insight could be used for various other coupling reactions.
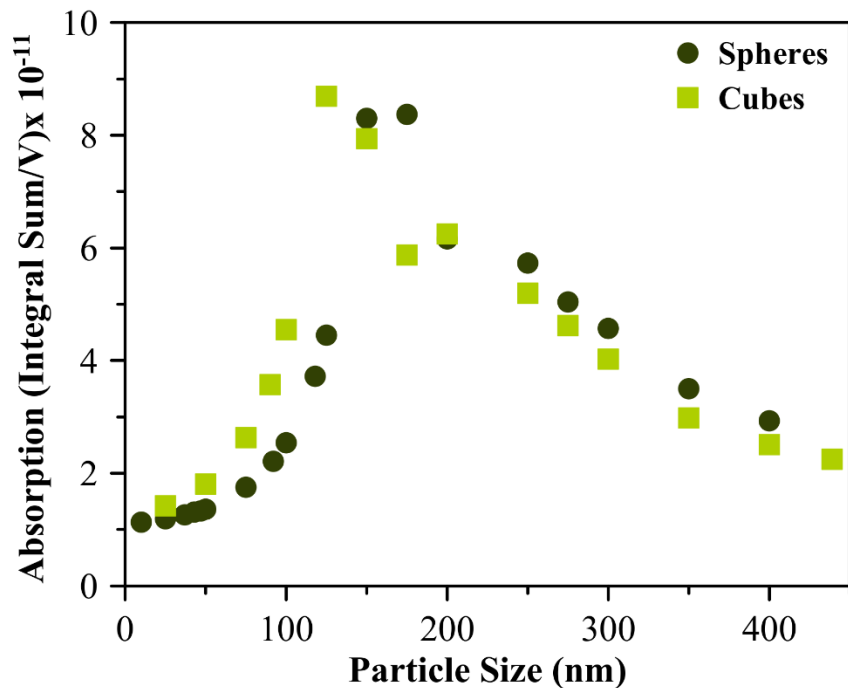
Figure 5.3 Volcano plot obtained from calculated spectral overlap of FDTD simulated absorption of Cu_2O Spheres, Cubes and Green LED light.
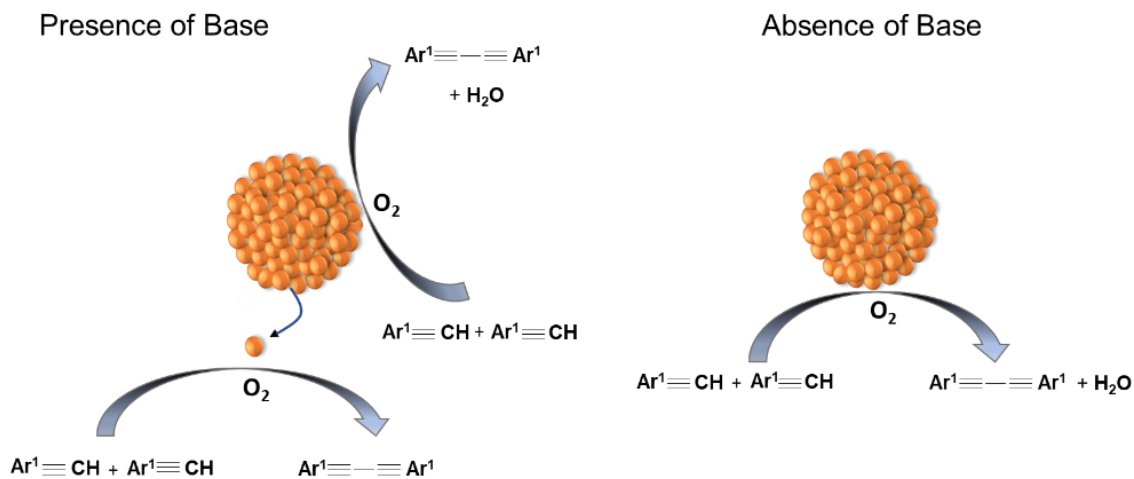
Figure 5.4 Schematic diagram showing the mechanism involved in homocoupling reactions in the presence and absence of base.

REFERENCES

(1)   Meinshausen, M.; Meinshausen, N.; Hare, W.; Raper, S. C. B.; Frieler, K.; Knutti, R.; Frame, D. J.; Allen, M. R. Greenhouse-Gas Emission Targets for Limiting Global Warming to 2 °C. *Nature* **2009**, *458* (7242), 1158–1162. https://doi.org/10.1038/nature08017.

(2)   *Climate Change 2014: Synthesis Report*; Pachauri, R. K., Mayer, L., Intergovernmental Panel on Climate Change, Eds.; Intergovernmental Panel on Climate Change: Geneva, Switzerland, 2015.

(3)   Statistical Review of World Energy 2020 | 69th Edition. bp 2020.

(4)   Nel, W. P.; Cooper, C. J. Implications of Fossil Fuel Constraints on Economic Growth and Global Warming. *Energy Policy* **2009**, *37* (1), 166–180. https://doi.org/10.1016/j.enpol.2008.08.013.

(5)   Palacios, A.; Barreneche, C.; Navarro, M. E.; Ding, Y. Thermal Energy Storage Technologies for Concentrated Solar Power – A Review from a Materials Perspective. *Renewable Energy* **2020**, *156*, 1244–1265. https://doi.org/10.1016/j.renene.2019.10.127.

(6)   Basit, M. A.; Dilshad, S.; Badar, R.; Rehman, S. M. S. ur. Limitations, Challenges, and Solution Approaches in Grid-Connected Renewable Energy Systems. *International Journal of Energy Research* **2020**, *44* (6), 4132–4162. https://doi.org/10.1002/er.5033.

(7)   Shao, M.; Han, Z.; Sun, J.; Xiao, C.; Zhang, S.; Zhao, Y. A Review of Multi-Criteria Decision Making Applications for Renewable Energy Site Selection. *Renewable Energy* **2020**, *157*, 377–403. https://doi.org/10.1016/j.renene.2020.04.137.

(8)   Tyagi, H.; Chakraborty, P. R.; Powar, S.; Agarwal, A. K. Introduction to Solar Energy: Systems, Challenges, and Opportunities. In *Solar Energy: Systems, Challenges, and Opportunities*; Tyagi, H., Chakraborty, P. R., Powar, S., Agarwal, A. K., Eds.; Energy, Environment, and Sustainability; Springer: Singapore, 2020; pp 3–12. https://doi.org/10.1007/978-981-15-0675-8_1.

(9)   Lucchi, E.; Lopez, C. S. P.; Franco, G. A Conceptual Framework on the Integration of Solar Energy Systems in Heritage Sites and Buildings. *IOP Conf. Ser.: Mater. Sci. Eng.* **2020**, *949*, 012113. https://doi.org/10.1088/1757-899X/949/1/012113.

(10) Linic, S.; Christopher, P.; Ingram, D. B. Plasmonic-Metal Nanostructures for Efficient Conversion of Solar to Chemical Energy. *Nature Mater* **2011**, *10* (12), 911–921. https://doi.org/10.1038/nmat3151.

(11) Glunz, S. W.; Preu, R.; Biro, D. 1.16 - Crystalline Silicon Solar Cells: State-of-the-Art and Future Developments. In *Comprehensive Renewable Energy*; Sayigh, A., Ed.; Elsevier: Oxford, 2012; pp 353–387. https://doi.org/10.1016/B978-0-08-087872-0.00117-7.

(12) Zou, X.; Ji, L.; Ge, J.; Sadoway, D. R.; Yu, E. T.; Bard, A. J. Electrodeposition of Crystalline Silicon Films from Silicon Dioxide for Low-Cost Photovoltaic Applications. *Nat Commun* **2019**, *10* (1), 5772. https://doi.org/10.1038/s41467-019-13065-w.

(13) Poortmans, J.; Arkhipov, V. *Thin Film Solar Cells: Fabrication, Characterization and Applications*; John Wiley & Sons, 2006.

(14) Singh, M.; Jiu, J.; Sugahara, T.; Suganuma, K. Thin-Film Copper Indium Gallium Selenide Solar Cell Based on Low-Temperature All-Printing Process. *ACS Appl. Mater. Interfaces* **2014**, *6* (18), 16297–16303. https://doi.org/10.1021/am504509r.

(15)	Dharmadasa, I. M. *Advances in Thin-Film Solar Cells*, 2nd ed.; Jenny Stanford Publishing: Boca Raton, 2018. https://doi.org/10.1201/9780429020841.

(16)	Chopra, K. L.; Paulson, P. D.; Dutta, V. Thin-Film Solar Cells: An Overview. *Progress in Photovoltaics: Research and Applications* **2004**, *12* (2–3), 69–92. https://doi.org/10.1002/pip.541.

(17)	Geisz, J. F.; France, R. M.; Schulte, K. L.; Steiner, M. A.; Norman, A. G.; Guthrey, H. L.; Young, M. R.; Song, T.; Moriarty, T. Six-Junction III–V Solar Cells with 47.1% Conversion Efficiency under 143 Suns Concentration. *Nat Energy* **2020**, *5* (4), 326–335. https://doi.org/10.1038/s41560-020-0598-5.

(18)	Kim, J. Y.; Lee, J.-W.; Jung, H. S.; Shin, H.; Park, N.-G. High-Efficiency Perovskite Solar Cells. *Chem. Rev.* **2020**, *120* (15), 7867–7918. https://doi.org/10.1021/acs.chemrev.0c00107.

(19)	Wenk, H.-R.; Bulakh, A. G. *Minerals: Their Constitution and Origin*; Cambridge University Press: Cambridge; New York, 2004.

(20)	Frost, J. M.; Walsh, A. What Is Moving in Hybrid Halide Perovskite Solar Cells? *Acc. Chem. Res.* **2016**, *49* (3), 528–535. https://doi.org/10.1021/acs.accounts.5b00431.

(21)	Ihly, R.; Dowgiallo, A.-M.; Yang, M.; Schulz, P.; Stanton, N. J.; Reid, O. G.; Ferguson, A. J.; Zhu, K.; Berry, J. J.; Blackburn, J. L. Efficient Charge Extraction and Slow Recombination in Organic–Inorganic Perovskites Capped with Semiconducting Single-Walled Carbon Nanotubes. *Energy Environ. Sci.* **2016**, *9* (4), 1439–1449. https://doi.org/10.1039/C5EE03806E.

(22)	Fang, Y.; Bi, C.; Wang, D.; Huang, J. The Functions of Fullerenes in Hybrid Perovskite Solar Cells. *ACS Energy Lett.* **2017**, *2* (4), 782–794. https://doi.org/10.1021/acsenergylett.6b00657.

(23)	Wang, J.; Liu, K.; Ma, L.; Zhan, X. Triarylamine: Versatile Platform for Organic, Dye-Sensitized, and Perovskite Solar Cells. *Chem. Rev.* **2016**, *116* (23), 14675–14725. https://doi.org/10.1021/acs.chemrev.6b00432.

(24)	Cho, A.-N.; Park, N.-G. Impact of Interfacial Layers in Perovskite Solar Cells. *ChemSusChem* **2017**, *10* (19), 3687–3704. https://doi.org/10.1002/cssc.201701095.

(25)	O'Regan, B.; Grätzel, M. A Low-Cost, High-Efficiency Solar Cell Based on Dye-Sensitized Colloidal TiO 2 Films. *Nature* **1991**, *353* (6346), 737–740. https://doi.org/10.1038/353737a0.

(26)	Green, M. A. Thin-Film Solar Cells: Review of Materials, Technologies and Commercial Status. *J Mater Sci: Mater Electron* **2007**, *18* (1), 15–19. https://doi.org/10.1007/s10854-007-9177-9.

(27)	Ren, Y.; Sun, D.; Cao, Y.; Tsao, H. N.; Yuan, Y.; Zakeeruddin, S. M.; Wang, P.; Grätzel, M. A Stable Blue Photosensitizer for Color Palette of Dye-Sensitized Solar Cells Reaching 12.6% Efficiency. *J. Am. Chem. Soc.* **2018**, *140* (7), 2405–2408. https://doi.org/10.1021/jacs.7b12348.

(28)	Sharma, K.; Sharma, V.; Sharma, S. S. Dye-Sensitized Solar Cells: Fundamentals and Current Status. *Nanoscale Research Letters* **2018**, *13* (1), 381. https://doi.org/10.1186/s11671-018-2760-6.

(29)	Trihutomo, P.; Soeparman, S.; Widhiyanuriyawan, D.; Yuliati, L. Performance Improvement of Dye-Sensitized Solar Cell- (DSSC-) Based Natural Dyes by Clathrin Protein. *International Journal of Photoenergy* **2019**, *2019*, e4384728. https://doi.org/10.1155/2019/4384728.

(30)	Bose, S.; Soni, V.; Genwa, K. R. Recent Advances and Future Prospects for Dye Sensitized Solar Cells: A Review. **2015**, *5* (4), 9.

(31)	Fan, H.; Yan, G.; Zhao, Z.; Hu, X.; Zhang, W.; Liu, H.; Fu, X.; Fu, T.; Zhang, X.-B.; Tan, W. A Smart Photosensitizer–Manganese Dioxide Nanosystem for Enhanced Photodynamic Therapy by Reducing Glutathione Levels in Cancer Cells. *Angewandte*

Chemie International Edition **2016**, *55* (18), 5477–5482. https://doi.org/10.1002/anie.201510748.

(32) Yang, T.-Y.; Gregori, G.; Pellet, N.; Grätzel, M.; Maier, J. The Significance of Ion Conduction in a Hybrid Organic–Inorganic Lead-Iodide-Based Perovskite Photosensitizer. *Angewandte Chemie International Edition* **2015**, *54* (27), 7905–7910. https://doi.org/10.1002/anie.201500014.

(33) Mathew, S.; Ashari Astani, N.; E. Curchod, B. F.; H. Delcamp, J.; Marszalek, M.; Frey, J.; Rothlisberger, U.; Khaja Nazeeruddin, M.; Grätzel, M. Synthesis, Characterization and Ab Initio Investigation of a Panchromatic Ullazine–Porphyrin Photosensitizer for Dye-Sensitized Solar Cells. *Journal of Materials Chemistry A* **2016**, *4* (6), 2332–2339. https://doi.org/10.1039/C5TA08728G.

(34) Cheng, Y.; Yang, G.; Jiang, H.; Zhao, S.; Liu, Q.; Xie, Y. Organic Sensitizers with Extended Conjugation Frameworks as Cosensitizers of Porphyrins for Developing Efficient Dye-Sensitized Solar Cells. *ACS Appl. Mater. Interfaces* **2018**, *10* (45), 38880–38891. https://doi.org/10.1021/acsami.8b12883.

(35) Zheng, J.; Zhang, K.; Fang, Y.; Zuo, Y.; Duan, Y.; Zhuo, Z.; Chen, X.; Yang, W.; Lin, Y.; Wong, M. S.; Pan, F. How to Optimize the Interface between Photosensitizers and TiO2 Nanocrystals with Molecular Engineering to Enhance Performances of Dye-Sensitized Solar Cells? *ACS Appl. Mater. Interfaces* **2015**, *7* (45), 25341–25351. https://doi.org/10.1021/acsami.5b07591.

(36) Mehmood, U.; Hussein, I. A.; Harrabi, K.; Ahmed, S. Density Functional Theory Study on the Electronic Structures of Oxadiazole Based Dyes as Photosensitizer for Dye Sensitized Solar Cells. *Advances in Materials Science and Engineering* **2015**, *2015*, e286730. https://doi.org/10.1155/2015/286730.

(37) Zhang, L.; Yang, X.; Wang, W.; Gurzadyan, G. G.; Li, J.; Li, X.; An, J.; Yu, Z.; Wang, H.; Cai, B.; Hagfeldt, A.; Sun, L. 13.6% Efficient Organic Dye-Sensitized Solar Cells by Minimizing Energy Losses of the Excited State. *ACS Energy Lett.* **2019**, *4* (4), 943–951. https://doi.org/10.1021/acsenergylett.9b00141.

(38) F. Pary, F.; Tirumala, R. T. A.; Andiappan, M.; L. Nelson, T. Copper(i) Oxide Nanoparticle-Mediated C–C Couplings for Synthesis of Polyphenylenediethynylenes: Evidence for a Homogeneous Catalytic Pathway. *Catalysis Science & Technology* **2021**, *11* (7), 2414–2421. https://doi.org/10.1039/D1CY00039J.

(39) Weng, Y.; Ding, B.; Liu, Y.; Song, C.; Chan, L.-Y.; Chiang, C.-W. Late-Stage Photoredox C–H Amidation of N-Unprotected Indole Derivatives: Access to N-(Indol-2-Yl)Amides. *Org. Lett.* **2021**, *23* (7), 2710–2714. https://doi.org/10.1021/acs.orglett.1c00609.

(40) Tirumala, R. T. A.; Dadgar, A. P.; Mohammadparast, F.; Bhardwaj Ramakrishnan, S.; Mou, T.; Wang, B.; Andiappan, M. Homogeneous versus Heterogeneous Catalysis in Cu 2 O-Nanoparticle-Catalyzed C–C Coupling Reactions. *Green Chemistry* **2019**, *21* (19), 5284–5290. https://doi.org/10.1039/C9GC01930H.

(41) Gomez, L.; Sebastian, V.; Arruebo, M.; Santamaria, J.; B. Cronin, S. Plasmon-Enhanced Photocatalytic Water Purification. *Physical Chemistry Chemical Physics* **2014**, *16* (29), 15111–15116. https://doi.org/10.1039/C4CP00229F.

(42) Tahir Mehmood, C.; Zhong, Z.; Zhou, H.; Zhang, C.; Xiao, Y. Immobilizing a Visible Light-Responsive Photocatalyst on a Recyclable Polymeric Composite for Floating and Suspended Applications in Water Treatment. *RSC Advances* **2020**, *10* (60), 36349–36362. https://doi.org/10.1039/D0RA06864K.

(43) Teoh, W. Y.; Scott, J. A.; Amal, R. Progress in Heterogeneous Photocatalysis: From Classical Radical Chemistry to Engineering Nanomaterials and Solar Reactors. *J. Phys. Chem. Lett.* **2012**, *3* (5), 629–639. https://doi.org/10.1021/jz3000646.

(44) Ulmer, U.; Dingle, T.; Duchesne, P. N.; Morris, R. H.; Tavasoli, A.; Wood, T.; Ozin, G. A. Fundamentals and Applications of Photocatalytic CO 2 Methanation. *Nat Commun* **2019**, *10* (1), 3169. https://doi.org/10.1038/s41467-019-10996-2.

(45) Pivovar, B.; Rustagi, N.; Satyapal, S. Hydrogen at Scale (H2 at Scale): Key to a Clean, Economic, and Sustainable Energy System. *Electrochem. Soc. Interface* **2018**, *27* (1), 47. https://doi.org/10.1149/2.F04181if.

(46) *Mechanism of Photocatalytic Water Splitting in TiO2. Reaction of Water with Photoholes, Importance of Charge Carrier Dynamics, and Evidence for Four-Hole Chemistry | Journal of the American Chemical Society*. https://pubs.acs.org/doi/abs/10.1021/ja8034637 (accessed 2021-07-31).

(47) Fujishima, A.; Honda, K. Electrochemical Photolysis of Water at a Semiconductor Electrode. *Nature* **1972**, *238* (5358), 37–38. https://doi.org/10.1038/238037a0.

(48) Serpone, N.; Emeline, A. V. Semiconductor Photocatalysis — Past, Present, and Future Outlook. *J. Phys. Chem. Lett.* **2012**, *3* (5), 673–677. https://doi.org/10.1021/jz300071j.

(49) Liu, B.; Wu, H.; Parkin, I. P. New Insights into the Fundamental Principle of Semiconductor Photocatalysis. *ACS Omega* **2020**, *5* (24), 14847–14856. https://doi.org/10.1021/acsomega.0c02145.

(50) Cao, W. *Semiconductor Photocatalysis: Materials, Mechanisms and Applications*; BoD – Books on Demand, 2016.

(51) Aguado, J.; van Grieken, R.; López-Muñoz, M.-J.; Marugán, J. A Comprehensive Study of the Synthesis, Characterization and Activity of TiO2 and Mixed TiO2/SiO2 Photocatalysts. *Applied Catalysis A: General* **2006**, *312*, 202–212. https://doi.org/10.1016/j.apcata.2006.07.003.

(52) Li, S.; Miao, P.; Zhang, Y.; Wu, J.; Zhang, B.; Du, Y.; Han, X.; Sun, J.; Xu, P. Recent Advances in Plasmonic Nanostructures for Enhanced Photocatalysis and Electrocatalysis. *Advanced Materials* **2021**, *33* (6), 2000086. https://doi.org/10.1002/adma.202000086.

(53) Twilton, J.; Le, C. (Chip); Zhang, P.; Shaw, M. H.; Evans, R. W.; MacMillan, D. W. C. The Merger of Transition Metal and Photocatalysis. *Nat Rev Chem* **2017**, *1* (7), 1–19. https://doi.org/10.1038/s41570-017-0052.

(54) Wang, B.; Cai, H.; Shen, S. Single Metal Atom Photocatalysis. *Small Methods* **2019**, *3* (9), 1800447. https://doi.org/10.1002/smtd.201800447.

(55) Aslam, U.; Chavez, S.; Linic, S. Controlling Energy Flow in Multimetallic Nanostructures for Plasmonic Catalysis. *Nature Nanotech* **2017**, *12* (10), 1000–1005. https://doi.org/10.1038/nnano.2017.131.

(56) Ingram, D. B.; Christopher, P.; Bauer, J. L.; Linic, S. Predictive Model for the Design of Plasmonic Metal/Semiconductor Composite Photocatalysts. *ACS Catal.* **2011**, *1* (10), 1441–1447. https://doi.org/10.1021/cs200320h.

(57) Cushing, S. K.; Li, J.; Meng, F.; Senty, T. R.; Suri, S.; Zhi, M.; Li, M.; Bristow, A. D.; Wu, N. Photocatalytic Activity Enhanced by Plasmonic Resonant Energy Transfer from Metal to Semiconductor. *J. Am. Chem. Soc.* **2012**, *134* (36), 15033–15041. https://doi.org/10.1021/ja305603t.

(58) Faucheaux, J. A.; Stanton, A. L. D.; Jain, P. K. Plasmon Resonances of Semiconductor Nanocrystals: Physical Principles and New Opportunities. *J. Phys. Chem. Lett.* **2014**, *5* (6), 976–985. https://doi.org/10.1021/jz500037k.

(59) Wu, N. Plasmonic Metal–Semiconductor Photocatalysts and Photoelectrochemical Cells: A Review. *Nanoscale* **2018**, *10* (6), 2679–2696. https://doi.org/10.1039/C7NR08487K.

(60) Zhang, X.; Ke, X.; Yao, J. Recent Development of Plasmon-Mediated Photocatalysts and Their Potential in Selectivity Regulation. *J. Mater. Chem. A* **2018**, *6* (5), 1941–1966. https://doi.org/10.1039/C7TA10375A.

(61) Dong, C.; Lian, C.; Hu, S.; Deng, Z.; Gong, J.; Li, M.; Liu, H.; Xing, M.; Zhang, J. Size-Dependent Activity and Selectivity of Carbon Dioxide Photocatalytic Reduction over

Platinum Nanoparticles. *Nat Commun* **2018**, *9* (1), 1252. https://doi.org/10.1038/s41467-018-03666-2.

(62) Christopher, P.; Xin, H.; Marimuthu, A.; Linic, S. Singular Characteristics and Unique Chemical Bond Activation Mechanisms of Photocatalytic Reactions on Plasmonic Nanostructures. *Nature Mater* **2012**, *11* (12), 1044–1050. https://doi.org/10.1038/nmat3454.

(63) Marimuthu, A.; Zhang, J.; Linic, S. Tuning Selectivity in Propylene Epoxidation by Plasmon Mediated Photo-Switching of Cu Oxidation State. *Science* **2013**, *339* (6127), 1590–1593. https://doi.org/10.1126/science.1231631.

(64) Christopher, P.; Linic, S. Shape- and Size-Specific Chemistry of Ag Nanostructures in Catalytic Ethylene Epoxidation. *ChemCatChem* **2010**, *2* (1), 78–83. https://doi.org/10.1002/cctc.200900231.

(65) Westrich, T. A.; Dahlberg, K. A.; Kaviany, M.; Schwank, J. W. High-Temperature Photocatalytic Ethylene Oxidation over TiO $_2$. *J. Phys. Chem. C* **2011**, *115* (33), 16537–16543. https://doi.org/10.1021/jp204405h.

(66) Kuznetsov, A. I.; Miroshnichenko, A. E.; Brongersma, M. L.; Kivshar, Y. S.; Luk'yanchuk, B. Optically Resonant Dielectric Nanostructures. *Science* **2016**, *354* (6314), aag2472. https://doi.org/10.1126/science.aag2472.

(67) Krasnok, A.; Makarov, S.; Petrov, M.; Savelev, R.; Belov, P.; Kivshar, Y. Towards All-Dielectric Metamaterials and Nanophotonics. *arXiv:1503.08857 [physics]* **2015**.

(68) Sain, B.; Meier, C.; Zentgraf, T. Nonlinear Optics in All-Dielectric Nanoantennas and Metasurfaces: A Review. *AP* **2019**, *1* (2), 024002. https://doi.org/10.1117/1.AP.1.2.024002.

(69) Khurgin, J. B. How to Deal with the Loss in Plasmonics and Metamaterials. *Nature Nanotech* **2015**, *10* (1), 2–6. https://doi.org/10.1038/nnano.2014.310.

(70) Khurgin, J. B.; Boltasseva, A. Reflecting upon the Losses in Plasmonics and Metamaterials. *MRS Bulletin* **2012**, *37* (8), 768–779. https://doi.org/10.1557/mrs.2012.173.

(71) Baffou, G.; Quidant, R. Thermo-Plasmonics: Using Metallic Nanostructures as Nano-Sources of Heat. *Laser & Photonics Reviews* **2013**, *7* (2), 171–187. https://doi.org/10.1002/lpor.201200003.

(72) Caldarola, M.; Albella, P.; Cortés, E.; Rahmani, M.; Roschuk, T.; Grinblat, G.; Oulton, R. F.; Bragas, A. V.; Maier, S. A. Non-Plasmonic Nanoantennas for Surface Enhanced Spectroscopies with Ultra-Low Heat Conversion. *Nat Commun* **2015**, *6* (1), 7915. https://doi.org/10.1038/ncomms8915.

(73) Haldavnekar, R.; Venkatakrishnan, K.; Tan, B. Non Plasmonic Semiconductor Quantum SERS Probe as a Pathway for in Vitro Cancer Detection. *Nat Commun* **2018**, *9* (1), 3065. https://doi.org/10.1038/s41467-018-05237-x.

(74) Danesi, S.; Gandolfi, M.; Carletti, L.; Bontempi, N.; Angelis, C. D.; Banfi, F.; Alessandri, I. Photo-Induced Heat Generation in Non-Plasmonic Nanoantennas. *Physical Chemistry Chemical Physics* **2018**, *20* (22), 15307–15315. https://doi.org/10.1039/C8CP01919C.

(75) Woessner, A.; Lundeberg, M. B.; Gao, Y.; Principi, A.; Alonso-González, P.; Carrega, M.; Watanabe, K.; Taniguchi, T.; Vignale, G.; Polini, M.; Hone, J.; Hillenbrand, R.; Koppens, F. H. L. Highly Confined Low-Loss Plasmons in Graphene–Boron Nitride Heterostructures. *Nature Mater* **2015**, *14* (4), 421–425. https://doi.org/10.1038/nmat4169.

(76) Ma, W.; Alonso-González, P.; Li, S.; Nikitin, A. Y.; Yuan, J.; Martín-Sánchez, J.; Taboada-Gutiérrez, J.; Amenabar, I.; Li, P.; Vélez, S.; Tollan, C.; Dai, Z.; Zhang, Y.; Sriram, S.; Kalantar-Zadeh, K.; Lee, S.-T.; Hillenbrand, R.; Bao, Q. In-Plane Anisotropic and Ultra-Low-Loss Polaritons in a Natural van Der Waals Crystal. *Nature* **2018**, *562* (7728), 557–562. https://doi.org/10.1038/s41586-018-0618-9.

(77) Zhu, L. Exploring Strategies for High Dielectric Constant and Low Loss Polymer Dielectrics. *J. Phys. Chem. Lett.* **2014**, *5* (21), 3677–3687. https://doi.org/10.1021/jz501831q.

(78) Shaheen, K.; Shah, Z.; Arshad, T.; Ma, L.; Liu, M.; Wang, Y.; Cui, J.; Ji, Y. T.; Suo, H. Electrical, Dielectric and Photocatalytic Applications of Iron-Based Nanocomposites. *Appl. Phys. A* **2020**, *126* (3), 149. https://doi.org/10.1007/s00339-020-3302-5.

(79) Kelly, K. L.; Coronado, E.; Zhao, L. L.; Schatz, G. C. The Optical Properties of Metal Nanoparticles: The Influence of Size, Shape, and Dielectric Environment. *J. Phys. Chem. B* **2003**, *107* (3), 668–677. https://doi.org/10.1021/jp026731y.

(80) Albella, P.; Shibanuma, T.; Maier, S. A. Switchable Directional Scattering of Electromagnetic Radiation with Subwavelength Asymmetric Silicon Dimers. *Sci Rep* **2015**, *5*, 18322. https://doi.org/10.1038/srep18322.

(81) Qin, M.; Xia, S.; Zhai, X.; Huang, Y.; Wang, L.; Liao, L. Surface Enhanced Perfect Absorption in Metamaterials with Periodic Dielectric Nanostrips on Silver Film. *Opt. Express, OE* **2018**, *26* (23), 30873–30881. https://doi.org/10.1364/OE.26.030873.

(82) Romano, S.; Zito, G.; Managò, S.; Calafiore, G.; Penzo, E.; Cabrini, S.; De Luca, A. C.; Mocella, V. Surface-Enhanced Raman and Fluorescence Spectroscopy with an All-Dielectric Metasurface. *J. Phys. Chem. C* **2018**, *122* (34), 19738–19745. https://doi.org/10.1021/acs.jpcc.8b03190.

(83) Albella, P.; Alcaraz de la Osa, R.; Moreno, F.; Maier, S. A. Electric and Magnetic Field Enhancement with Ultralow Heat Radiation Dielectric Nanoantennas: Considerations for Surface-Enhanced Spectroscopies. *ACS Photonics* **2014**, *1* (6), 524–529. https://doi.org/10.1021/ph500060s.

(84) Shalaev, V. M. *Nonlinear Optics of Random Media: Fractal Composites and Metal-Dielectric Films*; Springer, 2007.

(85) Wang, Y.; Zhang, T.; Zhou, F.-L.; Lun, M.-M.; Zhang, Y.; Fu, D.-W. Halogen Regulation Triggers NLO and Dielectric Dual Switches in Hybrid Compounds with Green Fluorescence. *Inorganic Chemistry Frontiers* **2021**. https://doi.org/10.1039/D1QI00736J.

(86) Maier, S. A. Dielectric and Low-Dimensional-Materials Nanocavities for Non-Linear Nanophotonics and Sensing. In *Advanced Photonics 2018 (BGPP, IPR, NP, NOMA, Sensors, Networks, SPPCom, SOF) (2018), paper SeW2E.4*; Optical Society of America, 2018; p SeW2E.4. https://doi.org/10.1364/SENSORS.2018.SeW2E.4.

(87) Cheng, Y.; Luo, H.; Chen, F.; Gong, R. Triple Narrow-Band Plasmonic Perfect Absorber for Refractive Index Sensing Applications of Optical Frequency. *OSA Continuum, OSAC* **2019**, *2* (7), 2113–2122. https://doi.org/10.1364/OSAC.2.002113.

(88) Mitrofanov, O.; Hale, L. L.; Vabishchevich, P. P.; Luk, T. S.; Addamane, S. J.; Reno, J. L.; Brener, I. Perfectly Absorbing Dielectric Metasurfaces for Photodetection. *APL Photonics* **2020**, *5* (10), 101304. https://doi.org/10.1063/5.0019883.

(89) Rasool, K.; Rafiq, M. A.; Ahmad, M.; Imran, Z.; Hasan, M. M. TiO2 Nanoparticles and Silicon Nanowires Hybrid Device: Role of Interface on Electrical, Dielectric, and Photodetection Properties. *Appl. Phys. Lett.* **2012**, *101* (25), 253104. https://doi.org/10.1063/1.4772068.

(90) Yang, Y.; Miller, O. D.; Christensen, T.; Joannopoulos, J. D.; Soljačić, M. Low-Loss Plasmonic Dielectric Nanoresonators. *Nano Lett.* **2017**, *17* (5), 3238–3245. https://doi.org/10.1021/acs.nanolett.7b00852.

(91) Xu, L.; Saerens, G.; Timofeeva, M.; Smirnova, D. A.; Volkovskaya, I.; Lysevych, M.; Camacho-Morales, R.; Cai, M.; Zangeneh Kamali, K.; Huang, L.; Karouta, F.; Tan, H. H.; Jagadish, C.; Miroshnichenko, A. E.; Grange, R.; Neshev, D. N.; Rahmani, M. Forward and Backward Switching of Nonlinear Unidirectional Emission from GaAs Nanoantennas. *ACS Nano* **2020**, *14* (2), 1379–1389. https://doi.org/10.1021/acsnano.9b07117.

(92)   Kuznetsov, A. I.; Miroshnichenko, A. E.; Fu, Y. H.; Zhang, J.; Luk'yanchuk, B. Magnetic Light. *Sci Rep* **2012**, *2* (1), 492. https://doi.org/10.1038/srep00492.

(93)   Mohammadparast, F.; Ramakrishnan, S. B.; Khatri, N.; Tirumala, R. T. A.; Tan, S.; Kalkan, A. K.; Andiappan, M. Cuprous Oxide Cubic Particles with Strong and Tunable Mie Resonances for Use as Nanoantennas. *ACS Appl. Nano Mater.* **2020**, *3* (7), 6806–6815. https://doi.org/10.1021/acsanm.0c01201.

(94)   Zhang, X.; Peng, T.; Song, S. Recent Advances in Dye-Sensitized Semiconductor Systems for Photocatalytic Hydrogen Production. *J. Mater. Chem. A* **2016**, *4* (7), 2365–2402. https://doi.org/10.1039/C5TA08939E.

(95)   Watanabe, M. Dye-Sensitized Photocatalyst for Effective Water Splitting Catalyst. *Science and Technology of Advanced Materials* **2017**, *18* (1), 705–723. https://doi.org/10.1080/14686996.2017.1375376.

(96)   Huang, J.-F.; Lei, Y.; Luo, T.; Liu, J.-M. Photocatalytic H2 Production from Water by Metal-Free Dye-Sensitized TiO2 Semiconductors: The Role and Development Process of Organic Sensitizers. *ChemSusChem* **2020**, *13* (22), 5863–5895. https://doi.org/10.1002/cssc.202001646.

(97)   Reginato, G.; Zani, L.; Calamante, M.; Mordini, A.; Dessì, A. Dye-Sensitized Heterogeneous Photocatalysts for Green Redox Reactions. *European Journal of Inorganic Chemistry* **2020**, *2020* (11–12), 899–917. https://doi.org/10.1002/ejic.201901174.

(98)   Yun, S.; Vlachopoulos, N.; Qurashi, A.; Ahmad, S.; Hagfeldt, A. Dye Sensitized Photoelectrolysis Cells. *Chem. Soc. Rev.* **2019**, *48* (14), 3705–3722. https://doi.org/10.1039/C8CS00987B.

(99)   Vedhanarayanan, B.; Chen, C.-C.; Lin, T.-W. Plasmon-Enhanced Photocatalytic Hydrogen Production by Dual Dye Sensitized Ternary Composite of MoS3/ Au Core-Ag Shell Nanoparticles/ Graphene. *Journal of Power Sources* **2020**, *477*, 229033. https://doi.org/10.1016/j.jpowsour.2020.229033.

(100) Wang, D.; Li, Y.; Li Puma, G.; Wang, C.; Wang, P.; Zhang, W.; Wang, Q. Dye-Sensitized Photoelectrochemical Cell on Plasmonic Ag/AgCl @ Chiral TiO2 Nanofibers for Treatment of Urban Wastewater Effluents, with Simultaneous Production of Hydrogen and Electricity. *Applied Catalysis B: Environmental* **2015**, *168–169*, 25–32. https://doi.org/10.1016/j.apcatb.2014.11.012.

(101) Zeng, J.; Zeng, W.; Zeng, H. In Situ Plasmonic Au Nanoparticle Anchored Nickel Ferrite: An Efficient Plasmonic Photocatalyst for Fluorescein-Sensitized Hydrogen Evolution under Visible Light Irradiation. *Journal of Solid State Chemistry* **2017**, *253*, 294–304. https://doi.org/10.1016/j.jssc.2017.06.005.

(102) Hou, W.; Pavaskar, P.; Liu, Z.; Theiss, J.; Aykol, M.; Cronin, S. B. Plasmon Resonant Enhancement of Dye Sensitized Solar Cells. *Energy Environ. Sci.* **2011**, *4* (11), 4650–4655. https://doi.org/10.1039/C1EE02120F.

(103) Chien, T.; Pavaskar, P.; Hung, W. H.; Cronin, S.; Chiu, S.-H.; Lai, S.-N. Study of the Plasmon Energy Transfer Processes in Dye Sensitized Solar Cells. *Journal of Nanomaterials* **2015**, *2015*, e139243. https://doi.org/10.1155/2015/139243.

(104) Ding, I.-K.; Zhu, J.; Cai, W.; Moon, S.-J.; Cai, N.; Wang, P.; Zakeeruddin, S. M.; Grätzel, M.; Brongersma, M. L.; Cui, Y.; McGehee, M. D. Plasmonic Dye-Sensitized Solar Cells. *Advanced Energy Materials* **2011**, *1* (1), 52–57. https://doi.org/10.1002/aenm.201000041.

(105) Mandal, P.; Sharma, S. Progress in Plasmonic Solar Cell Efficiency Improvement: A Status Review. *Renewable and Sustainable Energy Reviews* **2016**, *65*, 537–552. https://doi.org/10.1016/j.rser.2016.07.031.

(106) Rho, W.-Y.; Song, D. H.; Yang, H.-Y.; Kim, H.-S.; Son, B. S.; Suh, J. S.; Jun, B.-H. Recent Advances in Plasmonic Dye-Sensitized Solar Cells. *Journal of Solid State Chemistry* **2018**, *258*, 271–282. https://doi.org/10.1016/j.jssc.2017.10.018.

(107) Pandikumar, A.; Lim, S.-P.; Jayabal, S.; Huang, N. M.; Lim, H. N.; Ramaraj, R. Titania@gold Plasmonic Nanoarchitectures: An Ideal Photoanode for Dye-Sensitized Solar Cells. *Renewable and Sustainable Energy Reviews* **2016**, *60*, 408–420. https://doi.org/10.1016/j.rser.2016.01.107.

(108) Rai, P. Plasmonic Noble Metal@metal Oxide Core–Shell Nanoparticles for Dye-Sensitized Solar Cell Applications. *Sustainable Energy Fuels* **2018**, *3* (1), 63–91. https://doi.org/10.1039/C8SE00336J.

(109) Ding, I.-K.; Zhu, J.; Cai, W.; Moon, S.-J.; Cai, N.; Wang, P.; Zakeeruddin, S. M.; Grätzel, M.; Brongersma, M. L.; Cui, Y.; McGehee, M. D. Plasmonic Back Reflectors: Plasmonic Dye-Sensitized Solar Cells. *Advanced Energy Materials* **2011**, *1* (1), 51–51. https://doi.org/10.1002/aenm.201190003.

(110) Gong, J.; Liang, J.; Sumathy, K. Review on Dye-Sensitized Solar Cells (DSSCs): Fundamental Concepts and Novel Materials. *Renewable and Sustainable Energy Reviews* **2012**, *16* (8), 5848–5860. https://doi.org/10.1016/j.rser.2012.04.044.

(111) Ramakrishnan, S. B.; Tirumala, R. T. A.; Mohammadparast, F.; Mou, T.; Le, T.; Wang, B.; Andiappan, M. Plasmonic Photocatalysis. In *Catalysis*; 2021; pp 38–86. https://doi.org/10.1039/9781839163128-00038.

(112) Linic, S.; Christopher, P.; Ingram, D. B. Plasmonic-Metal Nanostructures for Efficient Conversion of Solar to Chemical Energy. *Nature Mater* **2011**, *10* (12), 911–921. https://doi.org/10.1038/nmat3151.

(113) Jain, P. K.; Lee, K. S.; El-Sayed, I. H.; El-Sayed, M. A. Calculated Absorption and Scattering Properties of Gold Nanoparticles of Different Size, Shape, and Composition: Applications in Biological Imaging and Biomedicine. *J. Phys. Chem. B* **2006**, *110* (14), 7238–7248. https://doi.org/10.1021/jp057170o.

(114) Li, J.; Cushing, S. K.; Meng, F.; Senty, T. R.; Bristow, A. D.; Wu, N. Plasmon-Induced Resonance Energy Transfer for Solar Energy Conversion. *Nature Photon* **2015**, *9* (9), 601–607. https://doi.org/10.1038/nphoton.2015.142.

(115) Cushing, S. K.; Li, J.; Bright, J.; Yost, B. T.; Zheng, P.; Bristow, A. D.; Wu, N. Controlling Plasmon-Induced Resonance Energy Transfer and Hot Electron Injection Processes in Metal@TiO2 Core–Shell Nanoparticles. *J. Phys. Chem. C* **2015**, *119* (28), 16239–16244. https://doi.org/10.1021/acs.jpcc.5b03955.

(116) Virtual Issue: Plasmon Resonances - A Physical Chemistry Perspective. *J. Phys. Chem. C* **2011**, *115* (31), 15121–15123. https://doi.org/10.1021/jp206376f.

(117) Mohammadparast, F.; Ramakrishnan, S. B.; Khatri, N.; Tirumala, R. T. A.; Tan, S.; Kalkan, A. K.; Andiappan, M. Cuprous Oxide Cubic Particles with Strong and Tunable Mie Resonances for Use as Nanoantennas. *ACS Appl. Nano Mater.* **2020**, *3* (7), 6806–6815. https://doi.org/10.1021/acsanm.0c01201.

(118) Chang, L.; Besteiro, L. V.; Sun, J.; Santiago, E. Y.; Gray, S. K.; Wang, Z.; Govorov, A. O. Electronic Structure of the Plasmons in Metal Nanocrystals: Fundamental Limitations for the Energy Efficiency of Hot Electron Generation. *ACS Energy Lett.* **2019**, *4* (10), 2552–2568. https://doi.org/10.1021/acsenergylett.9b01617.

(119) Tzarouchis, D.; Sihvola, A. Light Scattering by a Dielectric Sphere: Perspectives on the Mie Resonances. *Applied Sciences* **2018**, *8* (2), 184. https://doi.org/10.3390/app8020184.

(120) Kuznetsov, A. I.; Miroshnichenko, A. E.; Brongersma, M. L.; Kivshar, Y. S.; Luk'yanchuk, B. Optically Resonant Dielectric Nanostructures. *Science* **2016**, *354* (6314). https://doi.org/10.1126/science.aag2472.

(121) Sugimoto, H.; Fujii, M. Colloidal Mie Resonators for All-Dielectric Metaoptics. *Advanced Photonics Research* **2021**, *2* (4), 2000111. https://doi.org/10.1002/adpr.202000111.

(122) Cortés, E. Efficiency and Bond Selectivity in Plasmon-Induced Photochemistry. *Advanced Optical Materials* **2017**, *5* (15), 1700191. https://doi.org/10.1002/adom.201700191.

(123) Poblet, M.; Li, Y.; Cortés, E.; Maier, S. A.; Grinblat, G.; Bragas, A. V. Direct Detection of Optical Forces of Magnetic Nature in Dielectric Nanoantennas. *Nano Lett.* **2020**, *20* (10), 7627–7634. https://doi.org/10.1021/acs.nanolett.0c03157.

(124) Cambiasso, J.; König, M.; Cortés, E.; Schlücker, S.; Maier, S. A. Surface-Enhanced Spectroscopies of a Molecular Monolayer in an All-Dielectric Nanoantenna. *ACS Photonics* **2018**, *5* (4), 1546–1557. https://doi.org/10.1021/acsphotonics.7b01604.

(125) Fujishima, A.; Honda, K. Electrochemical Photolysis of Water at a Semiconductor Electrode. *Nature* **1972**, *238* (5358), 37–38. https://doi.org/10.1038/238037a0.

(126) Serpone, N.; Emeline, A. V. Semiconductor Photocatalysis — Past, Present, and Future Outlook. *J. Phys. Chem. Lett.* **2012**, *3* (5), 673–677. https://doi.org/10.1021/jz300071j.

(127) Ma, R.; Zhang, S.; Wen, T.; Gu, P.; Li, L.; Zhao, G.; Niu, F.; Huang, Q.; Tang, Z.; Wang, X. A Critical Review on Visible-Light-Response CeO2-Based Photocatalysts with Enhanced Photooxidation of Organic Pollutants. *Catalysis Today* **2019**, *335*, 20–30. https://doi.org/10.1016/j.cattod.2018.11.016.

(128) Tamirat, A. G.; Rick, J.; Dubale, A. A.; Su, W.-N.; Hwang, B.-J. Using Hematite for Photoelectrochemical Water Splitting: A Review of Current Progress and Challenges. *Nanoscale Horiz.* **2016**, *1* (4), 243–267. https://doi.org/10.1039/C5NH00098J.

(129) Bagal, I. V.; Chodankar, N. R.; Hassan, M. A.; Waseem, A.; Johar, M. A.; Kim, D.-H.; Ryu, S.-W. Cu2O as an Emerging Photocathode for Solar Water Splitting - A Status Review. *International Journal of Hydrogen Energy* **2019**, *44* (39), 21351–21378. https://doi.org/10.1016/j.ijhydene.2019.06.184.

(130) Hara, M.; Kondo, T.; Komoda, M.; Ikeda, S.; Kondo, J. N.; Domen, K.; Hara, M.; Shinohara, K.; Tanaka, A. Cu2O as a Photocatalyst for Overall Water Splitting under Visible Light Irradiation. *Chem. Commun.* **1998**, No. 3, 357–358. https://doi.org/10.1039/a707440i.

(131) Kumar, S.; Parlett, C. M. A.; Isaacs, M. A.; Jowett, D. V.; Douthwaite, R. E.; Cockett, M. C. R.; Lee, A. F. Facile Synthesis of Hierarchical Cu2O Nanocubes as Visible Light Photocatalysts. *Applied Catalysis B: Environmental* **2016**, *189*, 226–232. https://doi.org/10.1016/j.apcatb.2016.02.038.

(132) Li, J.; Cushing, S. K.; Meng, F.; Senty, T. R.; Bristow, A. D.; Wu, N. Plasmon-Induced Resonance Energy Transfer for Solar Energy Conversion. *Nature Photonics* **2015**, *9* (9), 601–607. https://doi.org/10.1038/nphoton.2015.142.

(133) Hou, W.; Cronin, S. B. A Review of Surface Plasmon Resonance-Enhanced Photocatalysis. *Adv. Funct. Mater.* **2013**, *23* (13), 1612–1619. https://doi.org/10.1002/adfm.201202148.

(134) Cushing, S. K.; Wu, N. Progress and Perspectives of Plasmon-Enhanced Solar Energy Conversion. *J. Phys. Chem. Lett.* **2016**, *7* (4), 666–675. https://doi.org/10.1021/acs.jpclett.5b02393.

(135) DeSario, P. A.; Pietron, J. J.; Dunkelberger, A.; Brintlinger, T. H.; Baturina, O.; Stroud, R. M.; Owrutsky, J. C.; Rolison, D. R. Plasmonic Aerogels as a Three-Dimensional Nanoscale Platform for Solar Fuel Photocatalysis. *Langmuir* **2017**, *33* (37), 9444–9454. https://doi.org/10.1021/acs.langmuir.7b01117.

(136) Link, S.; Masiello, D. J. Introduction: Plasmonics in Chemistry. *Chem. Rev.* **2018**, *118* (6), 2863–2864. https://doi.org/10.1021/acs.chemrev.8b00146.

(137) Brongersma, M. L.; Halas, N. J.; Nordlander, P. Plasmon-Induced Hot Carrier Science and Technology. *Nature Nanotech* **2015**, *10* (1), 25–34. https://doi.org/10.1038/nnano.2014.311.

(138) Tatsuma, T.; Nishi, H.; Ishida, T. Plasmon-Induced Charge Separation: Chemistry and Wide Applications. *Chem. Sci.* **2017**, *8* (5), 3325–3337. https://doi.org/10.1039/C7SC00031F.

(139) Jain, P. K.; Lee, K. S.; El-Sayed, I. H.; El-Sayed, M. A. Calculated Absorption and Scattering Properties of Gold Nanoparticles of Different Size, Shape, and Composition: Applications in Biological Imaging and Biomedicine. *J. Phys. Chem. B* **2006**, *110* (14), 7238–7248. https://doi.org/10.1021/jp057170o.

(140) Zhao, T.; Herbert, P. J.; Zheng, H.; Knappenberger, K. L. State-Resolved Metal Nanoparticle Dynamics Viewed through the Combined Lenses of Ultrafast and Magneto-Optical Spectroscopies. *Acc. Chem. Res.* **2018**, *51* (6), 1433–1442. https://doi.org/10.1021/acs.accounts.8b00096.

(141) Hartland, G. V.; Besteiro, L. V.; Johns, P.; Govorov, A. O. What's so Hot about Electrons in Metal Nanoparticles? *ACS Energy Lett.* **2017**, *2* (7), 1641–1653. https://doi.org/10.1021/acsenergylett.7b00333.

(142) Wu, N. Plasmonic Metal–Semiconductor Photocatalysts and Photoelectrochemical Cells: A Review. *Nanoscale* **2018**, *10* (6), 2679–2696. https://doi.org/10.1039/C7NR08487K.

(143) Kuznetsov, A. I.; Miroshnichenko, A. E.; Brongersma, M. L.; Kivshar, Y. S.; Luk'yanchuk, B. Optically Resonant Dielectric Nanostructures. *Science* **2016**, *354* (6314), aag2472. https://doi.org/10.1126/science.aag2472.

(144) Dimitrios Tzarouchis; Ari Sihvola. Light Scattering by a Dielectric Sphere: Perspectives on the Mie Resonances. *Applied Sciences* **2018**, *8* (2), 184. https://doi.org/10.3390/app8020184.

(145) Sugimoto, H.; Fujii, M. Colloidal Mie Resonators for All-Dielectric Metaoptics. *Adv Photo Res* **2021**, *2* (4), 2000111. https://doi.org/10.1002/adpr.202000111.

(146) Kim, S. J.; Thomann, I.; Park, J.; Kang, J.-H.; Vasudev, A. P.; Brongersma, M. L. Light Trapping for Solar Fuel Generation with Mie Resonances. *Nano Lett.* **2014**, *14* (3), 1446–1452. https://doi.org/10.1021/nl404575e.

(147) Brongersma, M. L.; Cui, Y.; Fan, S. Light Management for Photovoltaics Using High-Index Nanostructures. *Nature Mater* **2014**, *13* (5), 451–460. https://doi.org/10.1038/nmat3921.

(148) Sugawa, K.; Matsubara, M.; Tahara, H.; Kanai, D.; Honda, J.; Yokoyama, J.; Kanakubo, K.; Ozawa, H.; Watanuki, Y.; Kojima, Y.; Nishimiya, N.; Sagara, T.; Takase, K.; Haga, M.; Otsuki, J. Mie Resonance-Enhanced Light Absorption of FeS $_2$ Nanocubes in a Near-Infrared Region: Intraparticulate Synergy between Electronic Absorption and Mie Resonances. *ACS Appl. Energy Mater.* **2019**, *2* (9), 6472–6483. https://doi.org/10.1021/acsaem.9b01060.

(149) Marimuthu, A.; Zhang, J.; Linic, S. Tuning Selectivity in Propylene Epoxidation by Plasmon Mediated Photo-Switching of Cu Oxidation State. *Science* **2013**, *339* (6127), 1590–1593. https://doi.org/10.1126/science.1231631.

(150) Kavoulakis, G. M. Bose-Einstein Condensation of Excitons in Cu $_2$ O. *Phys. Rev. B* **2001**, *65* (3), 035204. https://doi.org/10.1103/PhysRevB.65.035204.

(151) Jolk, A.; Jörger, M.; Klingshirn, C. Exciton Lifetime, Auger Recombination, and Exciton Transport by Calibrated Differential Absorption Spectroscopy in Cu $_2$ O. *Phys. Rev. B* **2002**, *65* (24), 245209. https://doi.org/10.1103/PhysRevB.65.245209.

(152) Linic, S.; Aslam, U.; Boerigter, C.; Morabito, M. Photochemical Transformations on Plasmonic Metal Nanoparticles. *Nature Mater* **2015**, *14* (6), 567–576. https://doi.org/10.1038/nmat4281.

(153) Ertl, G. Reactions at Surfaces: From Atoms to Complexity (Nobel Lecture). *Angewandte Chemie International Edition* **2008**, *47* (19), 3524–3535. https://doi.org/10.1002/anie.200800480.

(154) Hu, B.; Getsoian, A. B.; Schweitzer, N. M.; Das, U.; Kim, H.; Niklas, J.; Poluektov, O.; Curtiss, L. A.; Stair, P. C.; Miller, J. T.; Hock, A. S. Selective Propane Dehydrogenation with Single-Site CoII on SiO2 by a Non-Redox Mechanism. *J. CATAL.* **2015**, *322*, 24–37. https://doi.org/10.1016/j.jcat.2014.10.018.

(155) Christopher, P.; Linic, S. Shape- and Size-Specific Chemistry of Ag Nanostructures in Catalytic Ethylene Epoxidation. *ChemCatChem* **2010**, *2* (1), 78–83. https://doi.org/10.1002/cctc.200900231.

(156) Hinrichsen, O.; Rosowski, F.; Hornung, A.; Muhler, M.; Ertl, G. The Kinetics of Ammonia Synthesis over Ru-Based Catalysts: 1. The Dissociative Chemisorption and Associative Desorption of N2. *Journal of Catalysis* **1997**, *165* (1), 33–44. https://doi.org/10.1006/jcat.1997.1447.

(157) Dellamorte, J. C.; Lauterbach, J.; Barteau, M. A. Palladium–Silver Bimetallic Catalysts with Improved Activity and Selectivity for Ethylene Epoxidation. *Applied Catalysis A: General* **2011**, *391* (1), 281–288. https://doi.org/10.1016/j.apcata.2010.06.023.

(158) Cleve, T. V.; Moniri, S.; Belok, G.; More, K. L.; Linic, S. Nanoscale Engineering of Efficient Oxygen Reduction Electrocatalysts by Tailoring the Local Chemical Environment of Pt Surface Sites. *ACS Catal.* **2017**, *7* (1), 17–24. https://doi.org/10.1021/acscatal.6b01565.

(159) Grabow, L. C.; Gokhale, A. A.; Evans, S. T.; Dumesic, J. A.; Mavrikakis, M. Mechanism of the Water Gas Shift Reaction on Pt: First Principles, Experiments, and Microkinetic Modeling. *J. Phys. Chem. C* **2008**, *112* (12), 4608–4617. https://doi.org/10.1021/jp7099702.

(160) Stamenkovic, V. R.; Fowler, B.; Mun, B. S.; Wang, G.; Ross, P. N.; Lucas, C. A.; Marković, N. M. Improved Oxygen Reduction Activity on Pt3Ni(111) via Increased Surface Site Availability. *Science* **2007**, *315* (5811), 493–497. https://doi.org/10.1126/science.1135941.

(161) Studt, F.; Abild-Pedersen, F.; Bligaard, T.; Sørensen, R. Z.; Christensen, C. H.; Nørskov, J. K. Identification of Non-Precious Metal Alloy Catalysts for Selective Hydrogenation of Acetylene. *Science* **2008**, *320* (5881), 1320–1322. https://doi.org/10.1126/science.1156660.

(162) Kliewer, C. J.; Bieri, M.; Somorjai, G. A. Hydrogenation of the Alpha,Beta-Unsaturated Aldehydes Acrolein, Crotonaldehyde, and Prenal over Pt Single Crystals: A Kinetic and Sum-Frequency Generation Vibrational Spectroscopy Study. *J Am Chem Soc* **2009**, *131* (29), 9958–9966. https://doi.org/10.1021/ja8092532.

(163) Haryanto, A.; Fernando, S.; Murali, N.; Adhikari, S. Current Status of Hydrogen Production Techniques by Steam Reforming of Ethanol: A Review. *Energy Fuels* **2005**, *19* (5), 2098–2106. https://doi.org/10.1021/ef0500538.

(164) Nikolla, E.; Holewinski, A.; Schwank, J.; Linic, S. Controlling Carbon Surface Chemistry by Alloying: Carbon Tolerant Reforming Catalyst. *J. Am. Chem. Soc.* **2006**, *128* (35), 11354–11355. https://doi.org/10.1021/ja0638298.

(165) Saavedra, J.; Whittaker, T.; Chen, Z.; Pursell, C. J.; Rioux, R. M.; Chandler, B. D. Controlling Activity and Selectivity Using Water in the Au-Catalysed Preferential Oxidation of CO in H2. *Nat Chem* **2016**, *8* (6), 584–589. https://doi.org/10.1038/nchem.2494.

(166) Marimuthu, A.; Zhang, J.; Linic, S. Tuning Selectivity in Propylene Epoxidation by Plasmon Mediated Photo-Switching of Cu Oxidation State. *Science* **2013**, *339* (6127), 1590–1593. https://doi.org/10.1126/science.1231631.

(167) Zhou, L.; Martirez, J. M. P.; Finzel, J.; Zhang, C.; Swearer, D. F.; Tian, S.; Robatjazi, H.; Lou, M.; Dong, L.; Henderson, L.; Christopher, P.; Carter, E. A.; Nordlander, P.; Halas, N. J. Light-Driven Methane Dry Reforming with Single Atomic Site Antenna-Reactor Plasmonic Photocatalysts. *Nature Energy* **2020**, *5* (1), 61–70. https://doi.org/10.1038/s41560-019-0517-9.

(168) Mohammadparast, F.; Ramakrishnan, S. B.; Khatri, N.; Tirumala, R. T. A.; Tan, S.; Kalkan, A. K.; Andiappan, M. Cuprous Oxide Cubic Particles with Strong and Tunable

Mie Resonances for Use as Nanoantennas. *ACS Appl. Nano Mater.* **2020**, *3* (7), 6806–6815. https://doi.org/10.1021/acsanm.0c01201.

(169) Merritt, J. M.; Andiappan, M.; Pietz, M. A.; Richey, R. N.; Sullivan, K. A.; Kjell, D. P. Mitigating the Risk of Coprecipitation of Pinacol during Isolation from Telescoped Miyaura Borylation and Suzuki Couplings Utilizing Boron Pinacol Esters: Use of Modeling for Process Design. *Org. Process Res. Dev.* **2016**, *20* (2), 178–188. https://doi.org/10.1021/acs.oprd.5b00324.

(170) Cooper, T. W. J.; Campbell, I. B.; Macdonald, S. J. F. Factors Determining the Selection of Organic Reactions by Medicinal Chemists and the Use of These Reactions in Arrays (Small Focused Libraries). *Angew. Chem. Int. Ed. Engl.* **2010**, *49* (44), 8082–8091. https://doi.org/10.1002/anie.201002238.

(171) Gao, H.-Y.; Wagner, H.; Zhong, D.; Franke, J.-H.; Studer, A.; Fuchs, H. Glaser Coupling at Metal Surfaces. *Angewandte Chemie International Edition* **2013**, *52* (14), 4024–4028. https://doi.org/10.1002/anie.201208597.

(172) Zhang, Y.-Q.; Kepčija, N.; Kleinschrodt, M.; Diller, K.; Fischer, S.; Papageorgiou, A. C.; Allegretti, F.; Björk, J.; Klyatskaya, S.; Klappenberger, F.; Ruben, M.; Barth, J. V. Homo-Coupling of Terminal Alkynes on a Noble Metal Surface. *Nature Communications* **2012**, *3*, 1286. https://doi.org/10.1038/ncomms2291.

(173) Gao, H.-Y.; Zhong, D.; Mönig, H.; Wagner, H.; Held, P.-A.; Timmer, A.; Studer, A.; Fuchs, H. Photochemical Glaser Coupling at Metal Surfaces. *J. Phys. Chem. C* **2014**, *118* (12), 6272–6277. https://doi.org/10.1021/jp411889e.

(174) Beaumont, S. K. Heterogeneously Catalyzing C-C Coupling Reactions with Precious Metal Nanoparticles. *Journal of chemical technology and biotechnology.* **2012**, *87*, 595–600. http://dx.doi.org/10.1002/jctb.3748.

(175) *Metal-catalyzed Cross-coupling Reactions*. Wiley.com. https://www.wiley.com/en-us/Metal+catalyzed+Cross+coupling+Reactions-p-9783527612208 (accessed 2019-04-03).

(176) Evano, G.; Blanchard, N. *Copper-Mediated Cross-Coupling Reactions, 2013*. Wiley.com.

(177) Rizkin, B. A.; Hartman, R. L. Catalytic Activity of Pd/Hydrophilic Phosphine Ligand in the Interface of an Aqueous-Phase Cu-Free Sonogashira Coupling. *React. Chem. Eng.* **2018**, *3* (3), 251–257. https://doi.org/10.1039/C8RE00021B.

(178) Domier, R. C.; Moore, J. N.; Shaughnessy, K. H.; Hartman, R. L. *Kinetic Analysis of Aqueous-Phase Pd-Catalyzed, Cu-Free Direct Arylation of Terminal Alkynes Using a Hydrophilic Ligand*. https://pubs.acs.org/doi/abs/10.1021/op4001274 (accessed 2019-05-07). https://doi.org/10.1021/op4001274.

(179) Thomas, A. M.; Sujatha, A.; Anilkumar, G. Recent Advances and Perspectives in Copper-Catalyzed Sonogashira Coupling Reactions. *RSC Adv.* **2014**, *4* (42), 21688–21698. https://doi.org/10.1039/C4RA02529F.

(180) Jana, R.; Pathak, T. P.; Sigman, M. S. Advances in Transition Metal (Pd, Ni, Fe)-Catalyzed Cross-Coupling Reactions Using Alkyl-Organometallics as Reaction Partners. *Chem. Rev.* **2011**, *111* (3), 1417–1492. https://doi.org/10.1021/cr100327p.

(181) Farina, V. High-Turnover Palladium Catalysts in Cross-Coupling and Heck Chemistry: A Critical Overview. *Advanced Synthesis & Catalysis* **2004**, *346* (13–15), 1553–1582. https://doi.org/10.1002/adsc.200404178.

(182) A Snapshot of Priority Technology Areas Across the Federal Government. February 2, 2017.

(183) Dunn, P. J.; Wells, A. S.; Williams, M. T. Future Trends for Green Chemistry in the Pharmaceutical Industry. In *Green Chemistry in the Pharmaceutical Industry*; John Wiley & Sons, Ltd, 2010; pp 333–355. https://doi.org/10.1002/9783527629688.ch16.

(184) Hutchings, G. *Nanocatalysis: Synthesis and ApplicationsHutchings, G. Nanocatalysis: Synthesis and Applications, 1 edition.; Polshettiwar, V., Asefa, T., Eds.; Wiley.* Wiley.com.

https://www.wiley.com/en-us/Nanocatalysis%3A+Synthesis+and+Applications-p-9781118148860 (accessed 2019-05-03).

(185) Fihri, A.; Bouhrara, M.; Nekoueishahraki, B.; Basset, J.-M.; Polshettiwar, V. Nanocatalysts for Suzuki Cross-Coupling Reactions. *Chem. Soc. Rev.* **2011**, *40* (10), 5181–5203. https://doi.org/10.1039/C1CS15079K.

(186) Balanta, A.; Godard, C.; Claver, C. Pd Nanoparticles for C–C Coupling Reactions. *Chem. Soc. Rev.* **2011**, *40* (10), 4973–4985. https://doi.org/10.1039/C1CS15195A.

(187) Yin; Liebscher, J. Carbon−Carbon Coupling Reactions Catalyzed by Heterogeneous Palladium Catalysts. *Chem. Rev.* **2007**, *107* (1), 133–173. https://doi.org/10.1021/cr0505674.

(188) Widegren, J. A.; Finke, R. G. A Review of the Problem of Distinguishing True Homogeneous Catalysis from Soluble or Other Metal-Particle Heterogeneous Catalysis under Reducing Conditions. *Journal of Molecular Catalysis A: Chemical* **2003**, *198* (1), 317–341. https://doi.org/10.1016/S1381-1169(02)00728-8.

(189) Schmidt, A. F.; Al-Halaiqa, A.; Smirnov, V. V. New Approaches to Heck Reaction Testing for Homogeneity-Heterogeneity. *Kinet Catal* **2008**, *49* (3), 395–400. https://doi.org/10.1134/S0023158408030129.

(190) Beaumont, S. K.; Kyriakou, G.; Lambert, R. M. Identity of the Active Site in Gold Nanoparticle-Catalyzed Sonogashira Coupling of Phenylacetylene and Iodobenzene. *J. Am. Chem. Soc.* **2010**, *132* (35), 12246–12248. https://doi.org/10.1021/ja1063179.

(191) Molnár, Á. Efficient, Selective, and Recyclable Palladium Catalysts in Carbon−Carbon Coupling Reactions. *Chem. Rev.* **2011**, *111* (3), 2251–2320. https://doi.org/10.1021/cr100355b.

(192) Phan, N. T. S.; Van Der Sluys, M.; Jones, C. W. On the Nature of the Active Species in Palladium Catalyzed Mizoroki–Heck and Suzuki–Miyaura Couplings – Homogeneous or Heterogeneous Catalysis, A Critical Review. *Advanced Synthesis & Catalysis* **2006**, *348* (6), 609–679. https://doi.org/10.1002/adsc.200505473.

(193) Pérez-Lorenzo, M. Palladium Nanoparticles as Efficient Catalysts for Suzuki Cross-Coupling Reactions. *J. Phys. Chem. Lett.* **2012**, *3* (2), 167–174. https://doi.org/10.1021/jz2013984.

(194) Song, H. M.; Moosa, B. A.; Khashab, N. M. Water-Dispersable Hybrid Au–Pd Nanoparticles as Catalysts in Ethanol Oxidation, Aqueous Phase Suzuki–Miyaura and Heck Reactions. *J. Mater. Chem.* **2012**, *22* (31), 15953–15959. https://doi.org/10.1039/C2JM32702C.

(195) Fang, P.-P.; Jutand, A.; Tian, Z.-Q.; Amatore, C. Au–Pd Core–Shell Nanoparticles Catalyze Suzuki–Miyaura Reactions in Water through Pd Leaching. *Angewandte Chemie International Edition* **2011**, *50* (51), 12184–12188. https://doi.org/10.1002/anie.201103465.

(196) Collins, G.; Schmidt, M.; O'Dwyer, C.; Holmes, J. D.; McGlacken, G. P. The Origin of Shape Sensitivity in Palladium-Catalyzed Suzuki-Miyaura Cross Coupling Reactions. *Angew. Chem. Int. Ed. Engl.* **2014**, *53* (16), 4142–4145. https://doi.org/10.1002/anie.201400483.

(197) Feng, L.; Chong, H.; Li, P.; Xiang, J.; Fu, F.; Yang, S.; Yu, H.; Sheng, H.; Zhu, M. Pd–Ni Alloy Nanoparticles as Effective Catalysts for Miyaura–Heck Coupling Reactions. *J. Phys. Chem. C* **2015**, *119* (21), 11511–11515. https://doi.org/10.1021/jp510988m.

(198) Zhu, M.; Diao, G. Magnetically Recyclable Pd Nanoparticles Immobilized on Magnetic Fe3O4@C Nanocomposites: Preparation, Characterization, and Their Catalytic Activity toward Suzuki and Heck Coupling Reactions. *J. Phys. Chem. C* **2011**, *115* (50), 24743–24749. https://doi.org/10.1021/jp206116e.

(199)   Park, J. C.; Heo, E.; Kim, A.; Kim, M.; Park, K. H.; Song, H. Extremely Active Pd@pSiO2 Yolk–Shell Nanocatalysts for Suzuki Coupling Reactions of Aryl Halides. *J. Phys. Chem. C* **2011**, *115* (32), 15772–15777. https://doi.org/10.1021/jp2021825.

(200)   Jang, Y.; Chung, J.; Kim, S.; Jun, S. W.; Kim, B. H.; Lee, D. W.; Kim, B. M.; Hyeon, T. Simple Synthesis of Pd–Fe3O4 Heterodimer Nanocrystals and Their Application as a Magnetically Recyclable Catalyst for Suzuki Cross-Coupling Reactions. *Phys. Chem. Chem. Phys.* **2011**, *13* (7), 2512–2516. https://doi.org/10.1039/C0CP01680B.

(201)   Elias, W. C.; Signori, A. M.; Zaramello, L.; Albuquerque, B. L.; de Oliveira, D. C.; Domingos, J. B. Mechanism of a Suzuki-Type Homocoupling Reaction Catalyzed by Palladium Nanocubes. *ACS Catal.* **2017**, *7* (2), 1462–1469. https://doi.org/10.1021/acscatal.6b03490.

(202)   Beletskaya, I. P.; Ananikov, V. P. Transition-Metal-Catalyzed C−S, C−Se, and C−Te Bond Formation via Cross-Coupling and Atom-Economic Addition Reactions. *Chem. Rev.* **2011**, *111* (3), 1596–1636. https://doi.org/10.1021/cr100347k.

(203)   Panova, Y. S.; Kashin, A. S.; Vorobev, M. G.; Degtyareva, E. S.; Ananikov, V. P. Nature of the Copper-Oxide-Mediated C–S Cross-Coupling Reaction: Leaching of Catalytically Active Species from the Metal Oxide Surface. *ACS Catal.* **2016**, *6* (6), 3637–3643. https://doi.org/10.1021/acscatal.6b00337.

(204)   Isotope Distribution Calculator, Mass Spec Plotter, Isotope Abundance Graphs, https://www.sisweb.com/mstools/isotope.htm, (accessed December 20, 2019)

APPENDICES

APPENDIX A

MIE RESONANCE-ENHANCED DYE SENSITIZATION
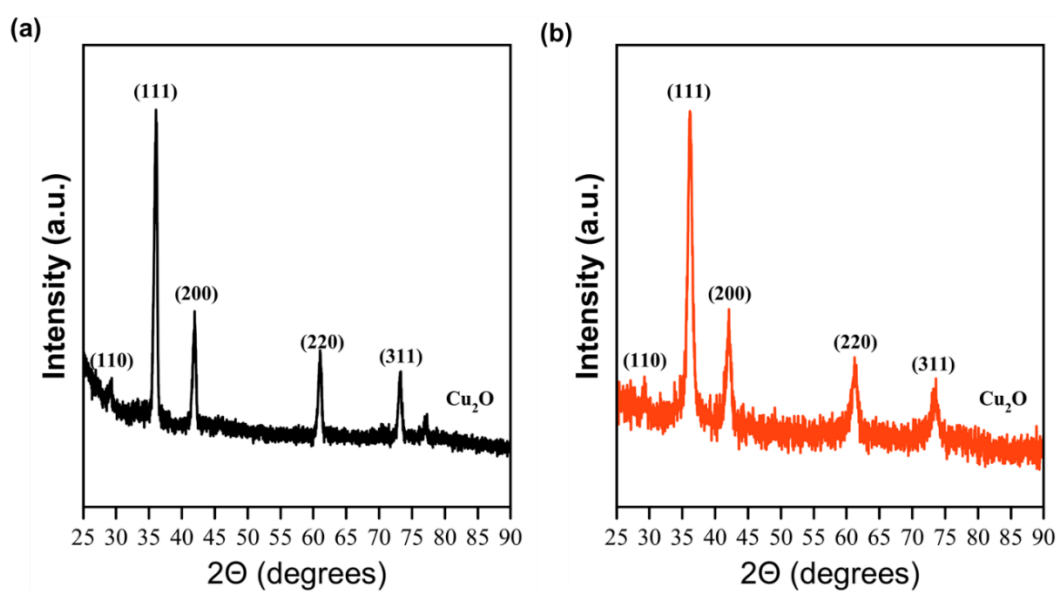
Figure A.S1. Representative XRD spectra of (**a**) Cu_2O nanospheres and (**b**) Cu_2O nanocubes
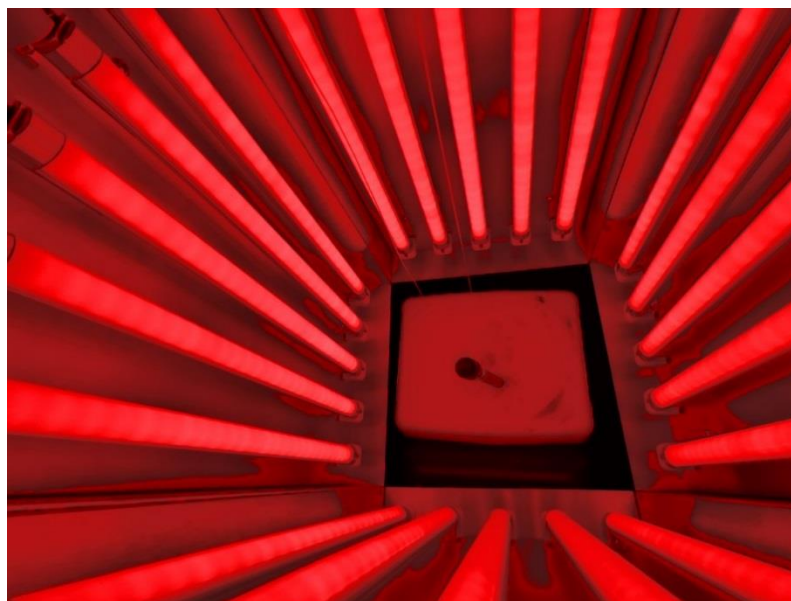
Figure A.S1 (c) Luzchem photoreactor experimental set up with red light illumination used for dye sensitization studies.
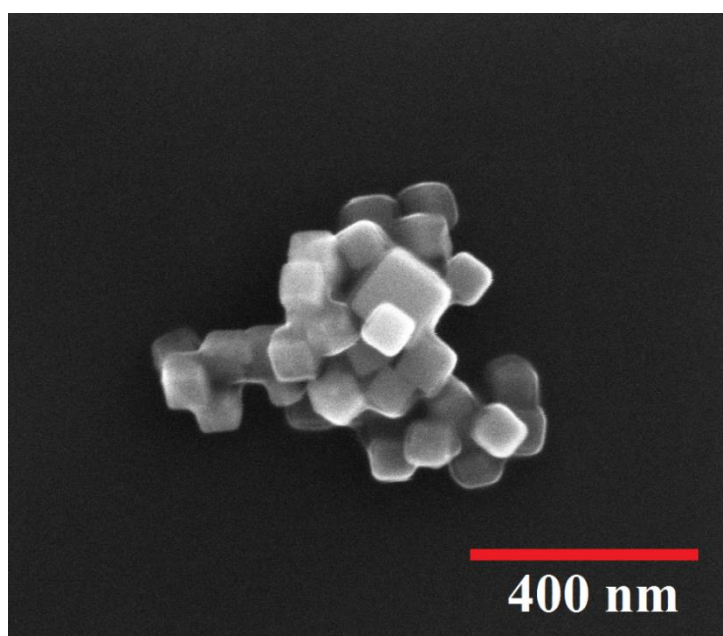
Figure A.S1 (d) Representative scanning electron microcopy image of large Cu_2O nanocubes of 92 ± 13 nm edge length synthesized using chemical reduction method.
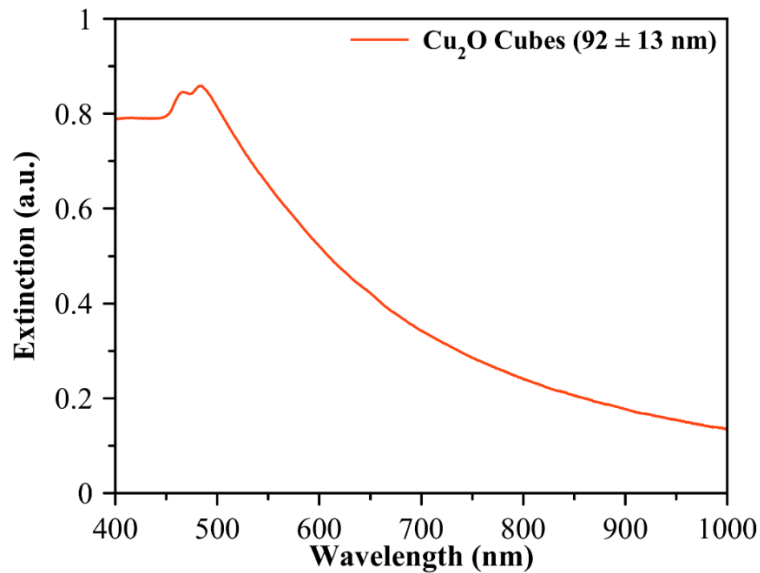
Figure A.S1 (e) Experimentally measured UV-Vis extinction spectra of Cu_2O nanocubes of 92 ± 13 nm edge length.
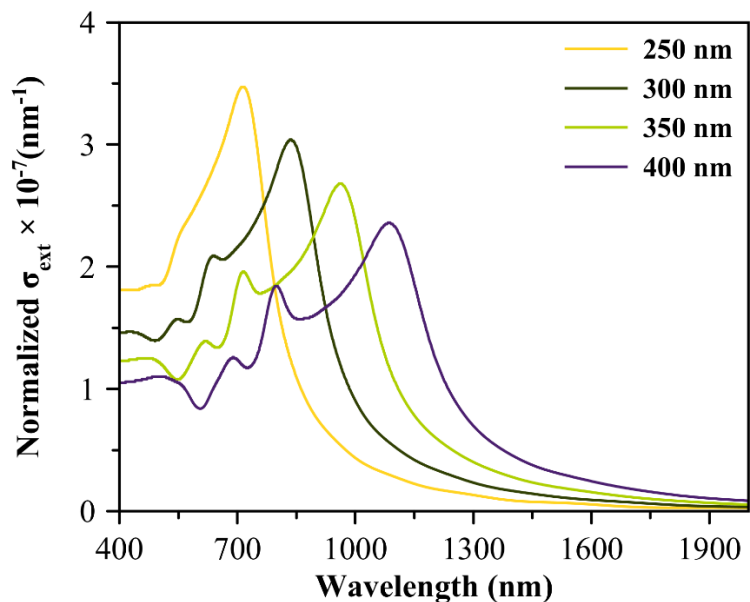
Figure A.S2 (b) FDTD-simulated normalized-extinction (normalized-σ_{Ext}) cross section of Cu_2O nanospheres of different edge lengths in the range 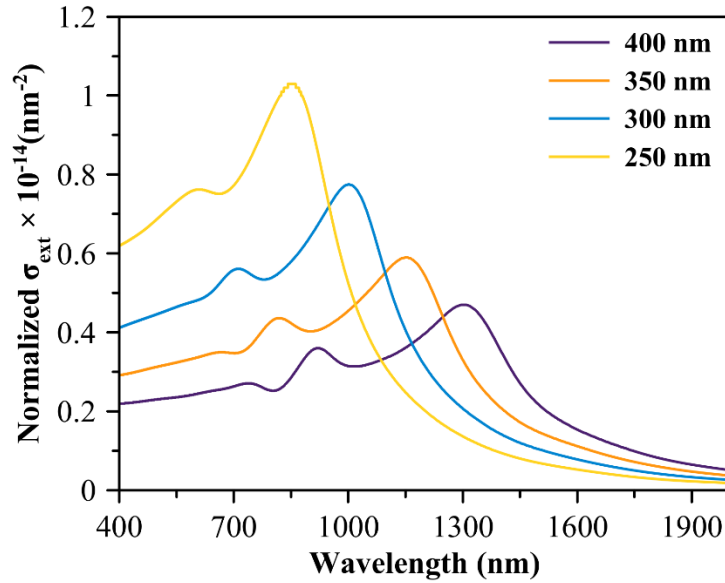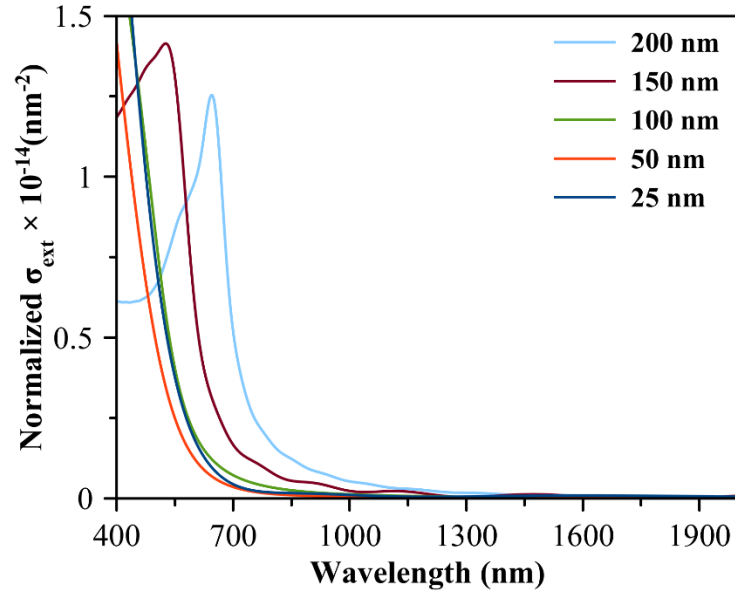of 250 to 400 nm as a function of incident light wavelength. Normalized-σ_{Ext} = Ratio of extinction cross section (σ_{Ext}) to the volume of the nanosphere

112
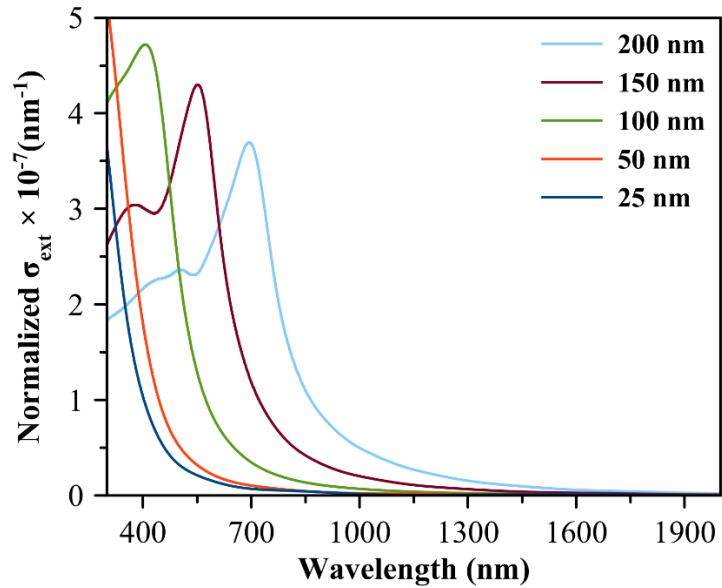
Figure A.S2 (c) FDTD-simulated normalized-extinction (normalized-σ_{Ext}) cross section of Cu_2O nanocubes of different edge lengths in the range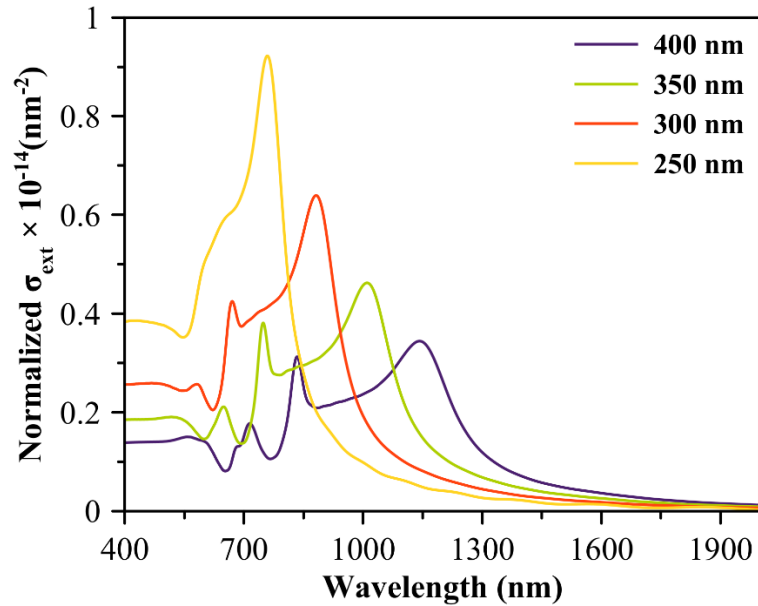 of 25 to 200 nm as a function of incident light wavelength. Normalized-σ_{Ext} = Ratio of extinction cross section (σ_{Ext}) to the volume of the nanocube.
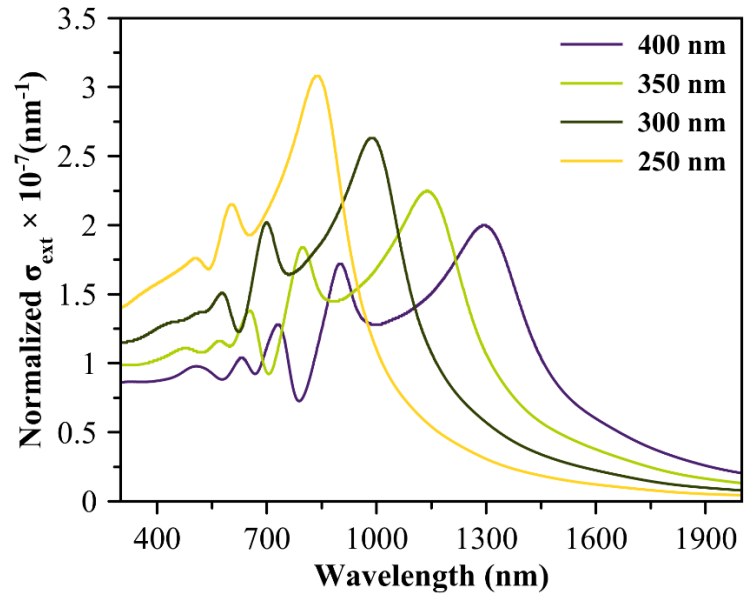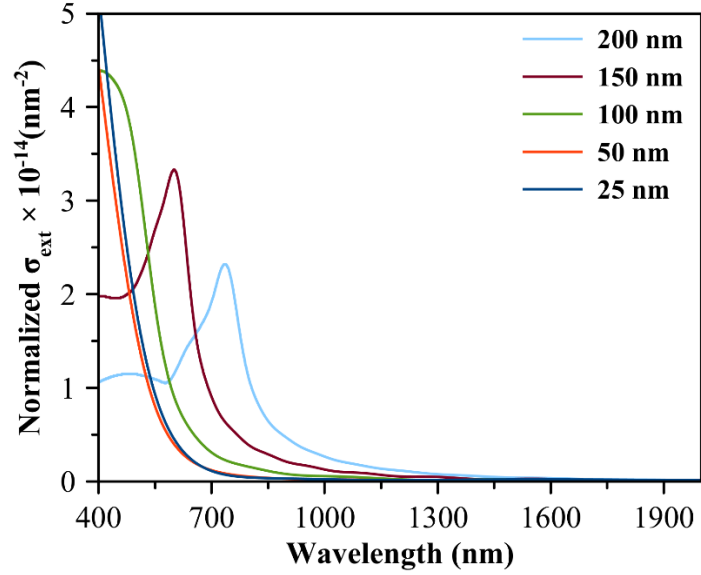
Figure A.S2 (d) FDTD-simulated normalized-extinction (normalized-σ_{Ext}) cross section of Cu_2O nanocubes of different edge lengths in the range of 250 to 400 nm as a function of incident light wavelength. Normalized-σ_{Ext} = Ratio of extinction cross section (σ_{Ext}) to the volume of the nanocube.
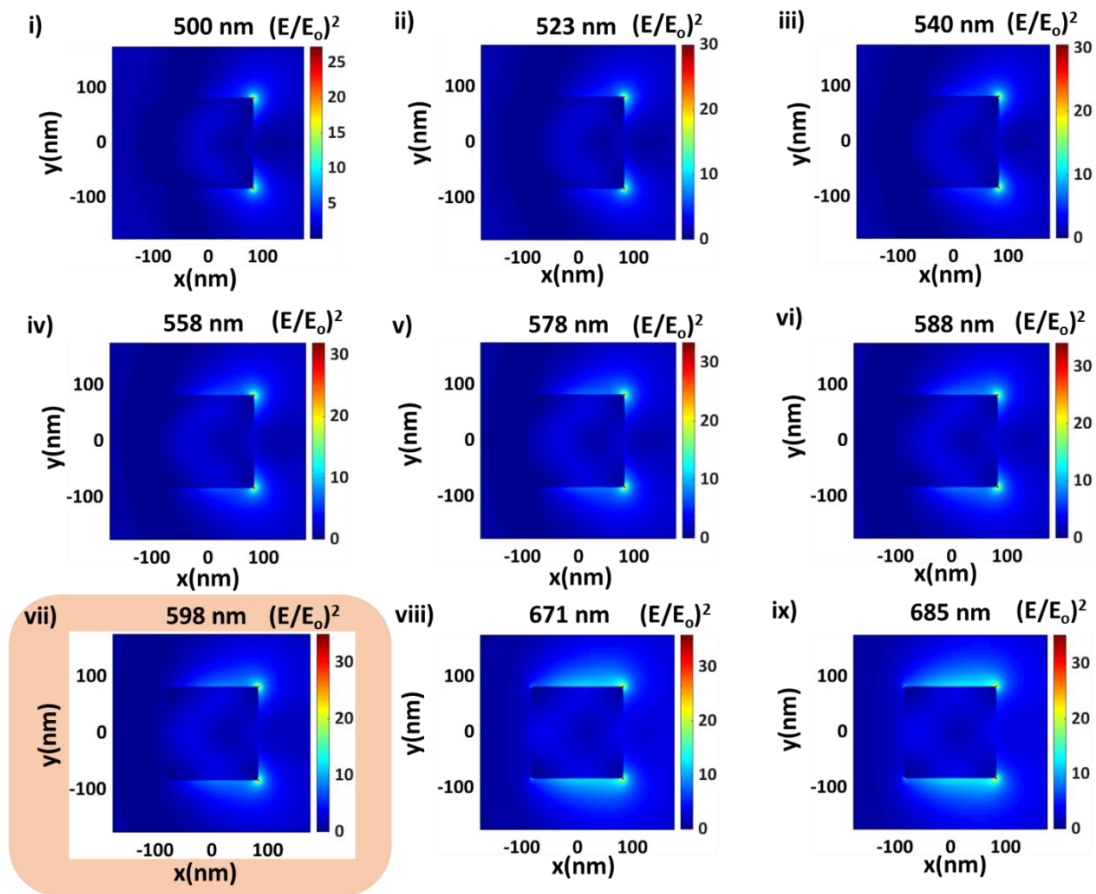
Figure A.S2 (e) i. Simulated spatial distribution of enhancement in electric field intensity $[E^2/E_0^2]$ in XY plane at different wavelengths across the Mie resonance peak wavelength (i.e., **598 nm**) for Cu_2O nanocubes with an edge length of 165 nm.
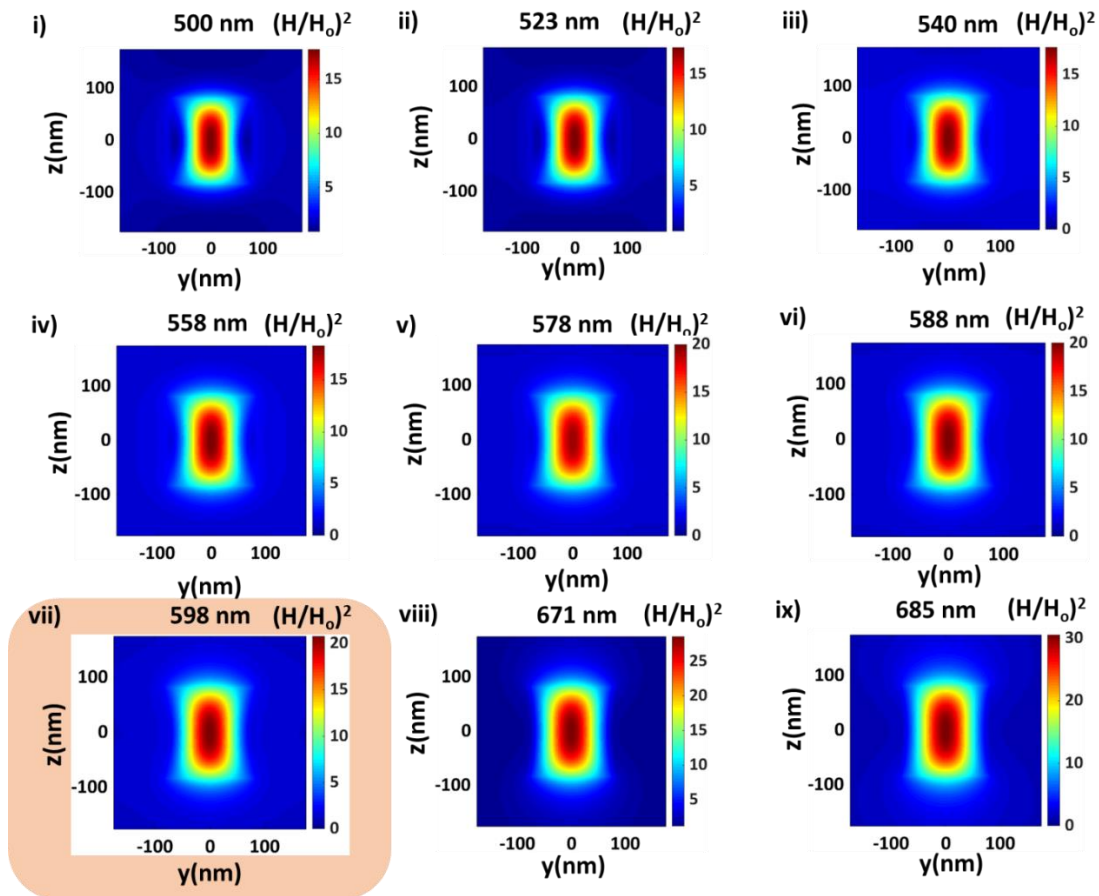
Figure A.S2 (e) ii. Simulated spatial distribution of enhancement in magnetic field intensity $[H^2/H_0^2]$ in YZ plane at different wavelengths across the Mie resonance peak wavelength (i.e., **598 nm**) for Cu_2O nanocubes with an edge length of 165 nm.
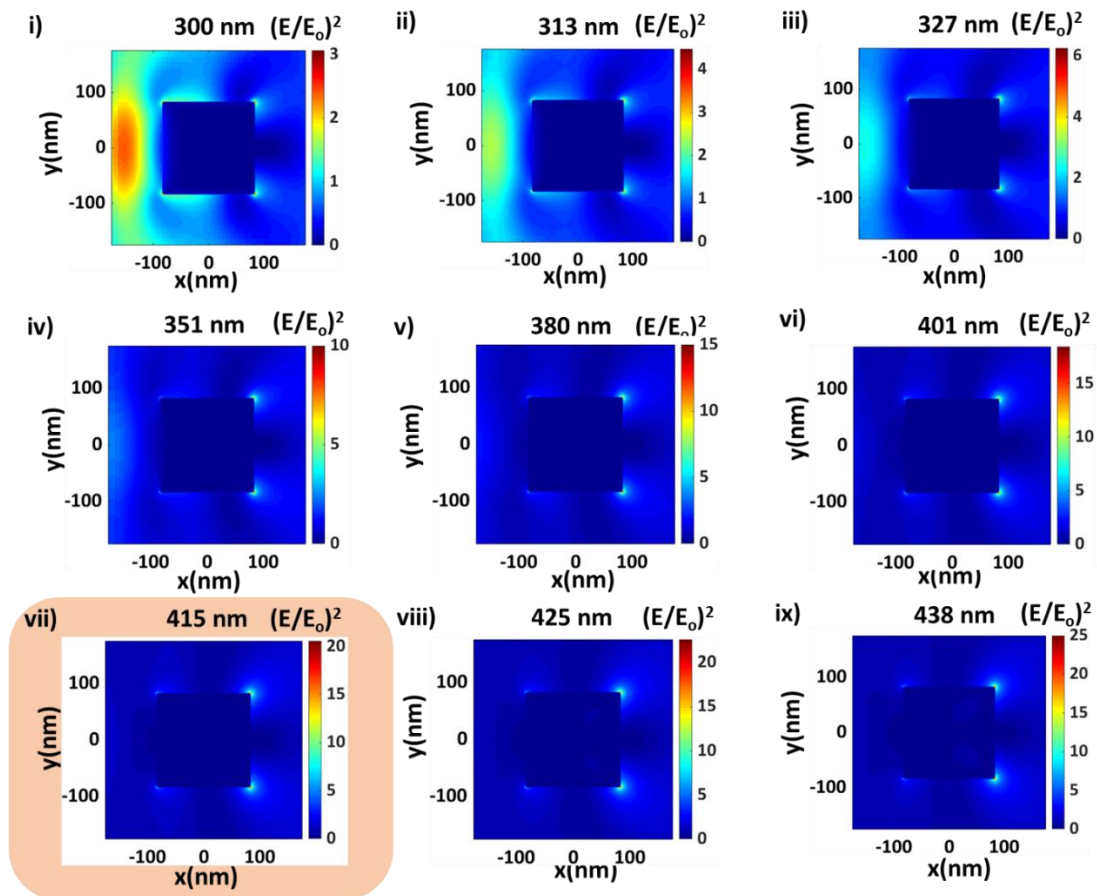
Figure A.S2 (f) i. Simulated spatial distribution of enhancement in electric field intensity [E^2/E_0^2] in XY plane at different wavelengths across the Mie resonance peak wavelength (i.e., **415 nm**) for Cu_2O nanocubes with an edge length of 165 nm.
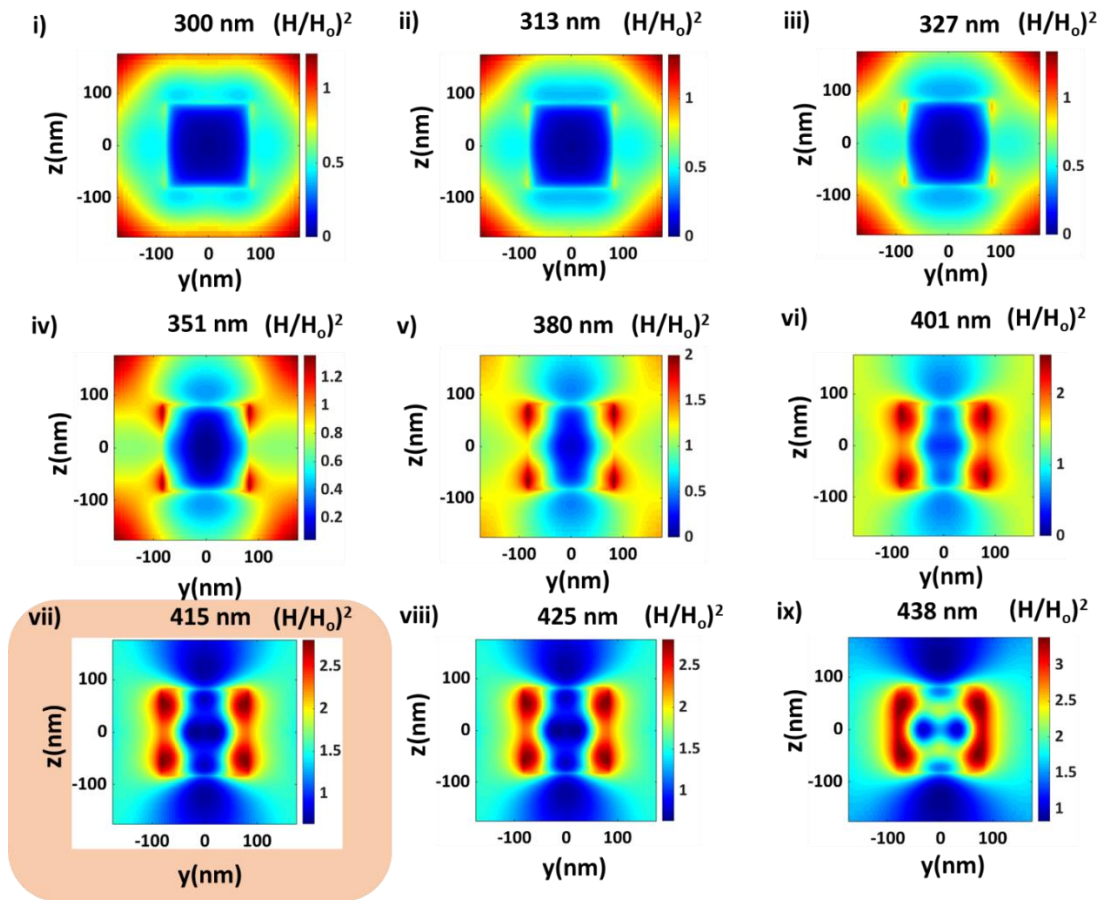
Figure A.S2 (f) ii. Simulated spatial distribution of enhancement in magnetic field intensity $[H^2/H_0^2]$ in YZ plane at different wavelengths across the Mie resonance peak wavelength (i.e., **415 nm**) for Cu_2O nanocubes with an edge length of 165 nm.
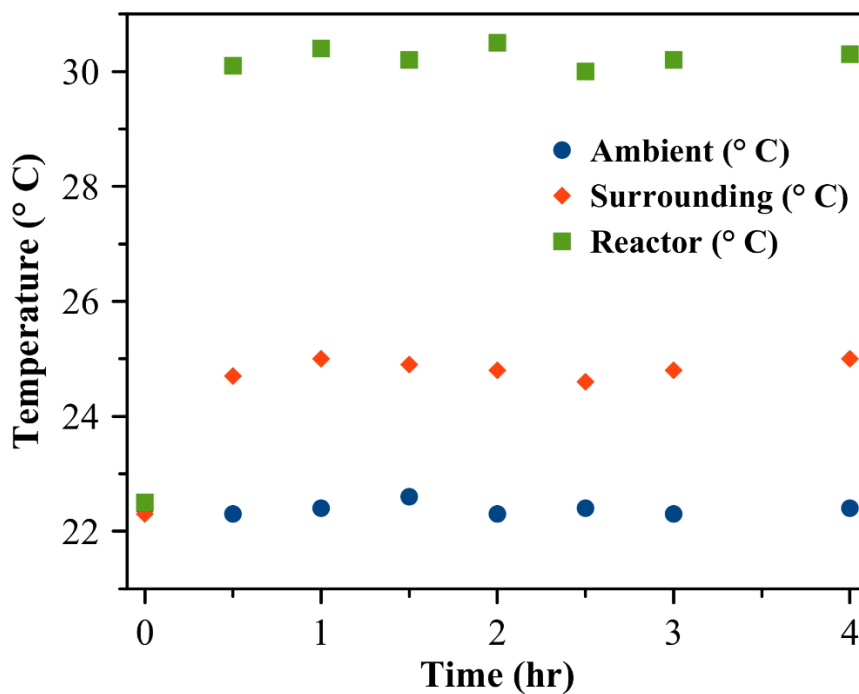
Figure A.S3(a). Temperature profile measured as a function of irradiation time for MB DSD in DMF using quasi-spherical Cu_2O nanoparticles of 37 ± 6 nm diameter.
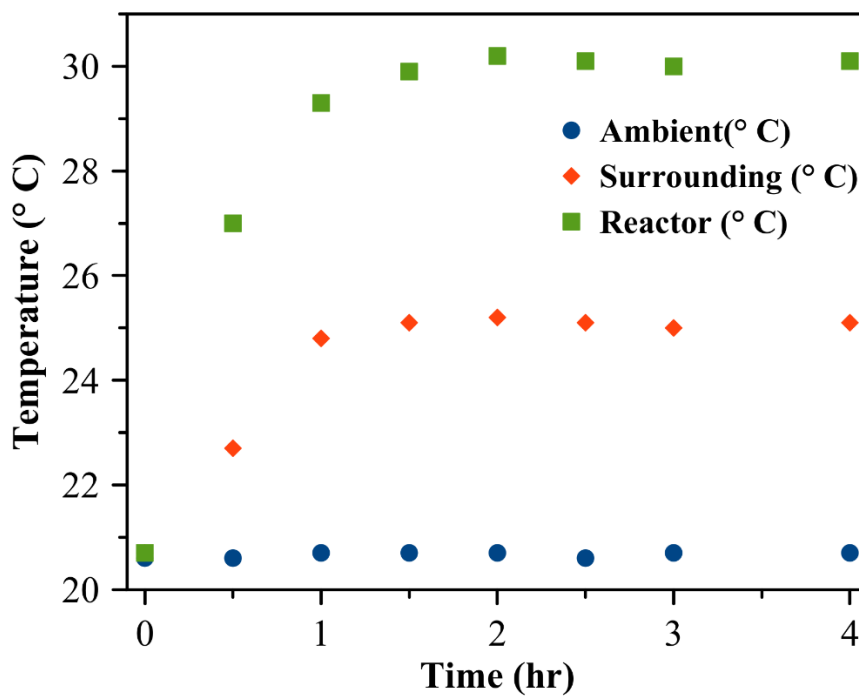
Figure A.S3(b). Temperature profile measured as a function of irradiation time for MB DSD in DMF using quasi-spherical Cu_2O nanoparticles of 145 ± 41 nm diameter.
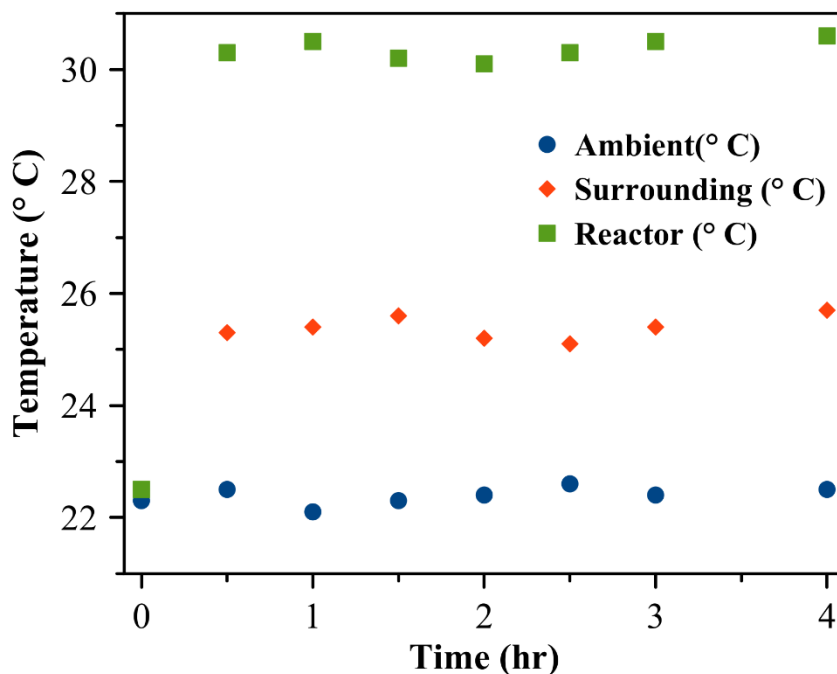
Figure A.S3(c). Temperature profile measured as a function of irradiation time for MB DSD in DMF using Cu_2O nanocubes of 165 ± 26 nm edge length.
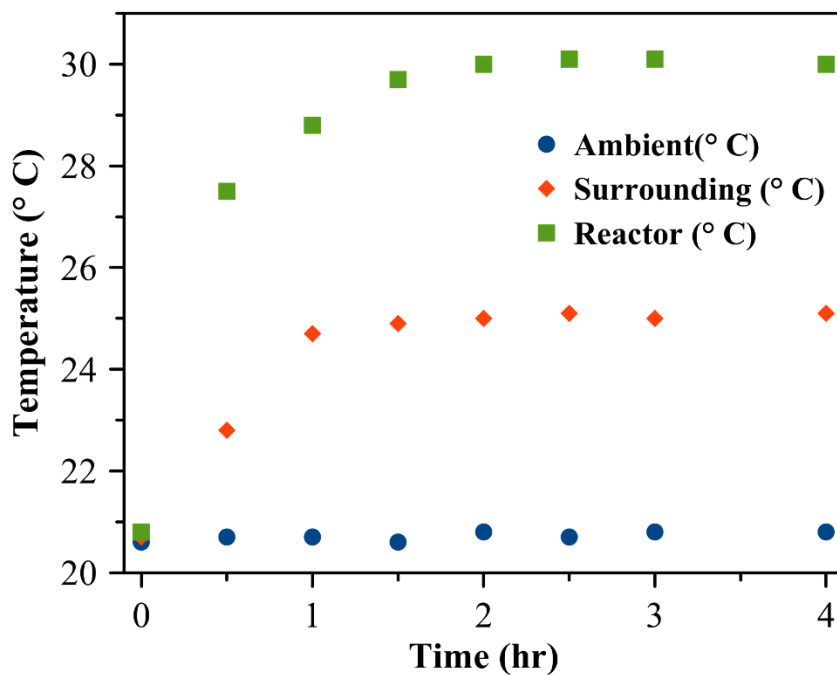
Figure A.S3(d). Temperature profile measured as a function of irradiation time for MB DSD in DMF using Cu_2O nanocubes of 325 ± 37 nm edge length.
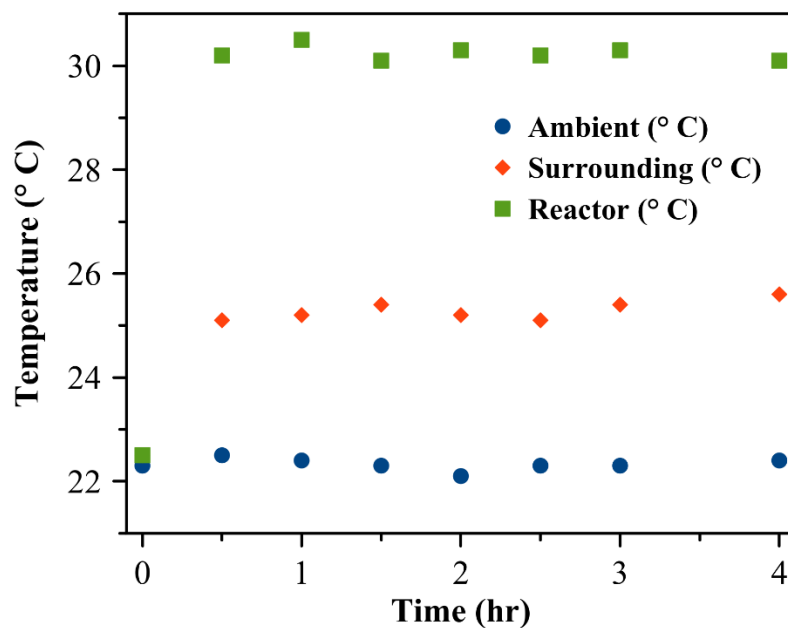
Figure A.S3(e). Temperature profile measured as a function of irradiation time for MB DSD in DMF under blank conditions in the absence of photocatalyst.
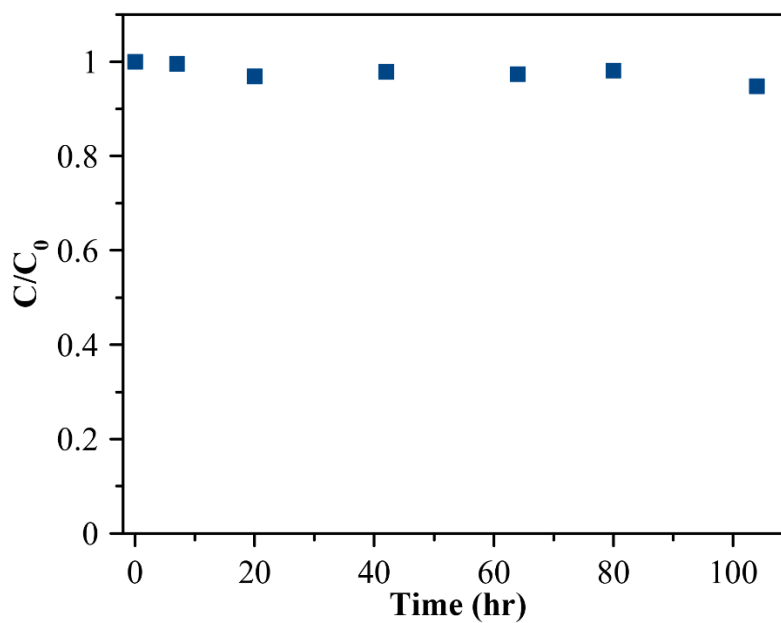
Figure A.S3(f). Plot of C/C_0 of methylene blue versus reaction time measured during heating experiments at 60 °C in the presence of large Cu_2O cubes for MB DSD under dark conditions in the absence of red-light irradiation.
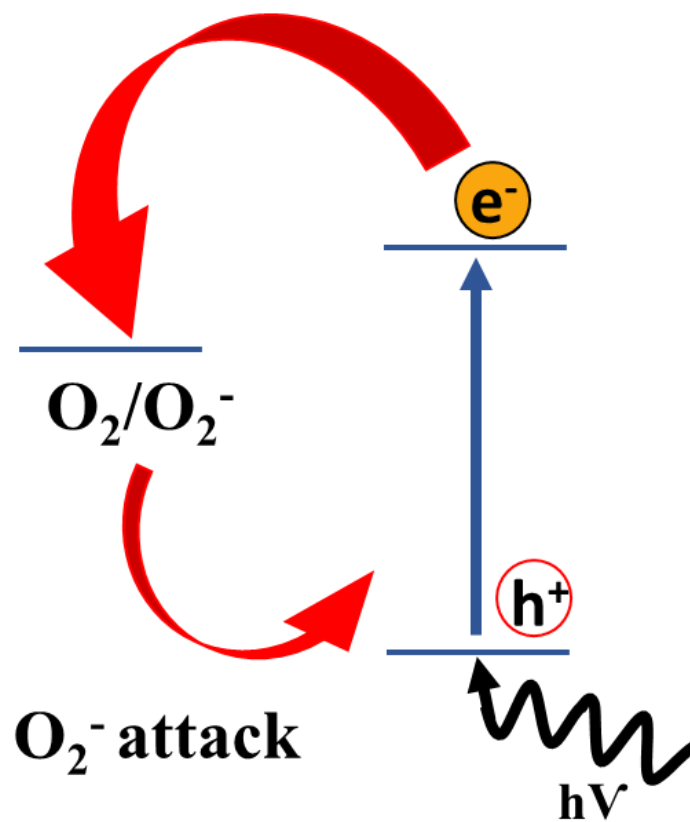
Figure A.S4 (a) Schematic diagram of dye-only dye degradation pathway. Dissolved oxygen in the solvent can capture the excited electron from the dye to form superoxide (O_2^-) radical, which can attack the dye and degrade it. (Reference: Rochkind, M.; Pasternak, S.; Paz, Y. Using Dyes for Evaluating Photocatalytic Properties: A Critical Review. Molecules 2015, 20 (1), 88–110)
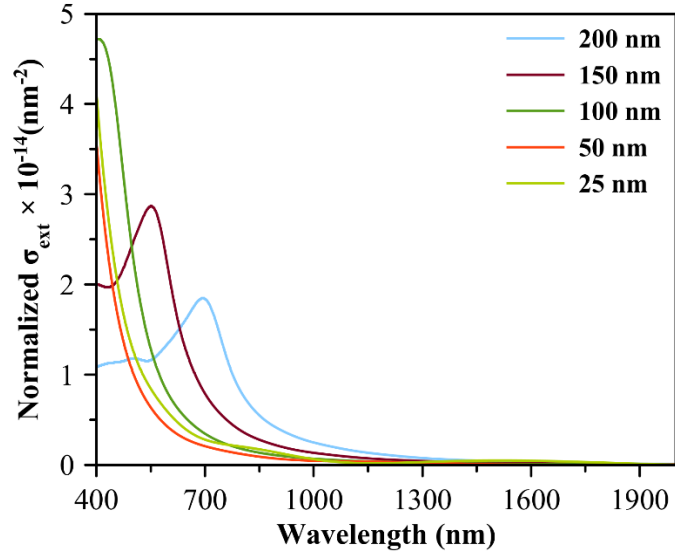
Figure A.S4 (b) FDTD-simulated normalized-extinction (normalized-σ_{Ext}) cross section of Cu_2O nanocubes of different edge lengths in the range of 25 to 200 nm as a function of incident light wavelength.
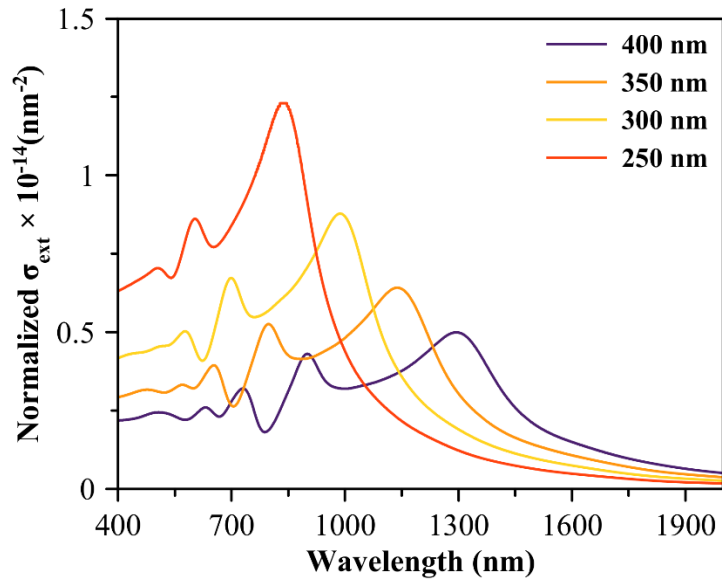
Figure A.S4 (c) FDTD-simulated normalized-extinction (normalized-σ_{Ext}) cross section of Cu_2O nanocubes of different edge lengths in the range of 250 to 400 nm as a function of incident light wavelength.
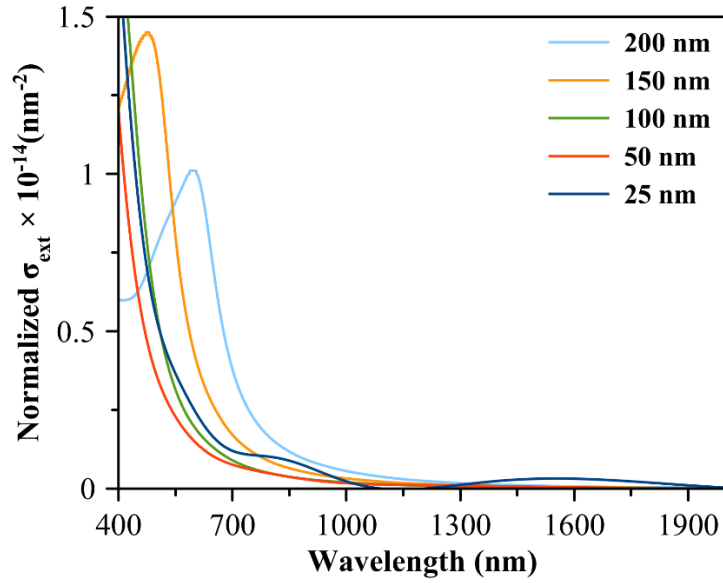
Figure A.S4 (d) FDTD-simulated normalized-extinction (normalized-σ_{Ext}) cross section of Cu_2O nanospheres of different edge lengths in the range of 25 to 200 nm as a function of incident light wavelength
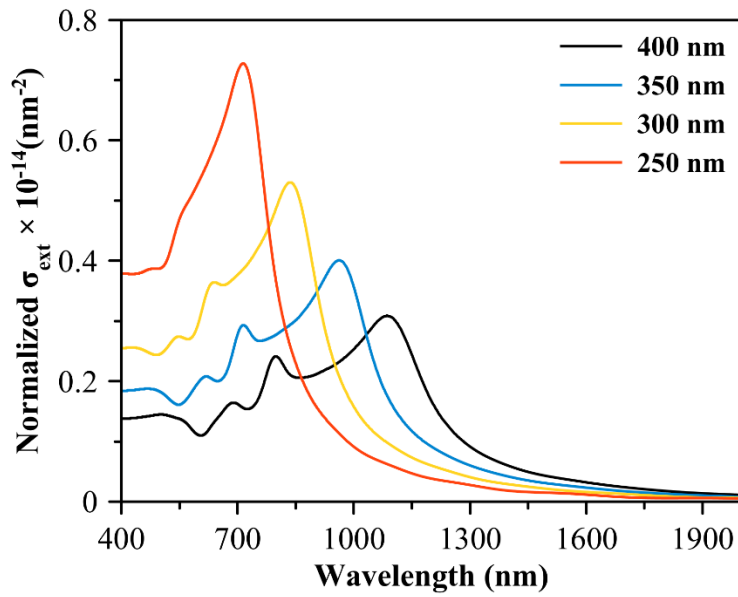
Figure A.S4 (e) FDTD-simulated normalized-extinction (normalized-σ_{Ext}) cross section of Cu_2O nanospheres of different edge lengths in the range of 250 to 400 nm as a function of incident light wavelength.
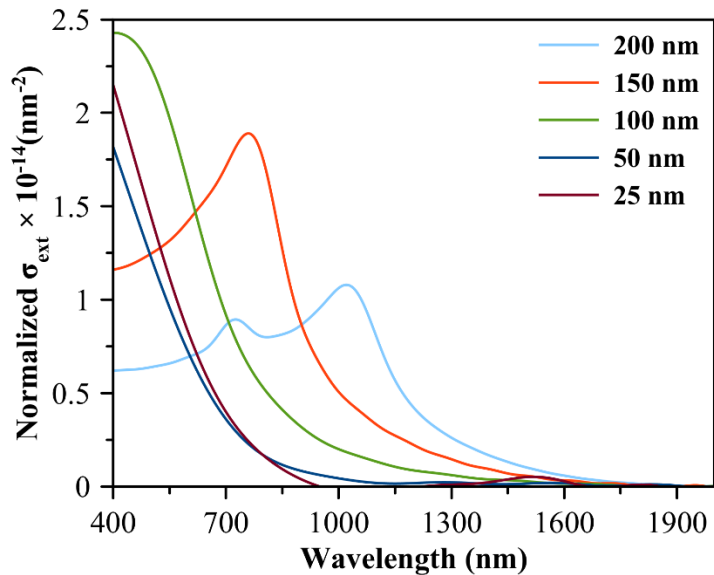
Figure A.S4 (f) FDTD-simulated normalized-extinction (normalized-σ_{Ext}) cross section of CeO$_2$ nanospheres of different diameter in the range of 25 to 200 nm as a function of incident light wavelength.
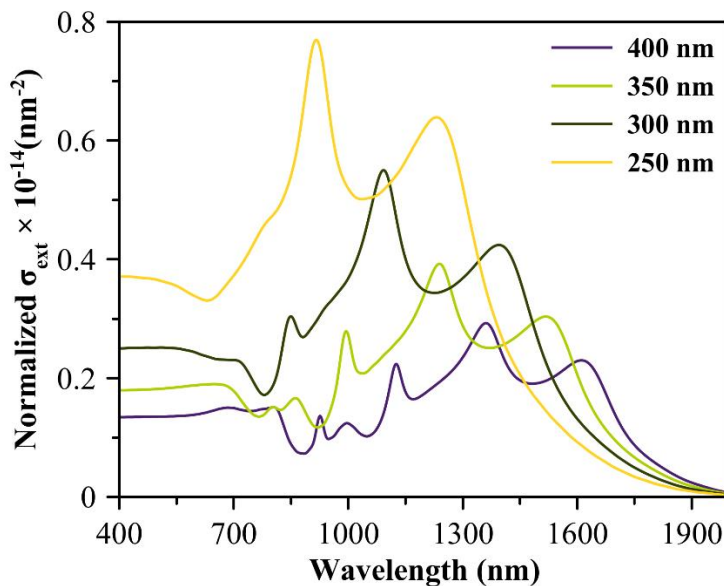
Figure A.S4 (g) FDTD-simulated normalized-extinction (normalized-σ_{Ext}) cross section of CeO$_2$ nanospheres of different diameter in the range of 250 to 400 nm as a function of incident light wavelength.
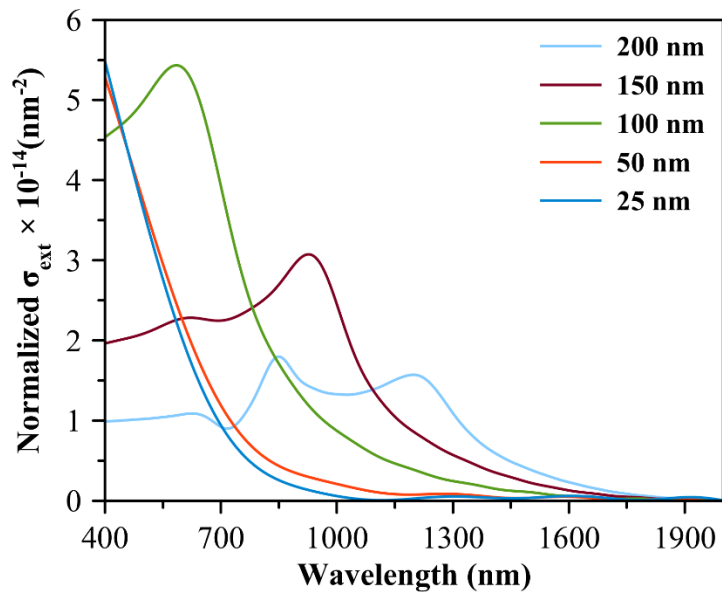
Figure A.S4 (h) FDTD-simulated normalized-extinction (normalized-σ_{Ext}) cross section of CeO$_2$ nanocubes of different edge length in the range of 25 to 200 nm as a function of incident light wavelength.
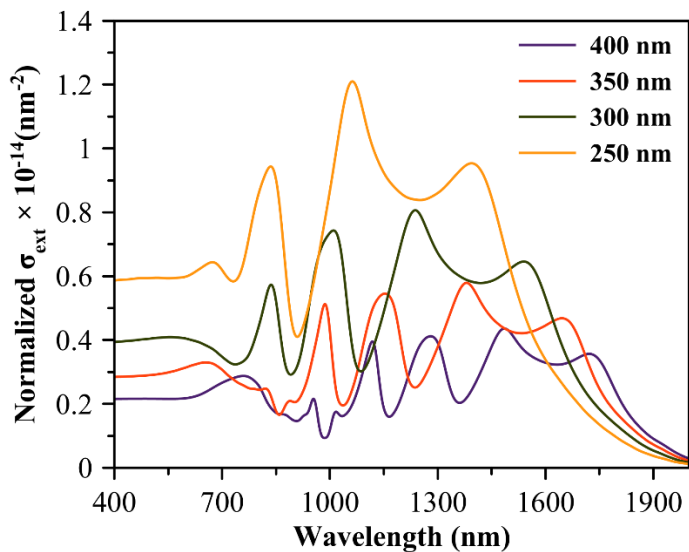
Figure A.S4 (i) FDTD-simulated normalized-extinction (normalized-σ_{Ext}) cross section of CeO$_2$ nanocubes of different edge length in the range of 250 to 400 nm as a function of incident light wavelength.
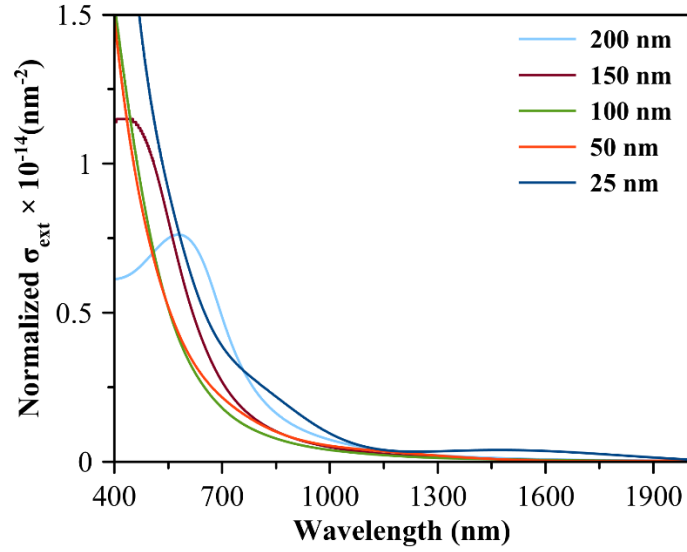
Figure A.S4 (j) FDTD-simulated normalized-extinction (normalized-σ_{Ext}) cross section of CuO nanospheres of different diameter in the range of 25 to 200 nm as a function of incident light wavelength.
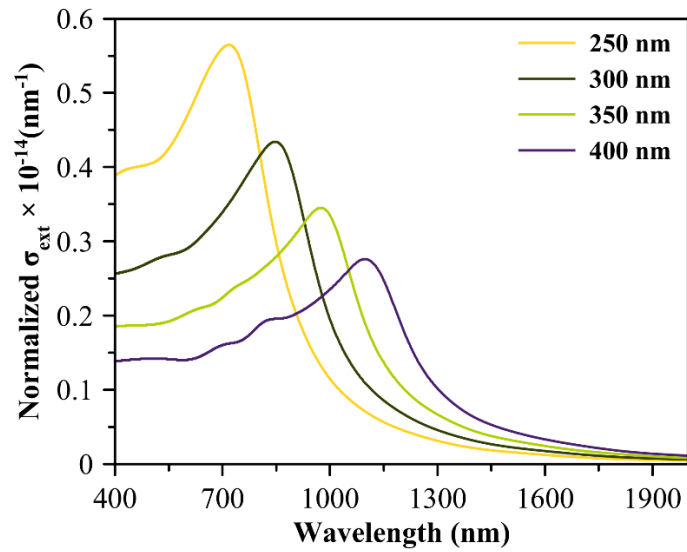
Figure A.S4 (k) FDTD-simulated normalized-extinction (normalized-σ_{Ext}) cross section of CuO nanospheres of different diameter in the range of 250 to 400 nm as a function of incident light wavelength.
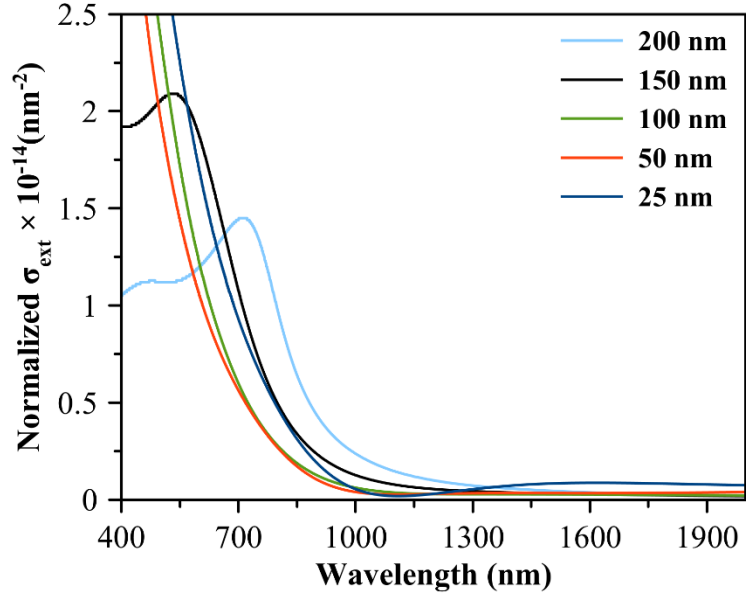
Figure A.S4 (l) FDTD-simulated normalized-extinction (normalized-σ_{Ext}) cross section of CuO nanocubes of different edge length in the range of 25 to 200 nm as a function of incident light wavelength.

Figure A.S4 (m) FDTD-simulated normalized-extinction (normalized-σ_{Ext}) cross section of CuO nanocubes of different edge length in the range of 250 to 400 nm as a function of incident light wavelength.

Figure A.S4 (n) FDTD-simulated normalized-extinction (normalized-σ_{Ext}) cross section of α-Fe$_2$O$_3$ nanospheres of different diameter in the range of 25 to 200 nm as a function of incident light wavelength.

Figure A.S4 (o) FDTD-simulated normalized-extinction (normalized-σ_{Ext}) cross section of α-Fe$_2$O$_3$ nanospheres of different diameter in the range of 250 to 400 nm as a function of incident light wavelength.

Figure A.S4 (p) FDTD-simulated normalized-extinction (normalized-σ_{Ext}) cross section of α-Fe$_2$O$_3$ nanocubes of different edge length in the range of 25 to 200 nm as a function of incident light wavelength.
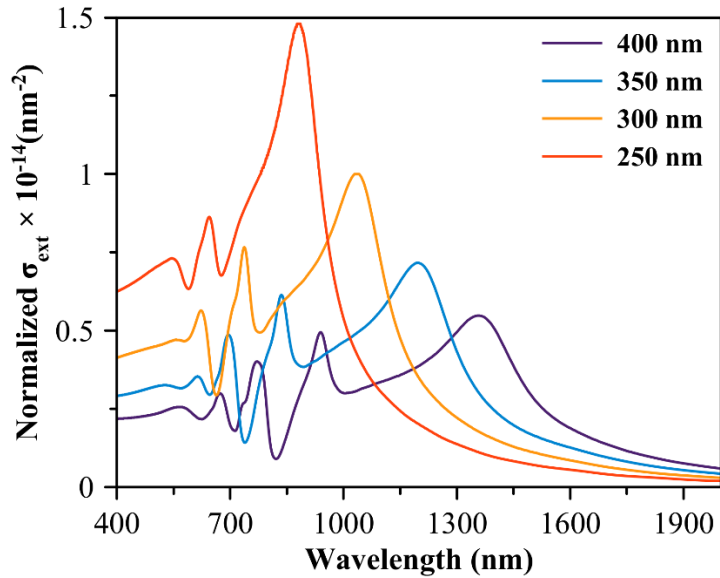
Figure A.S4 (q) FDTD-simulated normalized-extinction (normalized-σ_{Ext}) cross section of α-Fe$_2$O$_3$ nanocubes of different edge length in the range of 250 to 400 nm as a function of incident light wavelength.
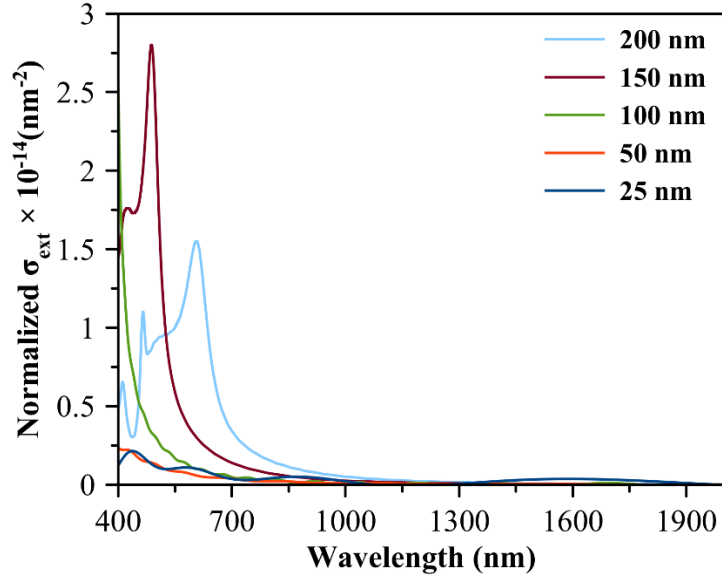
Figure A.S4 (r) FDTD-simulated normalized-extinction (normalized-σ_{Ext}) cross section of TiO$_2$ nanospheres of different diameter in the range of 25 to 200 nm as a function of incident light wavelength.
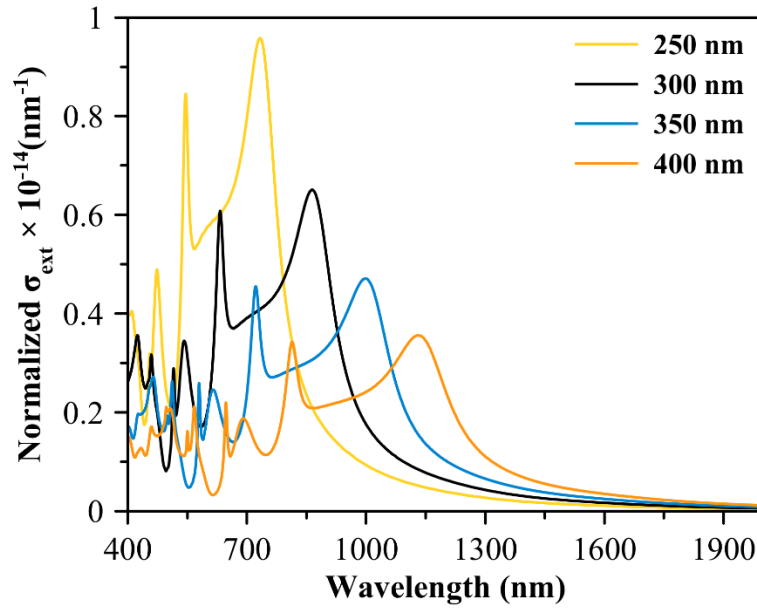
Figure A.S4 (s) FDTD-simulated normalized-extinction (normalized-σ_{Ext}) cross section of TiO$_2$ nanospheres of different diameter in the range of 250 to 400 nm as a function of incident light wavelength.
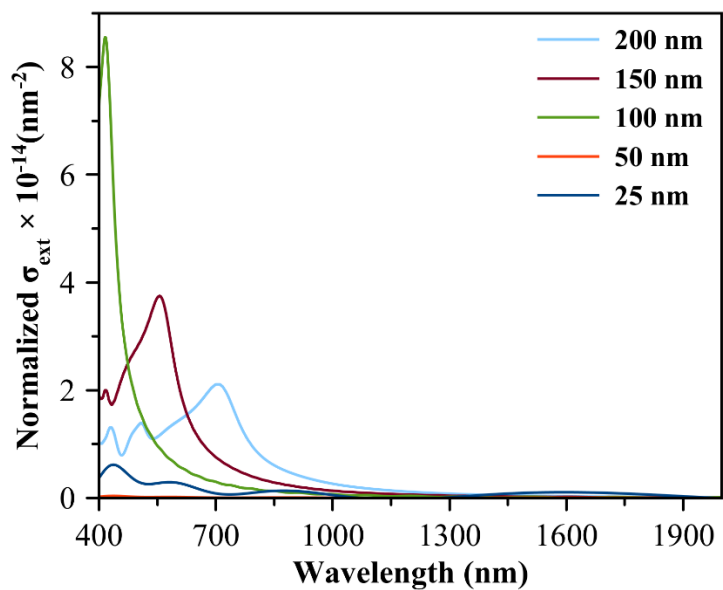
Figure A.S4 (t) FDTD-simulated normalized-extinction (normalized-σ_{Ext}) cross section of TiO$_2$ nanocubes of different edge length in the range of 25 to 200 nm as a function of incident light wavelength.
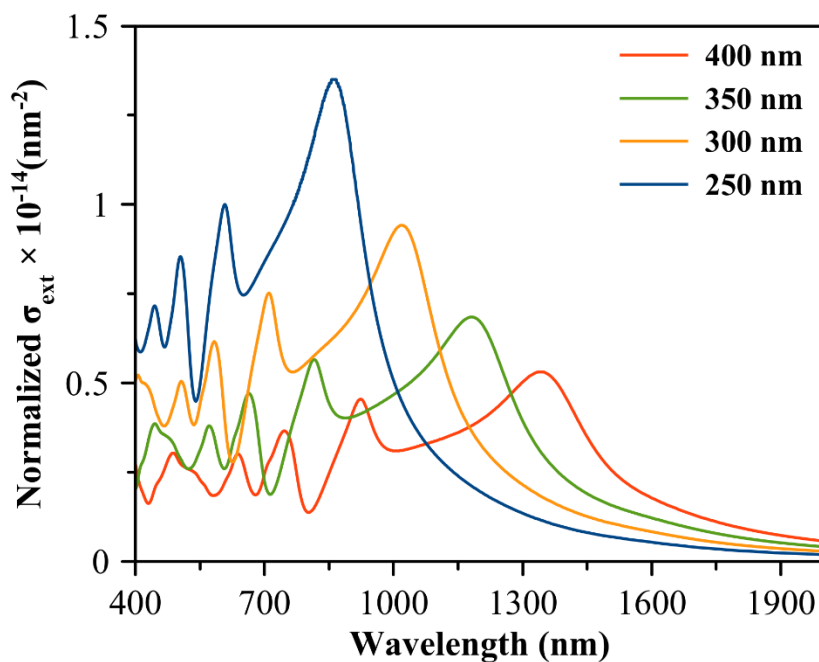
Figure A.S4 (u) FDTD-simulated normalized-extinction (normalized-σ_{Ext}) cross section of TiO$_2$ nanocubes of different edge length in the range of 250 to 400 nm as a function of incident light wavelength.
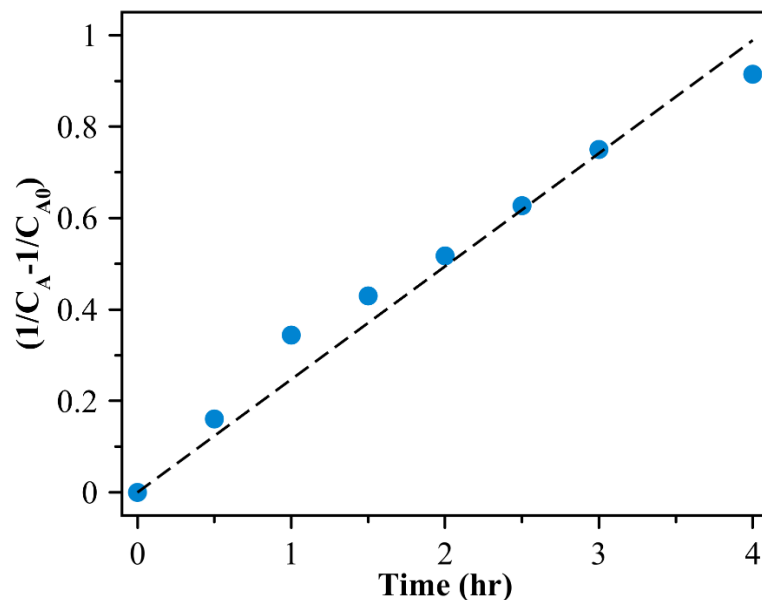
Figure A.S4 (v) Plot of Empirical fit with second order $(1/C_A - 1/C_{A0})$ versus irradiation time for MB DSD in DMF, using quasi-spherical Cu_2O nanoparticles of 37 ± 6 nm diameter and corresponding trendline and proportion of the variance.
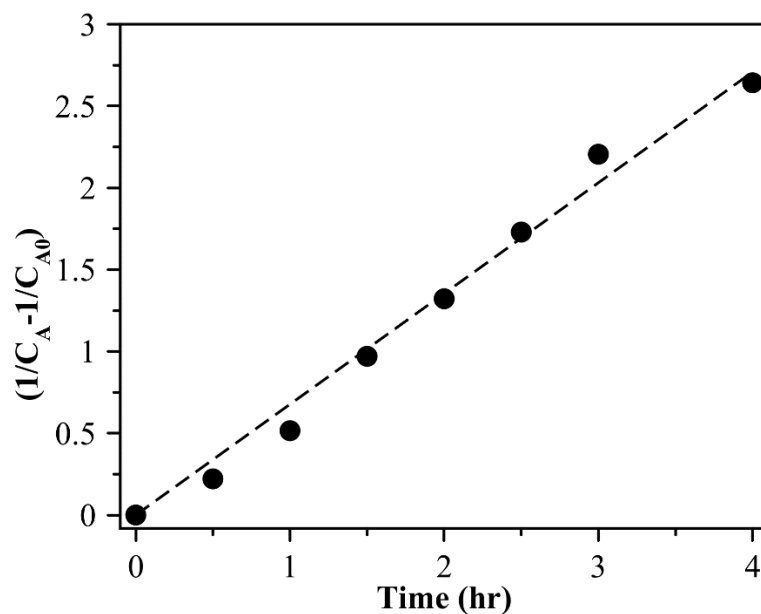
Figure A.S4 (w) Plot of Empirical fit with second order $(1/C_A - 1/C_{A0})$ versus irradiation time for MB DSD in DMF, using quasi-spherical Cu_2O nanoparticles of 145 ± 41 nm diameter and corresponding trendline and proportion of the variance.
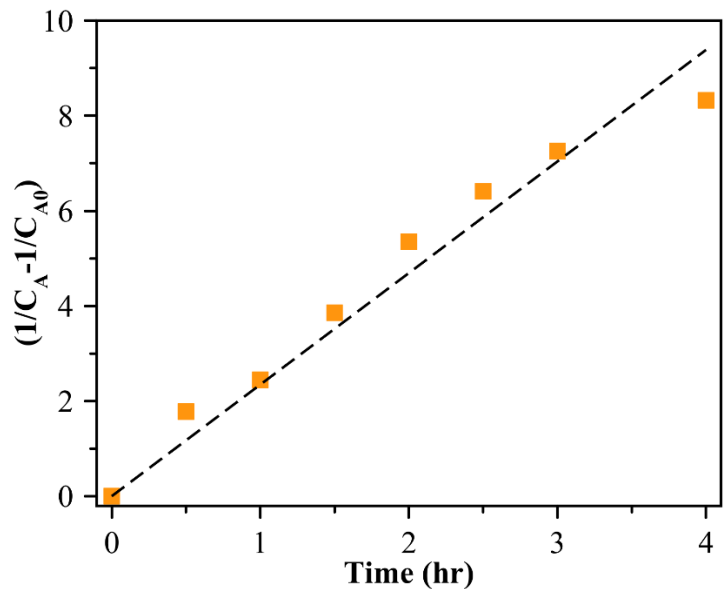
Figure A.S4 (x) Plot of Empirical fit with second order $(1/C_A - 1/C_{A0})$ versus irradiation time for MB DSD in DMF, using Cu_2O nanocubes of 165 ± 26 nm edge length and corresponding trendline and proportion of the variance.
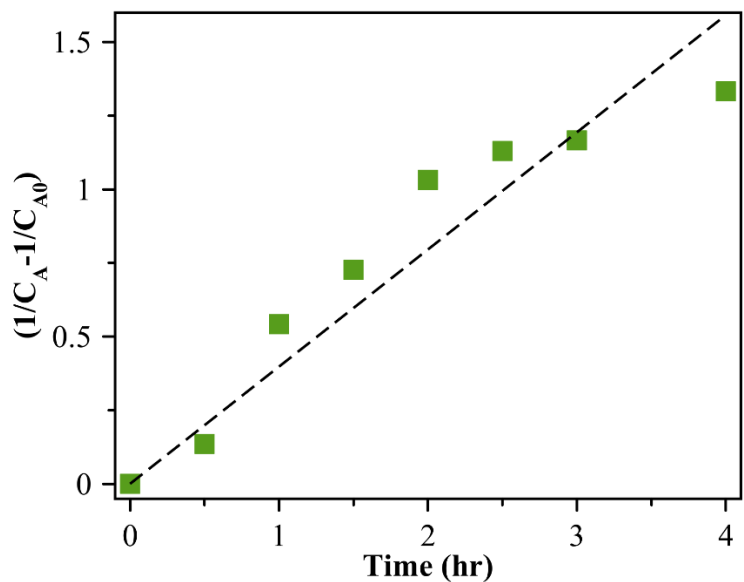
Figure A.S4 (y) Plot of Empirical fit with second order $(1/C_A - 1/C_{A0})$ versus irradiation time for MB DSD in DMF, using Cu_2O nanocubes of 325 ± 37 nm edge length and corresponding trendline and proportion of the variance.
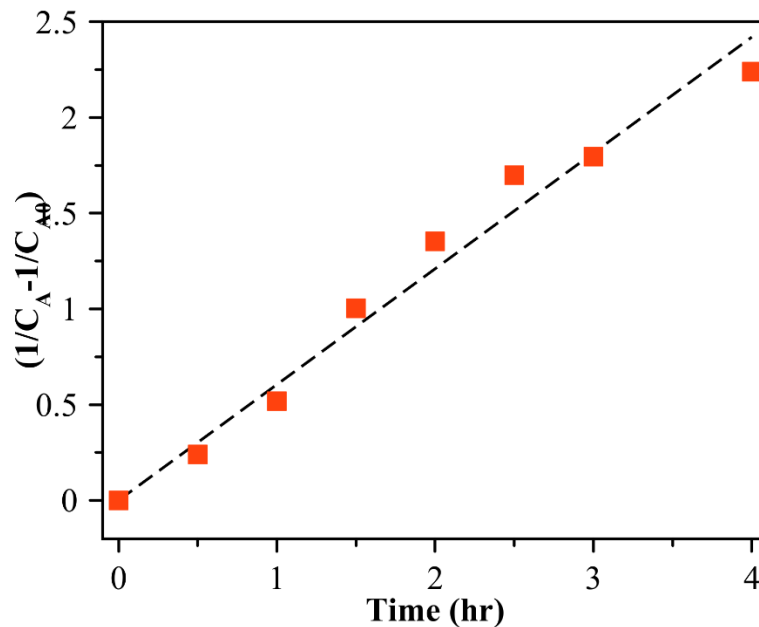
Figure A.S4 (z) Plot of Empirical fit with second order ($1/C_A - 1/C_{A0}$) versus irradiation time for MB DSD in DMF, using Cu_2O nanocubes of 92 ± 13 nm edge length and corresponding trendline and proportion of the variance.

Table A.S1. Fitted second-order rate constant values obtained from the MB dye-sensitization followed by degradation using Cu_2O nanospheres and nanocubes of different sizes.

Cu_2O Nanostructures	Apparent Rate Constant, kC_{A0} (hr^{-1})
Spheres (37±6 nm)	0.2548±0.0227
Spheres (145±41 nm)	0.637±0.0761
Cubes (92±13 nm)	0.676±0.083
Cubes (165±26 nm)	2.293±0.598
Cubes (325±37 nm)	0.394±0.0253

MIE RESONANCE-ENHANCED PHOTOCATALYSIS
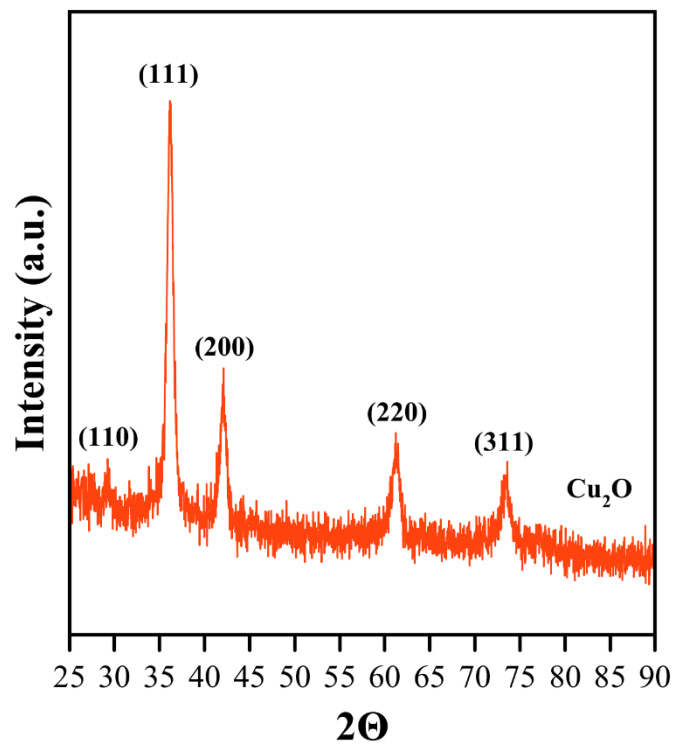
Figure B.S2a. Representative X-ray diffraction pattern of large Cu_2O nanocubes of 286 ± 47 nm edge length synthesized using chemical reduction method.
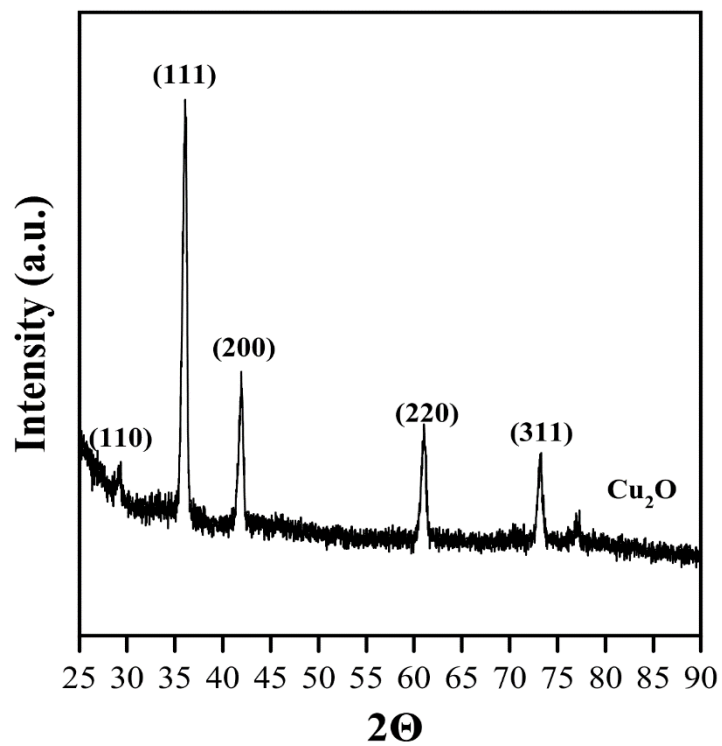
Figure B.S2b. Representative X-ray diffraction pattern of smaller Cu_2O nanospheres of 42 ± 6 nm diameter synthesized using microemulsion method.
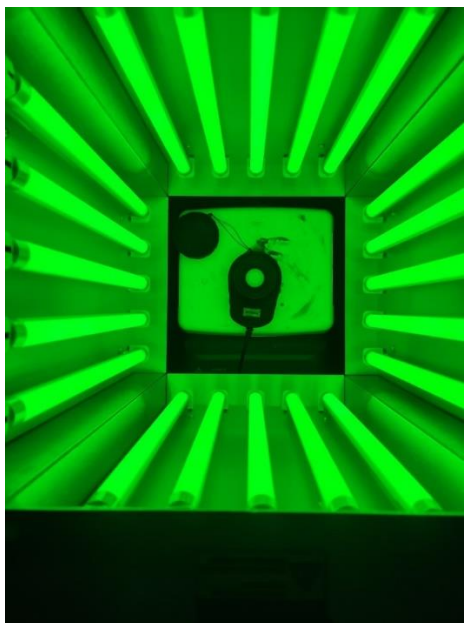
Figure B.S2c. Photoreactor reactor set up of Luzchem Exposure Panels connected with green LED lamps.
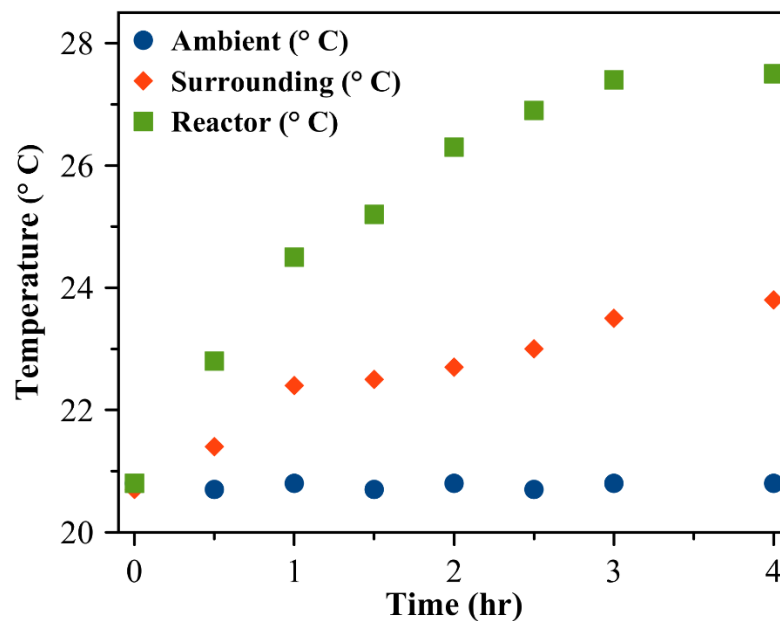
Figure B.S3a. Temperature profile measured as a function of irradiation time during photocatalytic degradation of MB under blank conditions in the absence of photocatalyst. The data represented by green squares, red diamonds, and blue circles show the temperature of the sample in the photoreactor, temperature of the reactor surrounding, and ambient room temperature of the laboratory, respectively.
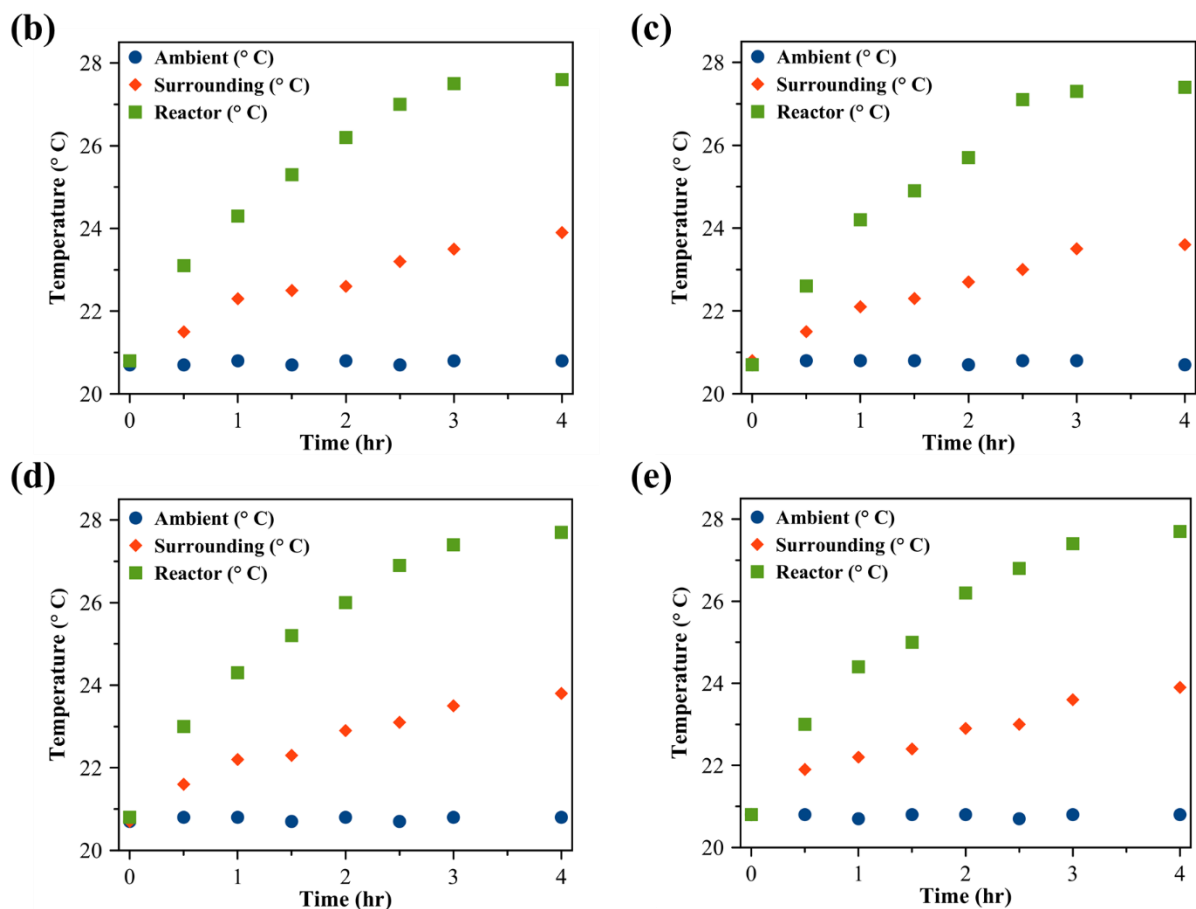
Figure B.S3b-e. Temperature profile measured as a function of irradiation time during photocatalytic degradation of MB for different conditions: (**b**) using Cu_2O nanospheres of 42 ± 6 nm diameter, (**c**) Cu_2O nanocubes of 92 ± 13 nm edge length. (**d**) Cu_2O nanocubes of 286 ± 47 nm edge length. (**e**) using Cu_2O nanospheres of 145 ± 41 nm diameter.
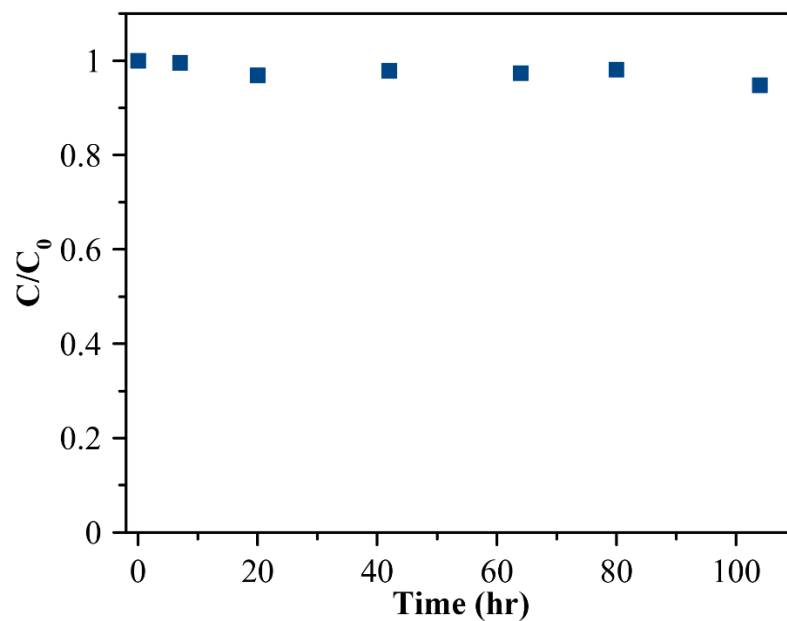
Figure B.S3f. Pot of C/C_0 of methylene blue versus reaction time measured during heating experiments at 60 °C in the presence of large Cu_2O cubes under dark conditions (i.e., in the absence of LED light exposure).
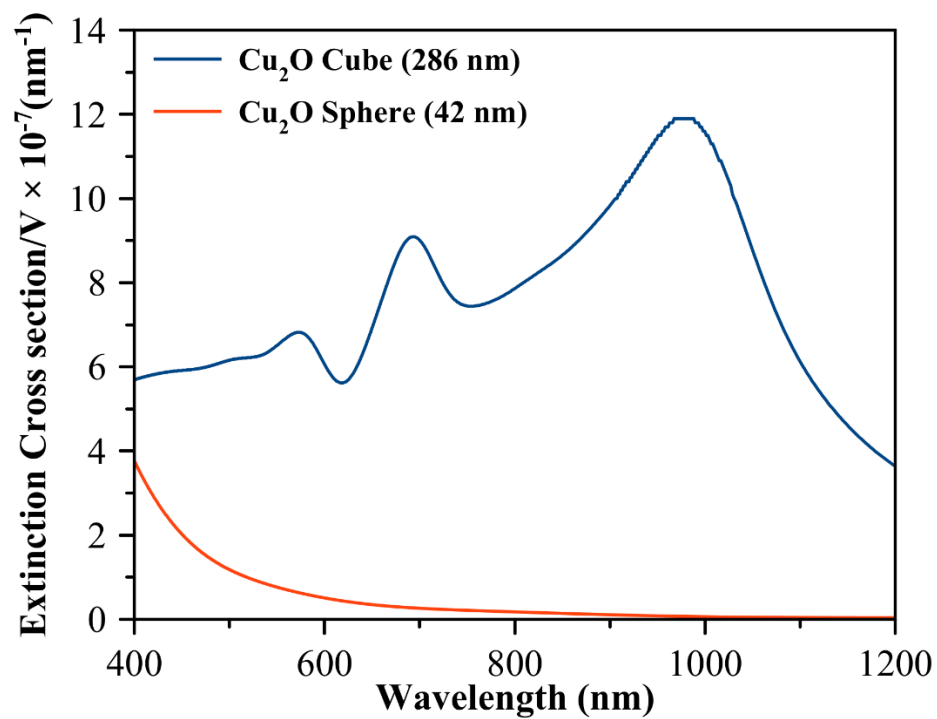
Figure B.S4a. FDTD-simulated volume-normalized extinction cross section of large Cu_2O nanocube of 286 nm edge length and small Cu_2O nanospheres of 42 nm diameter.
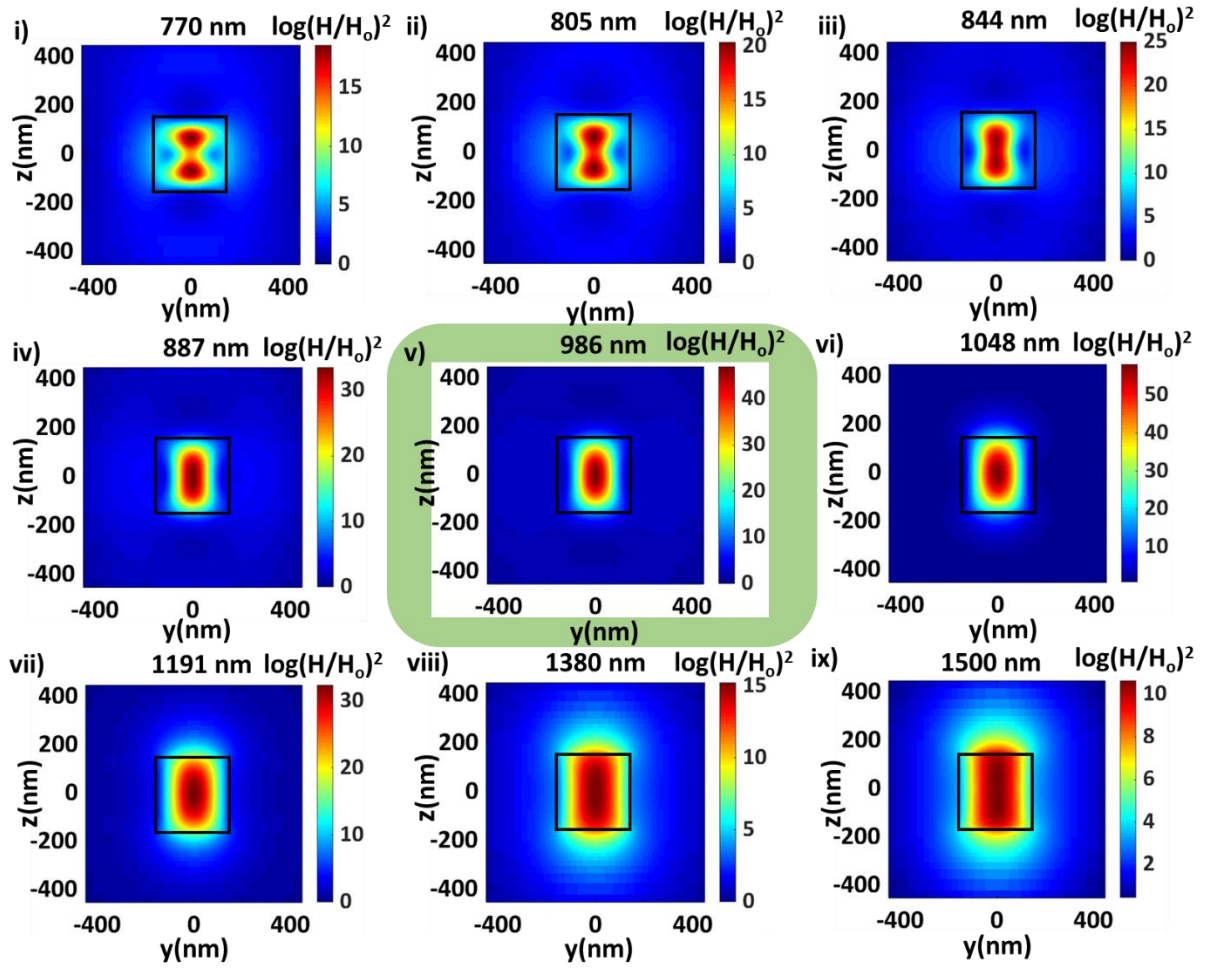
Figure B.S4b (I). FDTD-simulated spatial distribution of enhancement in magnetic field intensity [H^2/H_0^2] in YZ plane at different wavelengths across the lowest energy Mie resonance peak wavelength (i.e., 986 nm) for Cu_2O cube of 286 nm edge length.
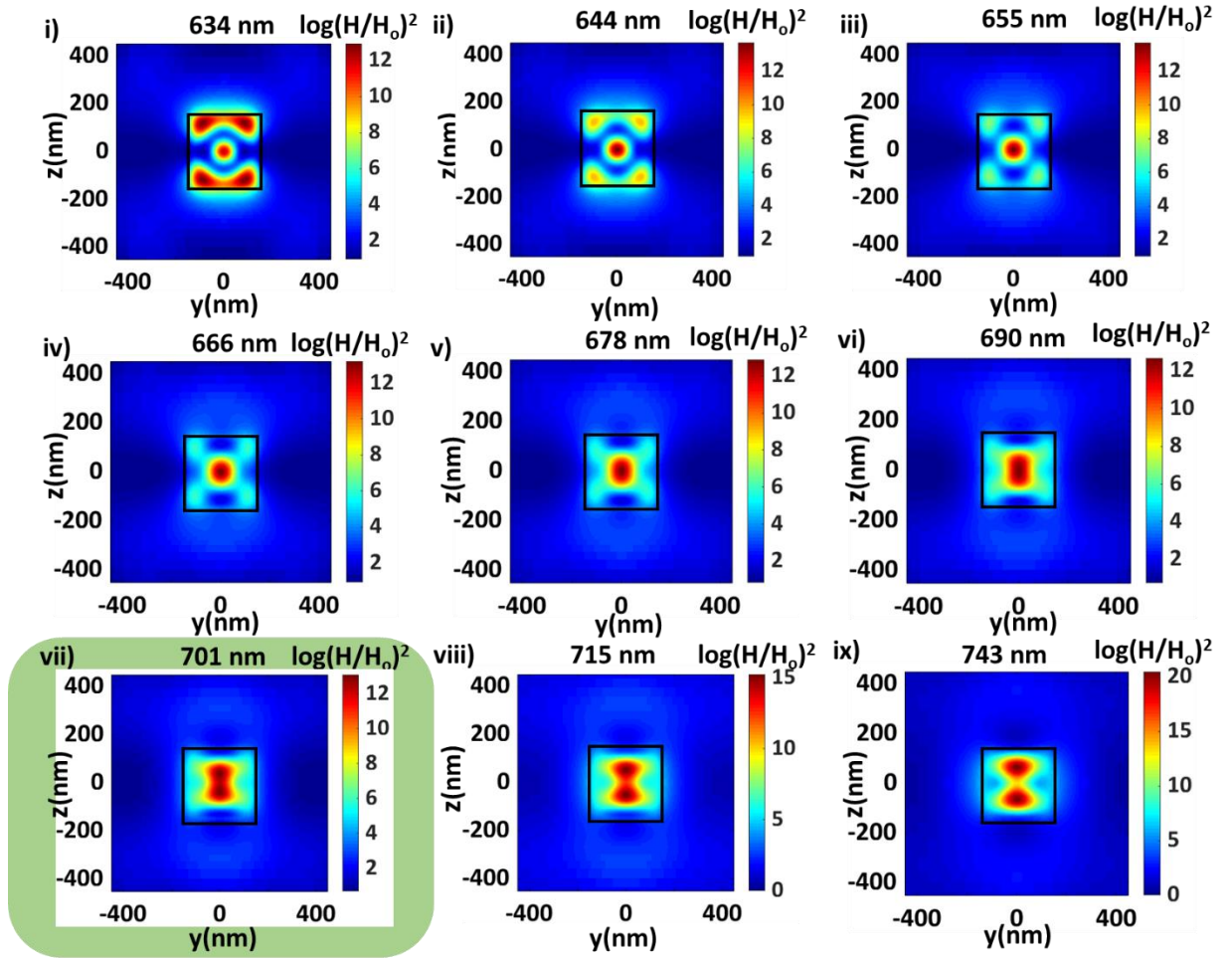
Figure B.S4b (II). FDTD-simulated spatial distribution of enhancement in magnetic field intensity [H^2/H_0^2] in YZ plane at different wavelengths across the second lowest energy Mie resonance peak wavelength (i.e., 701 nm) for Cu_2O cube of 286 nm edge length.
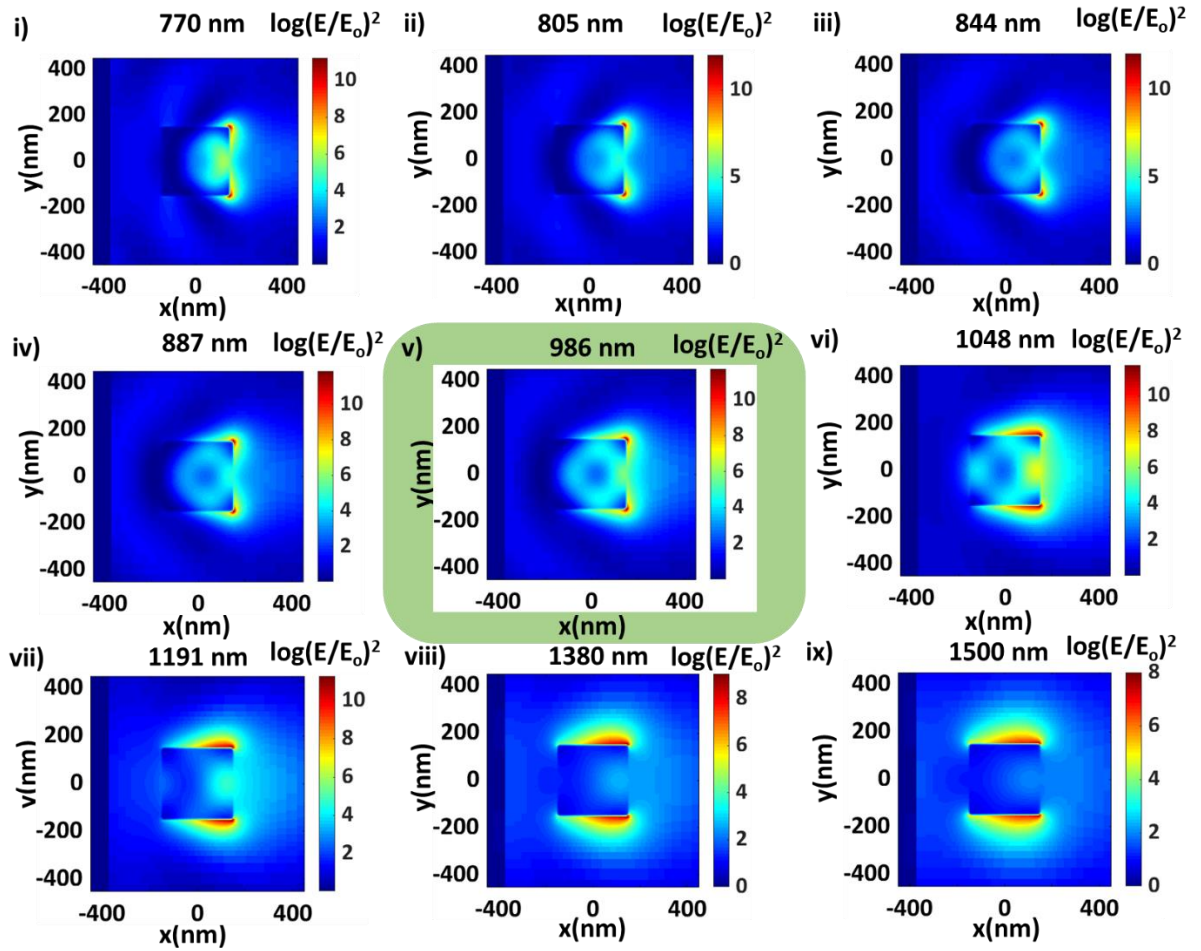
Figure BS4c (I). FDTD-simulated spatial distribution of enhancement in electric field intensity $[E^2/E_0^2]$ in XY plane at different wavelengths across the lowest energy Mie resonance peak wavelength (i.e., 986 nm) for Cu$_2$O cube of 286 nm edge length.
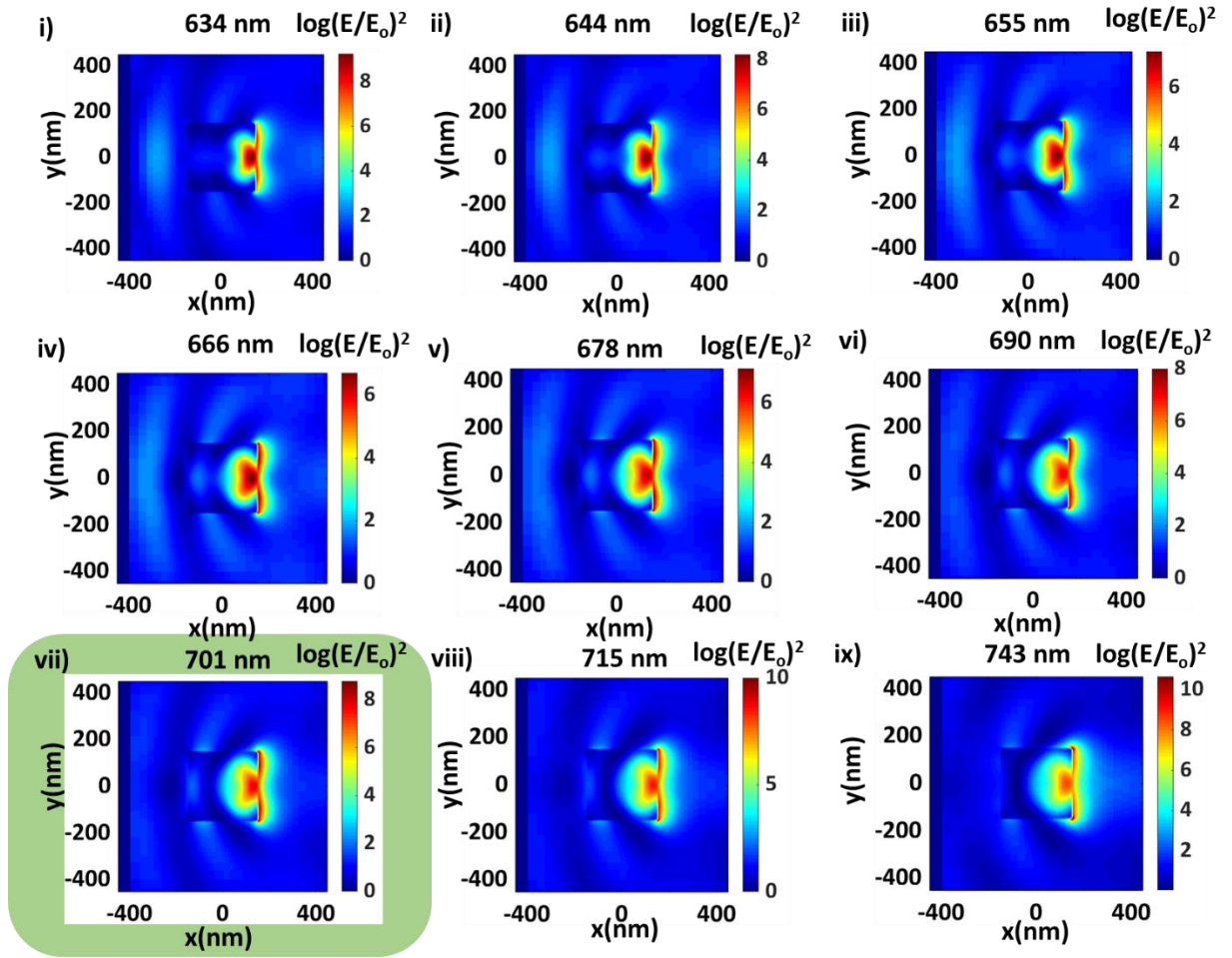
Figure B.S4c (II). FDTD-simulated spatial distribution of enhancement in electric field intensity $[E^2/E_0^2]$ in XY plane at different wavelengths across the second lowest energy Mie resonance peak wavelength (i.e., 701 nm) for Cu_2O cube of 286 nm edge length.
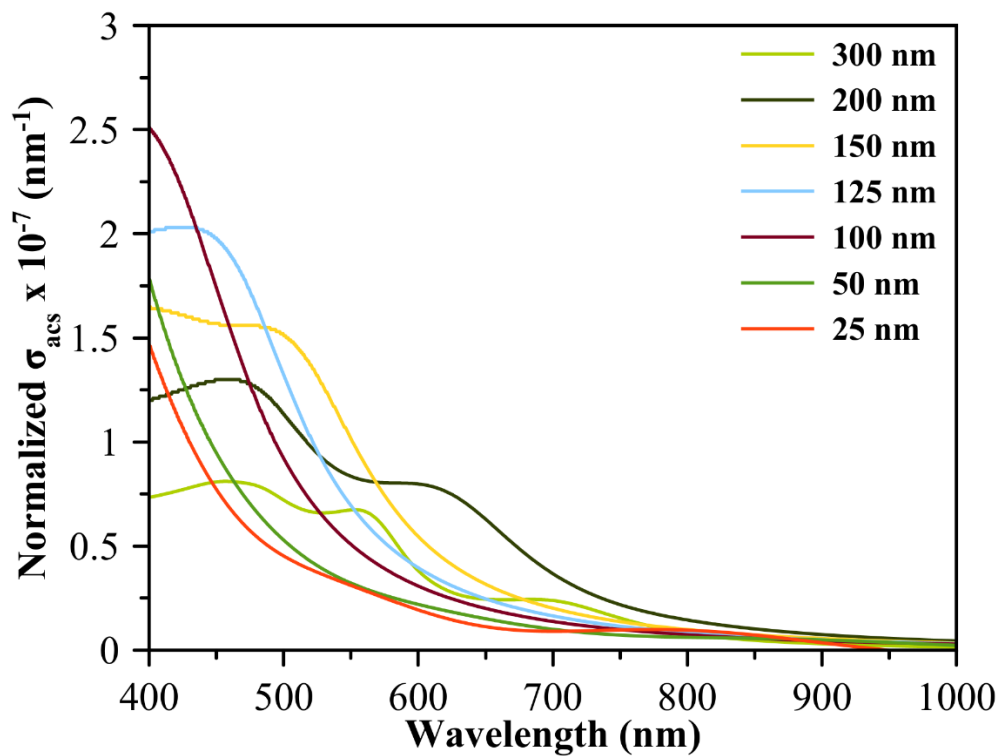
Figure B.S5a. FDTD-simulated volume-normalized absorption cross section (σ_{acs}) as a function of incident light wavelength for Cu_2O spherical nanoparticles of different sizes.
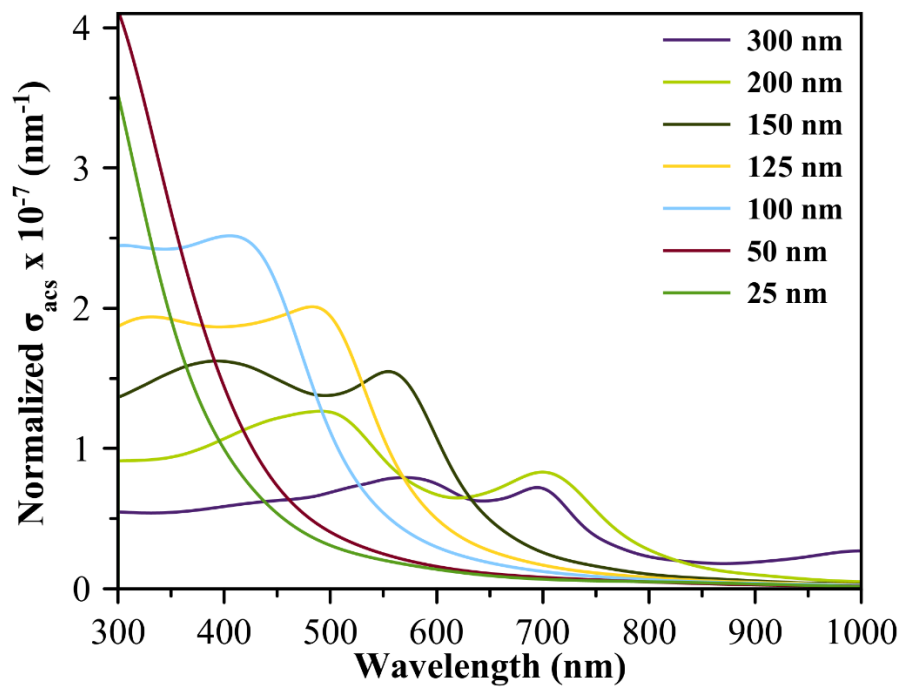
Figure B.S5b. FDTD-simulated volume-normalized absorption cross section (σ_{acs}) as a function of incident light wavelength for Cu_2O nanocubes of different sizes.
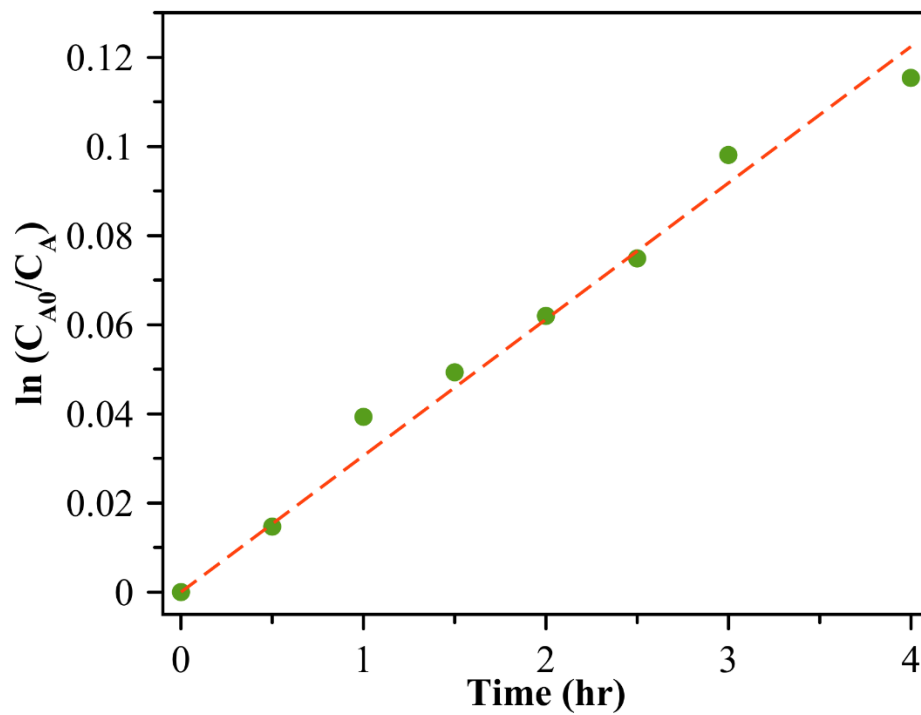
Figure B.S5c. Representative plot of empirical fit with first-order $\ln(C_{A0}/C_A)$ versus irradiation time for photocatalytic degradation of MB under green light illumination using Cu_2O nanospheres of 42 ± 6 nm diameter.
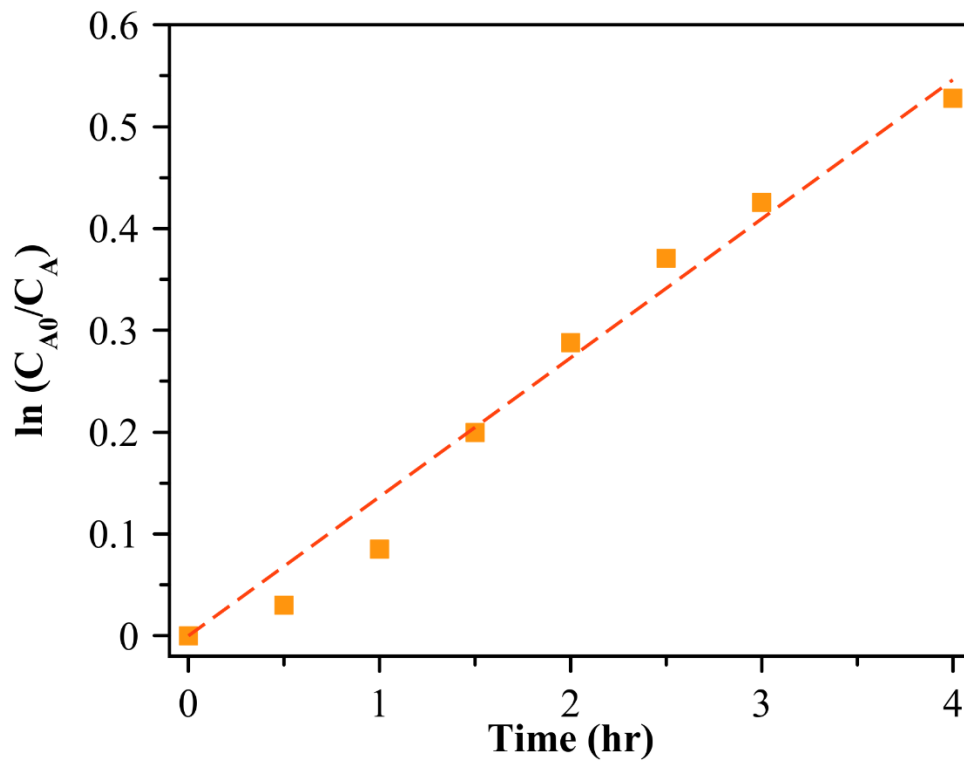
Figure B.S5d. Representative plot of empirical fit with first-order $\ln(C_{A0}/C_A)$ versus irradiation time for photocatalytic degradation of MB under green light illumination using Cu_2O nanocubes of 286 ± 47 nm edge length.
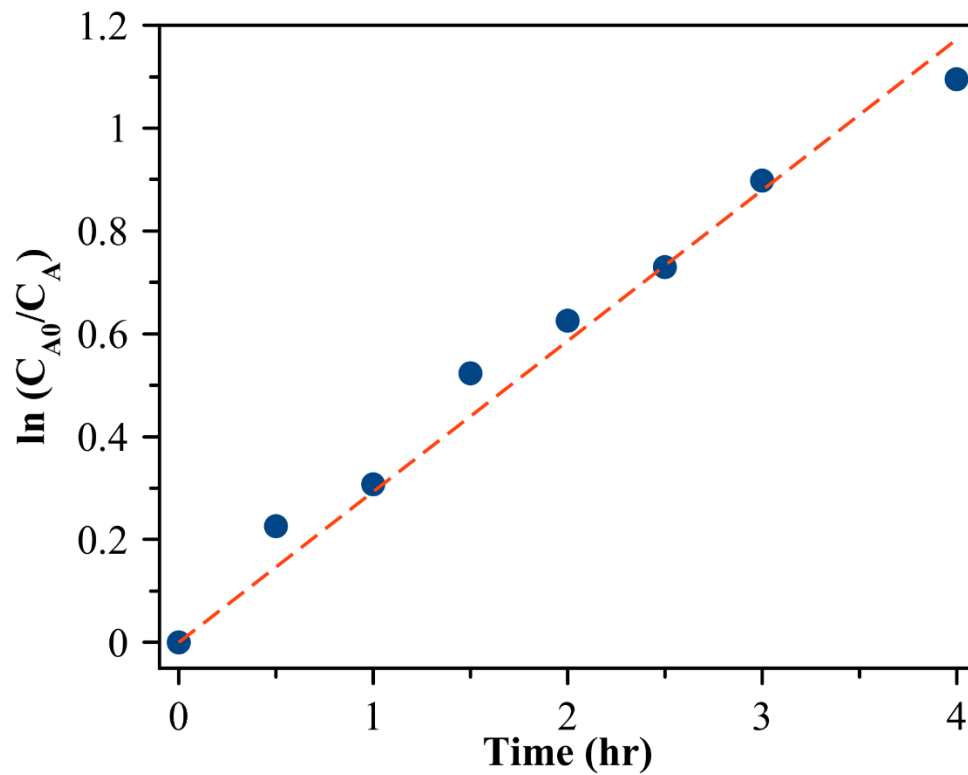
Figure B.S5e. Representative plot of empirical fit with first-order $\ln(C_{A0}/C_A)$ versus irradiation time for photocatalytic degradation of MB under green light illumination using Cu_2O nanospheres of 145 ± 41 nm diameter.
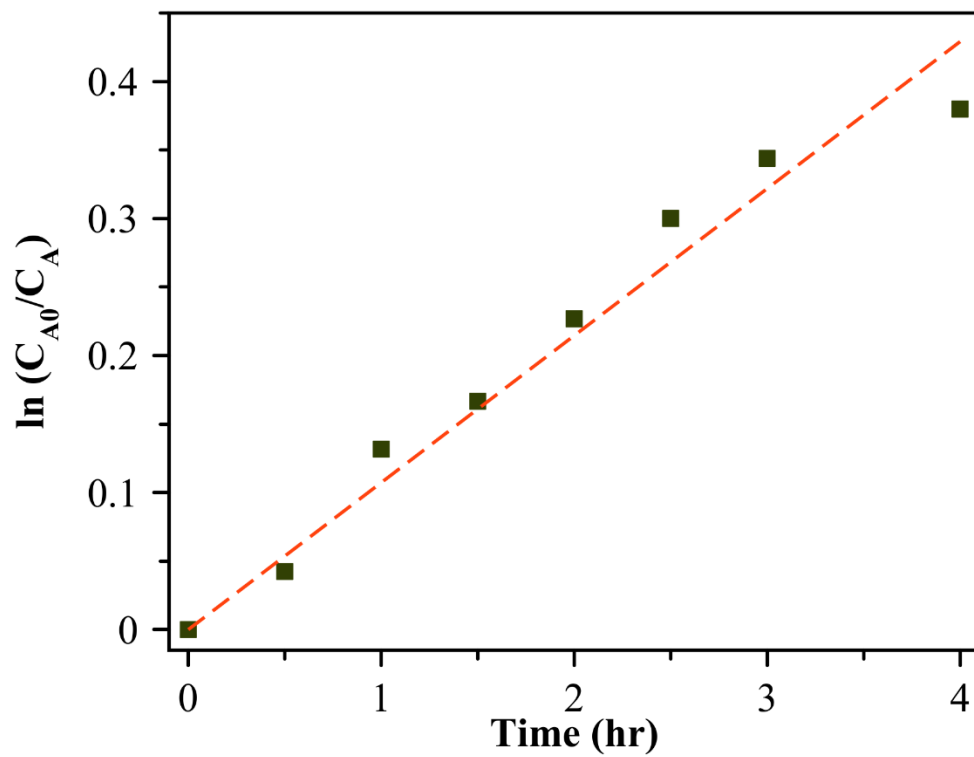
Figure B.S5f. Representative plot of empirical fit with first-order $\ln(C_{A0}/C_A)$ versus irradiation time for photocatalytic degradation of MB under green light illumination using Cu_2O nanocubes of 92 ± 13 nm edge length.
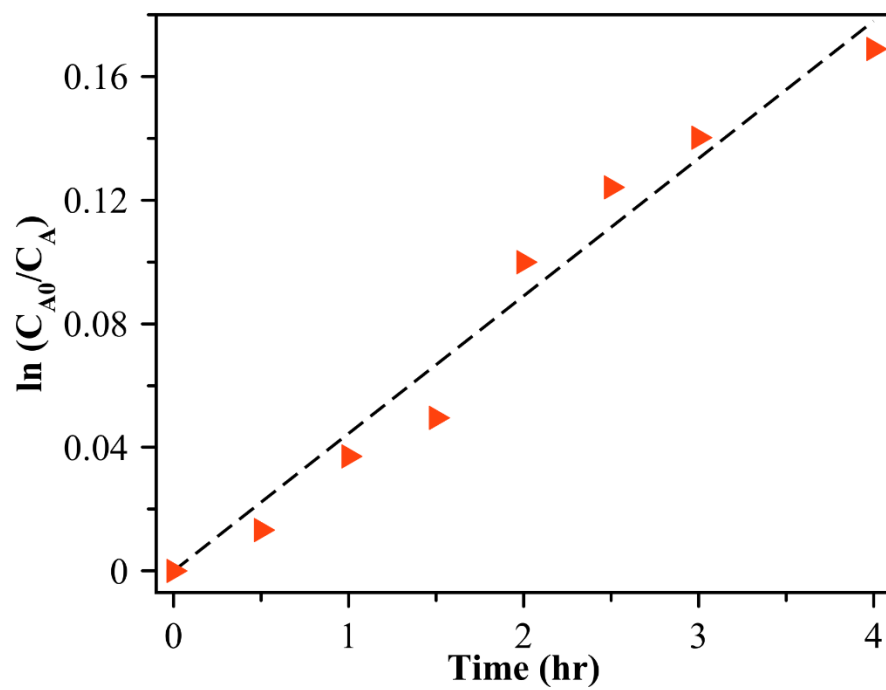
Figure B.S5g. Representative plot of empirical fit with first-order $\ln(C_{A0}/C_A)$ versus irradiation time for photocatalytic degradation under green light illumination using Cu_2O cubes of 456 ± 35 nm edge length.
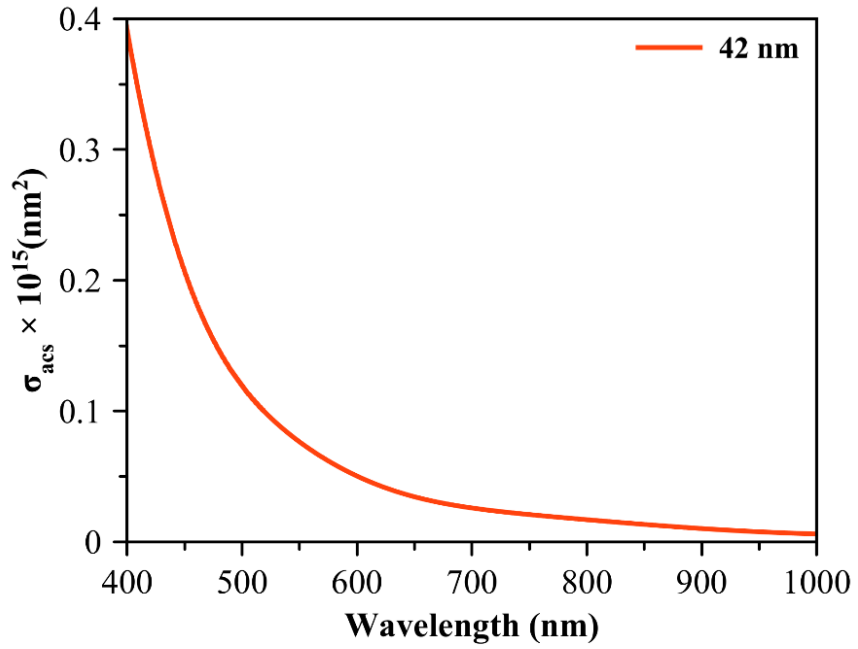
Figure B.S5h. FDTD-simulated absorption cross section (σ_{acs}) as a function of incident light wavelength for Cu_2O nanosphere of 42 nm diameter.
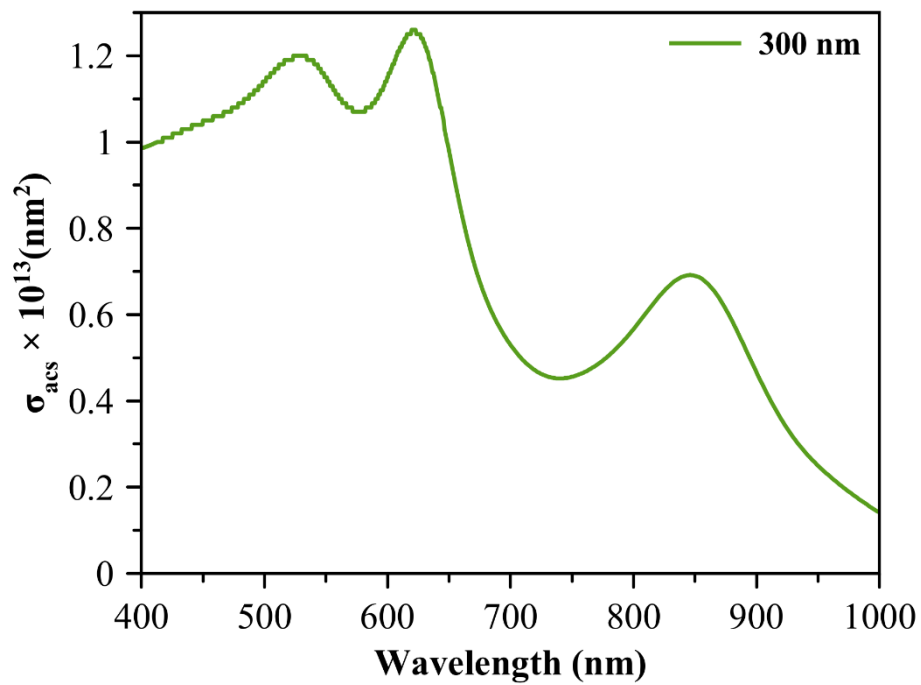
Figure B.S5i. FDTD-simulated absorption cross section (σ_{acs}) as a function of incident light wavelength for Cu_2O nanocube of 300 nm edge length.
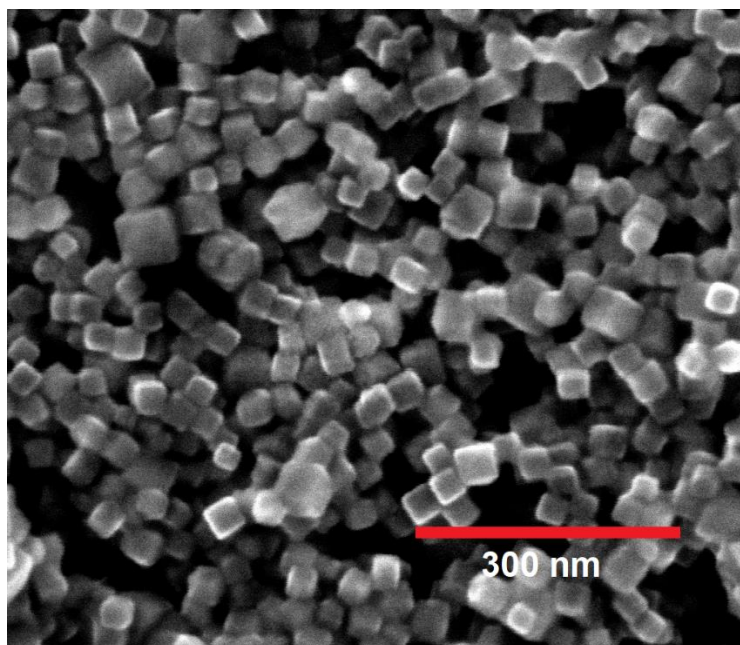
Figure B.S6a. Representative scanning electron microcopy image of Cu_2O nanocubes of 33 ± 6 nm edge length.
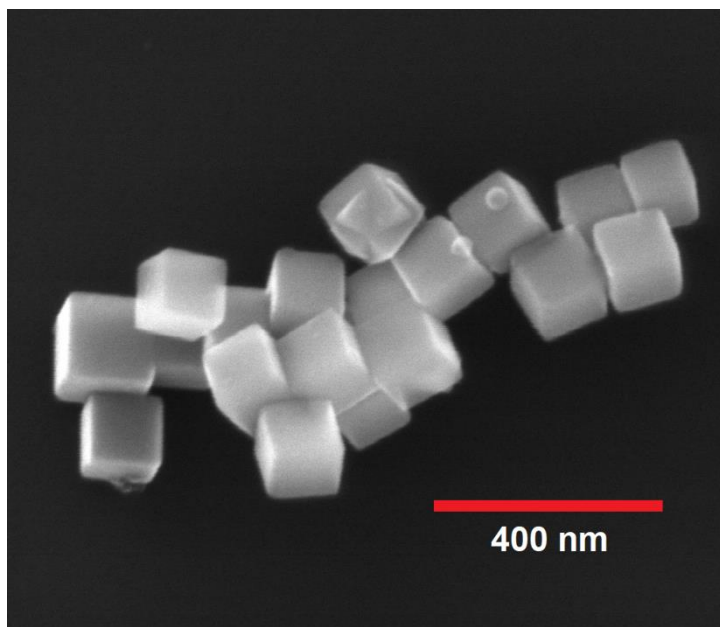
Figure B.S6b. Representative scanning electron microcopy image of Cu_2O nanocubes of 118 ± 21 nm edge length.
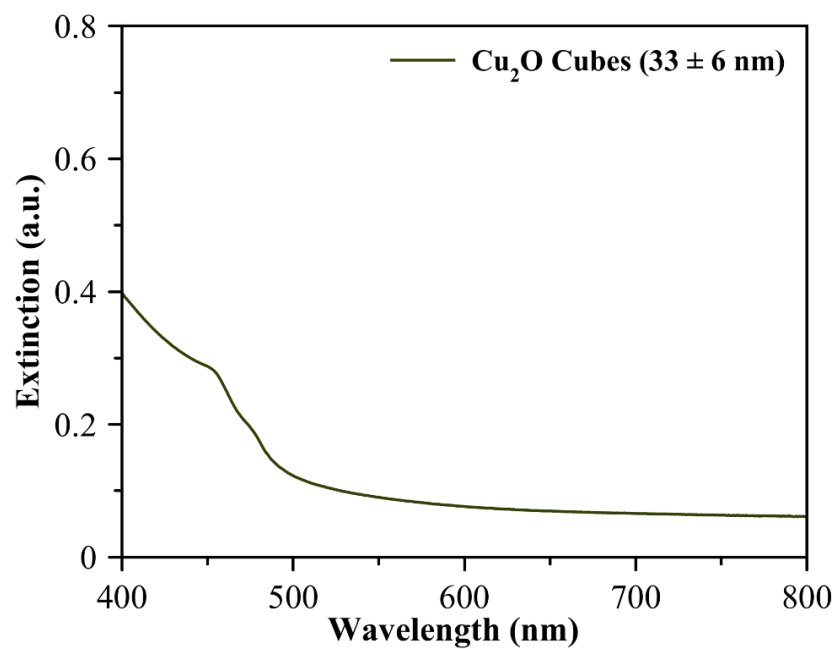
Figure B.S6c. Representative UV-Vis extinction spectrum of Cu_2O nanocubes of 33 ± 6 nm edge length.
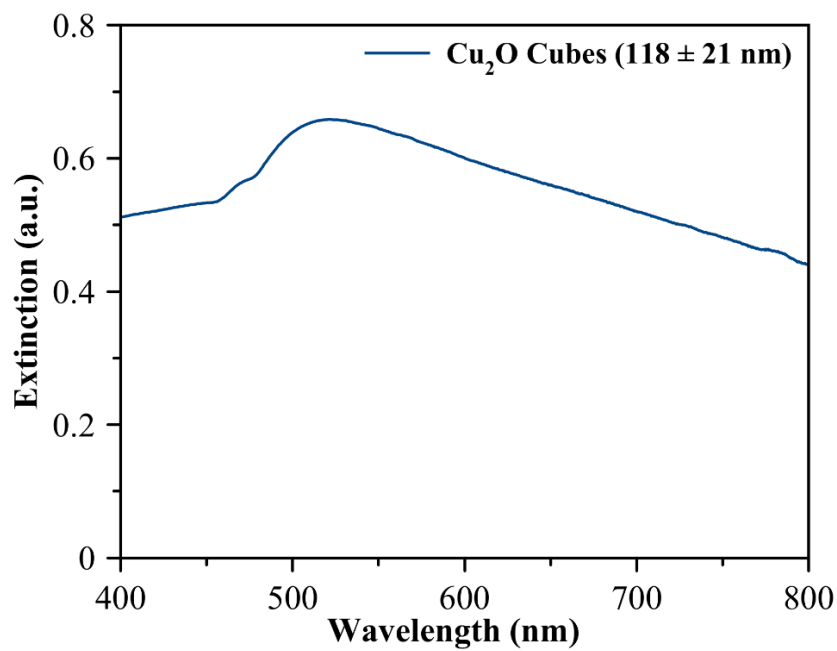
Figure B.S6d. Representative UV-Vis extinction spectrum of Cu_2O nanocubes of 118 ± 21 nm edge length.
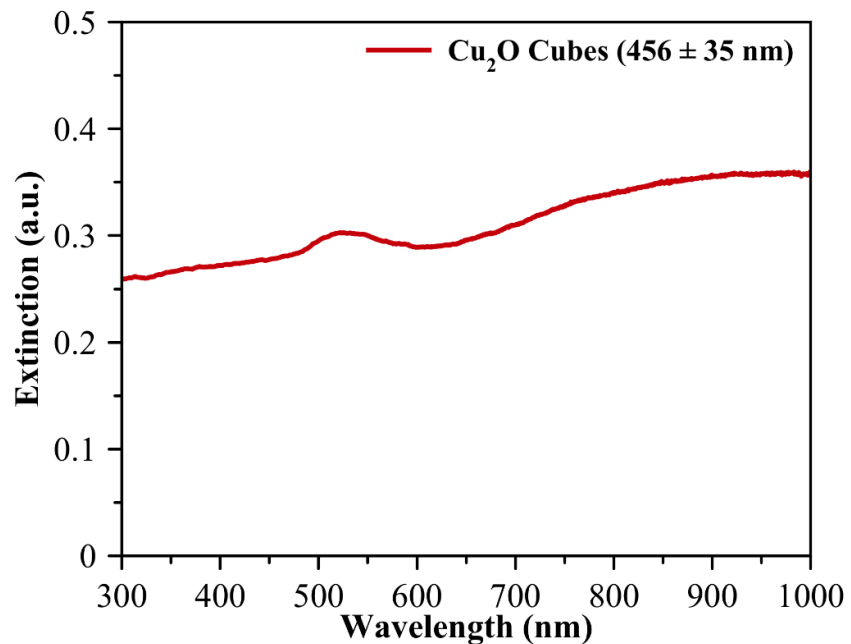
Figure B.S6e. Representative UV-Vis extinction spectrum of Cu₂O nanocubes of 456 ± 35 nm edge length.
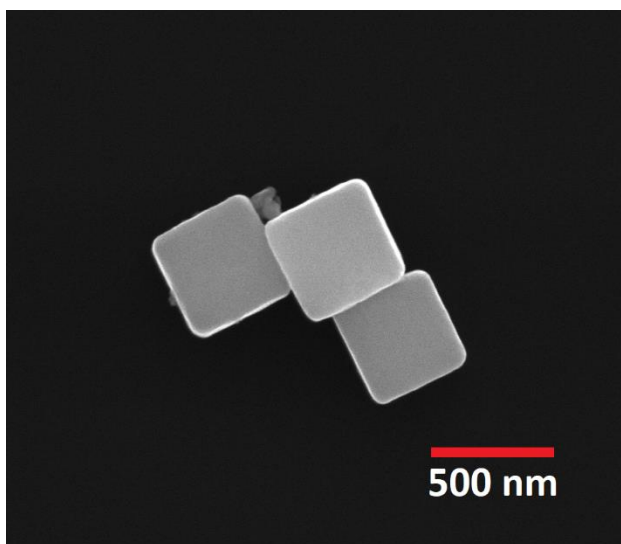
Figure B.S6f. Representative scanning electron microcopy image of as prepared Cu₂O nanocubes of 456 ± 35 nm edge length.
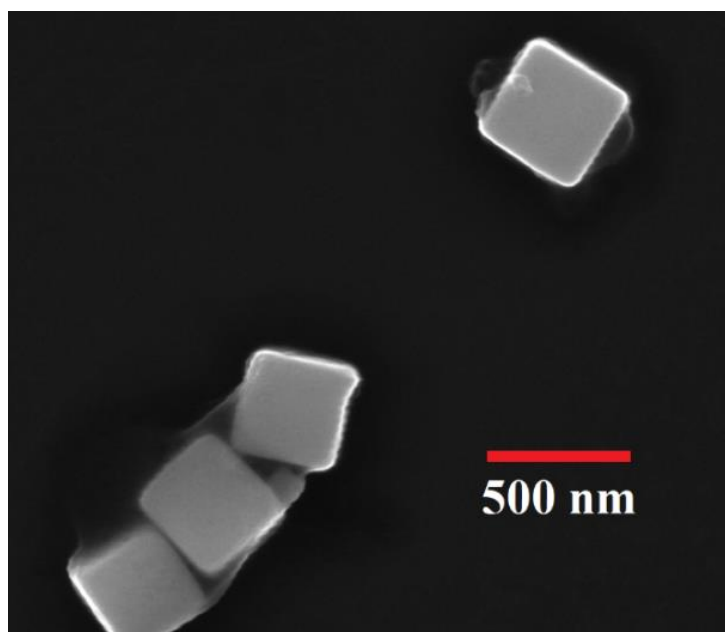
Figure B.S6g. Representative scanning electron microcopy image of used 456-nm Cu_2O nanocubes sample after exposing to 4 hours of photocatalytic reaction. No significant change in the morphology of the nanocubes was observed in the as prepared and used samples.
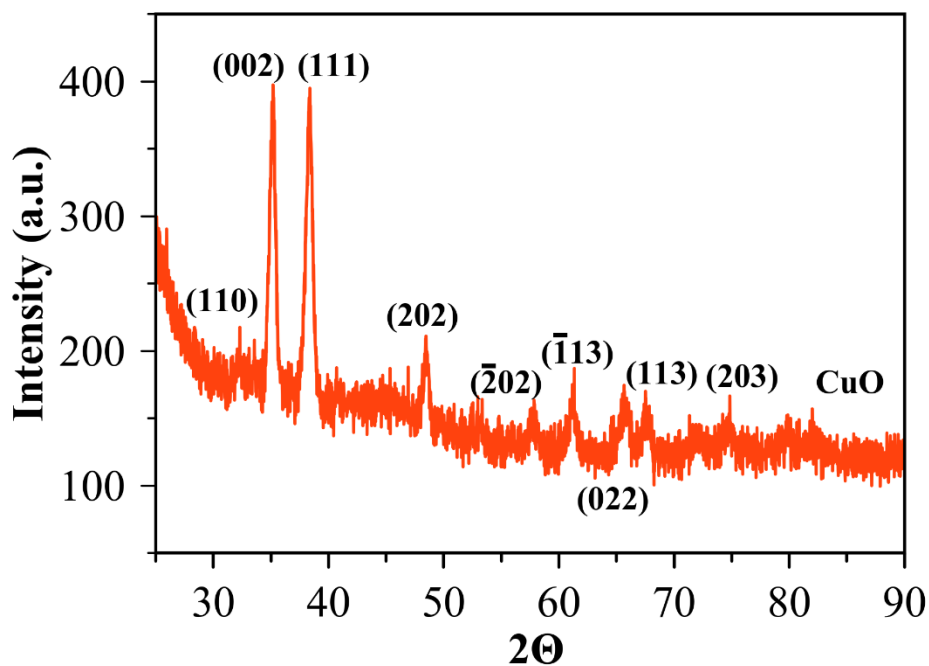
Figure B.S6h. Representative X-ray diffraction patterns of reference CuO sample. The reference CuO nanoparticles sample was obtained through the oxidation of the Cu_2O nanoparticles in a tubular furnace at 500 °C. The signals of the CuO facets are confirmed by comparing with the respective values reported in the literature.
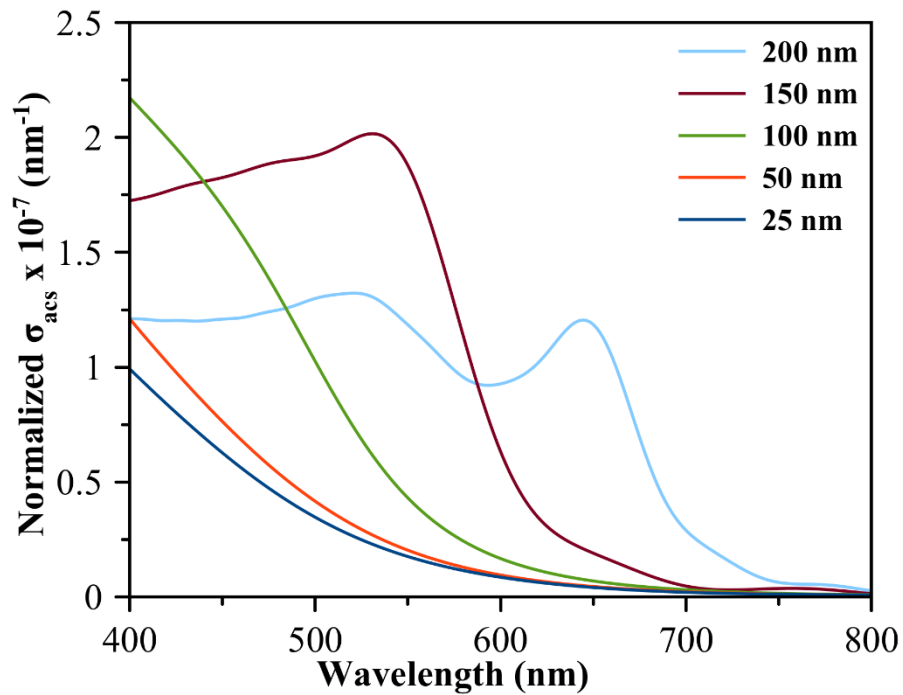
Figure B.S7a. FDTD-simulated volume-normalized absorption cross section (σ_{acs}) as a function of incident light wavelength for α-Fe$_2$O$_3$ nanospherical particles of different sizes.
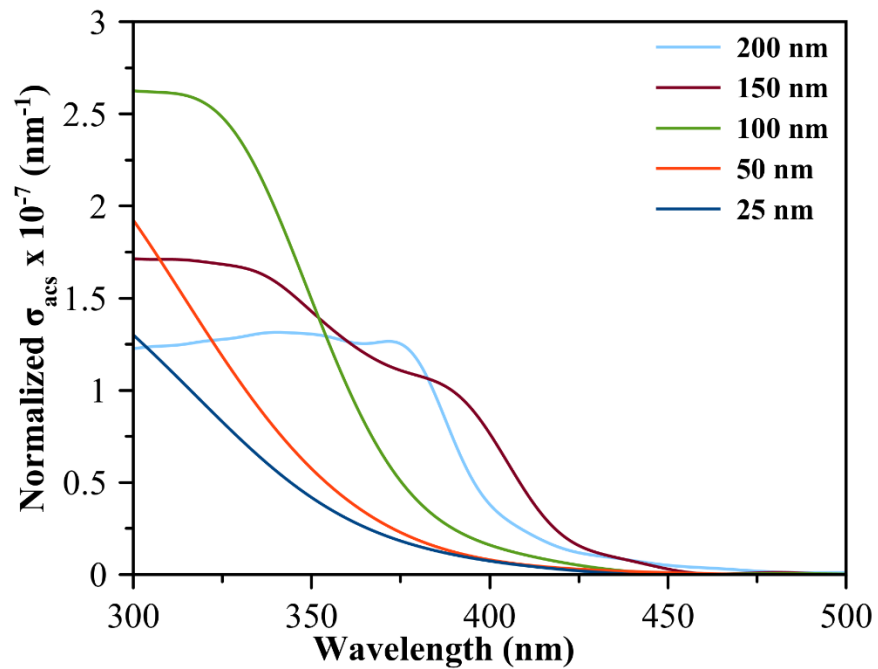
Figure B.S7b. FDTD-simulated volume-normalized absorption cross section (σ_{acs}) as a function of incident light wavelength for CeO_2 spherical nanoparticles of different sizes.
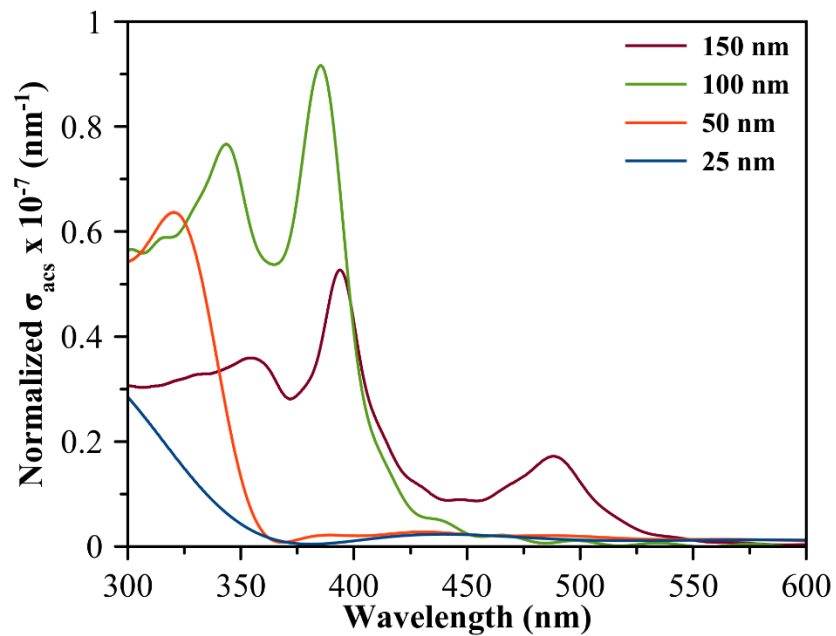
Figure B.S7c. FDTD-simulated volume-normalized absorption cross section (σ_{acs}) as a function of incident light wavelength for TiO_2 spherical nanoparticles of different sizes.

Table B.S1. Fitted first-order rate constant values obtained from the photocatalytic degradation of

MB using Cu_2O nanospheres and nanocubes of different sizes.

Cu_2O nanostructures	Rate Constant, k (hr^{-1})
Spheres (42±6 nm)	0.034 ± 0.004
Cubes (456±35 nm)	0.045 ± 0.001
Cubes (92±13 nm)	0.113 ± 0.003
Cubes (286±47 nm)	0.141 ± 0.006
Spheres (145±41 nm)	0.327 ± 0.040

Table B.S2. The real (n) and imaginary (k) parts of refractive index values of Cu_2O used in the simulations. (Ref: Palik, E. D. *Handbook of Optical Constants of Solids*; Academic Press, 1998.)

	Cu_2O	
λ (nm)	n	k
300	2	1.85
350	2.4	1.44
400	2.8	0.99
450	3.06	0.6
500	3.12	0.35
550	3.1	0.19
600	3.02	0.13
650	2.9	0.1
700	2.83	0.083
750	2.77	0.07
800	2.7	0.06
850	2.66	0.053
900	2.63	0.048
950	2.61	0.043
1000	2.6	0.04
1100	2.59	0.033
1200	2.58	0.027
1300	2.57	0.021
1400	2.57	0.017
1500	2.57	0.013
2000	2.56	0.002

Table B.S3. The real (n) and imaginary (k) parts of refractive index values of CeO$_2$ used in the simulations. (Ref: Hass, G.; Ramsey, J. B.; Thun, R. Optical Properties and Structure of Cerium Dioxide Films. *J. Opt. Soc. Am.* **1958**, *48* (5), 324.)

CeO$_2$											
λ (nm)	n	k	λ (nm)	n	k	λ (nm)	n	k	λ (nm)	n	k
401	2.47	0.11	624	2.16	0.00	854	2.13	0.00	929	2.12	0.00
410	2.41	0.08	635	2.15	0.00	864	2.13	0.00	940	2.12	0.00
421	2.38	0.03	646	2.15	0.00	876	2.13	0.00	951	2.12	0.00
429	2.36	0.02	657	2.15	0.00	886	2.13	0.00	962	2.11	0.00
439	2.31	0.01	668	2.15	0.00	897	2.12	0.00	973	2.11	0.00
450	2.29	0.01	679	2.15	0.00	908	2.12	0.00	984	2.11	0.00
461	2.28	0.00	690	2.15	0.00	919	2.12	0.00	996	2.11	0.00
471	2.25	0.00	701	2.15	0.00	929	2.12	0.00	929	2.12	0.00
483	2.24	0.00	712	2.14	0.00	940	2.12	0.00	940	2.12	0.00
494	2.22	0.00	722	2.15	0.00	951	2.12	0.00	951	2.12	0.00
504	2.21	0.00	733	2.15	0.00	962	2.11	0.00	962	2.11	0.00
516	2.20	0.00	744	2.14	0.00	973	2.11	0.00	973	2.11	0.00
526	2.19	0.00	755	2.14	0.00	984	2.11	0.00	984	2.11	0.00
537	2.18	0.00	766	2.14	0.00	996	2.11	0.00	996	2.11	0.00
548	2.18	0.00	777	2.14	0.00	854	2.13	0.00	929	2.12	0.00
559	2.18	0.00	788	2.14	0.00	864	2.13	0.00	940	2.12	0.00
570	2.18	0.00	799	2.13	0.00	876	2.13	0.00	951	2.12	0.00
581	2.17	0.00	810	2.14	0.00	886	2.13	0.00	962	2.11	0.00
592	2.16	0.00	821	2.13	0.00	897	2.12	0.00	973	2.11	0.00
602	2.16	0.00	831	2.13	0.00	908	2.12	0.00	984	2.11	0.00
613	2.16	0.00	842	2.13	0.00	919	2.12	0.00	996	2.11	0.00

Table B.S4. The real (n) and imaginary (k) parts of refractive index values of α-Fe_2O_3 used in the simulations.(Ref: Ordal, M. et. Al., R. Optical Properties of Fourteen Metals in the Infrared and Far Infrared: Al, Co, Cu, Au, Fe, Pb, Mo, Ni, Pd, Pt, Ag, Ti, V, and W. *Appl. Opt.* **1985**, *24* (24), 4493.)

	α-Fe_2O_3	
λ (nm)	n	k
400	2.756	1.294
450	3.181	1.02
500	3.282	0.675
550	3.318	0.498
600	3.265	0.149
650	3.074	0.057
700	2.972	0.031
750	2.903	0.021
800	2.853	0.02
850	2.824	0.027
900	2.805	0.024
950	2.789	0.022
1000	2.775	0.015
1050	2.759	0.011
1100	2.745	0.011
1150	2.734	0.01
1200	2.723	0.011

Table B.S5. The real (n) and imaginary (k) parts of refractive index values of TiO_2 used in the simulations.

TiO_2								
λ (nm)	**n**	**k**	**λ (nm)**	**n**	**k**	**λ (nm)**	**n**	**k**
180	1.37	1.998	330	5.291	1.5698	480	3.08	0.0001
190	1.535	1.831	340	4.969	1.0926	490	3.054	0.0001
200	1.536	1.696	350	4.477	0.6508	500	3.03	0.0001
210	1.46	1.65	360	3.87	0.251	510	3.014	0.0001
220	1.433	1.806	370	3.661	0.033	520	3	0.0001
230	1.443	2.084	380	3.498	0.0001	530	2.985	0.0001
240	1.363	2.454	390	3.375	0.0001	540	2.97	0.0001
250	1.365	2.847	400	3.286	0.0001	550	2.954	0.0001
260	1.627	3.197	410	3.225	0.0001	560	2.94	0.0001
270	1.952	3.432	420	3.186	0.0001	570	2.929	0.0001
280	3.355	3.561	430	3.162	0.0001	580	2.92	0.0001
290	3.835	3.535	440	3.149	0.0001	590	2.91	0.0001
300	4.732	3.28	450	3.141	0.0001	600	2.9	0.0001
310	5.235	2.734	460	3.13	0.0001	610	2.889	0.0001
320	5.391	2.076	470	3.104	0.0001	620	2.88	0.0001

	TiO₂							
λ (nm)	n	k	λ (nm)	n	k	λ (nm)	n	k
630	2.875	0.0001	780	2.8	0.0001	930	2.759	0.0001
640	2.87	0.0001	790	2.794	0.0001	940	2.76	0.0001
650	2.86	0.0001	800	2.79	0.0001	950	2.761	0.0001
660	2.85	0.0001	810	2.79	0.0001	960	2.76	0.0001
670	2.844	0.0001	820	2.79	0.0001	970	2.755	0.0001
680	2.84	0.0001	830	2.785	0.0001	980	2.75	0.0001
690	2.835	0.0001	840	2.78	0.0001	990	2.749	0.0001
700	2.83	0.0001	850	2.78	0.0001	1000	2.75	0.0001
710	2.825	0.0001	860	2.78	0.0001	1010	2.75	0.0001
720	2.82	0.0001	870	2.775	0.0001	1020	2.749	0.0001
730	2.814	0.0001	880	2.77	0.0001	1030	2.749	0.0001
740	2.81	0.0001	890	2.77	0.0001	1040	2.748	0.0001
750	2.81	0.0001	900	2.77	0.0001	1050	2.747	0.0001
760	2.81	0.0001	910	2.765	0.0001	1060	2.747	0.0001
770	2.806	0.0001	920	2.76	0.0001	1070	2.746	0.0001

TiO₂								
λ (nm)	n	k	λ (nm)	n	k	λ (nm)	n	k
1080	2.745	0.0001	1230	2.729	0.0001	1380	2.721	0.0001
1090	2.744	0.0001	1240	2.729	0.0001	1390	2.721	0.0001
1100	2.742	0.0001	1250	2.728	0.0001	1400	2.72	0.0001
1110	2.741	0.0001	1260	2.728	0.0001	1410	2.719	0.0001
1120	2.74	0.0001	1270	2.727	0.0001	1420	2.719	0.0001
1130	2.739	0.0001	1280	2.727	0.0001	1430	2.718	0.0001
1140	2.738	0.0001	1290	2.726	0.0001	1440	2.717	0.0001
1150	2.737	0.0001	1300	2.726	0.0001	1450	2.716	0.0001
1160	2.736	0.0001	1310	2.725	0.0001	1460	2.715	0.0001
1170	2.735	0.0001	1320	2.725	0.0001	1470	2.714	0.0001
1180	2.734	0.0001	1330	2.724	0.0001	1480	2.713	0.0001
1190	2.733	0.0001	1340	2.724	0.0001	1490	2.711	0.0001
1200	2.732	0.0001	1350	2.723	0.0001	1500	2.71	0
1210	2.731	0.0001	1360	2.723	0.0001			
1220	2.73	0.0001	1370	2.722	0.0001			

TUNING CATALYTIC ACTIVITY AND SELECTIVITY IN PHOTOCATALYSIS
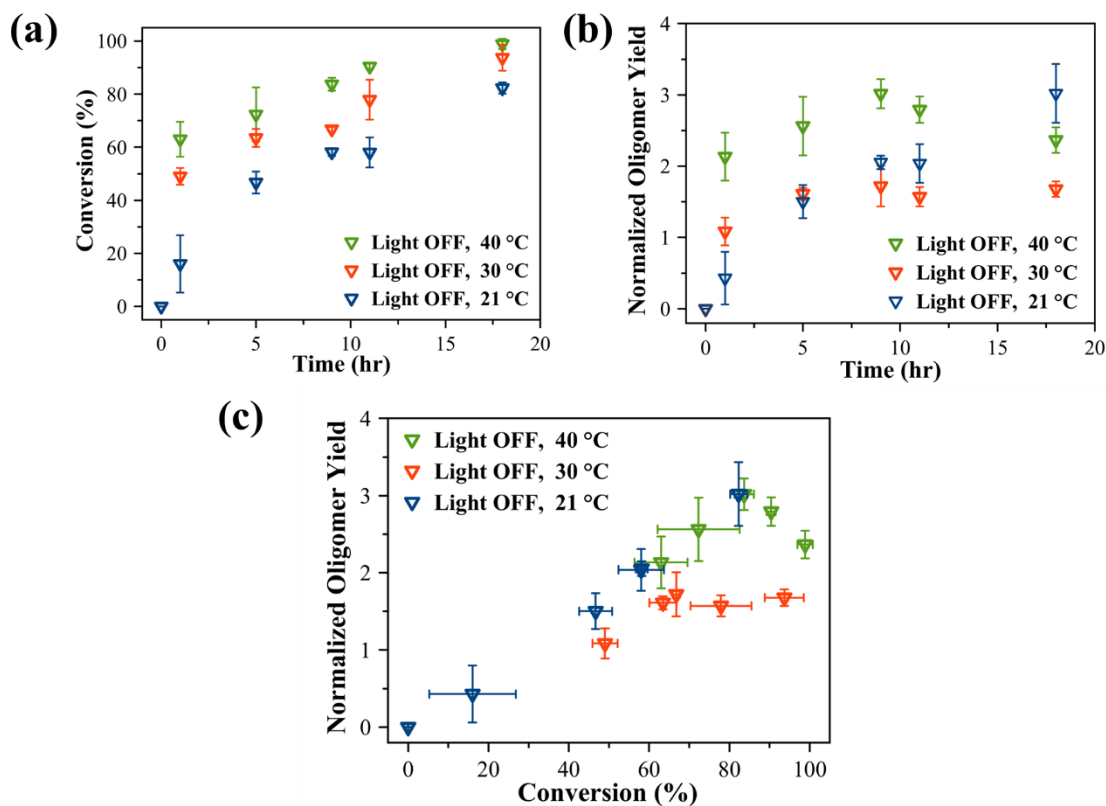
Figure C.S1. MB degradation with BPPs as photocatalyst under Light off conditions at different temperatures 20 °C, 30 °C**,** 40 °C **(a)** degradation of MB with time **(b)** Normalized Oligomer Yield with time **(c)** Normalized Oligomer Yield vs degradation.
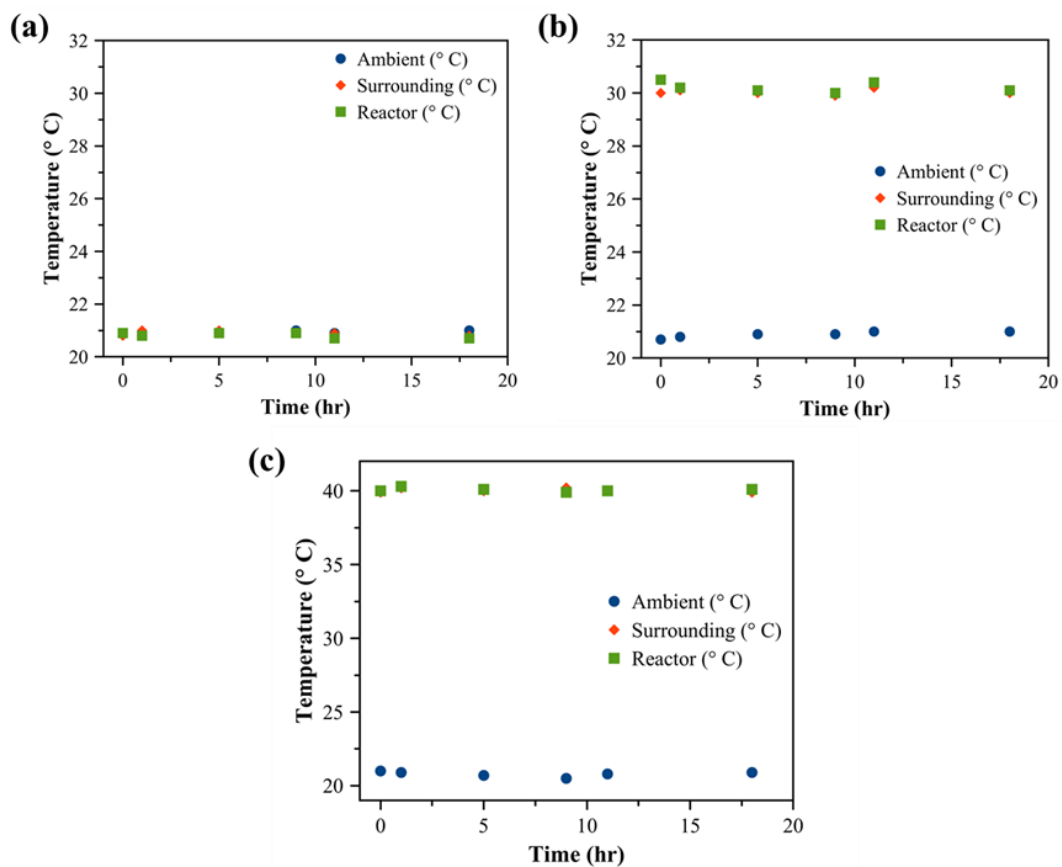
Figure C.S2. The temperature profile of methylene blue degradation in DMF under different conditions mentioned below **(a)** Dark 20 °C **(b)** Dark 30 °C **(c)** 40 °C
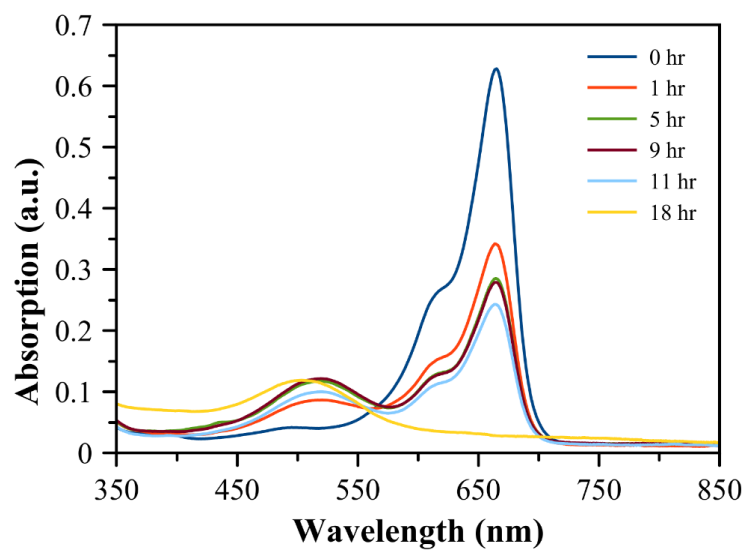
Figure C.S3. UV-Vis Spectra of MB degradation with BPPs as photocatalyst under Light off conditions at 30 °C
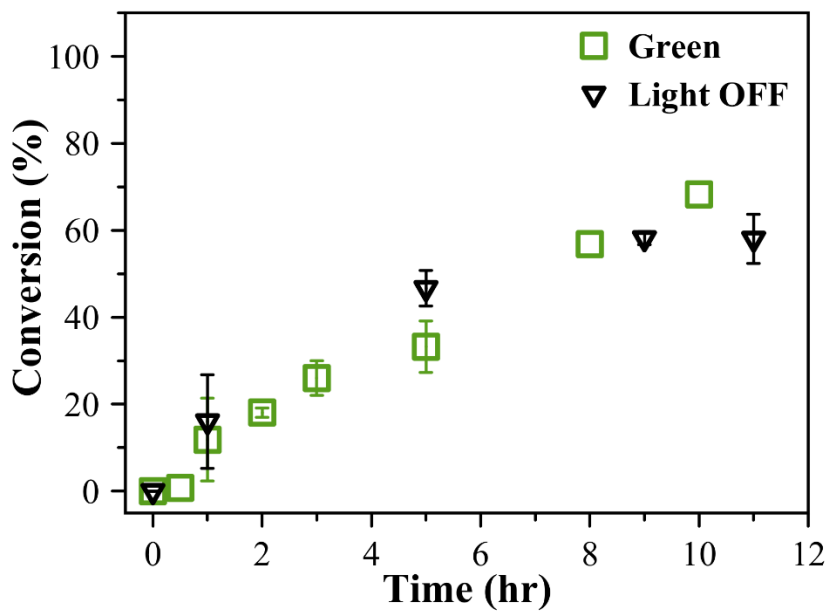
Figure C.S4. Comparison of Methylene Blue degradation under green light illumination and Light OFF conditions
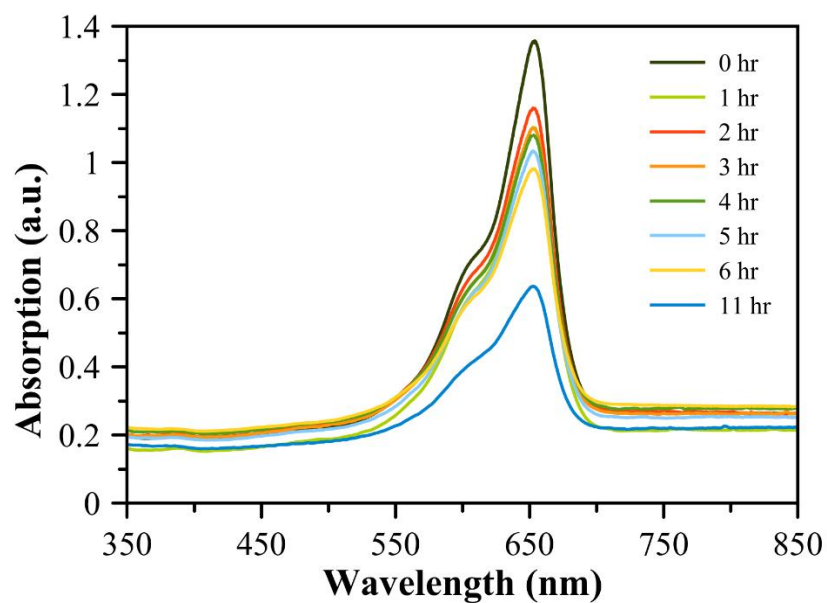
Figure C.S5. UV-Vis Spectra of MB degradation with BPPs as photocatalyst under Green Light Illumination.
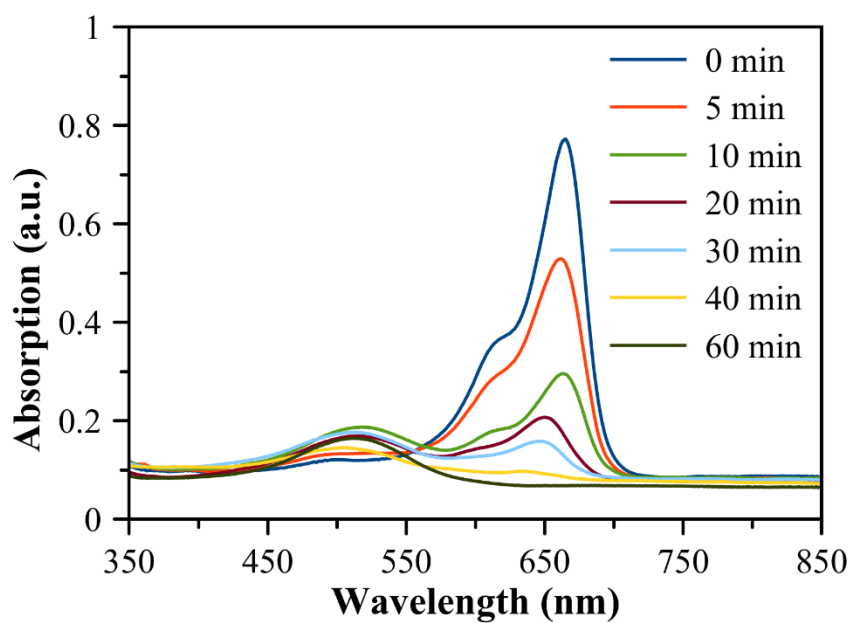
Figure C.S5. UV-Vis Spectra of MB degradation with BPPs as photocatalyst under Red Light Illumination.
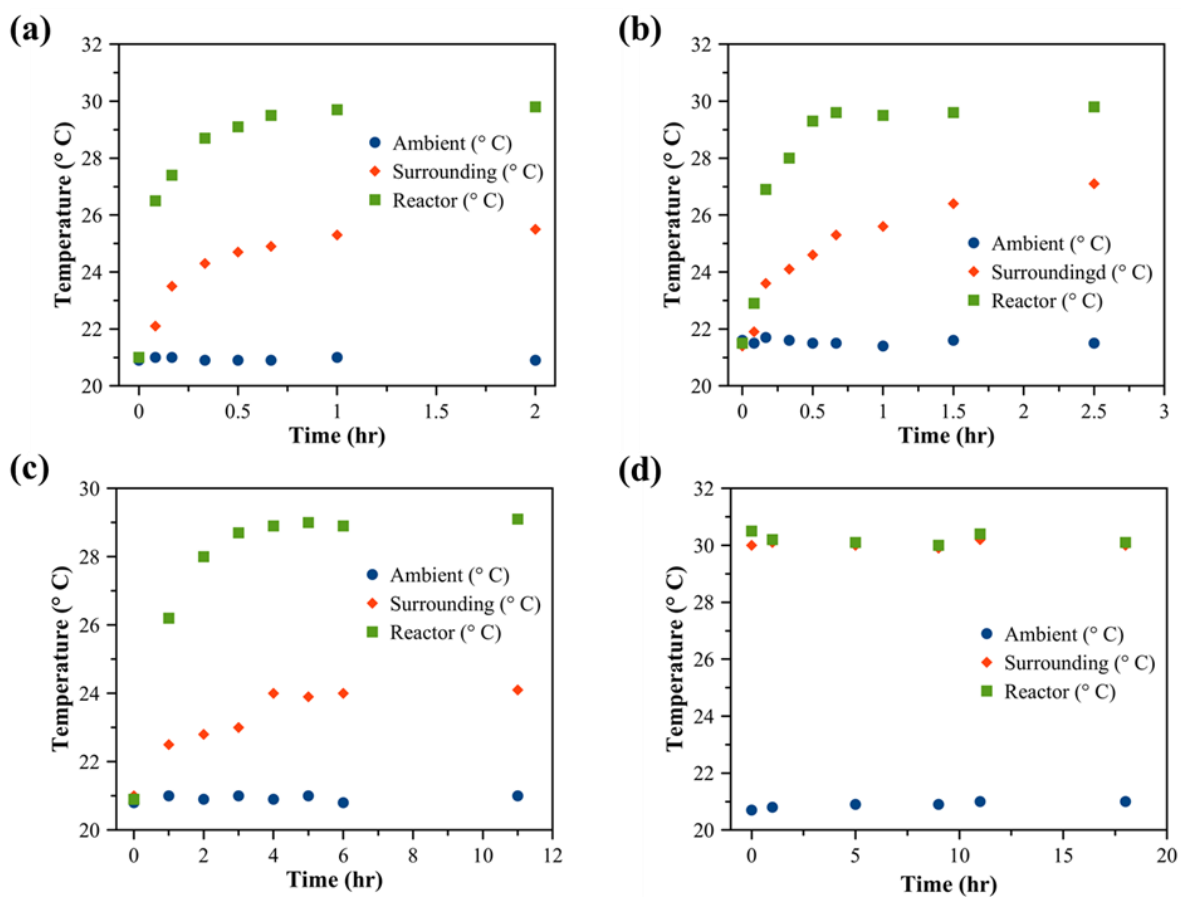
Figure C.S7. Temperature profile of methylene blue degradation in DMF under different conditions mentioned below **(a)** Red **(b)** Amber **(c)** Green illumination **(d)** Dark conditions at 30 °C
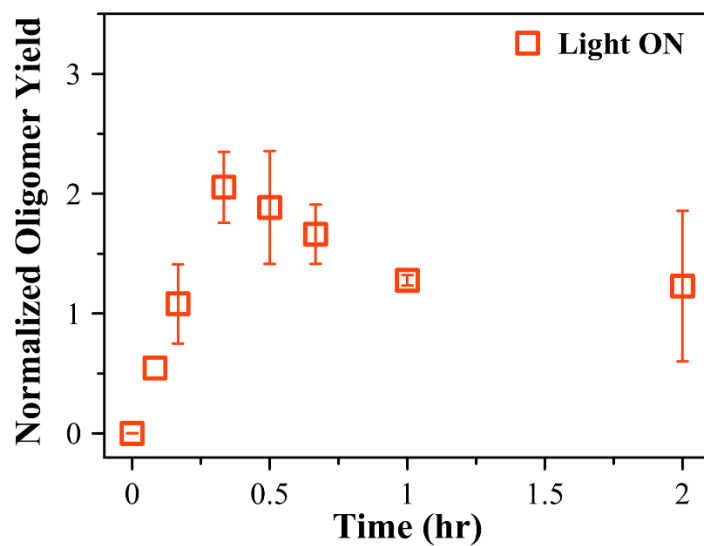
Figure C.S8. Normalized Oligomer Yield of methylene blue degradation under illumination of red light
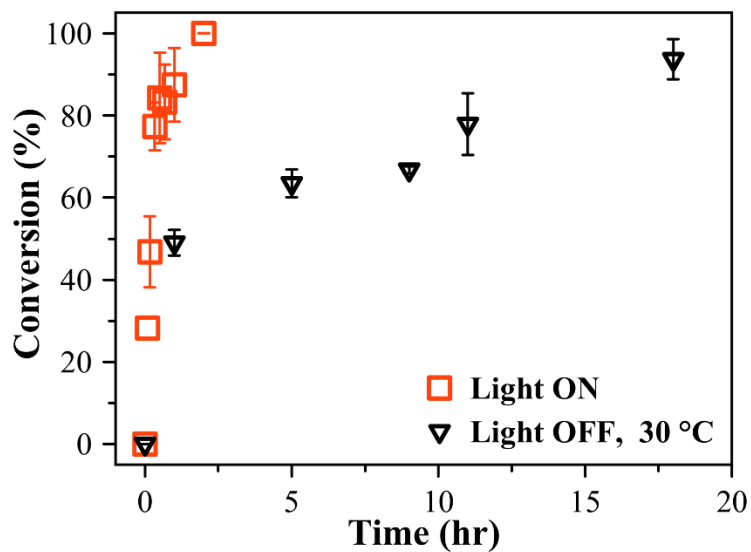
Figure C.S9. Comparison of Methylene Blue degradation under red light illumination and Light OFF conditions at 30 °C

APPENDIX D

MIE-RESONANCE ENHANCED C-C COUPLING REACTIONS

1-148 Cu + base_005.tif
1-148 Cu + base
Print Mag: 41600x @ 51 mm

100 nm

HV=200kV
Direct Mag: 20000x
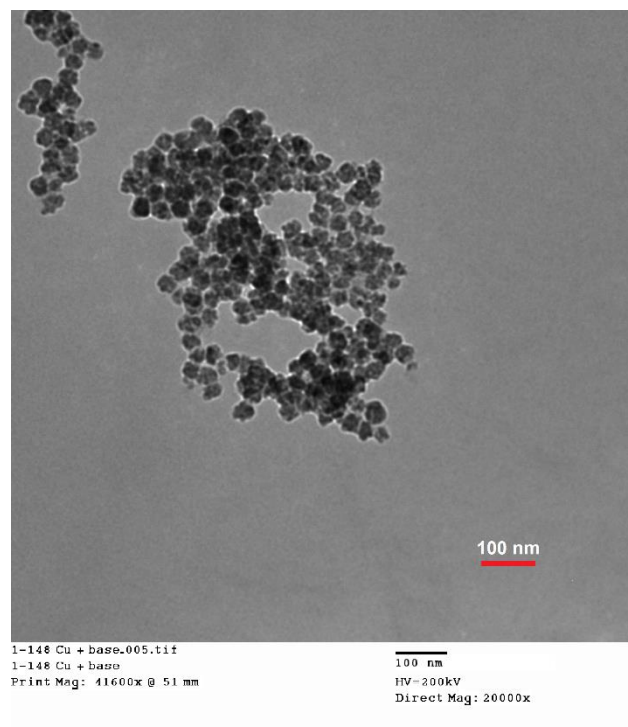
Figure. D.S1. A representative TEM image of the Cu_2O nanoparticles (diameter = 34 ± 4 nm).
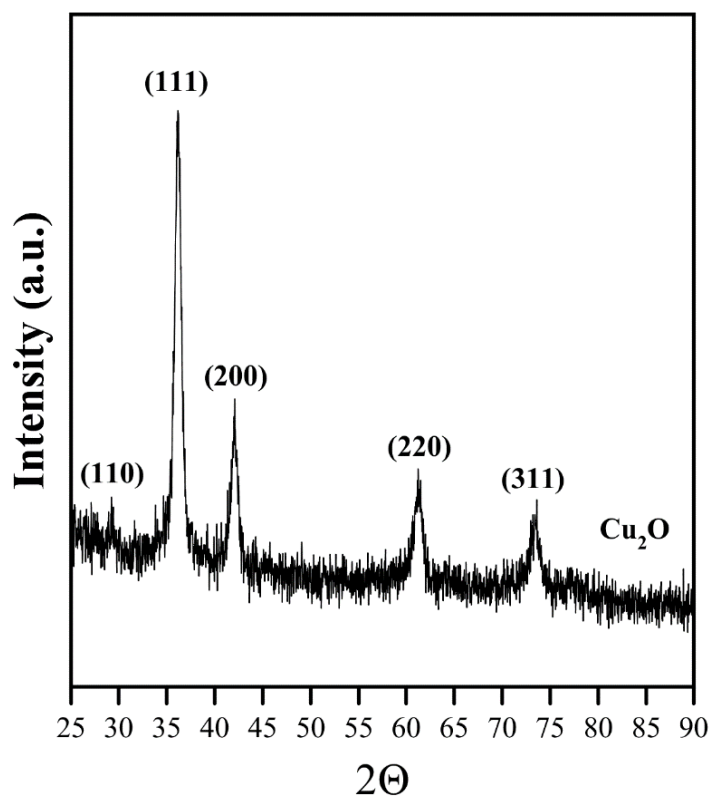
Figure.D.S2. The X-Ray diffraction pattern of the Cu_2O nanoparticles.
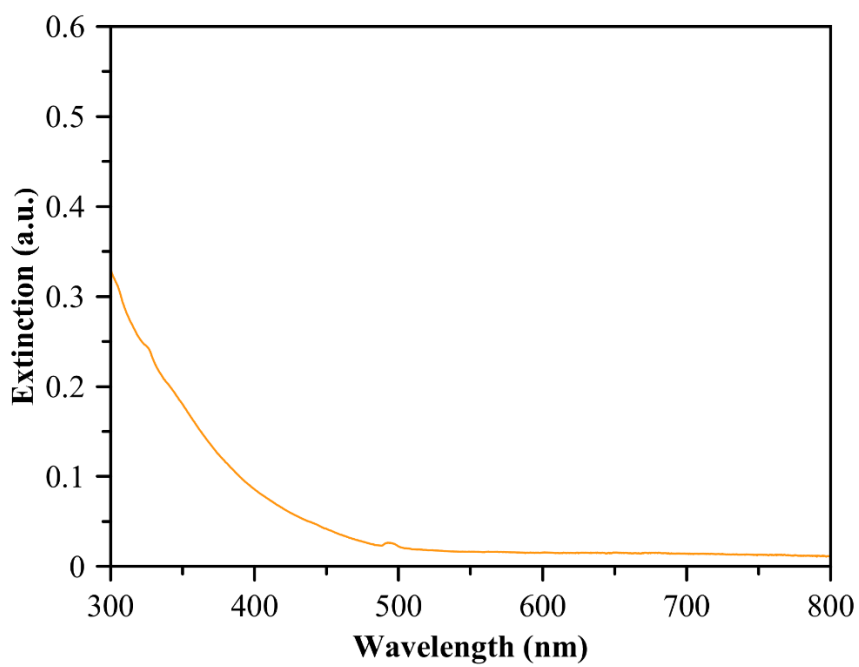
Figure. D.S3. The UV-Vis extinction spectrum of the Cu_2O nanoparticles.
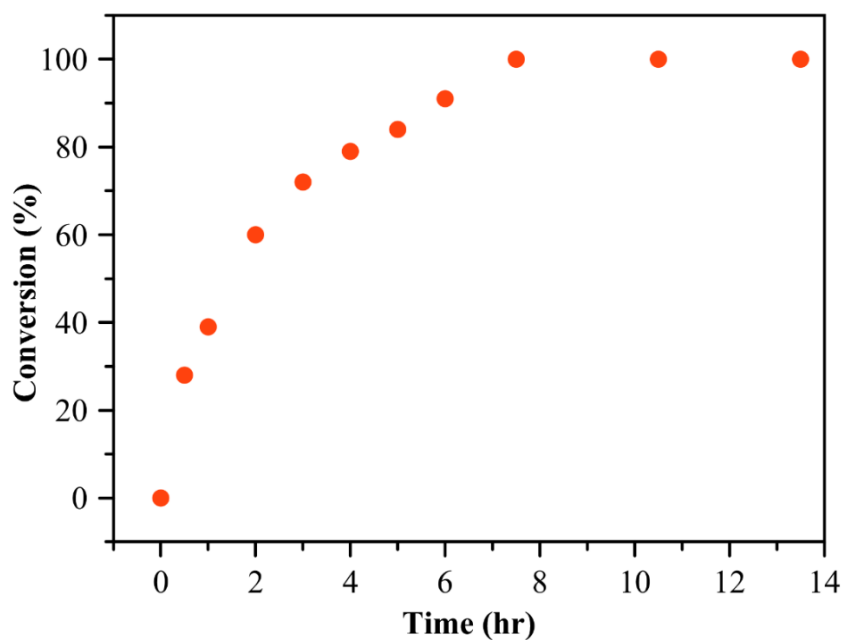
Figure. D.S4. Conversion as a function of Reaction Time for SCR at 147 °C (under reflux) in the presence of the base.
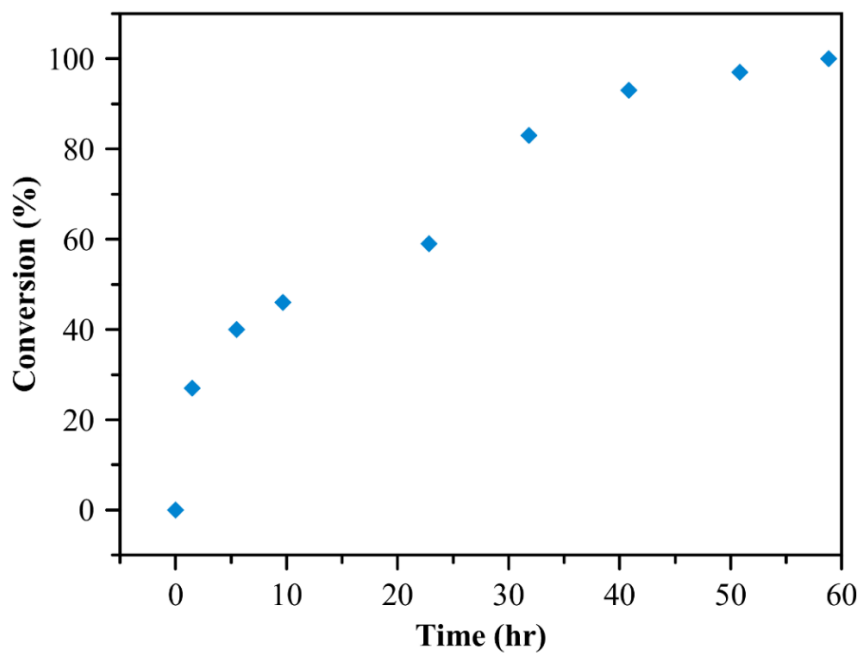
Figure. D.S5. Conversion as a function of Reaction Time for SCR at 147 °C (under reflux) in the absence of the base.
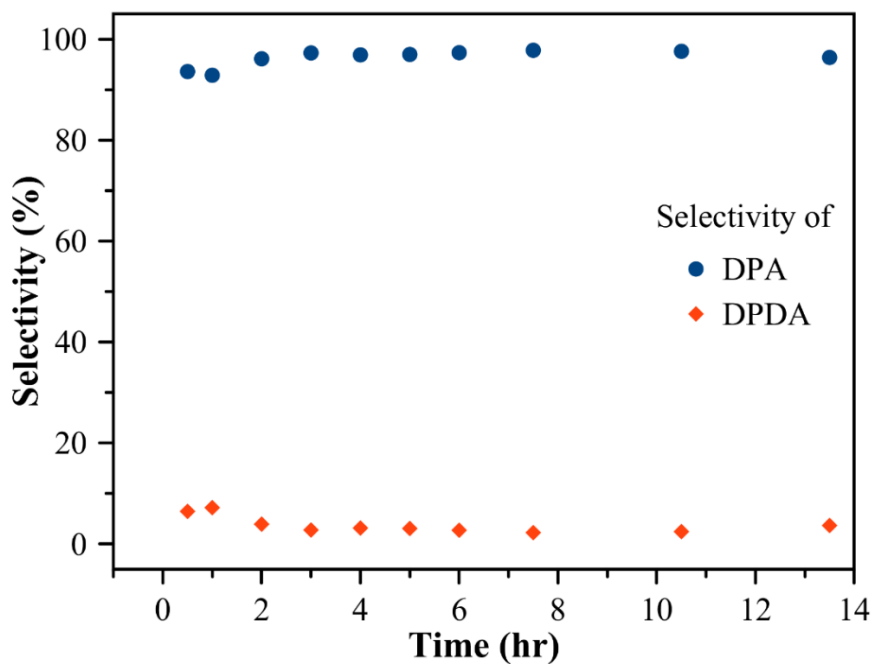
Figure. D.S6. The cross-coupling and homocoupling products DPA vs DPDA selectivity as a function of reaction time for SCR at 147 °C (under reflux) in the presence of the base.
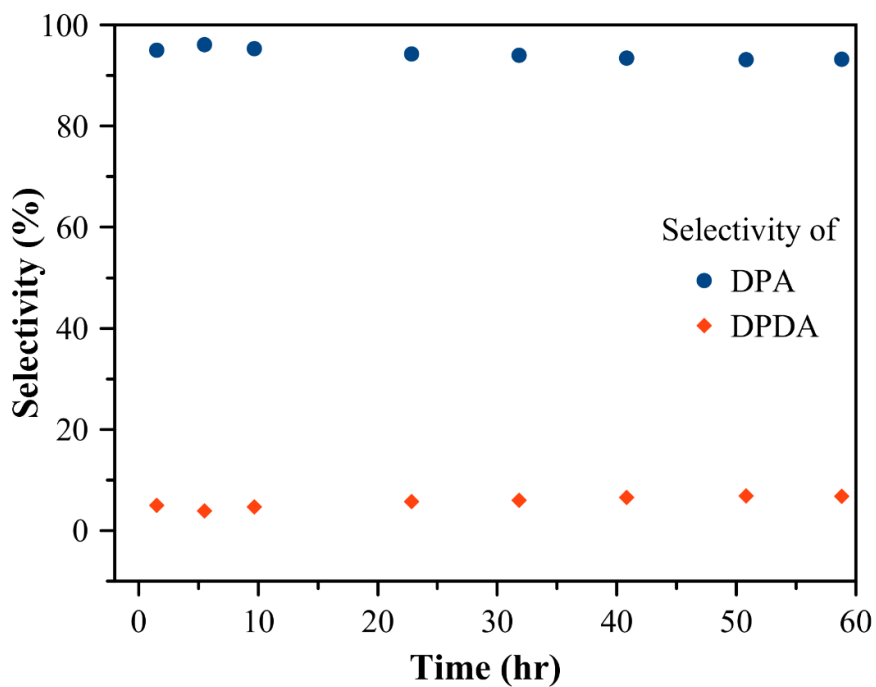
Figure. D.S7. The cross-coupling and homocoupling products DPA vs DPDA selectivity as a function of reaction time for SCR at 147 °C (under reflux) in the absence of base.
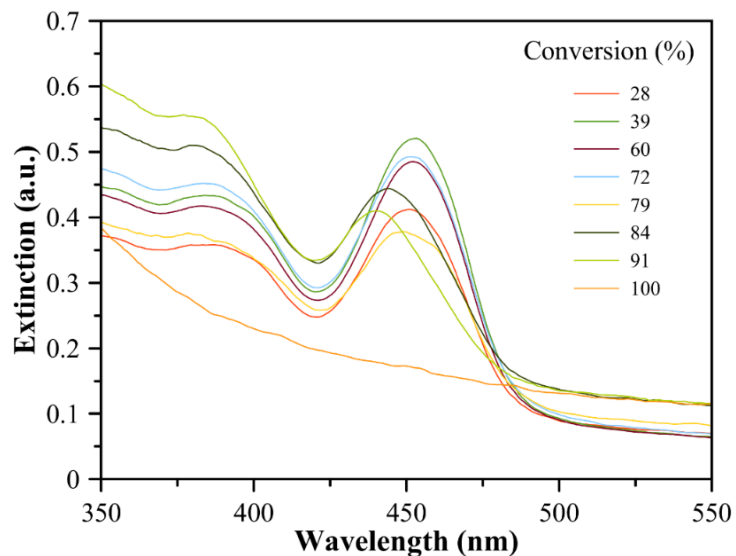
Figure. D.S8. UV-Vis extinction spectra of reaction mixture measured at different reaction conversions during SCR at 147 °C (under reflux) in the presence of base.

The extinction peaks centered at ~385 and ~450 nm in Fig. D.S8 are due to homogeneous Cu complexes in the reaction solution. These peaks are observed in the reaction solution only when both PA and base are present. We did not observe any leaching or the extinction peaks for the homogeneous Cu complexes when only IB and base were present (in the absence of PA).
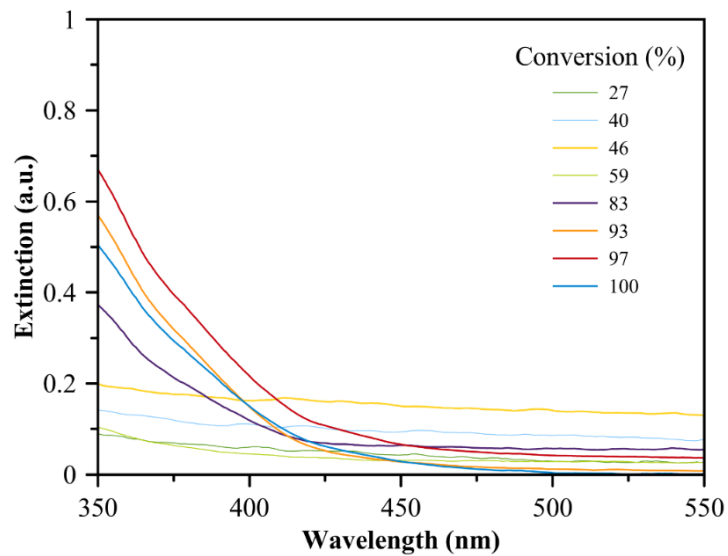
Figure. D.S9. UV-Vis extinction spectra of reaction mixture measured at different reaction conversions during SCR at 147 °C (under reflux) in the absence of the base.

The changes observed in the extinction spectra in Fig. D.S9 for different conversions are most likely due to the expected change in dielectric constant of the reaction mixture for the respective conversions.
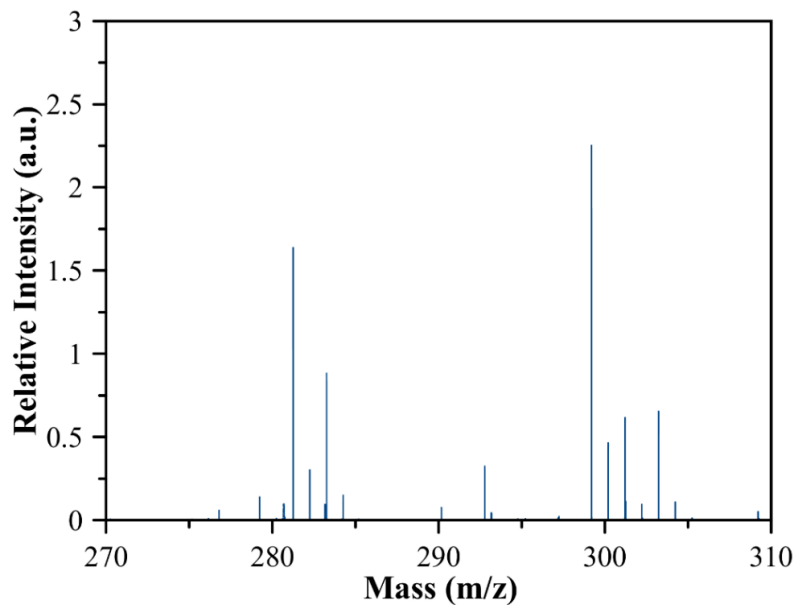
Figure. D.S10. The HR-ESI-MS spectrum measured in negative spray mode for the supernatant solution of the reaction mixture taken from Cu_2O nanoparticles-catalyzed SCR in the presence of the base.
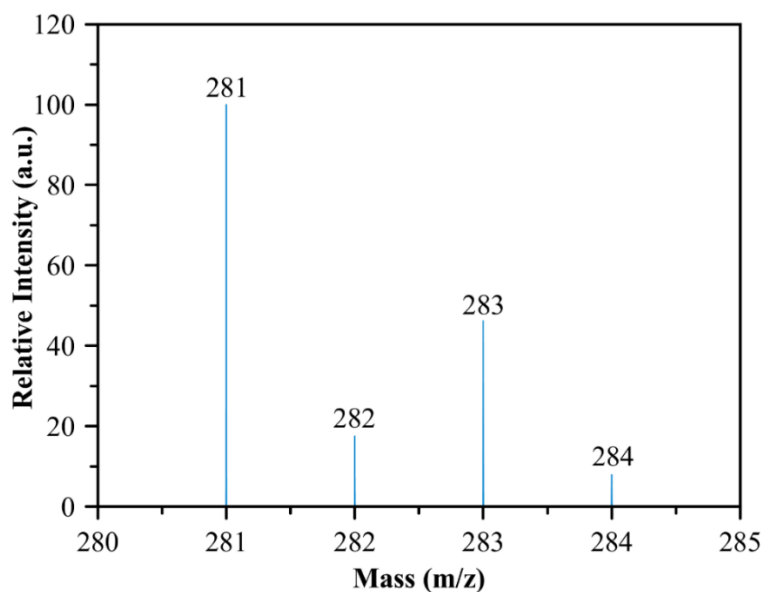
Figure. C.S11a. Predicted mass spectrum for the proposed copper complex with chemical formula, $[CuO(C_8H_5)_2]^-$.[204]
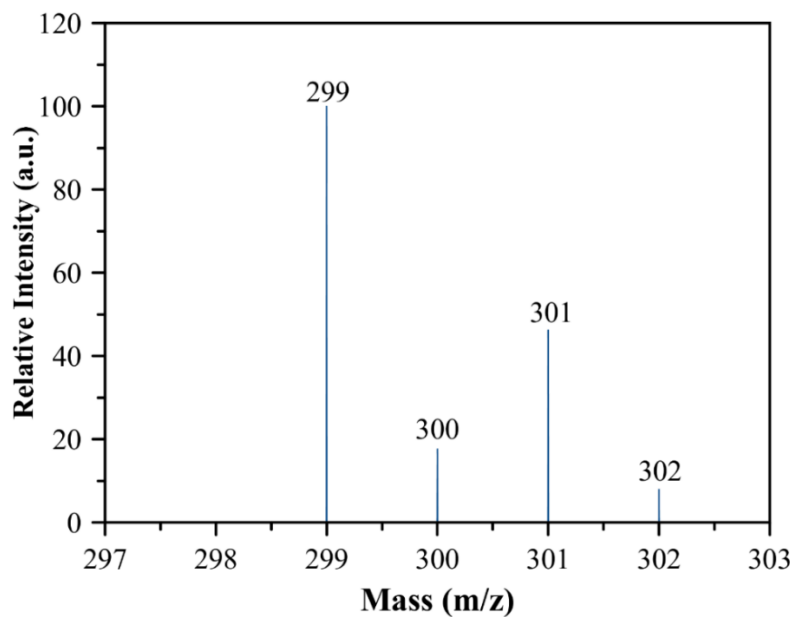
Figure. D.S11b. Predicted mass spectrum for the proposed copper complex with chemical formula, $[CuO(C_8H_5)_2H_2O]^-$. [204]
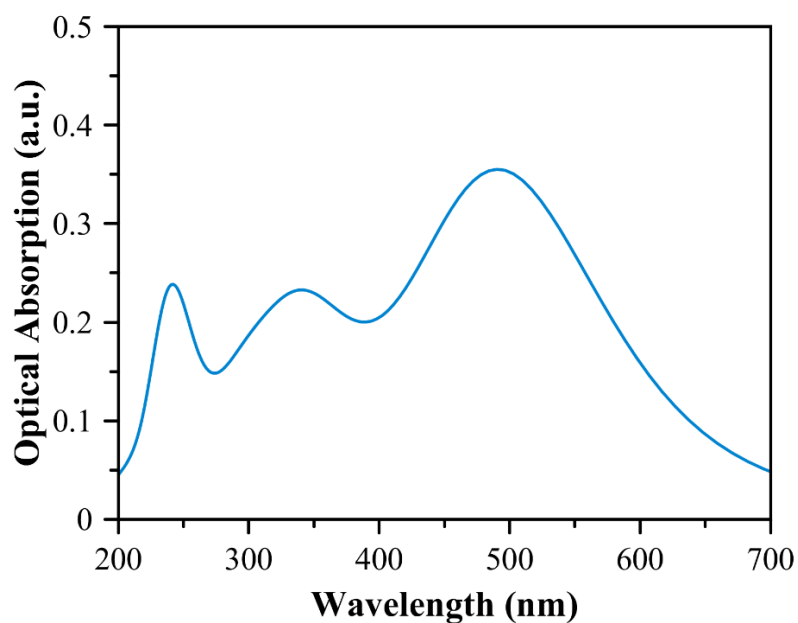
Figure. D.S11c. DFT calculated optical absorption spectra of homogeneous Cu complex, $[CuO(C_8H_5)_2H_2O]^-$.
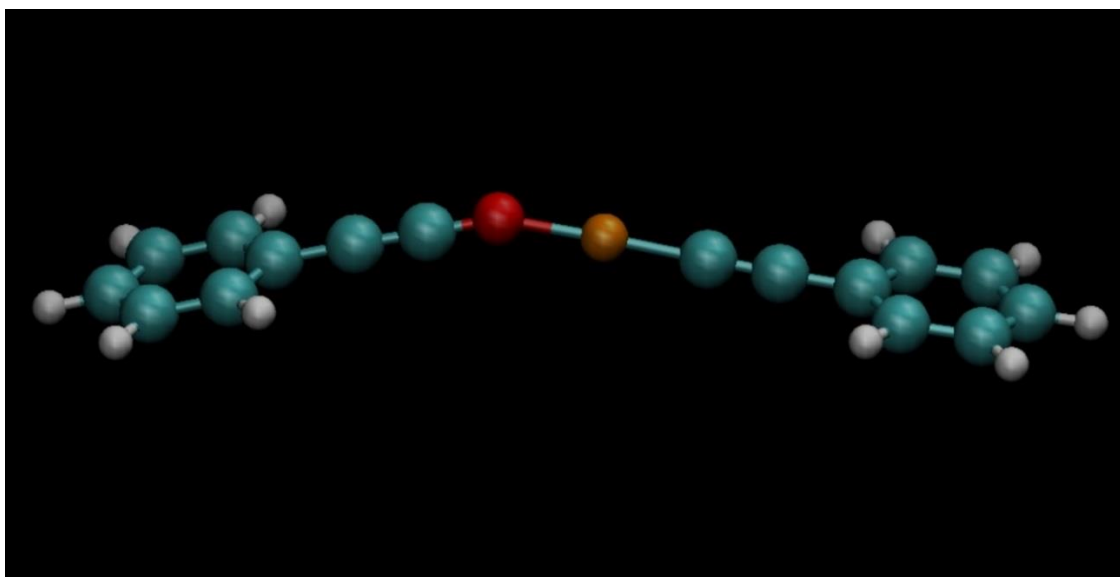
Figure. D.S11d. DFT-predicted Structure of homogeneous Cu complex, $[CuO(C_8H_5)_2]^-$. Color code: Orange - Copper atom; Red – Oxygen atom; Cyan-Blue – Carbon atom, White – Hydrogen atom.
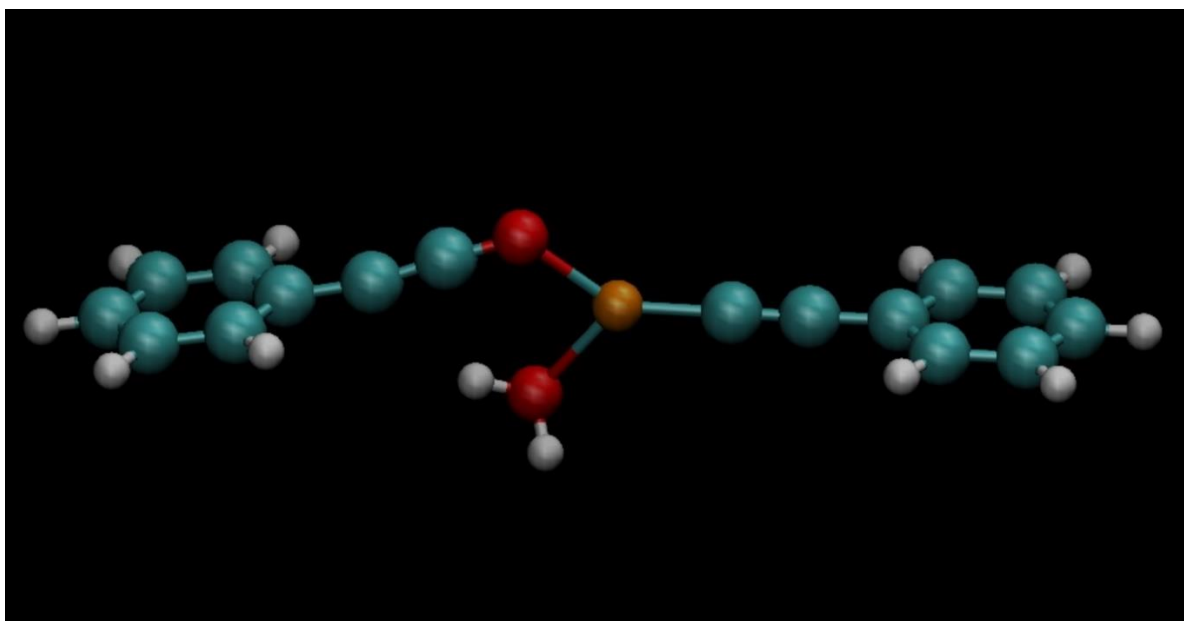
Figure. D.S11e. DFT-predicted Structure of homogeneous Cu complex, $[CuO(C_8H_5)_2H_2O]^-$. Color code: Orange - Copper atom; Red – Oxygen atom; Cyan-Blue – Carbon atom, White – Hydrogen atom.
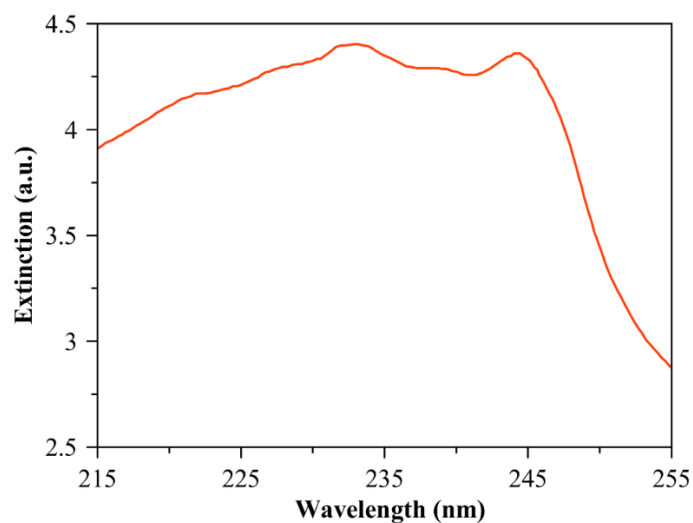
Figure. D.S12a. UV-Vis extinction spectrum of Phenylacetylene (PA) can be found in the reference. (Ref: Phenylethyne, https://webbook.nist.gov/cgi/cbook.cgi?ID=536-74-3, (accessed May 4, 2019)
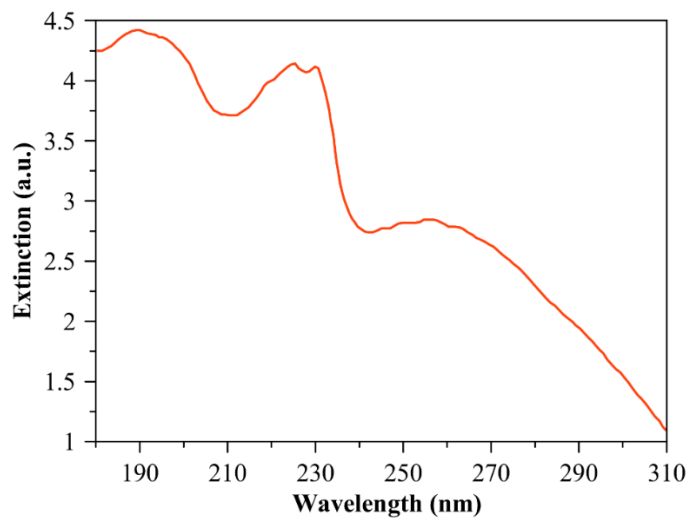
Figure. D.S12b. UV-Vis extinction spectrum of Iodo-Benzene (IB) can be found in the reference.(Ref:Benzene, iodo-, https://webbook.nist.gov/cgi/cbook.cgi?ID=C591504&Mask=400, (accessed May 4, 2019)
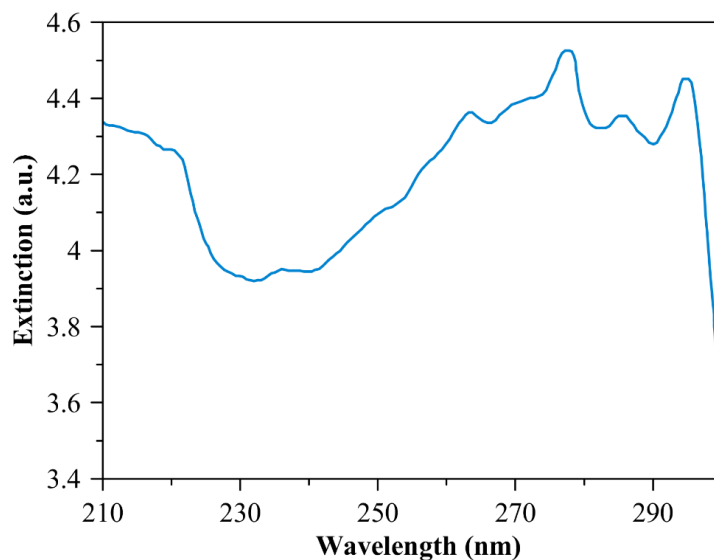
Figure. D.S12c. UV-Vis extinction spectrum of Di-phenyl Acetylene (DPA) can be found in the reference. (Diphenylacetylene, https://webbook.nist.gov/cgi/cbook.cgi?ID=C501655&Mask=400, (accessed May 4, 2019)
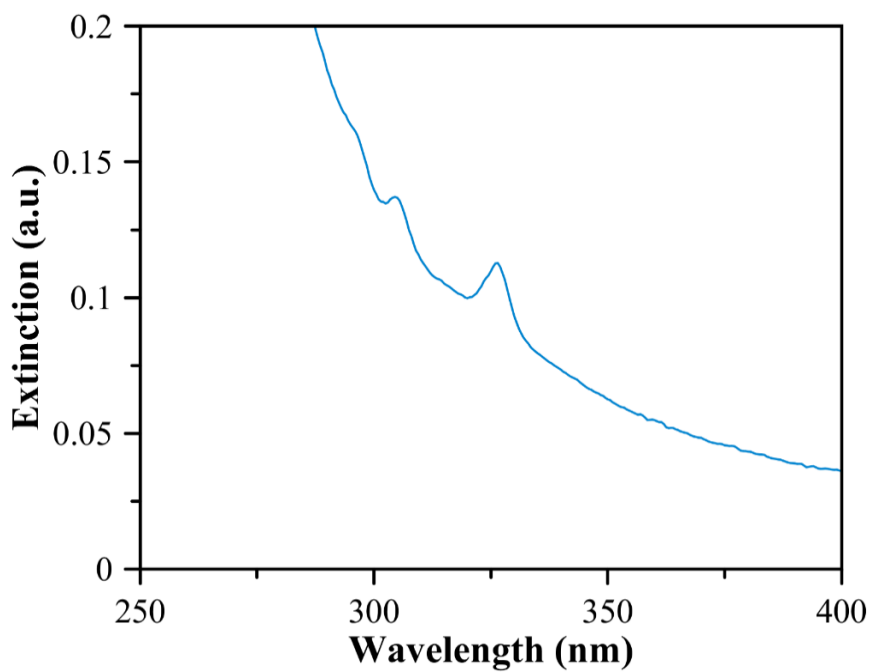
Figure. D.S12d. UV-Vis extinction spectrum of diphenyldiacetylene (DPDA).
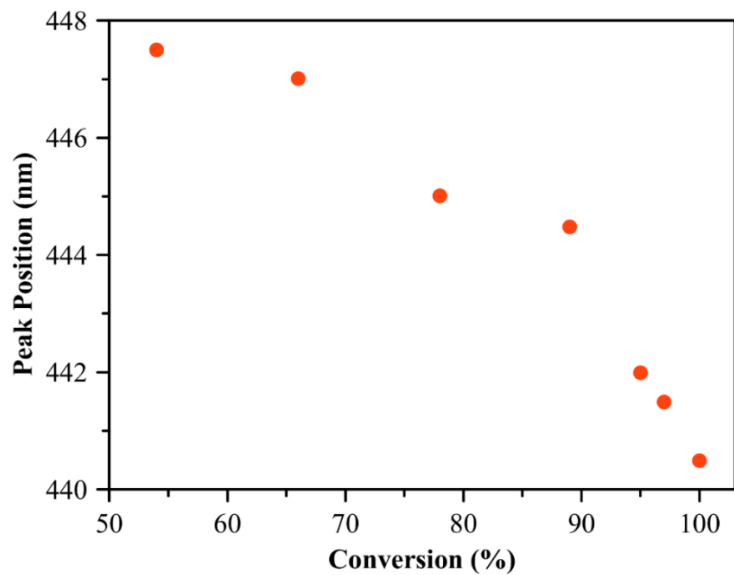
Figure. D.S13a. Extinction peak position in the 440-450 nm region of the UV-Vis extinction spectrum as a function of PA conversion for OHR in the presence of base.
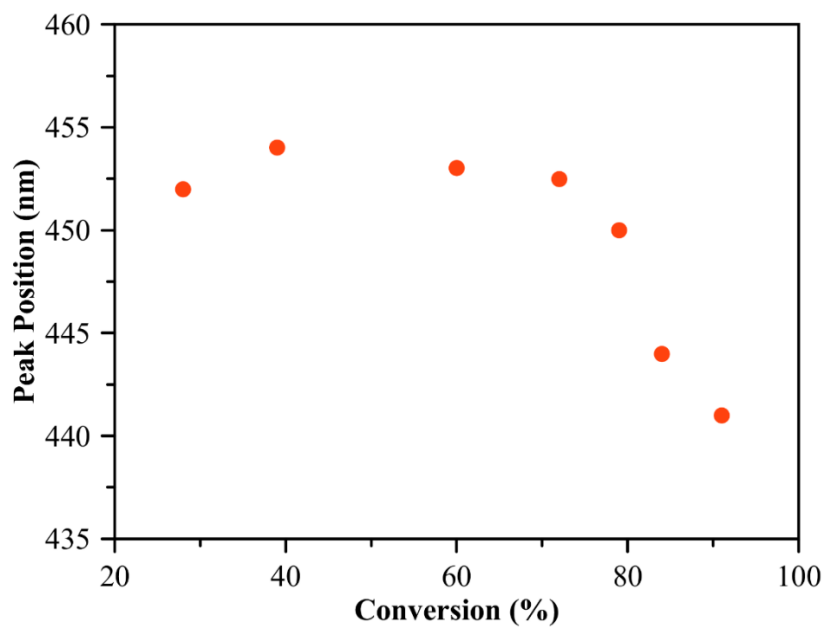

Figure. D.S13b. Extinction peak position in the 440-460 nm region of the UV-Vis extinction spectrum as a function of PA conversion for SCR between PA and iodobenzene (IB) in the presence of base.

Figure D.S13b shows that during the SCR between PA and IB, the peak position changes in the range of ~440-455 nm. We also observed that the maximum range of change in peak position depends on the aryl-halide (Ar-X) coupling partner. For example, when nitro-Iodobenzene is used as coupling partner, we observed the change in the peak position in the range of 440 to 481 nm. These results indicate that the homogeneous Cu species formed via PA-induced leaching of surface atoms further interact with the aryl-halide partner to form other homogeneous Cu species in the catalytic cycle. The extinction peaks of these Cu catalytic species are closely spaced, their combined extinction peaks appear as a single peak in the measured UV-Vis extinction spectrum. The results also suggest that the changes observed in the measured extinction peak position are due to the change in the relative concentration of these homogeneous Cu catalytic species with reaction time and conversion.
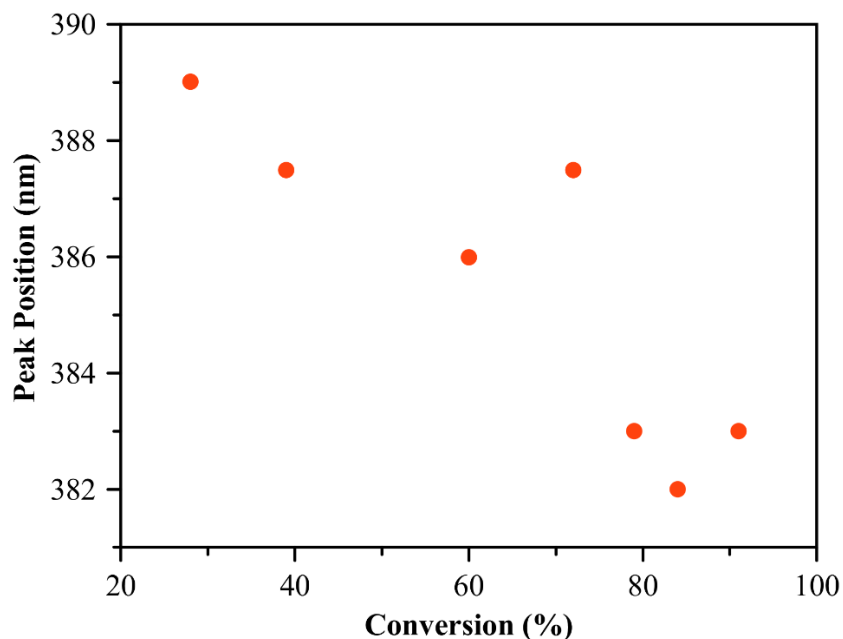

Figure. D.S13c. Extinction peak position in the 380-390 nm region of the UV-Vis extinction spectrum as a function of PA conversion for SCR in the presence of base.
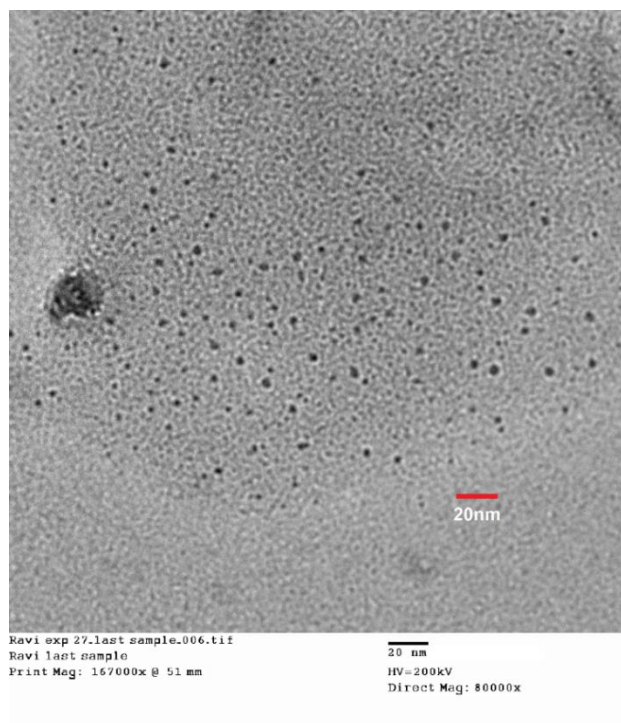
Figure. D.S14. Representative TEM image of blacked out Cu$_2$O nanoclusters (average size: 3 ± 0.7 nm) observed in the reaction solution at the end of OHR.
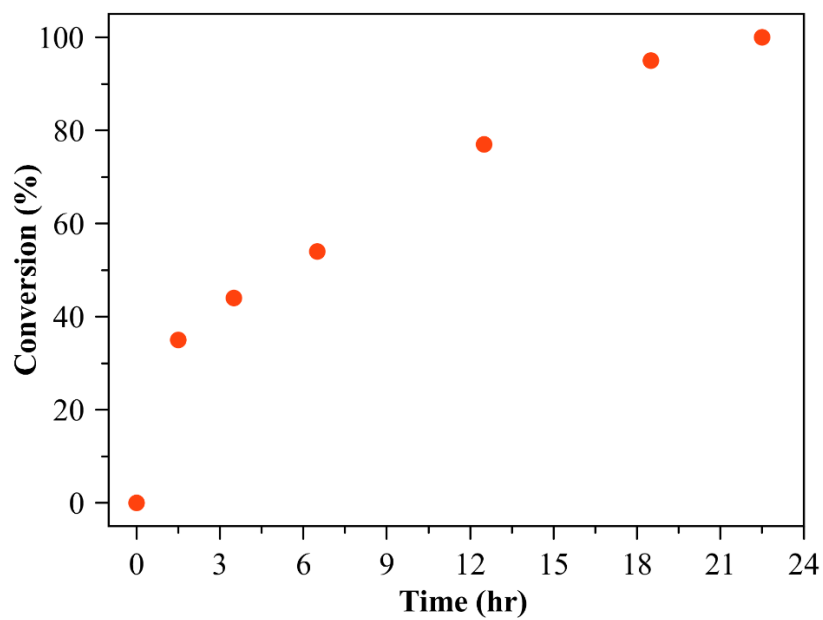

Figure. D.S15. Conversion as a function of Reaction Time for SCR with Bromo Benzene at 147 °C (under reflux) in the presence of the base.
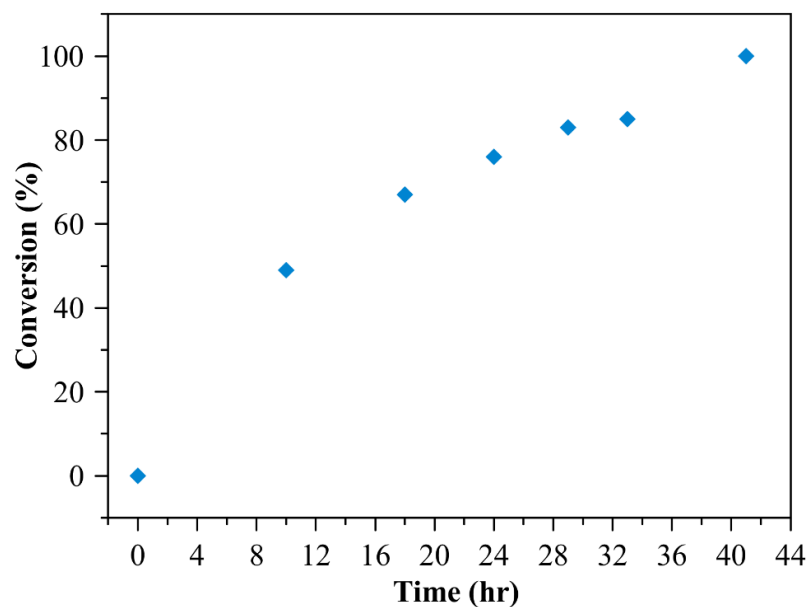
Figure. D.S16. Conversion as a function of Reaction Time for SCR with Bromo Benzene at 147 °C (under reflux) in the absence of the base.
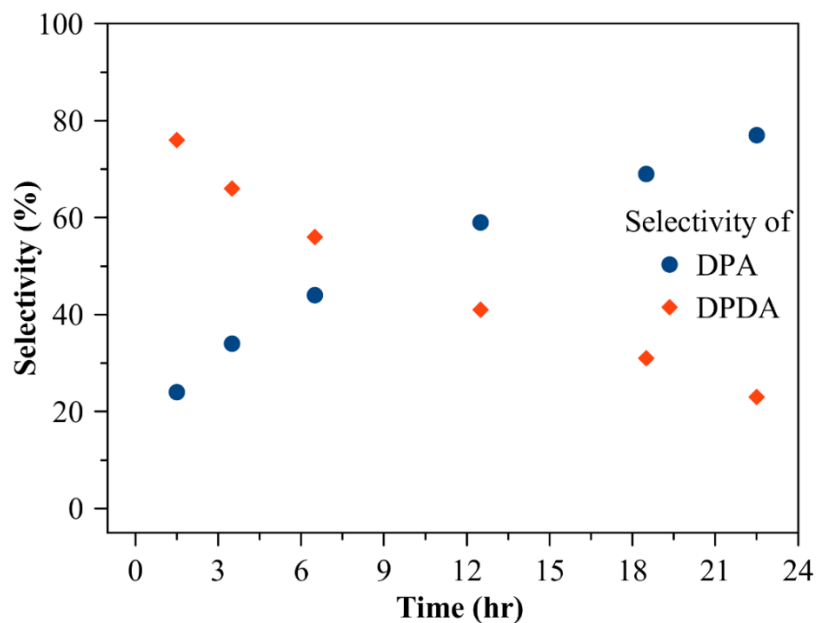

Figure. D.S17. The cross-coupling and homocoupling products DPA vs DPDA selectivity as a function of reaction time for SCR with Bromo Benzene at 147 °C (under reflux) in the presence of the base.
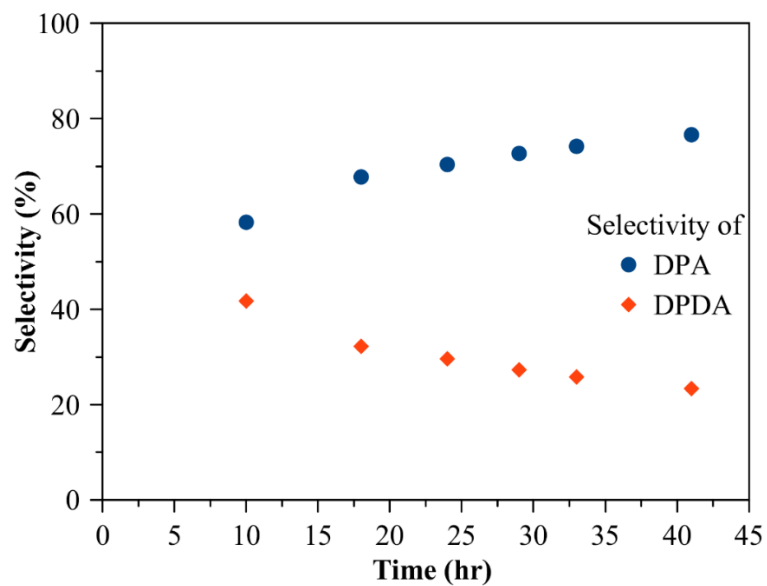
Figure. D.S18. The cross-coupling and homocoupling products DPA vs DPDA selectivity as a function of reaction time for SCR with Bromo Benzene at 147 °C (under reflux) in the absence of the base.
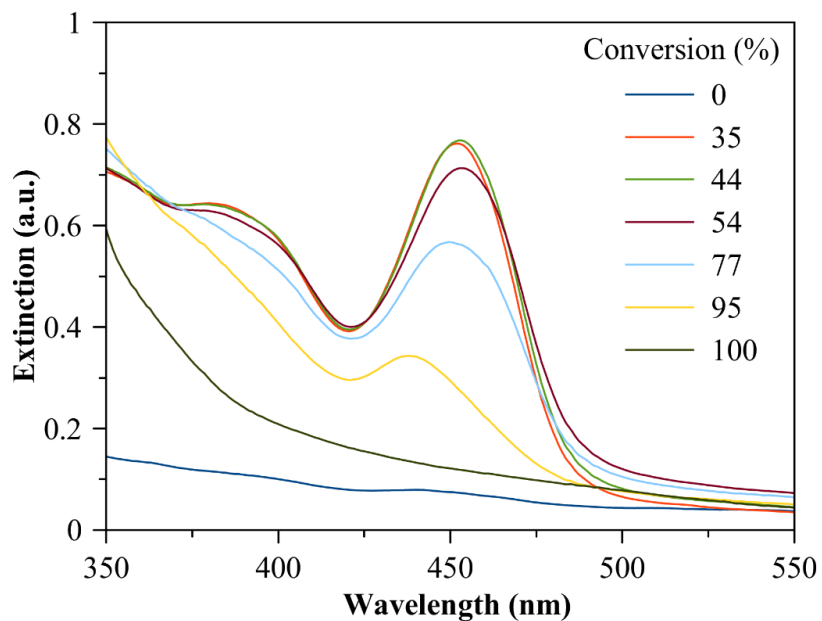

Figure. C.S19. UV-Vis extinction spectra of reaction mixture measured at different reaction conversions during SCR with Bromo Benzene at 147 °C (under reflux) in the presence of base.

The extinction peaks centered at ~385 and ~450 nm in Figure C.S8 are due to homogeneous Cu complexes in the reaction solution. These peaks are observed in the reaction solution only when both PA and base are present.
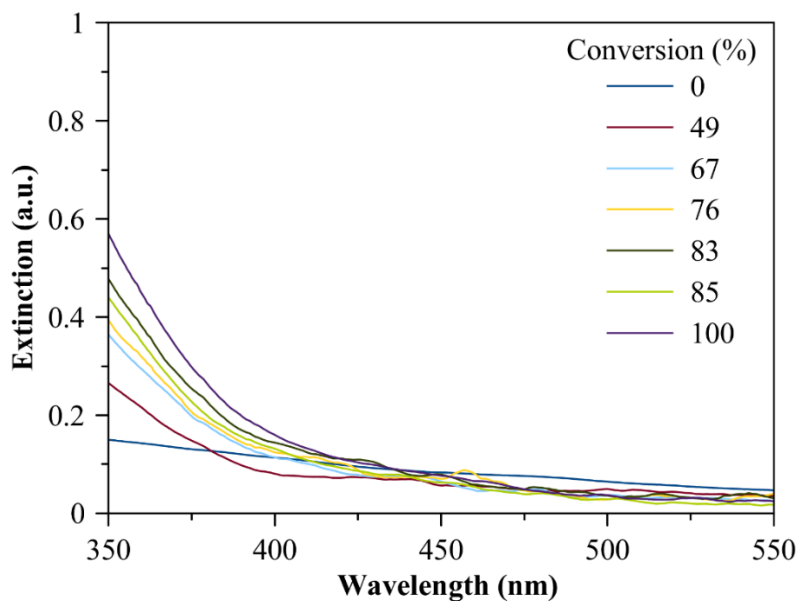

Figure. D.S20. UV-Vis extinction spectra of reaction mixture measured at different reaction conversions during SCR with Bromo Benzene at 147 °C (under reflux) in the absence of the base. The changes observed in the extinction spectra in Figure.C.S19 for different conversions are most likely due to the expected change in dielectric constant of the reaction mixture for the respective conversions.
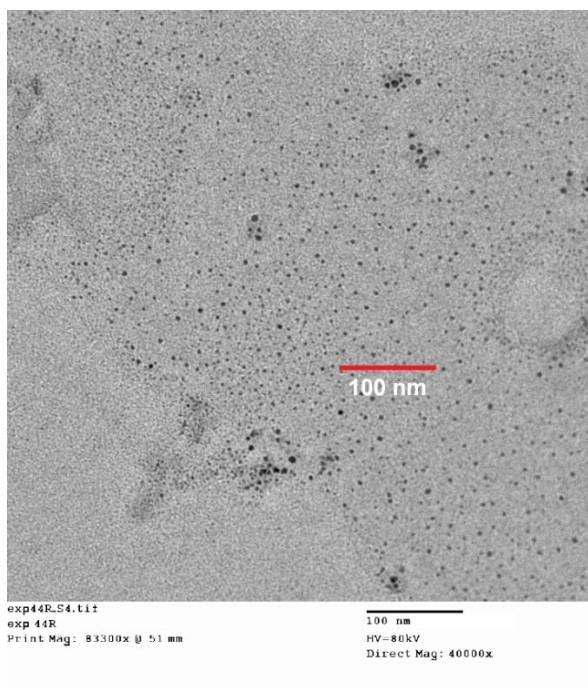
Figure. D.S21. Representative TEM image of blacked out Cu_2O nanoclusters (average size: 3.6 ± 0.94 nm) observed in the reaction solution at the end of SCR.

ROLE OF BASE, OXYGEN, SOLVENT IN C-C HOMOCOUPLING REACTION

Summary of Catalytic pathway of Cu$_2$O NPs-mediated oxidative C-C homocoupling of phenylacetylene:

The homocoupling of phenylacetylene (PA) was carried out at 110 °C using spherical Cu$_2$O NPs with an average size of 34 nm (see Figure E.S2a). The samples of the reaction mixture were taken at frequent time intervals to quantify the reaction conversion using GC-MS analysis. The samples were also characterized using UV-Vis extinction spectra measurements to identify any possible formation of homogeneous copper (Cu) complexes. In Figure E.S1a, we show the PA conversion as a function of reaction time. As seen from Figure E.S1a, the complete conversion was observed in less than 9 hours under the reaction conditions investigated in this study. Diphenyldiacetylene (DPDA) was the only observed product during the reaction. In Figure E.S1b, we show the UV-Vis extinction spectra of reaction mixture measured before the addition of substrate (i.e., PA) and at different reaction times. As seen from Figure E.S1b, the extinction spectrum acquired before the addition of PA (i.e., t=0) shows only the extinction features of Cu$_2$O NPs. As the reaction starts after the addition of PA, new extinction peaks at ~385 and ~450 nm are evolved. We verified that the homocoupling product, DPDA, exhibits absorption peaks only in the 200-350 nm region. Therefore, the appearance of the new extinction peaks upon PA addition indicates the in-situ formation of homogeneous Cu complexes via PA-induced leaching of Cu$_2$O NPs surface atoms.

The presence of homogeneous Cu complexes, $[CuO(C_8H_5)_2]^-$ and $[CuO(C_8H_5)2H_2O]^-$, are confirmed using ESI-MS analysis of the supernatant solution of the reaction mixture as shown in Figure E.S1c. The ESI-MS analyzed the structure of the Cu complex, $[CuO(C_8H_5)_2]$, suggests that

two PA (C_8H_6) molecules first adsorb on the surface of Cu_2O NPs (i.e., one molecule on surface Cu atom and another molecule on neighboring surface O atom), and subsequently cause the leaching of Cu and O surface atoms. The second complex, $[CuO(C_8H_5)2H_2O]^-$, can then form from the first complex, $[CuO(C_8H_5)_2]^-$, and water (H_2O) molecule, which is the expected byproduct of oxidative C-C homocoupling of terminal alkynes. The leaching of Cu_2O NPs is also confirmed using TEM. Specifically, the size of Cu_2O NPs was reduced from the initial size of 34 ± 4 nm (see Figure E.S2a) to 16 ± 4 nm at the end of the reaction as shown in Figure E.S1d.

Two homogenous complexes, $[CuO(C_8H_5)_2]^-$ and $[CuO(C_8H_5)2H_2O]^-$, are observed in the ESI-MS spectra (Figure E.S1c). The density functional theory (DFT) calculations reported in our previous contributions confirm that these two complexes are expected to exhibit the UV-Vis extinction peak wavelengths of ~385 nm and ~450 nm, respectively.[40] Therefore, we assign the complexes observed at ~385 nm and ~450 nm in the UV-Vis extinction spectra (Figure D.S1b) to $[CuO(C_8H_5)_2]^-$ and $[CuO(C_8H_5)2H_2O]^-$, respectively. To illustrate the role of the homogeneous Cu complexes in the C-C homocoupling reaction, in Figure E.S1e, we plot the extinction intensity of Cu complex, $[CuO(C_8H_5)2H_2O]^-$ which shows UV-Vis extinction peak intensity ~450 nm, as a function of reaction time. Similar plot for the complex $[CuO(C_8H_5)_2]$- is shown in Figure E.S3a. It can be concluded from Figures E.S1c and E.S1e and Figure E.S3a that the concentration of homogenous Cu complexes changes with time and PA conversion as expected for the homogeneous catalytic species that participate in the catalytic cycle. It can also be observed in Figure E.S1e and Figure E.S3a that the concentrations of Cu catalytic species exhibit maxima followed by decreasing trend as the concentration of the reactant (i.e., PA) gets depleted with time. This trend is expected for the in-situ generated homogeneous catalytic species. Specifically, we attribute the decreasing trends in Figure E.S1e to the blackout or precipitation of homogeneous Cu catalytic species with the decreasing concentration of stabilizing species (i.e., PA). The presence of blacked-out Cu clusters (size = 4 ± 0.8 nm) is also confirmed at the end of

the reaction sample as can be seen from the representative TEM image shown in Figure E.S1f. To further confirm that the observed homogenous Cu complexes are indeed catalytic species, we performed the reaction containing only the supernatant solution containing Cu complexes. The results from this experiment show that the Cu complexes are able to catalyze the homocoupling of phenylacetylene (PA) into complete conversion, as shown in Figure E.S3b.
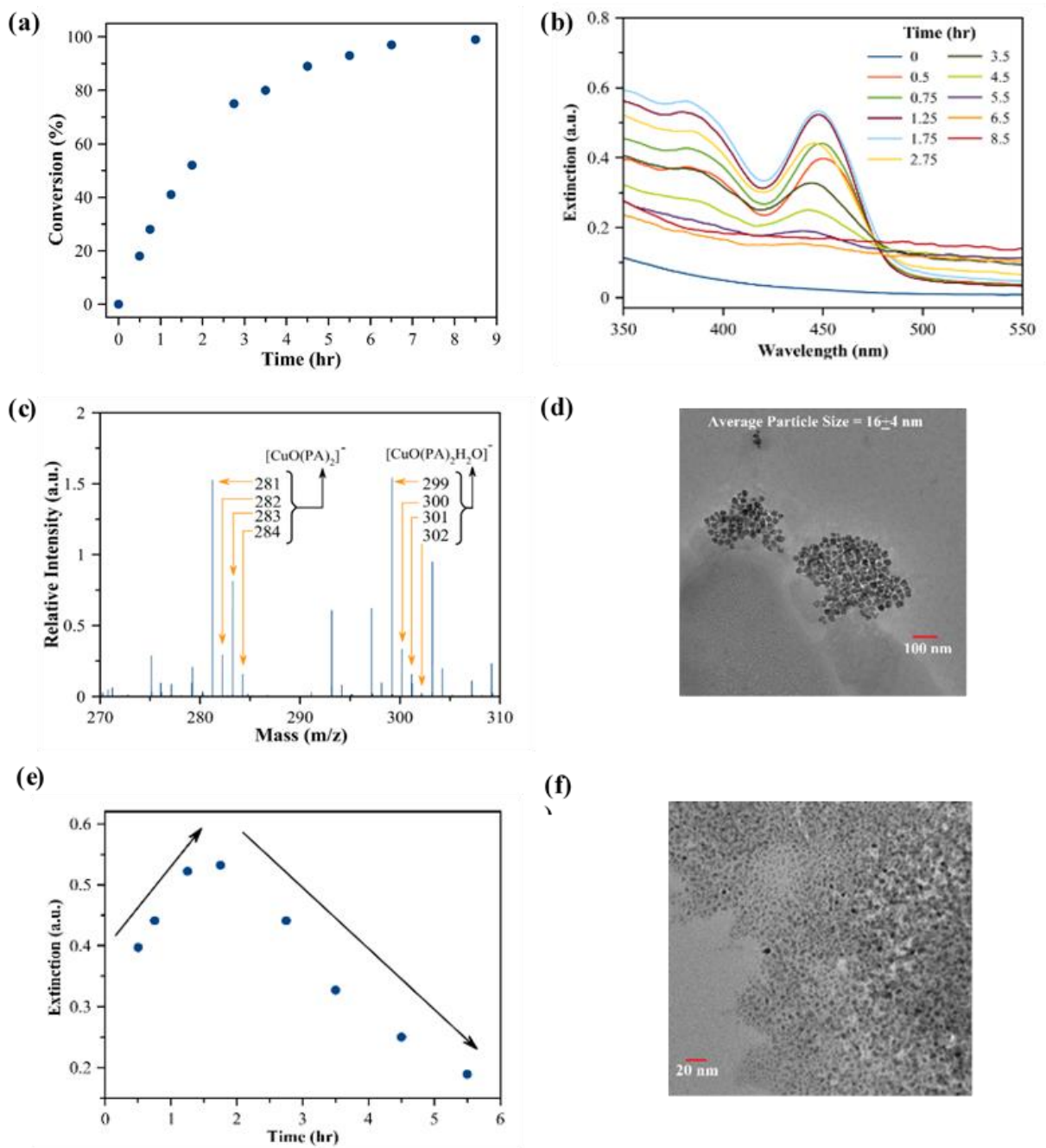
Figure. E.S1. (a) Conversion as a function of reaction time for the homocoupling reaction of PA at 110 °C. (b) UV-Vis extinction spectra of reaction mixture measured before the addition of PA (i.e., 0 % conversion) and at different reaction conversions during the homocoupling reaction of PA at 110°C. (c) Representative ESI-MS spectra of $[CuO(C_8H_5)_2]^-$ and $[CuO(C_8H_5)_2H_2O]^-$. (d) Representative TEM image of Cu_2O nanoparticles observed in the reaction mixture at the end of

the reaction (Average size of Cu_2O NPs = 16 ± 4 nm). (e) Extinction intensity at the peak

wavelength of ~450 nm in the UV-Vis extinction spectrum of the reaction mixture as a function

of reaction time. (f) Representative TEM image of blacked-out nanoclusters observed in the

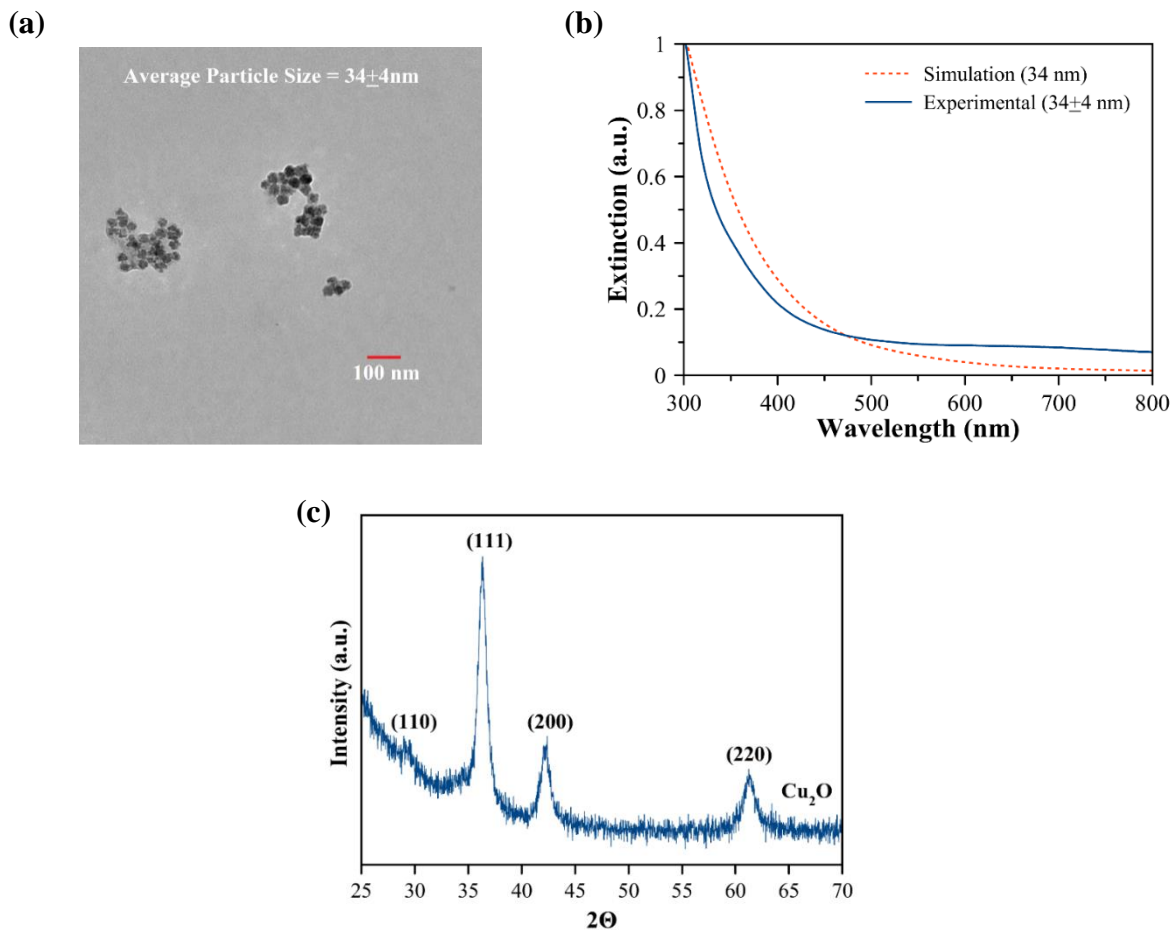reaction solution at the end of the reaction (Average size of nanoclusters = 4 ± 0.89 nm).

(a)

(b)

(c)

Figure. E.S2. (a) A representative TEM image of the Cu_2O nanoparticles (34±4 nm). (b)

Comparison of experimental and computational measurement of UV-Vis extinction spectrum for

Cu_2O nanoparticles for the particle size 34 nm. (c) The X-ray diffraction pattern of the Cu_2O
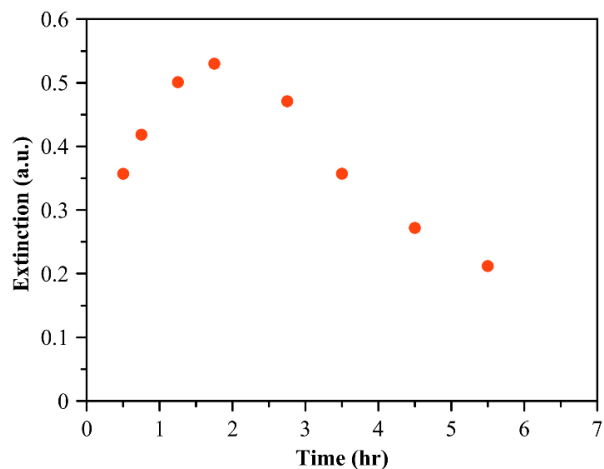
nanoparticles.

Figure. E.S3a. Extinction intensity at the peak wavelength of ~385 nm in the UV-Vis extinction spectrum of the reaction mixture as a function of reaction time.
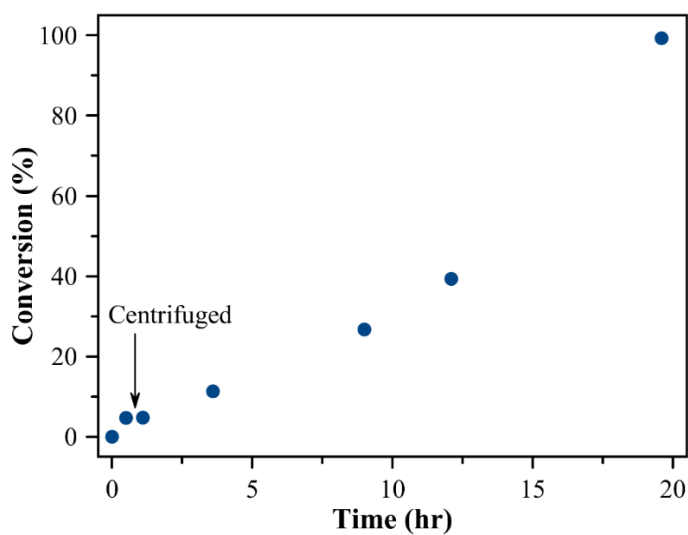

Figure. E.S3b. Conversion as a function of reaction time for homocoupling of PA at 110 °C, where the gas used was dry air. After the end of 30 minutes into the reaction, it was stopped and Cu_2O nanoparticles were removed from the reaction mixture using centrifugation. The reaction is continued under same conditions using Cu complexes in supernatant solution as the solitary catalyst.
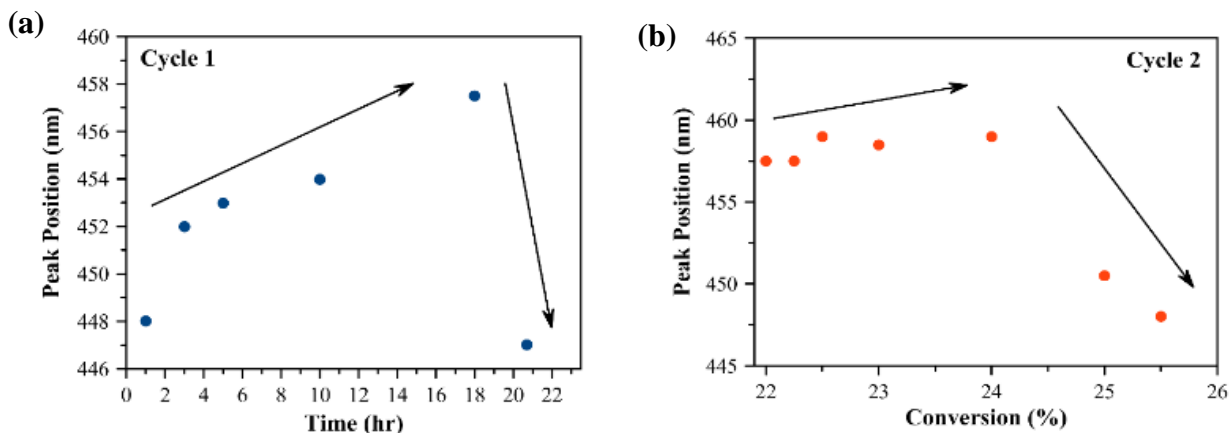
Figure. E.S4. (a) Peak position for OHR of PA at 110 °C in the presence of base, where the gas was switched from N_2 to Dry Air after 20 h of reaction time for Cycle 1. (b) Peak position for OHR of PA at 110 °C in the presence of base, where the gas was continued to be Dry Air after end of first cycle, for Cycle 2.
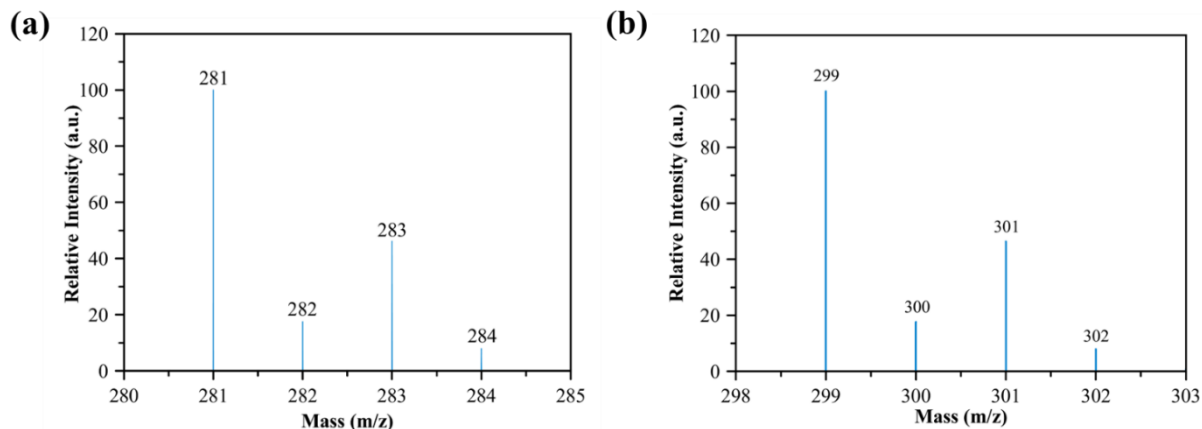

Figure. E.S5. (a) Predicted mass spectrum for the proposed copper complex with chemical formula, $[CuO(PA)_2]-$. (b) Predicted mass spectrum for the proposed copper complex with chemical formula, $[CuO(C_8H_5)2H_2O]-$.[204]

VITA

Ravi Teja Addanki Tirumala

Candidate for the Degree of

Doctor of Philosophy

Dissertation: EXPLOITING THE OPTICAL PROPERTIES OF EARTH ABUNDANT CUPROUS OXIDE NANOCATALYSTS FOR ENERGY AND HEALTH APPLICATIONS

Major Field: Chemical Engineering

Biographical:

Education:

Completed the requirements for the Doctor of Philosophy in Chemical Engineering at Oklahoma State University, Stillwater, Oklahoma in July, 2022.

Completed the requirements for the Master of Technology in Chemical Engineering at University of Petroleum and Energy Studies, Dehradun, India in 2015.

Completed the requirements for the Bachelor of Technology in Chemical Engineering at Sathyabama University, Chennai, India in 2013.

Experience:

Research Scientist-R&D, Pluss Advanced Technologies – Gurugram, India
        Jun 2015 – Jun 2017
Research Scholar, Indian Oil Corporation Limited (IOCL) R&D Centre, India
        Jun 2014 – Jun 2015
Served as Liaison, Vice President for Chemical Engineering Graduate Student Association, and Teaching Assistant for three semesters.

Professional Memberships:

AICHE, GPCS, ACS, NAMS